Phonon Dynamics and Damping in Three-Dimensional Acoustic Bandgap Cavity-Optomechanical Resonators

Thesis by
Gregory S. MacCabe

In Partial Fulfillment of the Requirements for the
Degree of
Doctor of Philosophy

CALIFORNIA INSTITUTE OF TECHNOLOGY
Pasadena, California

2019
Defended July 12th, 2018

Gregory S. MacCabe
ORCID: 0000-0003-2369-1580

ACKNOWLEDGEMENTS

To my advisor, Oskar, whose guidance in the course of this research made my graduate career possible: thank you for giving me the chance to learn from your brilliance in our field. There were numerous occasions when your insights, and discussions we had in your office or in the lab, revived my excitement for pushing the boundaries of our research together. I will always admire your determination and be imprinted with your optimism that good science is possible–even opportune–in the face of great technical difficulty. Thank you.

This thesis is a product of the accumulated experience, knowledge, and scientific tenacity which Oskar cultivates in his research Group at Caltech. I could not have performed the experiments presented here without relying heavily on the past developments and insights of the Group, and of Oskar – and I certainly did not do it alone. Thank you to all those who helped push this research as far as it's gone, and who have helped me personally in its course. The environment of teamwork, collaboration, and shared enthusiasm for doing things right in the Painter Group is irreplaceable in my heart.

When I finished my undergraduate time at the University of North Carolina, I didn't yet realize the extent to which my life would be enriched by traveling to California and studying physics in this historic place. I am deeply grateful to all the instructors and mentors I've been lucky enough to have through the years, both inside and outside Caltech. Jane Schelbe, Tom Clegg, Sean Washburn, Rich Superfine, Reyco Henning, John Engel, Tony Hotz, Rob Washeleski, Oskar Painter, numerous members of the physics and applied physics/materials science faculty at Caltech, and the friends and colleagues I've come to know along the way.

My greatest early influences in physics came from my dad, Stephen, and my older brother, Ken. I remember being about 12 years old when Ken first humored my curiosity about quantum oddities by telling me about the delayed-choice "quantum eraser." I think we have a shared respect for the fundamental mysteries of nature, but mine grew in large part from his. Some part of me has always found physics exciting because I knew that two of the people I admire most, Dad and Ken, shared in that excitement. Dad, thanks for always supporting my pursuit of science and math.

Justin Cohen, I am extremely grateful for the guidance you've given me through the

years. You brought me up to speed in the field and on projects for multiple years, and I'd hardly ever set foot in a cleanroom five years ago; now I only see right in yellow light. You gave me the instincts I needed to perform in this Group and you entrusted me with adding to your graduate work. I appreciate it. Seán Meenehan, I have an immense respect for your approach to problem-solving. Thanks for your guidance and discussions during my first couple years here.

To my closest collaborator and friend in the Group, Jared, what a journey it's been. How many thousands of hours have we spent together poring over the optical setups and the data streams? How many thousands of texts, calls, and emails to keep such complex experiments running efficiently, or to get those fab recipes working just in time for a cooldown? There's no replacing that, and there's no overstating how rewarding it has been to work with you on these projects. You have a very bright future ahead, Mr. False-Trigger.

Many other past and present Group members have impacted me throughout my time here. Mahmoud, thanks for being a consistent friend through five years in the Group. I owe special thanks to Tim Blasius, Johannes Fink, Szilard Szöke, Roger Liu, Kejie Fang, Mohammad Mirhosseini, Su-Peng Yu, Andrew McClung, Hannes Pfeiffer, Paul Dieterle, Michael Fang, Andrew Keller, Neil Krueger, Anthony Ardizzi, Hengyun Zhou, Ewan Painter, Neil Sinclair, and others. Thanks to Michelle Rodriguez for your crucial support and conversations that helped buoy my mental state, Barry Baker for years of fixing things together, and Jonathan Gross for absolute reliability and being softball MVP. Thank you Guy DeRose, Melissa Melendes, Alex Wertheim, Nathan Lee, and the rest of the KNI staff.

To my mom, your love has enabled me to do what I do.

To Elle, thank you for your continued support through some of the most intense and trying times in my pursuit of this thesis. May this be only the beginning.

ABSTRACT

Mechanical resonators are used in a wide variety of technical applications, from precision time keeping and sensing, to the delay and filtering of microwave signals in mobile communication systems. Critical to many of these applications is the ability of a mechanical object to store vibrational energy at a well defined frequency of oscillation and with minimal damping. Energy damping can occur through acoustic radiation into the resonator support structure, or through impurities and defects in the resonator material, and is highly dependent on the temperature of operation due to the inherent anharmonic motion of atoms within solid-state materials. Here, we present optical measurements down to milliKelvin temperatures of the acoustic mode properties of a crystalline silicon nanobeam cavity incorporating a three-dimensional phononic bandgap support structure for acoustic confinement. Utilizing pulsed laser light to excite a co-localized optical mode of the optomechanical crystal (OMC) device, we are able to measure the dynamics of the internal cavity acoustic modes which are coupled to the light field via radiation pressure. These measurements represent an almost ideal scenario in which the ringdown occurs free of any additional mechanical or probe field contact, and where elastic scattering or radiation of the acoustic field does not lead to energy damping due to the full bandgap shield. The resulting ringdown measurements for the fundamental 5 GHz acoustic mode of the cavity show an exponential increase in phonon lifetime versus phononic shield period number, which at a bath temperature of 35 milliKelvin saturates above six periods to a value as long as 1.5 seconds. This ultra-long lifetime, corresponding to an effective phonon propagation length of several kilometers, is found at the lowest temperatures to be consistent with damping from non-resonant tunneling states whose energy lies below the acoustic shield phononic bandgap, and which are most likely present in the amorphous etch-damaged region of the silicon surface. Other, more rapid forms of damping such as resonant tunneling state damping or three-phonon scattering are suppressed due to the phononic bandgap shield and the reduced density of phonon states in the effectively one-dimensional nanobeam geometry. Prospects for new applications of ultra-coherent nanoscale mechanical resonators include tests of various collapse models of quantum mechanics, or, if appropriately integrated with microwave superconducting quantum circuits, as miniature quantum memory or processing units with potentially many-orders of magnitude longer coherence time than their electromagnetic counterparts.

PUBLISHED CONTENT AND CONTRIBUTIONS

[1] G. S. MacCabe, H. Ren, J. Luo, J. D. Cohen, H. Zhou., A. Sipahigil, M. Mirhosseini, and O. J. Painter. "Phononic bandgap nano-acoustic cavity with ultralong phonon lifetime". In: *arXiv* 1.1901.04129 (2019).
G. S. M. Participated in fabricating the devices, planning and performing the experiments, analyzing the data, and preparing the manuscript.

[2] J.D. Cohen, S. M. Meenehan, G. S. MacCabe, S. Gröblacher, A. H. Safavi-Naeini, F. Marsili, M. D. Shaw, and O. J. Painter. "Phonon counting and intensity interferometry of a nanomechanical resonator". In: *Nature* 520 (2015), pp. 522–525. DOI: 10.1038/nature14349.
G. S. M. Participated in fabricating the devices, performing the measurements, and analyzing the data.

[3] S. M. Meenehan, J.D. Cohen, G. S. MacCabe, F. Marsili, M. D. Shaw, and O. J. Painter. "Pulsed Excitation Dynamics of an Optomechanical Crystal Resonator near Its Quantum Ground State of Motion". In: *Physical Review X* 5.041002 (2015). DOI: 10.1103/PhysRevX.5.041002.
G. S. M. Participated in fabricating the devices, planning and performing the measurements, analyzing the data, preparing the manuscript, and responding to peer reviewers.

TABLE OF CONTENTS

LIST OF ILLUSTRATIONS

LIST OF TABLES

To my parents

"And this I believe: that the free, exploring mind of the individual human is the most valuable thing in the world. And this I would fight for: the freedom of the mind to take any direction it wishes, undirected. And this I must fight against: any idea, religion, or government which limits or destroys the individual. This is what I am and what I am about."
—John Steinbeck, *East of Eden*

Table 0.1: Index of symbols and notation.

Symbol	Description
$\hbar$	Reduced Planck's constant
c	Speed of light
ϵ_0	Permittivity of free space
μ_0	Permeability of free space
k_B	Boltzmann's constant
G_th	Thermal conductance
ω_c	Optical cavity resonance frequency
ω_L	Laser drive frequency
ω_LO	Local oscillator frequency
Δ	Laser-cavity detuning, $\Delta = \omega_c - \omega_\mathrm{L}$
ω_m	Mechanical resonance frequency
γ_0	Intrinsic mechanical energy damping rate
Q_m	Mechanical quality factor
m_eff	Mechanical effective mass
κ	Optical cavity energy decay rate, $\kappa = \kappa_\mathrm{i} + \kappa_\mathrm{e}$
κ_i	Intrinsic optical cavity decay rate
κ_e	Extrinsic (coupling) optical cavity decay rate
$\hat{a}$ ($\hat{a}^\dagger$)	Optical cavity mode bosonic annihilation (creation) operator
$\hat{b}$ ($\hat{b}^\dagger$)	Mechanical mode bosonic annihilation (creation) operator
g_0	Vacuum optomechanical coupling rate
n_c	Intracavity photon number, $n_\mathrm{c} = \langle \hat{a}^\dagger \hat{a} \rangle$
G	Effective optomechanical coupling rate, $G = g_0\sqrt{n_\mathrm{c}}$
$\bar{n}$	Thermal phonon occupancy, $\bar{n} = (e^{\hbar\omega_m/k_\mathrm{B}T} - 1)^{-1}$
$\langle n \rangle$	Average phonon occupancy
n_p	Effective phonon occupancy of optically-induced heating bath
n_b	Effective phonon occupancy of total effective mechanical bath
γ_OM	Optomechanical scattering rate, $\gamma_\mathrm{OM} = 4g_0^2 n_\mathrm{c}/\kappa$ ($\Delta = \pm\omega_m$)
γ_p	Mechanical heating bath-induced damping rate
C_0	Bare optomechanical cooperativity, $C_0 = \gamma_\mathrm{OM}/\gamma_0$
C	Optomechanical cooperativity, $C = \gamma_\mathrm{OM}/(\gamma_0 + \gamma_\mathrm{p})$
C_eff	Effective (quantum) optomechanical cooperativity, $C_\mathrm{eff} = C/n_\mathrm{b}$
x_zpf	Mechanical zero-point fluctuation, $x_\mathrm{zpf} = \sqrt{\hbar/(2m_\mathrm{eff}\omega_m)}$
$\chi_a(\omega)$	Bare optical cavity susceptibility, $\chi_a(\omega) = (i(\Delta - \omega) + \kappa/2)^{-1}$
$\chi_b(\omega)$	Bare mechanical mode susceptibility, $\chi_b(\omega) = (i(\omega_m - \omega) + \gamma_i/2)^{-1}$
$S_{\hat{b}\hat{b}}[\omega]$	Two-sided spectral density of the mechanical mode, $S_{\hat{b}\hat{b}}[\omega] = \int_{-\infty}^{\infty} \frac{d\omega'}{2\pi} \langle \hat{b}^\dagger(\omega)\hat{b}(\omega') \rangle$
$\bar{S}_{\hat{b}\hat{b}}[\omega]$	Symmetrized spectral density of the mechanical mode, $\bar{S}_{\hat{b}\hat{b}}[\omega] = (S_{\hat{b}\hat{b}}[\omega] + S_{\hat{b}\hat{b}}[-\omega])/2$
n_NEP	Noise-equivalent phonon number
$\Gamma_\mathrm{SB,0}$	Per-phonon scattered photon flux

Chapter 1

PROLOGUE

The fact that light exerts a force on matter has been known in some degree for centuries. Early scientific attention to this notion took the form of comments upon observations of apparently unrelated physical phenomena, the earliest of which is thought to be Kepler's notes on the deflection of comet tails by solar irradiation in 1619 [1]. Over 250 years later, Sir William Crookes invented a hand-held radiometer device which rotates when irradiated with light—attracting a flurry of phenomenological theories aiming to explain its rotation as the result of an optical force [2]. In actuality the rotation of the Crookes radiometer is explained by thermodynamic effects [3], and the optical radiation pressure force as predicted by Maxwell's full theory of classical electromagnetism [4] would not find direct experimental confirmation for a further two decades. This came in 1901 when Nichols and Hull developed a new radiometer, very similar to that of Crookes, but with appropriate sensitivity to detect Maxwell's radiation pressure force to within 0.6% of its predicted magnitude [5].

In the decades that followed in the early 20^{th} century, the quantum theory of light and its interactions with matter was rapidly maturing with herculean experimental studies of the photoelectric effect and blackbody radiation by Millikan, Einstein, Planck, and others. Einstein considered the effects of radiation pressure fluctuations on a movable mirror [6] in helping to develop the theory of blackbody radiation. In parallel with this, theoretical work by the Dirac and others aimed at understanding the interaction of light and matter at the level of single quanta—in particular to develop a theory of atomic spontaneous emission and level shifts in Hydrogen. In this era nearing the middle of the 20^{th} century, the theoretical framework of quantum electrodynamics (QED) was resolving as the full quantum theory of light. The theoretical foundations provided by QED would underpin all later studies of the radiation pressure interaction at the quantum level.

Following the development of the laser in the late 1950s [7], a new frontier was opened in the study of radiation pressure and its potential applications to precision sensing and manipulation of matter. Laser feedback cooling of dielectric particles

and atomic clouds was demonstrated in the late 1970s [8, 9], in which the vibrational degrees of freedom of a test mass are cooled by appropriate frequency tuning of an impinging optical field, and optical scattering via radiation pressure was also finding use in the study of many-body physics in atomic clouds [10]. The possibility of using laser light to cool ever larger mechanical objects attracted a great deal of scientific interest in the 1970s. Braginsky, Dykman, and others scrutinized the interaction of suspended mirrors and cavity light fields, largely in the context of developing ever better optical interferometers for position sensing, and identified regimes in which vibrations of a mirror may be either damped (cooled) *or* amplified (heated) by interactions with the light field (although these early experimental works were performed in the more experimentally accessible microwave frequency regime). A pioneering experimental work by Dorsel [11] in 1983 found regimes of optical bi-stability arising from the radiation pressure in an optical cavity with a suspended movable end-mirror—begetting in the *optical* domain the field of cavity-optomechanics. In this field, the canonical physical picture is that of a Fabry-Perot cavity for which one of the end-mirrors is mechanically compliant and typically modeled as a harmonic oscillator linearly coupled to the circulating light field. In this picture, the motion of the end-mirror modulates either the phase or intensity of incident light, allowing readout of the position or momentum of the mechanical object with a sensitivity that may be limited only by quantum fluctuations in either the light field, the mirror position, or the detection electronics.

Questions regarding the ultimate precision with which the motion of an end-mirror may be sensed motivated a series of theoretical studies by Braginsky in the 1970s, which implied there exists a fundamental quantum-mechanical limitation to the accuracy with which the position of a mechanical element may be measured using optical probing. This imprecision, known later as the *Standard Quantum Limit* (SQL), arises from quantum fluctuations in the radiation pressure interaction which impart random momentum impulses upon the mechanical oscillator. In particular, as the measurement strength or optical intensity is increased, so are the random impulses on the mirror arising from optical shot noise, amounting to the presence of a measurement *back-action* on the motion of the mechanical oscillator. Such a limitation has direct consequences for gravitational wave detection, and specifically for the feasibility of using optical interferometers to sense optical path-length changes induced by a passing gravitational wave. Theoretical analyses by Caves [12] and others in the early 1980s treated this measurement imprecision problem thoroughly, and firmly established in the relevant scientific communities the formal origins of

the SQL in optical sensing. In the following decade various proposals for circumventing the SQL were made, usually relying either on injection of a squeezed optical vacuum to the interferometer—thereby suppressing quantum fluctuations in either the amplitude or phase quadrature—or by placing a Kerr medium in the optical path [13, 14]. Nevertheless, cavity-optomechanical systems (interferometers) have held great interest and demonstrated success as a platform for gravitational wave detection even in the presence of such an SQL.

In the last two decades, cavity-optomechanics has undergone a profound transformation as its versatility in probing the physics of light-matter interaction has become both more apparent and more experimentally accessible with proliferation of optical materials fabrication and nanofabrication techniques. The use of a confined optical mode to cool macroscopic mirrors in 1999 [15] was in many ways the beginning of an ongoing effort to realize control of the acoustic and optical fields, as well as their energy exchange, at ever more delicate levels. Presently, cavity-optomechanical experiments are used for extremely broad classes of studies in the physics of light-matter interaction, quantum information science, gravitational wave detection, force and rotation sensing, gas sensing, and more. The physical principles that describe the light-matter interaction in a cavity-optomechanical system are germane over enormous ranges in size scale, from individual atoms trapped in focused light fields to kilogram-scale mirrors in the gravitational wave detectors of LIGO and VIRGO. The fact that the same system Hamiltonian and governing equations of motion can be used to analyze the dynamics and measurement imprecision over such disparate size scales gives cavity-optomechanics great relevance to human understanding of natural principles.

In its applications to quantum information science and the physics of hybrid- and open-quantum systems, the field of cavity-optomechanics is particularly well suited to miniaturization and interfacing with disparate quantum systems at the nano- and meso-scale. One finds with simple consideration that for any optical cavity, given a number of circulating photons and making fairly general assumptions regarding the quality of the cavity, maximizing the force exerted by a photon on the end-mirror—and hence maximizing the sensitivity of the mechanical degree of freedom to the presence of a light field and vice versa—is achieved by decreasing the effective length of the cavity. In a general sense, then, this (as well as other considerations, such as increasing mechanical frequencies and thereby the *bandwidth* of cavity-optomechanical sensors) helped to motivate a trend of miniaturizing a large class

of cavity-optomechanical devices from the 1990s onward. This is the domain of the work presented in this dissertation, wherein nanoscale localized acoustic resonances coupled to wavelength-scale optical cavities are used to study low-temperature phonon dynamics in a highly engineered cavity-optomechanical device system known as an optomechanical crystal (OMC). These OMCs, which possess co-localized optical and acoustic modes with large coupling in a thin-film dielectric material, have previously been used to demonstrate sideband cooling of mesoscopic mechanical modes to the motional quantum ground state, optomechanically-induced transparency and slow-light, the generation of squeezed states of light, and more [16, 17, 18, 19, 20, 21]. The work presented here represents a concerted effort to optimize the technical performance of silicon OMCs with regard to manipulating phonon modes at the level of individual quanta, and generally to understand the physics governing their dynamical behavior at low temperature, in order that they may be useful in future hybrid quantum systems both for studying fundamental physics and for applications to the quantum control of matter using light.

1.1 Extremely Long-Lived Acoustic Resonances

A key figure of merit in cavity-optomechanical systems, and generally in oscillator systems which are coupled to a thermal environment, is the fQ-product of the coupled mechanical mode. The importance of the frequency and quality factor product can be understood by considering the number of coherent oscillations the resonator will experience before losing one quantum of energy to the thermal environment at temperature T. The heating rate of an oscillator coupled to a thermal environment with occupancy $n_{\mathrm{th}} = (e^{\hbar\omega_m/k_{\mathrm{B}}T} - 1)^{-1}$ is [22]

$$\Gamma = \gamma\hbar\omega_m\left(n_{\mathrm{th}} + \frac{1}{2}\right), \tag{1.1}$$

where γ is the energy decay rate of the oscillator ($Q = \omega_m/\gamma$). Then the time for one quantum of energy $\hbar\omega_m$ to be lost is $\tau_{\mathrm{th}} = (\gamma(n_{\mathrm{th}} + 1/2))^{-1}$, so the number of coherent oscillations is

$$\omega_m\tau_{\mathrm{th}} = \frac{\omega_m}{\gamma(n_{\mathrm{th}} + 1/2)} \approx Q\frac{\hbar\omega_m}{k_{\mathrm{B}}T}, \tag{1.2}$$

which scales as $\omega_m Q = 2\pi f Q$. The fQ-product, then, evidently quantifies the degree to which a system is protected from decoherence caused by interactions with its thermal environment. For example, at room temperature, a minimum fQ-product

of $fQ = Q\omega_m/2\pi \gg k_B T/\hbar \approx 10^{13}$ is required for coherent quantum optomechanics, whereas at typical dilution refrigerator base temperatures of 10 mK one requires a much more relaxed $fQ \gg 10^9$ due to a greatly reduced thermal bath occupancy at low temperature. Figure 1.1 gives a summary of the fQ products realized for the mechanical element in various optomechanical and electromechanical systems representing the state of the art, with data adapted from Refs. [23, 24, 25]. The 5 GHz acoustic modes presented in this thesis obtain unprecedented energy coherence, reaching $fQ = 2.6 \times 10^{20}$ and thermal decoherence times as large as $\tau_{th} = 1.5$ seconds.

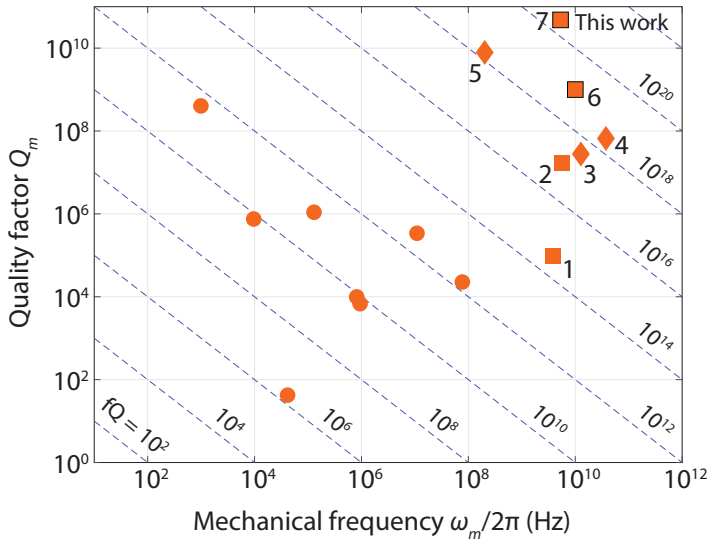

Figure 1.1: **Summary of fQ products achieved in cavity optomechanics and related systems**. Experiments in cavity optomechanics are represented by circles, with data adapted from Ref. [23], and the experiments presented in this work are represented by squares. Diamonds represent electromechanical/piezoelectric coupling to bulk acoustic modes, possessing some of the highest fQ products of any bulk material phonon modes prior to the work presented here [24, 25]. Item (1) is from Ref. [20], measured in a similar nanobeam OMC within the Painter Group prior to the work presented here, which is measured on an improved version of the same device platform. Items (2), (6), and (7) represent the work presented in this thesis [**MacCabe:etal:2018**, 26].

In our structures, we are primarily interested in acoustic mode frequencies of a few GHz, placing them in the microwave (or hypersonic) frequency regime. This is motivated by several considerations, including that we will be working in the sideband-resolved regime of cavity-optomechanics in which the mechanical resonance frequency ω_m is much greater than the optical cavity energy decay rate κ. In photonic crystal optical resonators, $\kappa \lesssim 1$ GHz is typical, so we will need

large mechanical frequencies to reach sideband resolution in OMCs – a prerequisite for protocols such as sideband cooling of the mechanical mode into its quantum ground state. These high mechanical frequencies also allow greater bandwidth of phonon-photon conversion processes, where the total conversion bandwidth will correspond to an optically-damped mechanical mode linewidth [19]. Moreover, at these frequencies the acoustic mode wavelength is close to the optical cavity mode wavelength (of order 1 μm), providing good mode overlap for generating optomechanical coupling through radiation pressure. High-mechanical-frequency acoustic modes also minimize thermal occupation (thermal noise), and in our devices we have measured phonon occupancy as low as 10^{-3} at an environmental temperature of 10 mK in a dilution refrigerator.

Perhaps most important, though, is the fact that our mechanical modes exist in the same frequency range as common superconducting qubits, suggesting a future for devices of this type in hybrid quantum systems which couple superconducting qubits to acoustic modes. With energy decay times greater than one second, these microwave acoustic modes present a potentially valuable resource in the context of superconducting quantum computing as energy storage elements. Ongoing efforts within the Painter Group are investigating the possibility of coupling similar vibrational modes in silicon to superconduting circuits in order to leverage their ultra-long lifetimes for storage of quantum information. The challenges in doing this are multitudinous, as one is then concerned with generating electromechanical coupling between the superconducting circuit and the localized acoustic mode without sacrificing the acoustic mode lifetime. This may be achieved with the use of a piezoelectric material (commonly aluminum nitride) which couples strain fields to electric fields. The technical challenges associated with introducing more complex materials systems into nanostructures harboring GHz cavity-acoustic modes are currently under investigation.

Going forward, the temptation to couple nonlinear quantum elements (e.g., qubits) to these high-Q acoustic modes is ever increasing. Various other research groups are pursuing similar programs of research in this emerging field of *quantum acoustodynamics* (QAD) [25, 27, 28, 29], and have already made extremely impressive demonstrations of peizo-electrical coupling between surface- or bulk-acoustic wave phonons (SAW, BAW) and superconducting qubit circuits. However, there is great promise in the possibility of miniaturizing the mechanical element by using a localized cavity acoustic mode like that studied in the silicon-based systems of this thesis,

with a footprint on-chip of only a few square microns owing to the slow speed of sound in silicon (or other future material systems) compared to that of microwaves in a superconducting circuit. Success in this endeavor may directly enable scalability of quantum-acoustodynamic devices simply because many hundreds or thousands of long-lived mechanical resonators can be placed in an on-chip area that would be occupied by only a handful of electrical microwave or SAW/BAW resonators.

1.2 Beginnings

My early work in the Painter Group was under the wings of Justin Cohen and Seán Meenahan, then already quite senior graduate students in their fifth year of study, who were more than helpful in getting me up to speed on their ongoing projects in low-temperature optomechanics. At that time the prospect of optically coupling to an OMC device in a dilution refrigerator was practically working but fairly new, and Seán and Justin had spent a great deal of time developing the optical coupling techniques and technical know-how to enable our cryogenic measurements. Working with Justin very closely, I tried to learn the team's methods and technical strategies while he and Seán made the group's first milliKelvin OMC measurements that would later be published in Ref. [30]. Justin spent an immense amount of time training me in the details of the device fabrication process, for which I am deeply grateful to him. My contributions to the team's efforts, aside from trying to learn the relevant physics as thoroughly as I could, began during our team's early development of the phonon-counting technique. We worked with Matt Shaw and Francesco Marsili, who (in collaboration with Sae Woo Nam's group at NIST) had developed incredibly high-performance superconducting nanowire single-photon detectors for the near-infrared with very low background count rates and high quantum efficiency. These detectors proved an invaluable tool in our group's efforts to start making time-domain mechanical dynamics measurements on our OMCs. The motivations for these types of measurements are several: first, many quantum-state preparation and heralding protocols rely on detection of single photons that herald the occurrence of an individual scattering event. Second, the fine timing resolution ($\lesssim$ 10 ns) afforded by these SPDs promised us a window into the short-timescale heating and damping dynamics of our mechanical mode, and ultimately enabled us to perform mechanical thermometry at the sensitivity level of 10^{-2} phonons. Third, the milliKelvin temperature measurement results in Ref. [30] proved to us the challenge of reaching high cooperativity in the presence of steady-state optical-absorption heating, which could be mitigated by using low duty-cycle pulsed excitation in

order to study temporal acoustic dynamics deep in the ground state (phonon number $\langle n \rangle \ll 1$).

1.3 Dil Fridge Days

With the demonstration of phonon intensity interferometry at room temperature in Ref. [31], the phonon-counting technique had matured. I became much more involved in performing measurements during this time period. Subsequent pulsed excitation measurements [26] of the *nanobeam* OMC device at milliKelvin temperatures inside the dilution fridge required substantial build-up of the measurement setup, protocols, and data handling capabilities. Those measurements set the stage for a program of low-temperature OMC research that forms the bulk of my thesis work, and has been the most rewarding and enjoyable technical pursuit I've made thus far.

With the indication that our breathing mode mechanical lifetime could approach a millisecond, we were motivated to for the first time make a systematic study of the effectiveness of the acoustic bandgap radiation shielding which had been used in all previous cryogenic measurements of the nanobeam OMC [20, 21, 30, 32]. Previous works had made use of the shielding on the basis of numerical modeling, which indicated that substantial localization of the mechanical mode energy could be achieved with by clamping with the full-bandgap material to eliminate clamping losses. To prepare for this series of measurements, we spent time to re-optimize the fabrication process used to make OMC samples suitable for end-fire optical coupling in the dilution refrigerator (Chapter 3.2). This would allow us nearly 100% reliable fabrication of device arrays for future experiments, and enable us to couple to several dozens of devices on an individual chip sample during one cooldown cycle of the dil fridge.

A key aspect of preparing for this experiment was to carefully optimize the SEM image fitting and lithography feedback to ensure the design geometry of the bandgap shield (and the OMC cavity) was being realized as faithfully as possible. This proved critical, as an initial round of measurements showed disappointingly little benefit to extending the number of bandgap shielding periods relative to modeling predictions, likely due to misalignment of the bandgap and the mechanical mode frequency due to subtleties of the lithography in fabrication. However, our ability to test large arrays of devices paid off, as a small degree of fabrication disorder yielded that some of the devices housed mechanical resonances further from the bandgap edge

than others. We observed a few devices with mechanical Q-factors above 1 billion and, knowing that there was substantial room for improvement, embarked to generate a round of devices in which the acoustic bandgap was optimally centered around the mechanical resonance frequency. After refining the lithography feedback to achieve this, later measurements of the mechanical lifetime showed a much clearer trend of mechanical-Q with acoustic shield depth as well as extremely large saturated mechanical-Q factors on the order of 40 billion for our 5 GHz mode.

Alongside the mechanical mode lifetime measurements was a course of study into the optical heating and resulting phonon bath dynamics present in our devices. Owing to the relatively large energy of a single photon (at 200 THz) compared to a single phonon (at 5 GHz) and the reduced thermal conductivity of silicon at low temperature, even a very small amount of parasitic optical absorption can generate a significant phonon bath which damps the cavity mode. In fact, an intracavity photon population as small as $\sim 10^{-6}$ average photons introduces an effective mechanical damping rate comparable to the intrinsic mechanical decay rate – a single intracavity photon generates a local bath temperature of $1-2$ K at an environmental temperature of order 10 mK. We developed various optical measurement techniques to study the bath damping and heating rates, generally using pump-probe techniques in which one laser is used to generate optical-absorption heating while another is used to probe the resulting dynamics. Around this time we had built the optical setup capabilities sufficiently that we were able to coherently excite the mechanics to large phonon amplitude and probe the decay in a minimally invasive way, decreasing the impact of bath effects on our studies of the mode lifetime. These measurements expanded into a study of the mechanical mode's spectral properties, including the dependence of the mechanical linewidth and frequency upon laser power and temperature, in a novel regime in cavity optomechanics where the mechanical dissipation and decoherence is driven dominantly by coupling to material defect tunneling states residing in the etch-damaged surface layer of the device material. These nanobeam device platforms have proved a unique resource for studying the low-temperature behaviors of strain-coupled tunneling state defects ubiquitous in amorphous surface layers of silicon.

Chapter 2

PRINCIPLES OF OPTOMECHANICAL CRYSTALS

The fundamental feature of a cavity-optomechanical system is an optical cavity resonance in which the resonance frequency is sensitive to the motion of a mechanical degree of freedom within the cavity. Consider for example the canonical optomechanical system in Figure 2.1, consisting of a Fabry-Perot cavity in which one end-mirror is mechanically compliant. Circulating photons inside the cavity impart an impulse to the mirror upon reflection, having magnitude $2\hbar k$ per photon where $k = 2\pi/\lambda$ is the wavenumber of a photon with wavelength λ. Given an average number N of photons circulating inside the cavity of length L with round-trip time $\tau = 2L/c$, one sees that the average radiation pressure force imparted on the mirror is $F_{\mathrm{RP}} = 2N\hbar ck/2L = N\hbar\omega/L$. In a general sense then, maximizing the force per photon is equivalent to decreasing the length (or effective length, in the case of a photonic crystal cavity) L of the cavity.

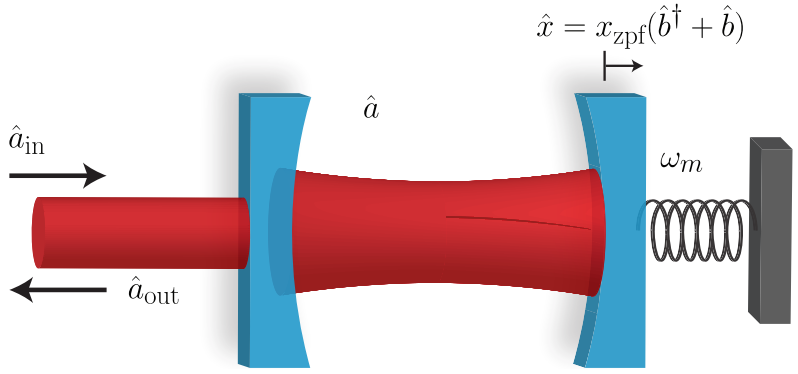

Figure 2.1: **Canonical cavity-optomechanical system.** The canonical optomechanical system can be modeled by a Fabry-Perot cavity of effective length L_{eff} in which one mirror is mechanically compliant. If the mirror has mass m and resonant frequency ω_m, its zero-point motion is given by $x_{\mathrm{zpf}} = \sqrt{\hbar/(2m\omega_m)}$, and the position operator is given by $\hat{x} = x_{\mathrm{zpf}}(\hat{b}^\dagger + \hat{b})$, where $\hat{b}$ is the bosonic annihilation operator for the mechanical degree of freedom. Similarly, the optical mode is described by the bosonic annihilation operator $\hat{a}$ and cavity frequency ω_c. The radiation pressure interaction causes a coupling by which ω_c depends explicitly on $\hat{x}$, approximately given by $\omega_0 = \omega_0(1 - \hat{x}/L_{\mathrm{eff}})$. Input and output to the system are described by $\hat{a}_{\mathrm{in}}$ and $\hat{a}_{\mathrm{out}}$ using the input-output formalism for open quantum systems.

The Fabry-Perot cavity implementation of an optomechanical device is suitable for many macroscopic applications of optomechanics, such as in kilometer-scale gravitational wave detectors. At the millimeter-to-centimeter scale, thin-film materials have instead been used in device architectures ranging from cantilever-mounted and torsional-oscillator mirrors for force sensing at high frequencies and near the quantum limit [33, 34, 35], to micro-fabricated membranes coupled to macroscopic optical cavities for microwave-to-optical transduction near the level of individual photons and generation of squeezed states of light [36, 37, 38, 39, 40], and in whispering gallery optical resonators [41]. At still smaller length scales, nanofabrication techniques allow replacement of the Fabry-Perot cavity architecture with analogous structures through patterning of dielectric and semiconductor materials down to feature sizes which are deeply sub-wavelength. The push to shorter length scales is partially driven by the desire to reduce the effective motional mass of the mechanical element, thereby increasing the acceleration imparted on the mechanics per reflected optical photon, as well as to achieve structures with large mechanical frequencies for the reasons outlined above. Each of these various implementations has advantages and disadvantages, but for the purpose of the work presented here, we will focus exclusively on photonic devices using near-IR light to couple to high-frequency mechanical modes in structures known as optomechanical crystals (OMCs), in which light can be confined to mode volumes near the theoretical minimum of $(\lambda/2n)^3$. These OMCs are crystals in the sense that they are formed through periodic patterning of semiconductor materials (here usually Si or SiN_x) to support co-localized photonic and mechanical/acoustic vibrational modes. Silicon-based OMCs are able to reach mechanical frequencies in the microwave regime ($\sim 1 - 10$ GHz) owing to the large speed of sound in silicon ($5 - 8$ km/s) with optical resonances in the telecommunications bands from $1200 - 1600$ nm reaching optical quality factors on the order of 10^6. Moreover, the extremely small photonic mode volume of these OMCs is accompanied by a correspondingly large electric field strength per photon, giving rise to the possibility for large optomechanical coupling rates through photoelastic coupling in which the refractive index change (effective cavity length) is sensitive to the electric field strength in the material.

2.1 Periodic Structures and Optomechanical Crystals

Optomechanical crystal devices are created by patterning periodic structures into thin-film semiconductor materials. Periodicity in any potential gives rise to propagating wave solutions for the fields experiencing that potential; here, both electro-

magnetic fields and acoustic (strain) fields experience periodic effective potentials which give rise to dispersive eigenmodes analogous to the cavity modes present in a Fabry-Perot cavity. In this sense optomechanical crystals are simultaneously photonic crystals and mechanical crystals. In the case of an electromagnetic or photonic structure, the supported eigenmodes can be understood by investigating the form of solutions to Maxwell's equations in a dielectric material:

$$\nabla \cdot \mathbf{B} = 0 \tag{2.1}$$

$$\nabla \cdot \mathbf{D} = 4\pi\rho \tag{2.2}$$

$$\nabla \times \mathbf{H} = \frac{1}{c}\frac{\partial \mathbf{D}}{\partial t} + \frac{4\pi}{c}\mathbf{J} \tag{2.3}$$

$$\nabla \times \mathbf{E} = -\frac{1}{c}\frac{\partial \mathbf{B}}{\partial t}. \tag{2.4}$$

We are interested in the solutions of these equations in dielectric materials in the absence of source terms ρ and $\mathbf{J}$, and which can be described as consisting of discrete regions of different dielectric constants $\varepsilon = \varepsilon(\mathbf{r}, \omega)$. For now we will consider only lossless materials for which ε is real, and ignore any frequency dispersion of ε. In general numerical methods for solving for the modes of a structure, such as the finite-element method (FEM) solver packages in COMSOL Multiphysics [42], the full complex-valued anisotropic dielectric tensor $\overleftrightarrow{\varepsilon}(\mathbf{r}, \omega)$ is used. The field amplitudes for general solutions of Maxwell's equations will be linear combinations of the normal modes which are harmonic in time, of the form $\mathbf{H}(\mathbf{r}, t) = \mathbf{H}(\mathbf{r})e^{i\omega t}$ and $\mathbf{E}(\mathbf{r}, t) = \mathbf{E}(\mathbf{r})e^{i\omega t}$. If we insert these temporal normal mode solutions into Maxwell's equations, we obtain two curl equations of motion for the fields:

$$\nabla \times \mathbf{E}(\mathbf{r}) + \frac{i\omega}{c}\mathbf{H}(\mathbf{r}) = 0 \tag{2.5}$$

$$\nabla \times \mathbf{H}(\mathbf{r}) - \frac{i\omega}{c}\varepsilon(\mathbf{r})\mathbf{E}(\mathbf{r}) = 0. \tag{2.6}$$

Eliminating the electric field from the coupled equations yields an electromagnetic master equation for the magnetic field:

$$\nabla \times \left[\frac{1}{\varepsilon(\mathbf{r})}\nabla \times \mathbf{H}(\mathbf{r})\right] = \left(\frac{\omega}{c}\right)^2 \mathbf{H}(\mathbf{r}). \tag{2.7}$$

Equation 2.7 has the familiar form of an eigenvalue problem in which the magnetic field profile in a given region parametrized by a dielectric constant $\varepsilon(\mathbf{r})$ can be determined as a function of frequency [43]. The solutions to the master equation will be a set of normal modes. Additionally, because we have assumed the media in which the solutions exist is free of source terms, the field patterns must be transverse, further limiting the spatial forms of solutions to the master equation. In the specific case of photonic crystals, the material (described by $\varepsilon(\mathbf{r})$) is patterned periodically, such that in addition to finding electromagnetic field solutions which are harmonic in time, we will search for modes which are also harmonic in space. Bloch's Theorem [44] tells us that the spatial normal modes will take the form of plane waves in a periodic medium,

$$\mathbf{H}(\mathbf{r}, t) = \mathbf{H}_0 e^{i\mathbf{k}\cdot\mathbf{r}} e^{i\omega t}, \tag{2.8}$$

where $\mathbf{k}$ is the wave-vector and and the transversality requirement amounts to requiring that $\mathbf{H}_0 \cdot \mathbf{k} = 0$. If we restrict ourselves to the case of a quasi-one-dimensional photonic crystal, in which periodicity of the material is realized in only one of the three spatial axes ($\hat{x}$), the solutions have the form $\mathbf{H}(\mathbf{r}, t) = \mathbf{H}_0(y, z)e^{ik_x x}e^{i\omega t}$. For a given frequency, then, we can calculate the spatial mode profiles using Equation 2.7, and catalogue the spatial mode profile solutions according to their spatial wave-vector eigenvalue k_x. Performing this calculation yields a *band structure* diagram for a structure, describing the relationship between frequency and wave-vector for each normal mode, where typically the band structure is accompanied by the assumption that the spatial symmetry extends to infinity or nearly infinity, i.e., that the plane-wave solutions are valid in all space. The generation of normal modes which are separated in frequency by virtue of a periodic electromagnetic potential (here, the dielectric constant) is a general result of solutions to the wave equation in the presence of a periodic material. Structures may be engineered in which the local periodicity of the potential (dielectric constant) is varied to create defects in which the effective potential is not uniformly periodic. Such defects to the periodicity of a photonic structure cause the approximate normal modes of the structure to vary from one unit cell to the next, and can result in localization of the field intensity to one region preferentially to another, as regions of higher dielectric constant will contain a greater electromagnetic energy density [43] (see Figure 2.2). In particular, it is routine to design structures in which one or more modes of a defect in a periodic structure has a frequency which lies in a bandgap of the surrounding

material, where no propagating modes exist at the frequency of the defect mode. In this way, electromagnetic energy can be confined in an effective optical potential in a qualitative analogy to confinement due to total internal reflection.

The Nanobeam OMC

In the devices studied in this work, the principles of quasi-1D photonic crystals are used to generate optical defect cavities in a nanobeam photonic crystal. The beam consists of a suspended thin-film (220 nm) Si layer patterned into regions of alternating *effective* dielectric constant by removing some of the dielectric material in elliptical holes, as shown in Figure 2.3. The resulting optical potential is then readily modulated by changing the relative filling fraction and lattice constant of a unit cell (see Figure 2.2). The optical cavity of the nanobeam consists of a series of "mirror" unit cells on either end of the nanobeam, in which a pseudo-bandgap at the defect mode resonance frequency exists due to the choice of lattice constant and filling fraction of the unit cells. The lattice constant is set by the wavelength of the defect mode in the material, here roughly $a_0 \sim \lambda/n_{\mathrm{Si}} = 450$ nm ($n_{\mathrm{Si}} = 3.48$ at 1550 nm). In the central defect region of the nanobeam, the lattice constant and elliptical hole geometry are modulated adiabatically along the length of the beam to form a symmetric optical potential [20], in which there exists a confined mode at approximately $\omega_c/2\pi = 194$ THz (free space wavelenth 1550 nm). Confinement in the transverse ($\hat{y}$) and out-of-plane ($\hat{z}$) directions are achieved by total internal reflection due to index contrast with the surrounding vacuum or air. However, there do exist radiation modes which are not confined to the $z = 0$ plane; these are classified by wave-numbers greater than the longitudinal wavenumber k_x, or equivalently, $\omega > ck_x$. These radiation modes form a *light cone*, as shown in Figure 2.2b. Due to the presence of the light cone and nearby bands which can couple strongly to radiation modes, the photonic bandgap of the mirror region is really a *pseudo*-bandgap. Nevertheless, it is possible to tailor a central defect in such a way that the guided mode in the defect region experiences large reflectivity at the mirror portion of the beam. A final comment here regards the polarization of the defect mode. The modes of interest in thin-film OMCs are usually $\hat{z}$-symmetric with E-fields largely in the z-plane; thus, we classify them as "transverse-electric-like" (TE-like) modes. Details of the nanobeam optical cavity design are given in Ref. [20], and the geometry of the structure and the defect optical mode are shown in Figure 2.3.

In analogy with the periodic solutions of the photonic master equation, the periodic-

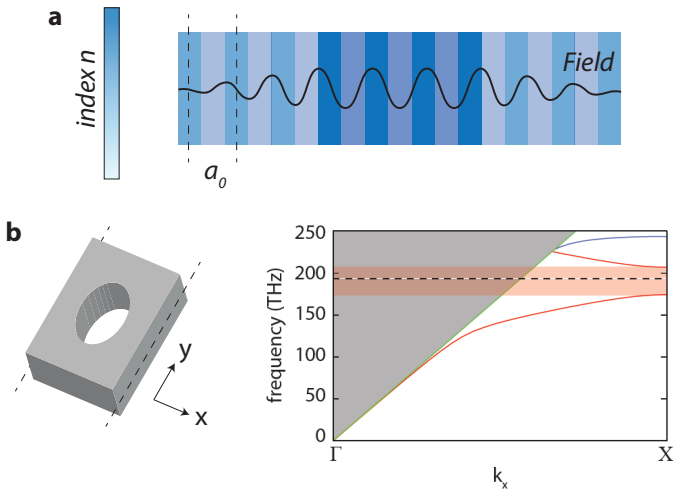

Figure 2.2: **Periodicity in 1D photonic crystals. a**, Alternating regions of high and low index with lattice constant a_0 can lead to constructive or destructive interference of propagating waves of wavelength $\lambda \approx a_0$. An optical cavity can be constructed by combining two end-mirror regions with central defect region of different effective refractive index. **b**, A unit cell of the end-mirror portion of a nanobeam OMC, which is periodic in the $\hat{x}$ direction, and the photonic band structure of the mirror portion [20]. Bands shown in red (blue) have odd (even) y-symmetry. Radiation modes exist for $\omega > ck_x$. A pseudo-bandgap exists near $\omega/2\pi = 200$ THz, in the vicinity of a defect mode of the central defect region of the nanobeam (dashed line).

ity of the nanobeam gives its structural acoustic normal modes a spatial periodicity as well. The central defect region of the nanobeam supports a so-called *breathing* acoustic resonance in the microwave frequency regime, here near 5 GHz. By tailoring the mechanical properties of the defect region relative to the mirror regions at either end of the beam, the acoustic breathing mode is localized to the defect region. The mirror regions support a partial acoustic bandgap at the breathing mode frequency. Note that because the acoustic modes cannot radiate into the vacuum (unlike electromagnetic modes), they are confined to the plane of the nanobeam, and therefore the band-structure diagrams for the modes in the longitudinal axis of the nanobeam ($\hat{x}$) do not contain light-cones of continuum modes.

Although the mechanical breathing mode is confined to the defect region of the nanobeam by the partial acoustic bandgap of the mirror portions of the nanobeam, it is still possible for the mode to couple to the bulk Si of the substrate chip via leaky mechanical modes in the mirror region. In particular, fabrication imperfections inevitably break the $\hat{z}$-symmetry of the device, so the realized resonant mode is not truly an eigenmode of $\hat{z}$-inversion. In this case, it has some overlap with the

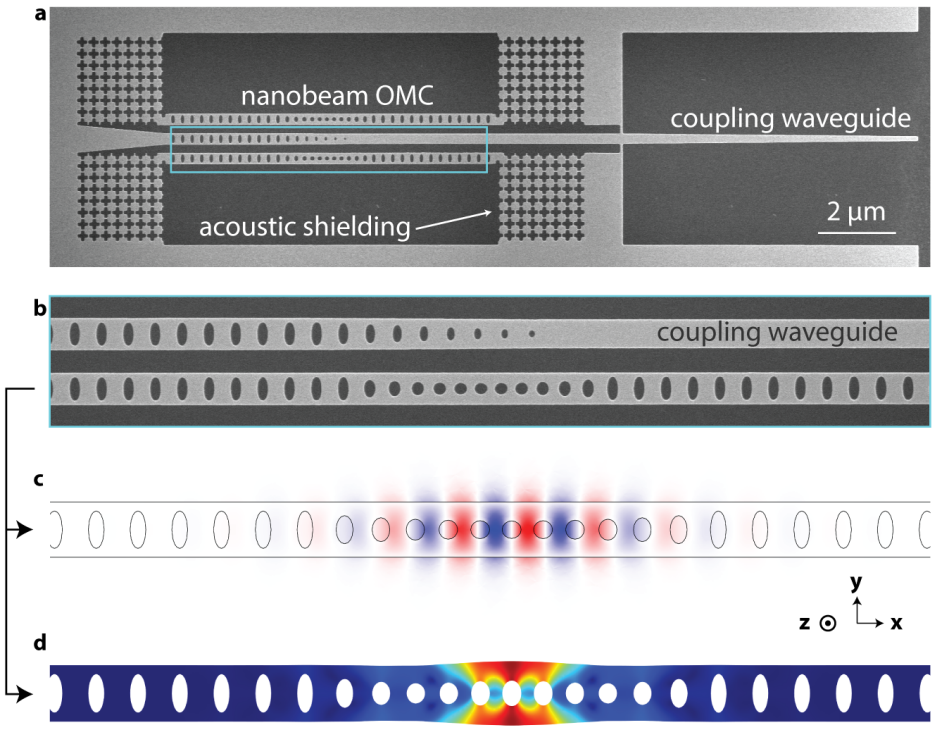

Figure 2.3: **Optical and acoustic modes of the nanobeam OMC. a**, Scanning electron microscope (SEM) image of a full nanobeam optomechanical crystal (OMC) device fabricated on silicon-on-insulator (SOI) with 7 periods of acoustic shielding. A central coupling waveguide allows for fiber-to-chip optical coupling as well as evanescent side-coupling to individual nanobeam OMC cavities. **b**, SEM image of an individual nanobeam OMC and the coupling waveguide, with enlarged illustration of an individual unit cell in the end-mirror portion of the nanobeam. **c**, Finite-element method (FEM) simulation of the transverse in-plane electric field magnitude $|E_y|$ for the fundamental optical mode at $\omega_c/2\pi = 194$ THz (free-space wavelength $\lambda_c \approx 1550$ nm). **d**, FEM simulation of the displacement field magnitude of the "breathing" acoustic mode at $\omega_m/2\pi = 5.0$ GHz. Distortion of the mechanical mode profile is exaggerated for clarity.

mode profile of propagating modes in the mirror portion of the nanobeam, and therefore the partial bandgap allows for energy dissipation of the confined mode by coupling to radiation modes. Since the experiments presented here will rely heavily on minimizing the acoustic loss rate of the OMC structure, additional design considerations must be made to better confine the acoustic mode and prevent radiation of phonons into the bulk Si. To accomplish this, we employ a quasi-2D periodic "cross shield" pattern for clamping the ends of the nanobeam, in which the effective mass of alternates between large and small from one half-unit cell to the next [20, 45]. The cross shield pattern is shown in Figures 2.4 and 2.5, and

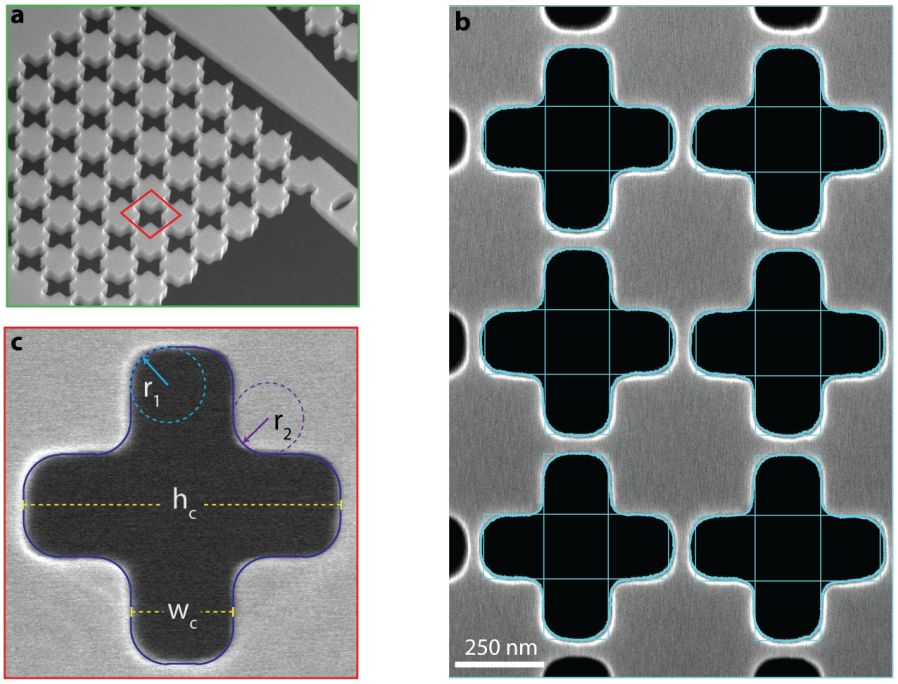

Figure 2.4: **Phononic crystal radiation shield image analysis and optimization.** **a**, SEM image of the clamping region of the nanobeam OMC, patterned with a phononic crystal "cross shield." **b**, Close view of several unit cells of the cross shield used for image fitting and analysis. **c**, SEM image of an individual unit cell of the cross-crystal acoustic shield. The dashed lines show fitted geometric parameters used in simulation, including cross height (h_c = 503 nm), cross width (w_c = 169 nm), inner fillet radius (r_1), and outer fillet radius (r_2).

the structure supports a full acoustic bandgap ≈ 3 GHz-wide around the breathing mode resonance frequency (gap-midgap ratio 0.6). The band structure of a realized cross shield is shown in Figure 2.5. The origin of the bandgap can be qualitatively understood as arising from the large difference in resonance frequencies of the square masses (high frequency) and narrow, floppy tethers by which they are connected (low frequency). In such a structure, the planar acoustic modes experience a full bandgap, and as the acoustic modes are also prohibited from radiating into the $\hat{z}$ direction, the bandgap is fully three-dimensional.

The importance of the three-dimensional microwave-frequency phononic bandgap is detailed in Chapter 6.1, in which the reduction in clamping losses by patterning of an increasing number of cross shield periods is studied numerically and experimentally. In the numerical studies performed using COMSOL, the geometric parameters of the structure are measured from scanning electron microscope (SEM) images of realized structures, as shown in Figure 2.4, and used to generate model geoemtries

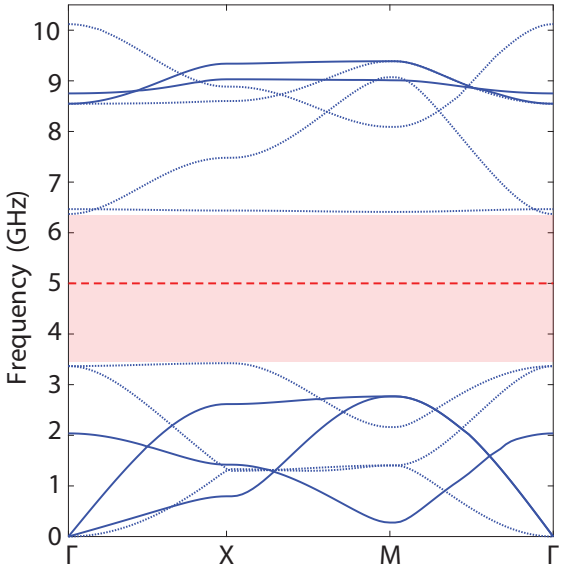

Figure 2.5: **Band structure of the phononic crystal radiation shield "cross" pattern.** Acoustic band structure of the realized cross-crystal shield unit cell, with the full acoustic bandgap highlighted in pink. Solid (dotted) lines correspond to modes of even (odd) symmetry in the direction normal to the plane of the unit cell. The dashed red line indicates the nanobeam mechanical breathing-mode frequency at $\omega_m/2\pi = 5.0$ GHz.

for calculation of band structure diagrams. Of particular importance in accurately modeling the acoustic bandgap structure is the inclusion of fillet curvature radii r_1 and r_2 of the concave and convex corners of the structure. This curvature arises from technical limitations of the lithography preventing the reliable fabrication of abrupt corners with curvature radii less than about 20 nm, and the fillet radii used in modeling substantially impact the frequencies of the upper and lower bandgap-edge modes. A lack of propagating modes in the acoustic shield region gives rise to an exponential decay of the acoustic field in that region as a function of position, which alternatively can be understood as a finite penetration depth of the acoustic mode in the bandgap material region. For sufficiently many periods of the acoustic shielding, the energy damping rate of the acoustic mode is not limited by radiation into the bulk (clamping losses), but becomes limited by other intrinsic material properties and defects, discussed in detail in Chapter 7.

Origins of Optomechanical Coupling

In the case of planar thin-film optomechanical crystals, coupling between the optical and mechanical modes arises differently than in the case of Fabry-Perot resonators.

Rather than the real distance between the two end-mirros becoming modulated by reflected photons, the *effective* dielectric constant in the cavity region experienced by circulating photons is modulated by the mechanical motion. There are two main ways in which this can occur. First, mechanical motion will physically displace the boundaries of the dielectric structure, modifying the band structure and thus the frequency of the photonic mode. This change in boundary condition is referred to as a "moving boundary" effect. Second, the presence of a strain field in the dielectric can change the dielectric constant of that bulk material through the photoelastic effect.

The magnitude of the optomechanical coupling rate, defined as the rate of change of the optical resonance frequency as a function of mechanical displacement $g_{\mathrm{OM}} = \partial\omega_c/\partial\alpha$ for a generalized position coordinate α, can be decomposed into contributions arising from the moving boundary effect and the photoelastic effect. This decomposition is useful in the design of OMCs, as the absolute and relative magnitudes of these contributions motivate the choice of which acoustic and electromagnetic modes should be used to tailor the device geometry. The total optomechanical coupling rate can be calculated by considering the effect of an infinitesimal mechanical displacement on the optical resonance frequency. The electromagnetic energy density depends on the electric field $\mathbf{E}$ and dielectric constant $\varepsilon(\mathbf{r})$, and to first order in perturbation theory the change in energy can be calculated using the non-perturbed normal modes according to [20, 46]

$$g_{\mathrm{OM}} = \frac{\partial\omega_c}{\partial\alpha} = -\frac{\omega_c}{2}\frac{\int d^3\mathbf{r}\ \mathbf{E}^*(\mathbf{r})\cdot\frac{\partial\varepsilon(\mathbf{r})}{\partial\alpha}\mathbf{E}(\mathbf{r})}{\int d^3\mathbf{r}\ \mathbf{E}^*(\mathbf{r})\cdot\varepsilon(\mathbf{r})\mathbf{E}(\mathbf{r})}. \tag{2.9}$$

Calculation of the moving boundary contribution to g_{OM} can be performed by ignoring the strain-induced changes in ε to first order in α. In terms of the unperturbed electric field mode profile and the mechanical mode profile $\mathbf{q}(\mathbf{r})$, the moving boundary contribution to g_{OM} is given by [47]

$$g_{\mathrm{OM,bnd}} = -\frac{\omega_c}{2}\frac{\int dA\ \mathbf{q}(\mathbf{r})\cdot\hat{n}(\mathbf{r})(\Delta\varepsilon\langle\mathbf{E}_{\parallel}(\mathbf{r})\rangle^2 - \Delta\varepsilon^{-1}\langle\mathbf{D}_{\perp}(\mathbf{r})\rangle^2)}{\int d^3\mathbf{r}\varepsilon(\mathbf{r})\langle\mathbf{E}(\mathbf{r})\rangle^2}, \tag{2.10}$$

where $\parallel$ and $\perp$ represent the parallel and perpendicular components of the fields with respect to the material surface. The integral in the numerator is performed over the boundaries of the material with surface normal vector $\hat{n}$, $\mathbf{q}$ is the normalized

mechanical mode profile, and $\Delta\varepsilon$ is the difference between the dielectric constants across the material boundary.

The contribution of the photoelastic effect to the optomechanical coupling rate, $g_{\mathrm{OM,ph}}$, can be calculated using an expression for the strain-induced change in dielectric constant for the material [48]:

$$\frac{d\varepsilon}{d\alpha} = \varepsilon\left(\frac{\mathbf{p}}{\epsilon_0 \mathbf{S}}\right). \tag{2.11}$$

Here $\mathbf{p}$ is the rank-four photoelastic tensor of the material and $\mathbf{S}$ is the mechanical mode strain tensor, with components

$$S_{\mathrm{ij}} = \left(\frac{\partial q_{\mathrm{i}}}{\partial r_{\mathrm{j}}} + \frac{\partial q_{\mathrm{j}}}{\partial r_{\mathrm{i}}}\right). \tag{2.12}$$

The resulting integral expression for $g_{\mathrm{OM,ph}}$ is

$$g_{\mathrm{OM,ph}} = \frac{\epsilon_0 \epsilon_{\mathrm{r}}^2 \omega_c}{2} \frac{\int dV E_{\mathrm{i}}^*(\mathbf{r}) E_{\mathrm{j}}(\mathbf{r}) p_{\mathrm{ijkl}} S_{\mathrm{kl}}(\mathbf{r})}{\int d^3\mathbf{r} \epsilon(\mathbf{r}) |\mathbf{E}(\mathbf{r})|^2}, \tag{2.13}$$

where the integral in the numerator is taken over the volume of the material. With expressions for $g_{\mathrm{OM,bnd}}$ and $g_{\mathrm{OM,ph}}$, the total optomechanical coupling rate $g_{\mathrm{OM}} = g_{\mathrm{OM,bnd}} + g_{\mathrm{OM,ph}}$ can be calculated using the eigenmode solutions for the field profiles $\mathbf{E}$ and $\mathbf{q}$ obtained by FEM simulations. The optomechanical coupling rate is conveniently expressed as $g_0 = x_{\mathrm{zpf}} g_{\mathrm{OM}}$, where x_{zpf} is the zero-point mechanical amplitude and g_0 therefore describes the optical cavity frequency shift due to the zero-point mechanical fluctuations (see Chapter 2.2). For the nanobeam OMC, typical contributions to the optomechanical coupling rate are numerically computed to be $x_{\mathrm{zpf}} g_{\mathrm{OM,bnd}}/2\pi = -90$ kHz and $x_{\mathrm{zpf}} g_{\mathrm{OM,ph}}/2\pi = 860$ kHz, giving $g_0/2\pi \approx 770$ kHz, in good agreement with the corresponding experimentally-determined coupling rates typically measured as $g_0/2\pi = 700 - 900$ kHz.

2.2 The Optomechanical System Hamiltonian

Let us more quantitatively investigate the origin of optomechanical coupling in the canonical cavity-optomechanical system. Let L_{eff} be the effective cavity length, m_{eff} be the effective mass of the movable mirror, k be the effective spring constant of the mirror. The mirror then has a mechanical resonance frequency $\omega_m = \sqrt{\mathrm{k}/m_{\mathrm{eff}}}$ and the optical cavity resonances occur at frequencies $\omega_{n-1} = n\pi c/L$, where n is a

positive integer. Consider the fundamental optical mode at frequency $\omega_0 = \pi c/L_{\text{eff}}$. As seen above, a single photon circulating in the cavity produces an average force $F_{\text{RP}} = \hbar\omega_0/L_{\text{eff}}$ on the end-mirror. By Hooke's Law this results in an average displacement of $x = \hbar\omega_0/(L_{\text{eff}}\text{k})$, i.e., the cavity length is $L + x$. This shift in cavity length results in a shift of the optical resonance frequencies, which are now written to depend explicitly on x:

$$\omega_{n-1}(x) \approx \frac{n\pi c}{L_{\text{eff}}} + \frac{d\omega_{n-1}}{dL_{\text{eff}}}x = \frac{n\pi c}{L_{\text{eff}}} - \frac{n\pi c}{L_{\text{eff}}^2}x = \omega_{n-1}(1 - x/L_{\text{eff}}). \tag{2.14}$$

Assuming $x \ll L_{\text{eff}}$. The fundamental mode frequency is shifted by $\Delta\omega_0 = -(x/L_{\text{eff}})\omega_0 = -\hbar\omega_0^2/(\text{k}L_{\text{eff}}^2)$.

Modeling the system quantum mechanically we describe the optical and mechanical modes as quantum harmonic oscillators at frequencies ω_0 and ω_m respectively, where $\hat{a}$ ($\hat{a}^\dagger$) is the bosonic annihilation (creation) operator for the optical mode and similarly $\hat{b}$ ($\hat{b}^\dagger$) are the bosonic operators for the mechanical mode. The Hamiltonian of the quantum cavity-optomechanical system can then be written in terms of the self-energy terms of the modes as:

$$\hat{H} = \hbar\omega_0\hat{a}^\dagger\hat{a} + \hbar\omega_m\hat{b}^\dagger\hat{b} + \hat{H}_{\text{int}}, \tag{2.15}$$

where the term $\hat{H}_{\text{int}}$ describes the interaction of the optical and mechanical modes. We can find an expression for $\hat{H}_{\text{int}}$ by writing ω_0 as an explicit function of the mirror's displacement $\hat{x}$, following the simplified analysis above, so that $\omega_0(\hat{x}) = \omega_0 + \frac{\partial\omega_0}{\partial\hat{x}}\hat{x}$ to first order in $\hat{x}$. Then

$$\hat{H} = \hbar\omega_0(\hat{x})\hat{a}^\dagger\hat{a} + \hbar\omega_m\hat{b}^\dagger\hat{b} = \hbar\left(\omega_0 + \frac{\partial\omega_0}{\partial\hat{x}}\hat{x}\right)\hat{a}^\dagger\hat{a} + \hbar\omega_m\hat{b}^\dagger\hat{b}, \tag{2.16}$$

from which we identify $\hat{H}_{\text{int}} = \hbar\frac{\partial\omega_0}{\partial\hat{x}}\hat{x}\hat{a}^\dagger\hat{a}$. Now, the mechanical position operator $\hat{x} = x_{\text{zpf}}(\hat{b}^\dagger + \hat{b})$ is written in terms of the zero-point fluctuations x_{zpf} of the mechanical oscillator, $x_{\text{zpf}} = \sqrt{\langle 0|\hat{x}^2|0\rangle} = \sqrt{\hbar/(2m_{\text{eff}}\omega_m)}$. Then the interaction Hamiltonian is expressed as

$$\hat{H}_{\text{int}} = \hbar x_{\text{zpf}}\frac{\partial\omega_0}{\partial\hat{x}}(\hat{b}^\dagger + \hat{b})\hat{a}^\dagger\hat{a}. \tag{2.17}$$

After defining a vacuum optomechanical coupling term

$$g_0 \equiv x_{\mathrm{zpf}} \frac{\partial \omega_0}{\partial \hat{x}}, \tag{2.18}$$

which physically represents the optical cavity frequency shift due to the zero-point fluctuations of the mechanical oscillator, we can write the full Hamiltonian

$$\hat{H} = \hbar\omega_0 \hat{a}^\dagger \hat{a} + \hbar\omega_m \hat{b}^\dagger \hat{b} + \hbar g_0 (\hat{b}^\dagger + \hat{b}) \hat{a}^\dagger \hat{a}. \tag{2.19}$$

Referring to Eqn. 2.14 we see that we can approximately write $g_0 = \omega_0(x_{\mathrm{zpf}}/L_{\mathrm{eff}})$, reinforcing our intuition that increasing the optomechanical coupling is equivalent to decreasing the effective length of the cavity.

Generally we are interested in the dynamics of the optical and mechanical fields governed by Eqn. (2.19) under the influence of a strong coherent driving tone with frequency ω_{L}. In this situation it is convenient to move into a reference frame rotating at the drive frequency–where the dynamics of the system operators on the optical timescale can be eliminated–in anticipation of later making a Rotating Wave Approximation. To do this, we define $\hat{A} \equiv \hbar\omega_{\mathrm{L}} \hat{a}^\dagger \hat{a}$ and the unitary operator $\hat{U} \equiv e^{-i\hat{A}t/\hbar}$, and make the unitary transformation to the Hamiltonian:

$$\hat{H} \longrightarrow \hat{U}^\dagger \hat{H} \hat{U} - \hat{A} \tag{2.20}$$

$$= \hbar\Delta \hat{a}^\dagger \hat{a} + \hbar\omega_m \hat{b}^\dagger \hat{b} + \hbar g_0 \hat{a}^\dagger \hat{a} (\hat{b}^\dagger + \hat{b}), \tag{2.21}$$

where the optical detuning is defined $\Delta \equiv \omega_c - \omega_{\mathrm{L}}$. The full Hamiltonian in general includes both additional driving and dissipation terms. We will append an explicit driving term $\hat{H}_{\mathrm{drive}} = \hbar\epsilon(\hat{a}^\dagger + \hat{a})$, but temporarily neglect dissipation. The constant ϵ here is proportional to the square root of the laser drive power, and is taken to be real. The system Hamiltonian is then

$$\hat{H}/\hbar = \Delta \hat{a}^\dagger \hat{a} + \omega_m \hat{b}^\dagger \hat{b} + g_0 \hat{a}^\dagger \hat{a} (\hat{b}^\dagger + \hat{b}) + \epsilon(\hat{a}^\dagger + \hat{a}). \tag{2.22}$$

Linearization Approximation

Using a semiclassical analysis one can show that the effect of the pump is to cause a static shift in the coherent amplitudes of the optical and mechanical fields. Intuitively this is the statement that the optical field will fluctuate around a large coherent amplitude, and similarly the mechanical oscillator will experience a static deflection

due to the average radiation pressure force. It is then useful to re-formulate the Hamiltonian (and resulting dynamics) in terms of fluctuations *about* these coherent amplitudes. To this end we make the substitutions

$$\begin{aligned} \hat{a} &\longrightarrow \alpha_{\rm ss} + \hat{a} \\ \hat{b} &\longrightarrow \beta_{\rm ss} + \hat{b}, \end{aligned} \tag{2.23}$$

where $\alpha_{\rm ss}, \beta_{\rm ss}$ are the coherent parts of the steady-state optical field and mechanical field, respectively. From here forward we drop the subscript "ss" for convenience. The substitution in Eqn. 2.23 is formally performed by applying a displacement to the Hamiltonian for each field:

$$\hat{H} \longrightarrow \hat{D}_{\hat{a}}^{\dagger}\hat{D}_{\hat{b}}^{\dagger}\hat{H}\hat{D}_{\hat{b}}\hat{D}_{\hat{a}}, \tag{2.24}$$

with $\hat{D}_{\hat{a}} = e^{\alpha\hat{a}^{\dagger} - \alpha^{*}\hat{a}}$ and $\hat{D}_{\hat{b}} = e^{\beta(\hat{b}^{\dagger} - \hat{b})}$ and β taken to be real. We then have

$$\hat{H}/\hbar = \Delta(\alpha^{*}+\hat{a}^{\dagger})(\alpha+\hat{a})+\omega_m(\beta+\hat{b}^{\dagger})(\beta+b)+\epsilon(\alpha^{*}+\alpha+\hat{a}^{\dagger}+\hat{a})+g_0(\alpha^{*}+\hat{a}^{\dagger})(\alpha+\hat{a})(\hat{b}^{\dagger}+\hat{b}+2\beta). \tag{2.25}$$

Ignoring constant terms which have no effect on the dynamics, this is

$$\begin{aligned} \hat{H}/\hbar = {} & (\Delta + 2\beta)\hat{a}^{\dagger}\hat{a} + \omega_m\hat{b}^{\dagger}\hat{b} + (\Delta + 2g_0\beta)(\alpha^{*}\hat{a} + \alpha\hat{a}^{\dagger}) + (\omega_m\beta + g_0|\alpha|^2)(\hat{b}^{\dagger} + \hat{b}) \\ & + \epsilon(\hat{a}^{\dagger} + \hat{a}) + g_0[(\alpha^{*}\hat{a}^{\dagger} + \alpha\hat{a})(\hat{b}^{\dagger} + \hat{b}) + \hat{a}^{\dagger}\hat{a}(\hat{b}^{\dagger} + \hat{b})]. \end{aligned} \tag{2.26}$$

Taking α to be real, which amounts to using the phase of the coherent part of the optical field as a reference and therefore loses no generality,

$$\begin{aligned} \hat{H}/\hbar = {} & (\Delta + 2\beta)\hat{a}^{\dagger}\hat{a} + \omega_m\hat{b}^{\dagger}\hat{b} + (\Delta + 2g_0\beta)\alpha(\hat{a} + \hat{a}^{\dagger}) + (\omega_m\beta + g_0|\alpha|^2)(\hat{b}^{\dagger} + \hat{b}) \\ & + \epsilon(\hat{a}^{\dagger} + \hat{a}) + g_0[\alpha(\hat{a}^{\dagger} + \hat{a})(\hat{b}^{\dagger} + \hat{b}) + \hat{a}^{\dagger}\hat{a}(\hat{b}^{\dagger} + \hat{b})]. \end{aligned}$$

Now we observe that the effective driving terms for two fields, which are of the form $(\hat{a}^{\dagger} + \hat{a})$ and $(\hat{b}^{\dagger} + \hat{b})$ respectively, can be eliminated if we substitute the appropriate steady-state field amplitudes:

$$\begin{aligned} \alpha &= \frac{-\epsilon}{\Delta + 2g_0\beta}, \\ \beta &= \frac{-g_0|\alpha|^2}{\omega_m}. \end{aligned} \tag{2.27}$$

Then

$$\hat{H}/\hbar = \left(\Delta - \frac{2g_0|\alpha|^2}{\omega_m}\right)\hat{a}^\dagger\hat{a} + \omega_m\hat{b}^\dagger\hat{b} + g_0[\alpha(\hat{a}^\dagger + \hat{a}) + \hat{a}^\dagger\hat{a}](\hat{b}^\dagger + \hat{b}). \tag{2.28}$$

We see from this that the optical cavity obtains an effective frequency shift $2g_0\alpha^2/\omega_m$. This term is typically small, but can become large compared to the optical cavity linewidth κ at high intracavity photon number α^2. It is simplest to re-define the optical detuning Δ to incorporate this shift. Further, we note that the interaction part of the Hamiltonian consists of terms which are products of two field operators and terms which are products of three field operators. The resulting Heisenberg equations of motion for these terms will respectively be linear and quadratic in the field operators; thus it will be useful to restrict the analysis to the terms which yield linear equations of motion. This *linearization approximation* is most valid in the limit of large α, where the nonlinear term $\hat{a}^\dagger\hat{a}(\hat{b}^\dagger + \hat{b})$ is smaller by a factor of α than the dominant coupling terms. Under the linearization approximation, the full optomechanical system Hamiltonian can be written

$$\hat{H}_{\mathrm{OM}}/\hbar = \Delta\hat{a}^\dagger\hat{a} + \omega_m\hat{b}^\dagger\hat{b} + g_0\alpha(\hat{a}^\dagger + \hat{a})(\hat{b}^\dagger + \hat{b}). \tag{2.29}$$

We make a few observations about this optomechanical system Hamiltonian. First, the coupling strength g_0 is *parametrically enhanced* by $\alpha = \sqrt{N}$, the square root of the intracavity photon number. This is a central result in linearized optomechanics, as it allows the effective coupling rate to be boosted and controlled by simply adjusting the input power to the system. We will follow a usual convention and define the enhanced effective coupling $G \equiv g_0\sqrt{N}$. Next, we note that the interaction part of the Hamiltonian $\hat{H}_{\mathrm{int}} = G(\hat{a}^\dagger + \hat{a})(\hat{b}^\dagger + \hat{b})$ in general contains four product terms $(\hat{a}^\dagger\hat{b}^\dagger, \hat{a}^\dagger\hat{b}, \hat{a}\hat{b}^\dagger, \hat{a}\hat{b})$, but that we can identify regimes in which it is simplified to include only energy-conserving "exchange" terms. In particular, recall that we have moved into a reference frame rotating at the drive frequency $\omega_{\mathrm{L}} = \omega_c - \Delta$. In the lab frame, we may write the field operators as the slowly varying amplitudes $\hat{a}$ and $\hat{b}$ rotating at their respective frequencies relative to the lab frame:

$$\begin{aligned}\hat{a}_{\mathrm{lab}} &\sim \hat{a}e^{-i\omega_{\mathrm{L}}t} = \hat{a}e^{-i(\omega_c-\Delta)t},\\ \hat{b}_{\mathrm{lab}} &\sim \hat{b}e^{-i(\omega_{\mathrm{L}}+\omega_{\mathrm{m}})t} = \hat{b}e^{-i(\omega_c-\Delta+\omega_{\mathrm{m}})t}.\end{aligned} \tag{2.30}$$

It is straightforward to see then that depending on the choice of detuning Δ, some of the product terms will be rapidly-varying at twice the optical frequency, while some will be slowly-varying at approximately the timescale of ω_m. We will make a *Rotating Wave Approximation* (RWA) by neglecting the rapidly-varying terms in the Hamiltonian, which we will see correspond to energy non-conserving scattering processes within an intuitive picture of the optomechanical interaction.

Much like in the context of Raman scattering spectroscopy, in cavity optomechanics one is often interested in the Stokes and anti-Stokes motional optical sidebands generated by the acoustic mode through the optomechanical interaction. Thus the two non-resonant detuning parameters of greatest interest will be the higher-frequency (blue-detuned, Stokes-like) choice of $\Delta = -\omega_m$ and the lower-frequency (red-detuned, anti-Stokes-like) choice of $\Delta = +\omega_m$. Upon closer inspection of $\hat{H}_{\mathrm{int}}$ above, we observe that for these choices of pump detuning we obtain

$$\hat{H}_{\mathrm{int}} = \begin{cases}\hbar G(\hat{a}^\dagger\hat{b}^\dagger + \hat{a}\hat{b}) & \text{if } \Delta = -\omega_m\\ \hbar G(\hat{a}^\dagger\hat{b} + \hat{a}\hat{b}^\dagger) & \text{if } \Delta = +\omega_m,\end{cases}$$

where we have applied the RWA. In the case of $\Delta = -\omega_m$ the interaction term takes form of a two-mode squeezing Hamiltonian, and the terms describe the creation of a correlated cavity photon and phonon pair by the scattering of a blue-detuned photon into the cavity frequency (and the reverse process, its Hermitian conjugate). This interaction effectively produces amplification or heating of the acoustic mode by parametric driving, as well as anti-damping of the mechanics. Chapter 4 also describes how a blue-detuned optical probe can yield self-oscillation of the mechanical resonator [31]. Conversely, for $\Delta = +\omega_m$ the interaction takes the form of a beam-splitter Hamiltonian between the optical and acoustic modes. The interaction is described by scattering events in which a red-detuned photon is scattered into the cavity frequency via the absorption of a phonon (and the Hermitian conjugate of this process). As this process absorbs energy from the acoustic mode, red-detuning is the regime of optomechanical cooling, and, as we shall see, additional damping of the mechanics.

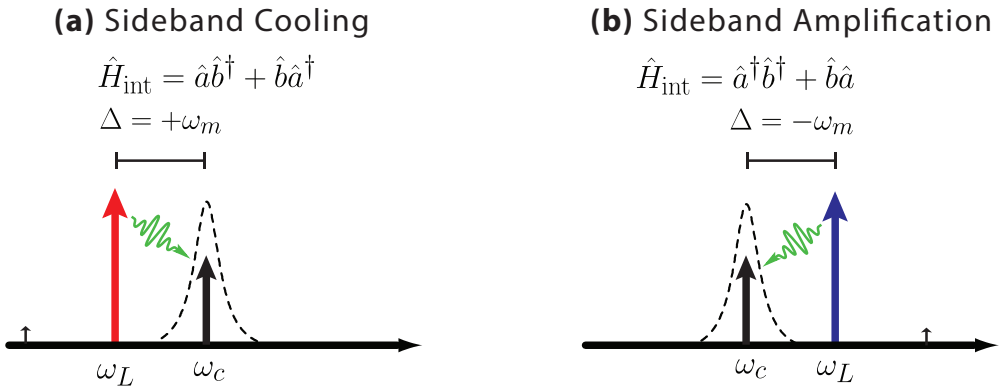

Figure 2.6: **The scattering picture for red- and blue-detuned driving.** (a) Under the linearization approximation, the interaction Hamiltonian for a red-detuned ($\Delta = +\omega_m$) optical pump takes the form of a beam-splitter Hamiltonian. Pump photons are scattered into the cavity frequency ω_c via absorption of a phonon, cooling and damping the mechanics. (b) For blue-detuned ($\Delta = -\omega_m$) driving, the interaction takes the form of a two-mode squeezing Hamiltonian, whereby pump photons are scattered into the cavity frequency by emission of a phonon. This gives rise to correlated pairs of cavity photons and phonons, as well as amplification and anti-damping of the mechanics. For both $\Delta = \pm\omega_m$, the scattered sideband at $\omega_c \mp 2\omega_m$ is suppressed by the reduced cavity susceptibility (according to the sideband resolution parameter $\kappa/(2\omega_m)$).

2.3 Dynamical Back-Action

The full optomechanical Hamiltonian (2.19) does not account for damping of the optical or mechanical mode annihilation operators, or noise inputs from the surrounding environment. In principle, the dynamics of the system will be governed in the Heisenberg picture by the equation of motion for any system operator $\hat{A}$, given by $\dot{\hat{A}} = -(i/\hbar)[\hat{A}, \hat{H}] + \partial\hat{A}/\partial t$. However, in order to incorporate damping and noise inputs it is standard to use the *input-output* formalism of quantum optics describing cavities coupled to a noisy environment. The input-output formalism [49] allows the equations of motion for the optical and mechanical mode annihilation operators to be written:

$$\dot{\hat{a}} = -\left(i\Delta + \frac{\kappa}{2}\right)\hat{a} - ig_0\hat{a}(\hat{b}^\dagger + \hat{b}) + \sqrt{\kappa_{\rm e}}\hat{a}_{\rm in} - \sqrt{\kappa_{\rm i}}\hat{a}_{\rm in,i}, \tag{2.31}$$

$$\dot{\hat{b}} = -\left(i\omega_m + \frac{\gamma_i}{2}\right)\hat{b} - ig_0\hat{a}^\dagger\hat{a} + \sqrt{\gamma_i}\hat{b}_{\rm in}, \tag{2.32}$$

where we have introduced several terms describing damping and noise inputs: $\kappa = \kappa_{\rm i} + \kappa_{\rm e}$ is the total energy loss rate of the optical mode, $\kappa_{\rm e}$ is the *extrinsic* loss

rate to detection channels, and κ_i is the *intrinsic* loss rate to undetected channels (e.g., through scattering out of the cavity mode or absorption). The operator $\hat{a}_\mathrm{in}$ describes input to the cavity mode in the input-output formalism, and $\hat{a}_\mathrm{in,i}$ describes noise input to the cavity mode via intrinsic loss channels (hereafter we will write $\hat{a}_i$ for notational convenience). Similarly, γ_i is the total mechanical energy damping rate, where $\hat{b}_\mathrm{in}$ is a stochastic noise operator describing noise inputs to the mechanics which satisfies the bosonic commutation relation $[\hat{b}_\mathrm{in}(t), \hat{b}^\dagger_\mathrm{in}(t')] = \delta(t - t')$. The input-output formalism yields a boundary condition for computing the output field at the extrinsic optical channel:

$$\hat{a}_\mathrm{out} = \hat{a}_\mathrm{in} - \sqrt{\kappa_\mathrm{e}}\hat{a}. \tag{2.33}$$

While the expressions 2.32 hold for general noise inputs, we usually assume that the mechanical mode is in thermal equilibrium at a temperature T_b having average phonon occupancy $n_\mathrm{b} = (e^{\hbar\omega/k_\mathrm{B}T_\mathrm{b}} - 1)^{-1}$. This gives rise to the noise correlators

$$\langle \hat{b}^\dagger_\mathrm{in}(t)\hat{b}_\mathrm{in}(t')\rangle = n_\mathrm{b}\delta(t - t'), \tag{2.34}$$
$$\langle \hat{b}_\mathrm{in}(t)\hat{b}^\dagger_\mathrm{in}(t')\rangle = (n_\mathrm{b} + 1)\delta(t - t'). \tag{2.35}$$

Using the Fourier Transform convention outlined in Appendix A, these can be written in the frequency domain as

$$\langle \hat{b}^\dagger_\mathrm{in}(\omega)\hat{b}_\mathrm{in}(\omega')\rangle = n_\mathrm{b}\delta(\omega + \omega'), \tag{2.36}$$
$$\langle \hat{b}_\mathrm{in}(\omega)\hat{b}^\dagger_\mathrm{in}(\omega')\rangle = (n_\mathrm{b} + 1)\delta(\omega + \omega'). \tag{2.37}$$

Similarly for the optical mode noise inputs we have the commutation relations $[\hat{a}_\mathrm{in}(t), \hat{a}^\dagger_\mathrm{in}(t')] = \delta(t - t')$ and $[\hat{a}_\mathrm{in,i}(t), \hat{a}_\mathrm{in,i}(t')] = \delta(t - t')$ for the extrinsic and intrinsic noise channels, respectively. The intrinsic noise is usually assumed to be thermal as well, but the corresponding noise occupancy of the optical bath is negligible at frequencies on the optical scale, effectively leading to $\hat{a}_i$ as a vacuum noise input. Therefore, we use the correlators

$$\langle \hat{a}^\dagger_i(t)\hat{a}_i(t')\rangle = 0, \tag{2.38}$$
$$\langle \hat{a}_i(t)\hat{a}^\dagger_i(t)\rangle = \delta(t - t'), \tag{2.39}$$

and in the frequency domain

$$\langle \hat{a}_i^\dagger(\omega)\hat{a}_i(\omega')\rangle = 0, \tag{2.40}$$
$$\langle \hat{a}_i(\omega)\hat{a}_i^\dagger(\omega')\rangle = \delta(\omega+\omega'). \tag{2.41}$$

In the preceding discussion we have explicitly separated the input optical noise into extrinsic (i.e., via a measurement channel) and intrinsic loss channels. We note that the noise on the extrinsic optical input $\hat{a}_{\rm in}$ is generally assumed to be vacuum noise unless otherwise stated, such that $\hat{a}_{\rm in}$ satisfies the same two-time correlators as $\hat{a}_i$.

In analogy with Section 2.2, we aim to simplify the analysis of system dynamics by making a linearization approximation by which we replace the system operators with operators describing fluctuations about some steady-state displacements α and β. By solving Eqn. 2.32 in the steady-state, one finds the steady-state amplitudes in direct analogy with Eqn. 2.27 as

$$\begin{aligned}\alpha &= \frac{\sqrt{\kappa_{\rm e}}\alpha_{\rm in}}{i(\Delta + g_0(\beta^*+\beta)) + \kappa/2},\\ \beta &= \frac{-ig_0 n_{\rm c}}{i\omega_m + \gamma_i/2},\end{aligned} \tag{2.42}$$

where we have used $n_{\rm c} = |\alpha|^2$ is the intracavity photon number. Once again we choose the phase of α to be real without loss of generality going forward. As before we re-define the optical detuning to incorporate the static shift $g_0(\beta^*+\beta) \approx 2g_0^2 n_{\rm c}/\omega_m$. Note that the steady-state drive amplitude $\hat{a}_{\rm in}$ is related to the generalized drive parameter in Eqn. 2.27 by $\hat{a}_{\rm in} = \sqrt{\kappa_{\rm e}}\epsilon$. Now we may obtain the linearized Heisenberg-Langevin equations of motion by one of two equivalent methods: either by substitution of $\hat{a} \longrightarrow \alpha + \hat{a}$, $\hat{b} \longrightarrow \beta + \hat{b}$, $\hat{a}_{\rm in} \longrightarrow \alpha_{\rm in} + \hat{a}_{\rm in}$ into Eqn. 2.32 (ignoring terms beyond first order in the noise operators), or by using our linearized optomechanical Hamiltonian 2.29 along with the Heisenberg-picture prescription $\dot{\hat{A}} = -(i/\hbar)[\hat{A},\hat{H}] + \partial\hat{A}/\partial t$. In either case we again include damping and noise terms according to the input-output formalism and arrive at the full linearized Heisenberg-Langevin equations of motion for the system annihilation operators:

$$\begin{aligned}\dot{\hat{a}} &= -\left(i\Delta + \frac{\kappa}{2}\right)\hat{a} - iG(\hat{b}^\dagger + \hat{b}) + \sqrt{\kappa_{\rm e}}\hat{a}_{\rm in} - \sqrt{\kappa_{\rm i}}\hat{a}_{\rm in,i},\\ \dot{\hat{b}} &= -\left(i\omega_m + \frac{\gamma_i}{2}\right)\hat{b} - iG(\hat{a}^\dagger + \hat{a}) + \sqrt{\gamma_i}\hat{b}_{\rm in},\end{aligned} \tag{2.43}$$

where again $G = g_0\alpha$ is the parametrically-enhanced optomechanical coupling rate. We can solve for the field amplitudes in the frequency domain by taking the Fourier Transform of Eqn. 2.43. In the frequency domain,

$$\hat{a}(\omega) = \frac{-iG(\hat{b}^\dagger(\omega) + \hat{b}(\omega)) + \sqrt{\kappa_\mathrm{e}}\hat{a}_\mathrm{in}(\omega) + \sqrt{\kappa_\mathrm{i}}\hat{a}_i(\omega)}{i(\Delta - \omega) + \kappa/2}, \tag{2.44}$$

$$\hat{b}(\omega) = \frac{\sqrt{\gamma_\mathrm{i}}\hat{b}_\mathrm{in}(\omega) - iG(\hat{a}(\omega) + \hat{a}^\dagger(\omega))}{i(\omega_m - \omega) + \gamma_i/2}. \tag{2.45}$$

Inserting Eqn. 2.44 into Eqn. 2.45, we obtain an expression for the mechanical fluctuations entirely in terms of coherent and noise optical inputs:

$$\hat{b}(\omega) = \frac{1}{i(\omega_m - \omega) + \gamma_i/2}\left(\sqrt{\gamma_i}\hat{b}_\mathrm{in}(\omega) - iG\left[\frac{-iG(\hat{b}^\dagger(\omega) + \hat{b}(\omega)) + \sqrt{\kappa_\mathrm{e}}\hat{a}_\mathrm{in}(\omega) + \sqrt{\kappa_\mathrm{i}}\hat{a}_i(\omega)}{i(\Delta - \omega) + \kappa/2}\right.\right. \tag{2.46}$$

$$\left.\left. + \frac{iG(\hat{b}^\dagger(\omega) + \hat{b}(\omega)) + \sqrt{\kappa_\mathrm{e}}\hat{a}^\dagger_\mathrm{in}(-\omega) + \sqrt{\kappa_\mathrm{i}}\hat{a}^\dagger_i(-\omega)}{-i(\Delta - \omega) + \kappa/2}\right]\right). \tag{2.47}$$

Defining the bare optical and mechanical susceptibilities, respectively $\chi_a(\omega) \equiv (i(\Delta - \omega) + \kappa/2)^{-1}$ and $\chi_b(\omega) \equiv (i(\omega_m - \omega) + \gamma_i/2)^{-1}$, we can re-write this as

$$\hat{b}(\omega) = (1 - G^2\chi_b(\omega))[\chi_a(\omega) - \chi^*_a(\omega)]^{-1}(-\sqrt{\gamma_i}\chi_b(\omega)\hat{b}_\mathrm{in}(\omega) \tag{2.48}$$

$$- iG\chi_b(\omega)[\chi_a(\omega)(\sqrt{\kappa_\mathrm{e}}\hat{a}_\mathrm{in}(\omega) + \sqrt{\kappa_\mathrm{i}}\hat{a}_i(\omega)) + \chi^*_a(-\omega)(\sqrt{\kappa_\mathrm{e}}\hat{a}^\dagger_\mathrm{in}(-\omega) + \sqrt{\kappa_\mathrm{i}}\hat{a}^\dagger_i(-\omega))]). \tag{2.49}$$

Let us group the optical driving terms by defining $\hat{A}_\mathrm{in}(\omega) \equiv \chi_a(\omega)(\sqrt{\kappa_\mathrm{e}}\hat{a}_\mathrm{in}(\omega) + \sqrt{\kappa_\mathrm{i}}\hat{a}_i(\omega)) + \chi^*_a(-\omega)(\sqrt{\kappa_\mathrm{e}}\hat{a}^\dagger_\mathrm{in}(-\omega) + \sqrt{\kappa_\mathrm{i}}\hat{a}^\dagger_i(-\omega))$. Then the mechanical mode annihilation operator in the frequency domain is

$$\hat{b}(\omega) = \frac{-\sqrt{\gamma_i}\hat{b}_\mathrm{in}(\omega)}{i(\omega'_m - \omega) + \gamma/2} - \frac{iG\hat{A}_\mathrm{in}(\omega)}{i(\omega'_m - \omega) + \gamma/2}. \tag{2.50}$$

The mechanical fluctuations are now found to be peaked around an optomechanically-shifted mechanical frequency ω'_m, where $\omega'_m \equiv \omega_m + \delta\omega_m$, with a new total damping rate of $\gamma = \gamma_i + \delta\gamma$, and the optomechanical *back-action* induced shifts given by

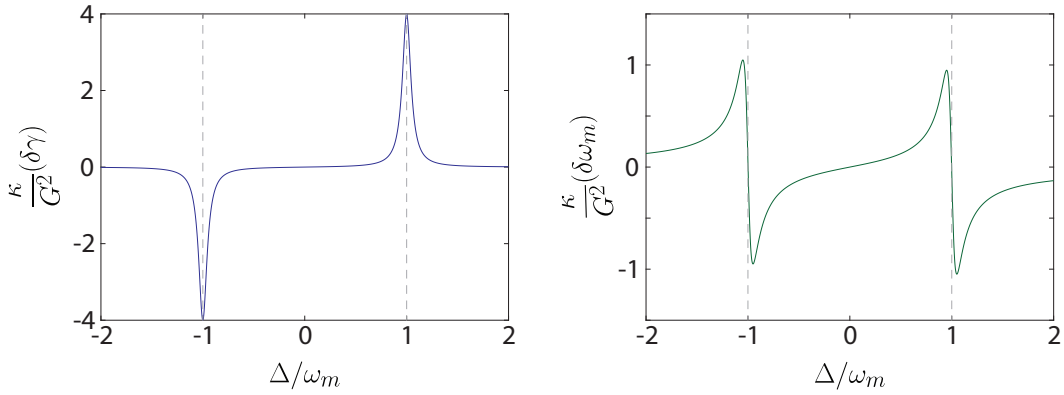

Figure 2.7: **Dynamical back-action damping and the optical spring effect.** Plots of the normalized optical back-action modification to the mechanical damping rate (left) and to the mechanical frequency (right) as a function of detuning Δ, where we have chosen a ratio $\kappa/\omega_m = 0.1$ typical to the sideband-resolved systems in this work.

$$\delta\omega_m(\Delta) = G^2\,\mathrm{Im}\{\chi_a(\omega) - \chi_a^*(-\omega)\} \tag{2.51}$$

$$= G^2\,\mathrm{Im}\left\{\frac{1}{i(\Delta-\omega_m)+\kappa/2} - \frac{1}{-i(\Delta+\omega_m)+\kappa/2}\right\}, \tag{2.52}$$

$$\delta\gamma(\Delta) = 2G^2\mathrm{Re}\{\chi_a(\omega) - \chi_a^*(-\omega)\} \tag{2.53}$$

$$= 2G^2\mathrm{Re}\left\{\frac{1}{i(\Delta-\omega_m)+\kappa/2} - \frac{1}{-i(\Delta+\omega_m)+\kappa/2}\right\}. \tag{2.54}$$

These dynamical back-action induced optical shifts to the mechanical frequency and damping rate are plotted schematically in Figure 2.7. In the second equality of the above expressions we have substituted $\omega \longrightarrow \omega_m$ since the mechanical response will be approximately constant over the bandwidth of the optical cavity, as $\gamma \ll \kappa$ holds in all systems considered in this work, and hence the mechanical response is only significant for frequencies $|\omega - \omega_m| \lesssim \gamma \ll \kappa$.

Sideband Resolved Systems

Most relevant to the experiments presented in this work is the resolved sideband regime in which the optical cavity linewidth satisfies $\kappa \ll \omega_m$. We will see that for typical devices we have studied here with microwave-frequency mechanical resonances the *sideband resolution ratio* is $\kappa/(2\omega_m) \sim 5\times10^{-2}$, placing us securely

in the resolved sideband regime. In particular we consider the two detuning scenarios most relevant to experiment, $\Delta = \pm\omega_m$, and find that we can write the optomechanical corrections to the mechanical frequency (the "optical spring") and damping rate as:

$$\delta\omega_m(\Delta = \pm\omega_m) = \pm\frac{G^2}{2\omega_m}\left(\frac{1}{1 + (\kappa/(2\omega_m))^2}\right) \approx \frac{G^2}{2\omega_m}, \tag{2.55}$$

$$\delta\gamma(\Delta = \pm\omega_m) = \pm\frac{4G^2}{\kappa}. \tag{2.56}$$

The mechanical frequency shift $\delta\omega_m \approx (G^2/2\omega_m)$ is typically small and unimportant in the studies presented here, but the optomechanical damping $\delta\gamma$ is critically important. For convenience we will follow the convention to define the optomechanical damping term at $\Delta = \pm\omega_m$ as

$$\gamma_{\mathrm{OM}}\Big|_{\Delta=\pm\omega_m} \equiv |\delta\omega_m(\Delta = \pm\omega_m)| = \frac{4G^2}{\kappa} = \frac{4g_0^2 n_{\mathrm{c}}}{\kappa}, \tag{2.57}$$

which is a strictly positive quantity, such that the total mechanical damping rate is given by $\gamma = \gamma_i \pm \gamma_{\mathrm{OM}}$ for $\Delta = \pm\omega_m$ (red- or blue-detuning, respectively).

Generally we are interested in calculating and measuring the output optical field $\hat{a}_{\mathrm{out}}$ in a cavity-optomechanical system using the boundary condition given by the input-output formalism, and by this we are motivated to find simplified expressions for the optical fluctuation operator $\hat{a}$ in terms of coherent and noise inputs from both the optics and mechanics. We consider the special case of red-detuning with $\Delta = +\omega_m$, where we find that we can write the mechanical fluctuation operator in Eqn. 2.50 in a simplified way:

$$\hat{b}(\omega)\Big|_{\Delta=+\omega_m} = \chi_b'(\omega)\Big(- \sqrt{\gamma_i}\hat{b}_{\mathrm{in}}(\omega) - iG\chi_a(\omega)\Big(\sqrt{\kappa_{\mathrm{e}}}\hat{a}_{\mathrm{in}}(\omega) + \sqrt{\kappa_{\mathrm{i}}}\hat{a}_i(\omega)\Big)\Big). \tag{2.58}$$

In the above expression we have defined a shifted mechanical susceptibility $\chi_b'(\omega) = (i(\omega_m' - \omega) + \gamma/2)^{-1}$ and also chosen to neglect terms involving products of terms peaked near $\approx +\omega_m$ and terms peaked near $\approx -\omega_m$, in particular $\chi_b'(\omega) \times \chi_a^*(-\omega)$, as ω_m being $\ll \kappa, \gamma$ implies that the product of these susceptibility functions will be negligible. This expression can be rewritten

$$\hat{b}(\omega)\Big|_{\Delta=+\omega_m} = \chi_b'(\omega)\Big(- \sqrt{\gamma_i}\hat{b}_{\rm in}(\omega) - i\sqrt{\frac{\gamma_{\rm OM}}{\kappa}}(\sqrt{\kappa_{\rm e}}\hat{a}_{\rm in}(\omega) + \sqrt{\kappa_{\rm i}}\hat{a}_i(\omega))\Big). \quad (2.59)$$

Substituting 2.59 into 2.44, and making use of the input-output boundary condition 2.33, we write an expression for the optical output fluctuations in terms of only optical inputs, optical noise, and mechanical noise fluctuation operators:

$$\hat{a}_{\rm out}(\omega)\Big|_{\Delta=+\omega_m} \approx r(\omega;+)\hat{a}_{\rm in}(\omega) + n(\omega;+)\hat{a}_i(\omega) + s(\omega;+)\hat{b}_{\rm in}(\omega), \quad (2.60)$$

where $r(\omega;\pm)$, $n(\omega;\pm)$, $s(\omega;\pm)$ are optomechanical scattering matrix elements given explicitly in Appendix A.4. In a similar way we obtain for blue-detuning

$$\hat{a}_{\rm out}(\omega)\Big|_{\Delta=-\omega_m} \approx r(\omega;-)\hat{a}_{\rm in}(\omega) + n(\omega;-)\hat{a}_i(\omega) + s(\omega;-)\hat{b}^\dagger_{\rm in}(\omega). \quad (2.61)$$

2.4 Heterodyne Detection

Here we will give a brief review of *heterodyne detection*, a method used in the work presented throughout this thesis to observe the mechanical noise power spectral density imprinted on the intracavity light field. Heterodyne detection (heterodyning) is a linear detection technique as it involves measuring a photocurrent proportional to the squared field amplitudes incident on a receiver. In heterodyne detection setups, a strong local oscillator (L.O.) amplifies a signal tone and mixes it into a frequency range which is convenient for detection. A special case of heterodyne detection–known as homodyne detection–in which the L.O. frequency is equal to the signal frequency, is also discussed for comparison to heterodyning. In homodyne detection, the L.O. frequency is matched to the signal frequency (often they are derived from the same laser source), allowing the relative phase of the L.O. to be controlled to perform detection of any desired quadrature of the signal. In general, the L.O. frequency may be chosen for a host of reasons, but is commonly used to either place the desired signal tone within a narrow radio-frequency detection bandwidth or to spectrally separate it from technical L.O. noise. These concepts are illustrated schematically in Figure 2.8.

Single-Port Heterodyne Detection

The simplest implementation of heterodyne detection is illustrated in Figure 2.9, in which a signal beam $\hat{a}$ and a local oscillator $\hat{b}$ are combined on a beam-splitter,

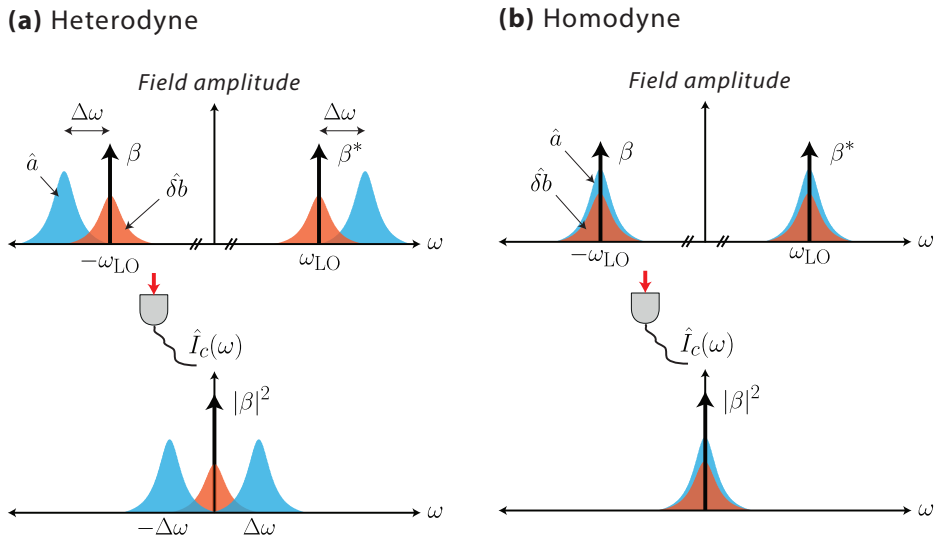

Figure 2.8: **Comparison of heterodyne and homodyne detection methods. a**, In heterodyne detection, an offset frequency $\Delta\omega$ between the L.O. and the signal frequency of interest (contained in the operator $\hat{a}$) is used to place the signal in a desired frequency band. This may be performed to mix a high-frequency signal to a lower frequency within the bandwidth of a receiver. In this work, a 5 GHz mechanical noise spectrum is routinely mixed to < 100 MHz for detection on a high-gain RF photoreceiver. Noise on the local oscillator (indicated as $\delta\hat{b}$) is generically centered at ω_{LO}. Upon photodetection, a photocurrent is generated proportional to the squared field amplitude. Local oscillator noise is mixed to near DC while the signal spectrum is offset by $\Delta\omega$. **b**, In homodyne detection, in which ω_{LO} matches the signal frequency, L.O. noise is generically centered at the same frequency as the signal. Upon photodetection, the signal is mixed to to near DC. Because the L.O. and signal frequency are at the same frequency, the relative phase of the L.O. may be controlled in order to perform detection on any desired quadrature of the signal.

with one output $\hat{c}$ measured on a photodetector producing a photocurrent $\hat{I}_c(t)$. For simplicity we will assume that the input and output ports of the beamsplitter are single-mode and single-polarization, allowing us to neglect any concerns of spatial mode-matching. In this context the input and output mode operators are bosonic mode continuum operators, in the Schrödinger picture, indexed by frequency (or in general, wave-vector), $\hat{a} = \hat{a}_\omega$. They satisfy the usual bosonic commutation relations,

$$[\hat{a}_\omega, \hat{a}^\dagger_{\omega'}] = \delta(\omega - \omega'), \tag{2.62}$$

and have units of $\mathrm{Hz}^{-1/2}$. It is convenient to define a corresponding time-domain operator,

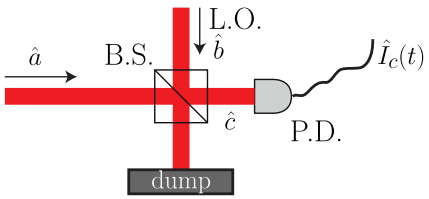

Figure 2.9: **A simple single-port heterodyne detection setup.** An input signal $\hat{a}$ and a strong local oscillator (L.O.) are incident upon a beam-splitter with transmission coefficient T and reflection R = 1-T. A beat note appears at the sum and difference frequency of the signal and local oscillator (frequency ω_{LO}). At the output of the beam-splitter, one port is used to generate a photocurrent (here, mode $\hat{c}$), which will consist of the beat-note terms as well as a DC term and terms arising from noise on the LO.

$$\hat{a}(t) = \int_{-\infty}^{\infty} \frac{d\omega}{2\pi} e^{-i\omega t} \hat{a}_{\omega}, \tag{2.63}$$

as having units of square root of flux $\mathrm{Hz}^{1/2} \sim \sqrt{\text{photons/s}}$. These $\hat{a}(t)$ should not be confused with the Heisenberg picture operators used in the quantum Heisenberg-Langevin formalism of the previous section, but instead are simply constructs written in terms of the Schrödinger-picture continuum operators. It is straightforward to show that the Heisenberg operator $\hat{a}(\omega)$ is related to the continuum operator by $\hat{a}(\omega) = 2\pi \hat{a}_{\omega}(0)$.

Now, a main objective of heterodyne detection is to amplify a weak signal by a strong coherent local oscillator (L.O.) amplitude, and hence we will assume the local oscillator amplitude may be written as

$$\hat{b}(t) \cong \beta e^{-i\omega_{\mathrm{LO}} t} + \hat{\delta b}(t), \tag{2.64}$$

where $\beta \in \mathbb{C}$ is a large coherent field amplitude, equal to the square root of the average L.O. photon flux, and $\hat{\delta b}(t)$ contains all the L.O. noise, including both vacuum noise and technical noise. If we assume an ideal detection quantum efficiency $\eta_{\mathrm{QE}} = 1$ and a beam-splitter transmission coefficient $T = 1 - R$, we may write the (normalized) photocurrent generated by the output $\hat{c}$ as

$$\hat{I}_c(t) = T\hat{a}^{\dagger}\hat{a} + R\hat{b}^{\dagger}\hat{b} + i\sqrt{TR}(\hat{b}^{\dagger}\hat{a} - \hat{a}^{\dagger}\hat{b}). \tag{2.65}$$

We will typically assume that $|\beta|$ is sufficiently large that we can ignore the term $T\hat{a}^{\dagger}\hat{a}$. We will also use a convenient notation to denote the slowly-varying parts of

the relevant fields relative to the L.O. For example, $\hat{a}(t) = \tilde{\hat{a}}(t)e^{-i\omega_{\mathrm{LO}}t}$. Then the photocurrent becomes

$$\hat{I}_c(t) \approx |\beta|^2 + i\beta(e^{i\phi_{\mathrm{LO}}}\tilde{\hat{a}}(t) - e^{i\phi_{\mathrm{LO}}}\tilde{\hat{a}}^\dagger(t)) + \beta\sqrt{R}(e^{-i\phi_{\mathrm{LO}}}\tilde{\delta\hat{b}} - e^{i\phi_{\mathrm{LO}}}\tilde{\delta\hat{b}}^\dagger). \tag{2.66}$$

Referring the quadrature operator definitions as introduced in Appendix A.2, we can write this in a simpler form:

$$\hat{I}_c(t) \approx |\beta|^2 - \sqrt{2}\beta\left(\hat{x}_{\mathrm{a},\,\phi_{\mathrm{LO}}+\pi/2} - i\sqrt{R}\hat{x}_{\delta\mathrm{b},\,\phi_{\mathrm{LO}}+\pi/2}\right). \tag{2.67}$$

We will refer to this result later, using the fact that the photocurrent consists of the position quadrature of the signal field amplified linearly by the local oscillator amplitude. The measured photocurrent consists of a DC term, quadrature of the signal mode $\hat{a}$, and a quadrature of the L.O. noise operator $\hat{\delta b}$. In this case, both the signal and noise terms are linearly amplified by the L.O. strength β. A more powerful measurement technique might be desired to eliminate such noise terms on the output photocurrent.

Balanced Heterodyne Detection

The photocurrent obtained in Equation 2.67 contains both a large D.C. offset term and an amplified local oscillator noise term proportional to $\beta\hat{x}_{\delta\mathrm{b},\,\phi_{\mathrm{LO}}}$. These *common mode* noise terms can in principle be eliminated with the use of a more sophisticated technique known as *balanced heterodyne* (*homodyne*), in which the previously discarded output port of the beam-splitter is used as a resource for noise reduction by measuring the difference in photocurrents at the two beam splitter output ports.

The generic balanced heterodyne setup is sketched in Figure 2.10, in which the output field $\hat{a}_{\mathrm{out}}$ from a cavity-optomechanical system is sent to to an idealized beam-splitter along with a strong L.O. tone. The difference photocurrent $\hat{I}_-(t)$ between the two output port photocurrents is measured. In direct analogy to Equation 2.65 it is straightforward to see that the difference photocurrent may be written

$$\hat{I}_-(t) \cong i|\beta|\left(e^{-i\phi_{\mathrm{LO}}}\tilde{\hat{a}}(t) - e^{i\phi_{\mathrm{LO}}}\tilde{\hat{a}}^\dagger(t)\right) \tag{2.68}$$

for a signal input $\hat{a} = \hat{a}_\omega$, where we have assumed $|\beta|$ is sufficiently large that we may ignore terms of order $\hat{\delta b}$. Note that in contrast to single-port heterodyne

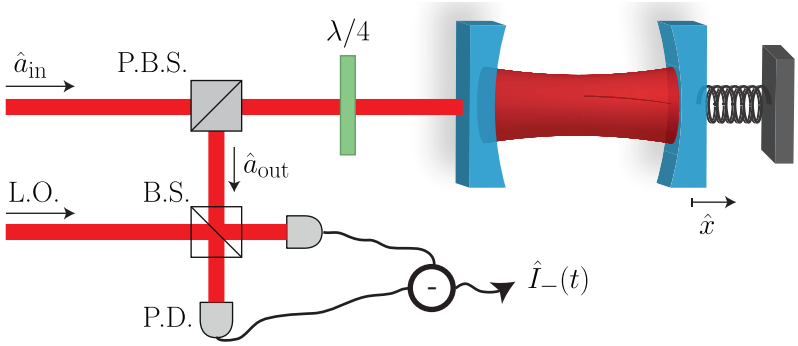

Figure 2.10: **Balanced heterodyne detection of a cavity-optomechanical system output field.** A single-mode, single-polarization field $\hat{a}_{\rm in}$ is input to a cavity-optomechanical system. The output field $\hat{a}_{\rm out}$ is sent to a balanced heterodyne/homodyne detection setup, here modeled as an ideal 50/50 beam-splitter and two photodetectors. A local oscillator of frequency $\omega_{\rm LO}$ is mixed with the signal $\hat{a}_{\rm out}$ on the beam-splitter. Measuring the difference photocurrent from the two photodetectors allows common-mode noise of the local oscillator to be rejected (to some common-mode rejection ratio CMRR, typically 35 – 60 dB).

detection, here we do not have any noise terms going like $\beta\hat{\delta b}$, amplified by the local oscillator. In our Heisenberg-Langevin formalism using the input-output operators as expressed in Equations 2.60 and 2.61, this can then be written in the frequency domain as

$$\hat{I}_-(\omega) \cong 2\pi i|\beta|\left(e^{-i\phi_{\rm LO}}\hat{a}_{\rm out}(\omega) - e^{i\phi_{\rm LO}}\hat{a}^\dagger_{\rm out}(\omega)\right) = 2\sqrt{2}\pi|\beta|\hat{x}_{\rm out,\ \phi_{\rm LO}+\pi/2}. \tag{2.69}$$

Let us consider as an illustrative example the case of a sideband-resolved system under red-detuned ($\Delta = +\omega_m$) driving as measured on a balanced heterodyne detection setup. Then Equation 2.60 gives the output field in terms of reflection coefficients and fluctuation operators, and we may directly write an expression for the power spectral density of the difference photocurrent using Equation A.8:

$$S_{\hat{I}_-\hat{I}_-}[\omega] = \int_{-\infty}^{\infty}\frac{d\omega'}{2\pi}\,\langle\hat{I}^\dagger_-(\omega)\hat{I}_-(\omega')\rangle \tag{2.70}$$

$$= 2\pi|\beta|^2\int_{-\infty}^{\infty}d\omega'\left(\langle\hat{a}^\dagger_{\rm out}(-\omega)\hat{a}_{\rm out}(\omega')\rangle + \langle\hat{a}_{\rm out}(-\omega)\hat{a}^\dagger_{\rm out}(\omega')\rangle\right. \tag{2.71}$$

$$\left. + e^{2i\phi_{\rm LO}}\langle\hat{a}^\dagger_{\rm out}(-\omega)\hat{a}^\dagger_{\rm out}(\omega')\rangle + e^{-2i\phi_{\rm LO}}\langle\hat{a}_{\rm out}(-\omega)\hat{a}_{\rm out}(-\omega')\rangle\right). \tag{2.72}$$

Recognizing that the terms going like $\langle \hat{a}^\dagger_{\text{out}} \hat{a}^\dagger_{\text{out}} \rangle$ and $\langle \hat{a}_{\text{out}} \hat{a}_{\text{out}} \rangle$ will vanish due to the noise input correlation relations, we can simplify this expression, keeping only the terms independent of the L.O. phase. Explicitly, using Eqn. 2.60, we have

$$S_{\hat{I}_-\hat{I}_-}[\omega] = 2\pi|\beta|^2 \int_{-\infty}^{\infty} d\omega' \left(r^*(\omega;+) r(\omega';+) \langle \hat{a}^\dagger_{\text{in}}(-\omega) \hat{a}_{\text{in}}(\omega') \rangle \right. \tag{2.73}$$

$$+ n^*(\omega;+) n(\omega';+) \langle \hat{a}^\dagger_i(-\omega) \hat{a}_i(\omega') \rangle \tag{2.74}$$

$$+ s^*(\omega;+) s(\omega';+) \langle \hat{b}^\dagger_{\text{in}}(-\omega) \hat{b}_{\text{in}}(\omega') \rangle \tag{2.75}$$

$$+ r(\omega;+) r^*(\omega';+) \langle \hat{a}_{\text{in}}(\omega) \hat{a}^\dagger_{\text{in}}(-\omega') \rangle \tag{2.76}$$

$$+ n(\omega;+) n^*(\omega';+) \langle \hat{a}^\dagger_i(\omega) \hat{a}_i(-\omega') \rangle \tag{2.77}$$

$$\left. + s(\omega;+) s^*(\omega';+) \langle \hat{b}_{\text{in}}(\omega) \hat{b}^\dagger_{\text{in}}(-\omega') \rangle \right) \tag{2.78}$$

$$= |r(\omega;+)|^2 + |n(\omega;+)|^2 + |s(\omega;+)|^2 (n_{\text{b}} + 1) + |s(-\omega;+)|^2 n_{\text{b}}. \tag{2.79}$$

The scattering matrix elements have the property $|r(\omega;+)|^2 + |n(\omega;+)|^2 + |s(\omega;+)|^2 = 1$, allowing us to write

$$S_{\hat{I}_-\hat{I}_-}[\omega]\Big|_{\Delta=+\omega_m} = 2\pi|\beta|^2 \left(1 + n_{\text{b}} (|s(\omega;+)|^2 + |s(-\omega;+)|^2) \right) \tag{2.80}$$

$$= 2\pi|\beta|^2 \left(1 + 2\frac{\kappa_{\text{e}}}{\kappa} \gamma_{\text{OM}} \bar{S}_{\hat{b}\hat{b}}[\omega; n_{\text{b}}] \right), \tag{2.81}$$

where $\bar{S}_{\hat{b}\hat{b}}$ is the symmetrized PSD of $\hat{b}$ as defined in Appendix A.3. Similarly, for the case of blue detuning ($\Delta = -\omega_m$), we have

$$S_{\hat{I}_-\hat{I}_-}[\omega]\Big|_{\Delta=-\omega_m} = 2\pi|\beta|^2 \left(1 + n_{\text{b}} (|s(\omega;+)|^2 + |s(-\omega;+)|^2) \right) \tag{2.82}$$

$$= 2\pi|\beta|^2 \left(1 + 2\frac{\kappa_{\text{e}}}{\kappa} \gamma_{\text{OM}} \bar{S}_{\hat{b}^\dagger\hat{b}^\dagger}[\omega; n_{\text{b}}] \right). \tag{2.83}$$

In a real balanced heterodyne setup there will be a sub-unity quantum efficiency in detection $\eta_{\text{QE}} < 1$, as well as technical and vacuum noise on the local oscillator. To consider this, we will modify the local oscillator field as

$$\hat{b}(t) = \beta e^{-i\omega_{\text{LO}} t} (1 + n(t)) + \delta\hat{b}_v, \tag{2.84}$$

where $n(t)$ is a time-dependent stochastic variable modeling amplitude noise of the L.O., and $\hat{\delta b}_v$ is the vacuum noise of the L.O. field. It is straightforward to show that the difference current may now be written

$$\hat{I}_-(t) \approx 2\pi\eta_{\mathrm{QE}}|\beta|^2(1+2n(t)) + 2\pi\eta_{\mathrm{QE}}\beta\left(e^{-i\phi_{\mathrm{LO}}}\tilde{\delta b}_v + e^{i\phi_{\mathrm{LO}}}\tilde{\delta b}_v^\dagger\right) \tag{2.85}$$

$$+ 2\pi i|\beta|\eta_{\mathrm{QE}}\sqrt{1-\eta_{\mathrm{QE}}}\left(e^{i\phi_{\mathrm{LO}}}\hat{a}_{\mathrm{out}}^\dagger(t) - e^{-i\phi_{\mathrm{LO}}}\hat{a}_{\mathrm{out}}(t)\right). \tag{2.86}$$

The corresponding spectral density is found to be

$$S_{\hat{I}_-\hat{I}_-}[\omega]\Big|_{\Delta=+\omega_m} = \eta_{\mathrm{QE}}^2|\beta|^4 + 2\pi|\beta|^2 + 2\pi|\beta|^4(\delta(\omega) + 2\mathcal{S}_{nn}[\omega]) \tag{2.87}$$

$$+ 2\pi|\beta|^2\eta_{\mathrm{QE}}\sqrt{1-\eta_{\mathrm{QE}}}\left(2\frac{\kappa_{\mathrm{e}}}{\kappa}\gamma_{\mathrm{OM}}\bar{S}_{\hat{b}\hat{b}}[\omega;n_{\mathrm{b}}]\right), \tag{2.88}$$

where $\mathcal{S}_{nn}[\omega]$ is the classical NPSD of the amplitude noise $n(t)$. As usual, for $\Delta = -\omega_m$ we obtain an analogous result with the replacement $\bar{S}_{\hat{b}\hat{b}}[\omega;n_{\mathrm{b}}] \longrightarrow \bar{S}_{\hat{b}^\dagger\hat{b}^\dagger}[\omega;n_{\mathrm{b}}]$. The spectral density is illustrated schematically in Figure 2.11. The experimentally measured quantity will be a symmetrized $\bar{S}_{\hat{I}_-\hat{I}_-}[\omega]$, where the overall magnitude of the signal is scaled according to gain and loss characteristics of the detectors.

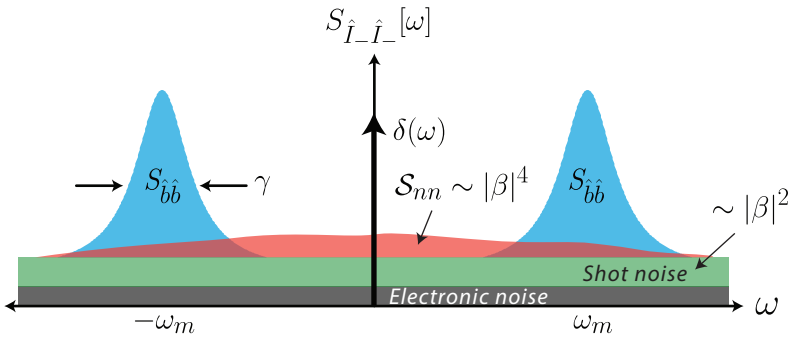

Figure 2.11: **Balanced heterodyne output spectrum illustration.** The spectral density of the difference photocurrent generated by a balanced heterodyne detection setup used in a sideband-resolved cavity-optomechanical system. The output will consist of a DC term, electronic (dark) detector noise, shot noise proportional to the L.O. photon flux $|\beta|^2$, the amplitude noise power spectral density, and signal terms proportional to annihilation or creation operator spectral densities $S_{\hat{b}\hat{b}}$ and $S_{\hat{b}^\dagger\hat{b}^\dagger}$.

Chapter 3

DEVICE NANOFABRICATION AND LOW-TEMPERATURE OPTICAL METHODS

In this chapter various technical and experimental details will be presented briefly in order to give a more complete picture of how device fabrication and low-temperature characterization are performed in the Painter Lab.

3.1 Nanofabrication Methods

Virtually all of the device fabrication summarized in this thesis was performed in cleanroom laboratories on the Caltech campus. The Painter Group maintains a dedicated class 10,000/1,000 cleanroom containing a variety of instruments suitable for processing photonic devices, optomechanical crystals, micro- and nano-electromechanical systems (MEMS and NEMS), as well as superconducting quantum circuits. Additionally, the work presented here made heavy use of the shared campus cleanroom facilities of the Kavli Nanoscience Institute (KNI), in particular for lithographic exposures for both electron-beam and photo-lithography. The nanobeam and other silicon optomechanical crystal devices were fabricated on silicon-on-insulator (SOI) wafers from Soitec, with a device layer Si thickness 220 nm, buried oxide (BOX) layer 3 μm, handle Si thickness 500 μm, crystal orientation $\langle 1,0,0\rangle$, resistivity $\rho \sim 5-15\ \Omega\cdot$cm, diced into die of either 5×13 mm or 5×10 mm. Silicon-on-insulator is a natural choice of substrate as it allows the ease of fabrication of suspended nanoscale structures within the thin membrane of the silicon device layer by simply removing or undercutting the buried oxide layer, and the standard fabrication processes for SOI are very mature in both industrial and academic applications. An overview of the fabrication process for nanobeam OMCs is shown in Figure 3.1. In its simplest form this process involves only a single layer of lithography to fabricate suspended silicon structures. These steps are shown schematically in Figure 3.1. The main process steps are:

1. *Pre-cleaning of the chip*. This step prepares the substrate chip for application of resist. Chips will typically retain some protective coating after the wafer-dicing process, either in the form of an adhesive film or a layer of photoresist.

In either case, a solvent rinse in acetone (ACE) followed by isopropanol (IPA) is usually sufficient to obtain a clean chip surface.

2. *Spinning and baking of electron-beam (e-beam) resist*. We typically use a ZEON ZEP-520A e-beam resist for its high resolution and high selectivity against common plasma etch chemistries. The resist is hardened by baking using a hot-plate or oven.

3. *Electron-beam (e-beam) lithography exposure*. The optomechanical crystal device pattern is defined in the resist using e-beam lithography, including proximity effect corrections to refine the dose exposing the resist.

4. *Resist development*. The chip is submerged in a developing solvent to relieve the patterns, in the case of ZEP-520A the developer used here is ZED-N50.

5. *Plasma etching*. Inductively-coupled plasma reactive-ion etching (ICP-RIE) is used to transfer the device pattern from the resist into the silicon layer.

6. *Resist stripping*. A chemical cleaning is performed to remove the resist layer, typically by submerging the chip in a piranha solution (3:1 sulfuric acid to hydrogen peroxide), in which a highly exothermic reaction chemically burns organics such as resist from the chip and mechanically scrubs debris.

7. *Oxide undercutting or device layer release*. To remove the buried oxide in the vicinity of the OMC device, hydrofluoric acid (HF) is used as an etchant. This is typically performed using anhydrous vapor-HF, but may also be performed with an aqueous solution.

8. *Final surface cleaning and hydrophobic passivation*. The HF etching of the release step removes any native or chemically-grown oxide at the silicon surface and passivates the silicon surface with hydrogen bonds.

As the techniques and principles used for plasma etching of silicon are quite well-known and understood across both industry and academia [50, 51], only a brief review of silicon etching principles will be given here as it pertains to fabricating nanophotonic devices. We are concerned with realizing photonic structures with feature sizes down to several tens of nm in device layer silicon with a thickness of 220 nm. A standard technique for etching patterns defined in e-beam resist is reactive-ion etching (RIE), in which a combination of reactive species gases is

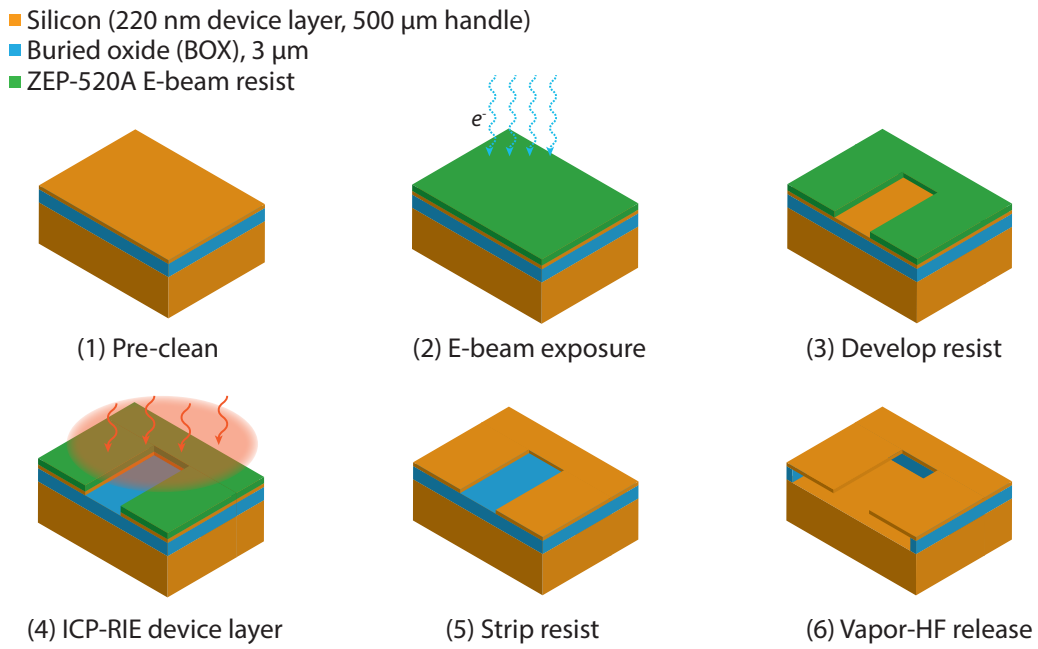

Figure 3.1: **Silicon-on-insulator single-layer process flow.** For fabrication of suspended devices a single lithography layer process is used. Optical coupling to these planar devices must be performed using an out-of-plane coupling method, e.g. optical tapered-fiber coupling. The resist is patterned via e-beam lithography to define the OMC and coupling waveguide. Plasma etching (ICP-RIE) is used to transfer the pattern into the 220 nm silicon device layer. After the resist is stripped, the buried oxide layer is removed via vapor-HF etching to suspend the optical structures.

driven into a plasma phase by application of a large radio-frequency (RF) voltage. The etching process depends in detail upon the choice and relative flow rates of reactive species, as well as the RF voltage and resulting DC bias voltage across the plasma chamber which emerges upon separation of the gases into radicals, ions, and electrons. An enhancement to RIE etching known as inductively-coupled plasma (ICP-RIE) is frequently implemented, in which a second RF field is applied to the plasma at high power (typically $1 - 2$ kW), increasing the density of ions for better control of etch rates and other process variables. We use a combination of reactive species C_4F_8 and SF_6 in a standard *pseudo-Bosch* etching process [52]. In a regular Bosch process, these two gases are introduced to the etch chamber in alternation. The C_4F_8 serves to form a protective film, or passivation layer, at the Si surface, while also mechanically milling some Si. Volatile species are desorbed from the surface and pumped out of the chamber, then SF_6 is introduced. The reactive species produced by SF_6 break down the passivation layer and chemically etch the

underlying Si for a fixed time, then the chamber is pumped out and the cycle is repeated. This cyclic Bosch process is the primary technique for deep reactive-ion etching (DRIE) of high-aspect ratio features deep into a substrate material (aside from cryo-DRIE).

Chemical etching by SF_6 is less rapid on sidewall features than on bottom features owing to the directionality of particle acceleration by the applied bias voltage, and thus by tuning the relative flow rates of the gases in their respective recipe steps one can control the directionality of the etch profile. Pseudo-Bosch is an analogous process, in which the alternation of gases is eliminated and both (or multiple) species are admitted to the chamber simultaneously. In this type of etch, which is used for the majority of the plasma etching in this work, the etch profile is primarily controlled by the relative flow rates or pressures of the reactive gases and the applied RF power (and resulting DC bias voltage) as well as the applied ICP power. A recipe with a relatively high ratio of SF_6 to C_4F_8 flow will tend toward isotropic etching, yielding features with side-walls that are narrower at the top and bottom of the Si layer and wider near the center. A low ratio of SF_6 to C_4F_8 will overly passivate the sidewall features, slowing etching by the SF_6, and result in side-walls which are wide at the top and narrow at the bottom. To obtain structures nearly vertical side-walls, we refine the gas flow rates and applied DC bias voltage iteratively during successive rounds of device fabrication until the recipe parameters are optimized. Some optimized recipe parameters used for fabrication of the devices in this work are given in Table 3.3. Good verticality of the side-wall profiles are important in OMC devices as symmetry in the $\hat{z}$ direction has a significant impact on the realized optical and mechanical quality factor. Etch selectivity is not typically a limiting factor for thin-film OMC devices, as the ZEP-520A e-beam resist we have chosen has better than $1:1$ selectivity for relevant process parameters and its film thickness is $\gtrsim 240$ nm.

End-Fire Device Fabrication

In practice, additional process steps are generally carried out to enable a desired method of optical coupling. In particular, the process above results in suspended silicon structures which may be optically addressed by a tapered fiber or other out-of-plane mechanism (such as an on-chip grating), but it does not allow *end-fire* coupling via a lensed optical fiber tip. In order to enable end-fire coupling, an on-chip waveguide facet as shown in Figure 2.3a must be accessible by an aligned fiber tip in the plane of the silicon device layer. There are several ways in which

Table 3.1: End-fire process flow details.

Step	Parameter	Value	Time/Notes
Pre-cleaning	Rinse ACE, IPA	-	N_2 blow-dry
Spin ZEP-520A resist	Spin speed	8000 rpm	60 s
	Ramp rate	2500 rpm/s	-
	Bake	180 °C	2 min
Electron-beam exposure	Dose	200 μC/cm^2	Beam current 140 pA, resolution $1 - 2.5$ nm
Develop	ZED-N50 developer	-	2 min 30 s
	MIBK rinse	-	30 s
Si etch	-	-	See Table 3.3
Resist stripping	ZDMAC	90 °C	60 s
	Piranha clean	80 °C	10 min, DI water rinse (x3)
Surface preparation	Buffered-HF (10 : 1)	-	10 s, DI water rinse (x3)
Spin Megaposit SPR 220-7.0 resist	Spin speed	4000 rpm	60 s
	Ramp rate	1500 rpm/s	-
Edge-bead removal	-	-	Wet polyester swab with TCE, swipe
Soft-bake resist	Pre-bake	90 °C	60 s
	Bake	115 °C	3 min
Photolithography exposure	Source	365 nm (*i*-line)	40 s, 280 W, soft exposure, 30 μm W.E.C.
	Resist settling	-	Let sit 75 min
Post-bake resist	Ramp temperature	$100 - 115$ °C	2 min, let cool completely
Develop	MF CD-26	-	90 s, inspect, continue in 30 s increments as needed
	DI water rinse	-	5 s
Si etch	-	-	See Table 3.3
Silicon oxide etch	-	-	See Table 3.3
Silicon handle etch	-	-	See Table 3.3
Resist stripping	NMP	90 °C	Pipette after 60 s to remove crust layer, let sit 2 hours
	Rinse ACE, IPA	-	N_2 blow dry
Release	Vapor HF	-	4 μm undercut etch
Cleaning	Piranha clean	80 °C	10 min, DI water rinse (x3)
Surface preparation	Vapor HF	-	Flash cycle etch

Table 3.3: ICP-RIE optimized etch recipe parameters.

Parameter	**Substrate SOI layer**		
	Device-layer Si	SiO_2	Handle Si
C_4F_8 flow (sccm)	84	70	0
SF_6 flow (sccm)	30	0	300
O_2 flow (sccm)	0	5	0
RF power (W)	15.5	150	0
ICP power (W)	600	2200	1200
D.C. bias (V)	76	165	0
Chamber pressure (mTorr)	15	10	100
Helium pressure (Torr)	10	5	10
Helium flow (sccm)	5.0-6.0	5.0-6.0	5.0-6.0
Table temperature (°C)	15	15	20
Etch rate (nm/min)	45	220	2500

one might accomplish fiber-coupling in the plane of the device layer. First, one may envision patterning the waveguide and OMC devices directly at the edge of the chip, so that the waveguide facet is coplanar with the edge of the chip, and a fiber might simply be brought into proximity with the edge of the chip. This method is flawed, however, due to the tendency of resists to form an *edge-bead*–a thickened strip along the edges of a sample–during spin-coating. With local variations in the resist thickness near the edge of the chip, the e-beam exposure becomes unpredictable and non-repeatable, and realizing highly-optimized nanophotonic structures with tight geometric constraints is unsound. In practice, the edge-bead extends $1-2$ mm from the chip edge. Clearly it is desirable to restrict pattern exposures to the central region of the chip where the effects of edge-bead formation are minimal, and the resist thickness is the most spatially uniform. With this in mind, two further options for end-fire fabrication are apparent. After defining the patterns, one may cleave the chip along an axis in or near the plane of the waveguide facet, effectively forming a new chip edge. This is a viable method, but it relies on scribing and cleaving the sample, which is a relatively high-risk process that can result in either breakage of devices near the cleave or contamination from particulates of silicon or silicon oxide which are released during scribing and cleaving. Alternatively, one may follow the patterning lithography step with a deep etch into the handle silicon wafer in the region abutting the waveguide facets, forming a *trench* in the silicon. Assuming the device layer is effectively masked during this process, the final result is a sample

which has been exposed only to resists and dry plasma etches, and is therefore fabricated with a high degree of repeatability. It is also possible to perform such a trench etching process with a wet chemical etch of the handle silicon, and in fact such a process was used in the Painter Group to fabricate some of the early generation end-fire coupled nanobeam devices as presented in Refs. [26, 30, 31]. This wet etch process relied upon a photoresist mask (ProTEK-PSB) to encapsulate the devices during chemical etching of silicon with either tetramethylammonium hydroxide (TMAH) or potassium hydroxide (KOH). While the process is often successful, it is particularly sensitive to a failure caused by etchants attacking the interface layer between the photoresist and the oxide layer. This can result in partial delamination of the photoresist layer, and subsequent etching of the devices. To avoid yield issues associated with wet chemical etching of a substrate with a vulnerable resist-oxide interface, we sought to develop a recipe based upon dry plasma etching with a large degree of directionality (anisotropy) to perform the deep trench etch.

We have developed a fabrication process for fabrication of end-fire-coupled devices using a thick photoresist (Megaposit SPR220-7.0) to mask the devices during the dry plasma etch into the handle silicon layer. Details of the fabrication process incorporating the end-fire process are given in Table 3.1 and shown schematically in Figure 3.2. After plasma etching of the device layer silicon and removal of the e-beam resist, the photoresist (PR) is spun onto the sample to an average thickness of 7 μm. The edge-bead of the photoresist, which can reach thicknesses up to ~ 500 μm, is removed by hand using a swab applicator wetted with trichloroethylene (TCE). The PR is then exposed using UV light (365 nm *i*-line exposure) using a Karl Suss MA6 Mask Aligner to form a simple rectangular mask pattern which encapsulates all the devices on the chip and leaves the trench region of the substrate unmasked. The edge of the PR mask is roughly aligned to the waveguide facets, but withdrawn by a stand-off distance of 70 μm. The purpose of this stand-off distance is to compensate for lateral etching during the final etch into the silicon handle. The final handle-layer etch is largely isotropic, and will etch the handle toward the waveguide while it clears a depth of $\gtrsim$ 100 μm into the handle (see Figure 3.3). The trench region is formed by a series of etches outlined in Table 3.3. First, the silicon device layer is etched using a recipe identical to that used to pattern the devices. Second, the BOX layer is etched anisotropically using a high-DC-bias ($>$ 150 V) plasma etch using C_4F_8 and O_2. Lastly, the silicon handle is etched with an isotropic plasma etch using pure SF_6 and no DC bias. Following the final etching steps, the PR is removed using a heated solution of N-Methyl-2-pyrrolidone (NMP)

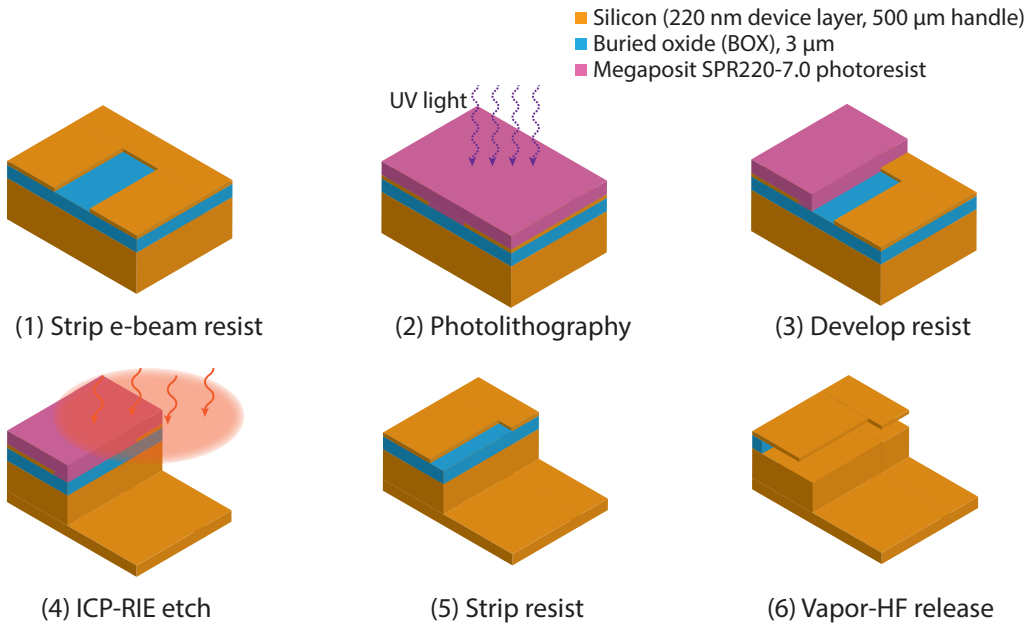

Figure 3.2: **End-fire device process flow.** Illustration beginning with a patterned silicon device layer of an SOI sample. A 7 μm-thick photoresist (Megaposit SPR220-7.0) is used in a photolithography layer to protect the device region of the chip while exposing a *trench* region to subsequent etches. A highly anisotropic ICP-RIE etch is used to etch the device layer and buried oxide in the trench region, and a further deep etch is performed to clear the handle silicon to a depth of $\sim$ 100 μm in order to allow fiber access to waveguides patterend in the device layer. The deep etch may be either (1) an isotropic SF_6 etch with no DC voltage bias, or (2) a standard Bosch etch using C_4F_8 and SF_6 in alternation. The photoresist is then stripped and the sample is cleaned in piranha solution. Finally, a vapor-HF undercut releases the end-fire devices.

followed by solvent rinsing. A subsequent piranha cleaning step is performed to remove any residual resist fragments. Finally, the devices are released using an anhydrous vapor-HF undercutting etch to remove the BOX layer and suspend the devices. The result of this fabrication process is a fully suspended membrane featuring optomechanical structures as shown in Figure 3.3. We fabricate arrays of suspended OMC devices formed in the silicon device layer, where the deep trench now allows an optical fiber to address the on-chip waveguides in an end-fire coupling scheme compatible with measurements in the dilution fridge. Figure 3.4 shows a representative final fabricated device array in detail, and Figure 3.5 shows the optomechanical cavity region of one representative device having seven periods of acoustic bandgap shielding.

The end-fire fabrication process outlined in Figure 3.2 is versatile, particularly be-

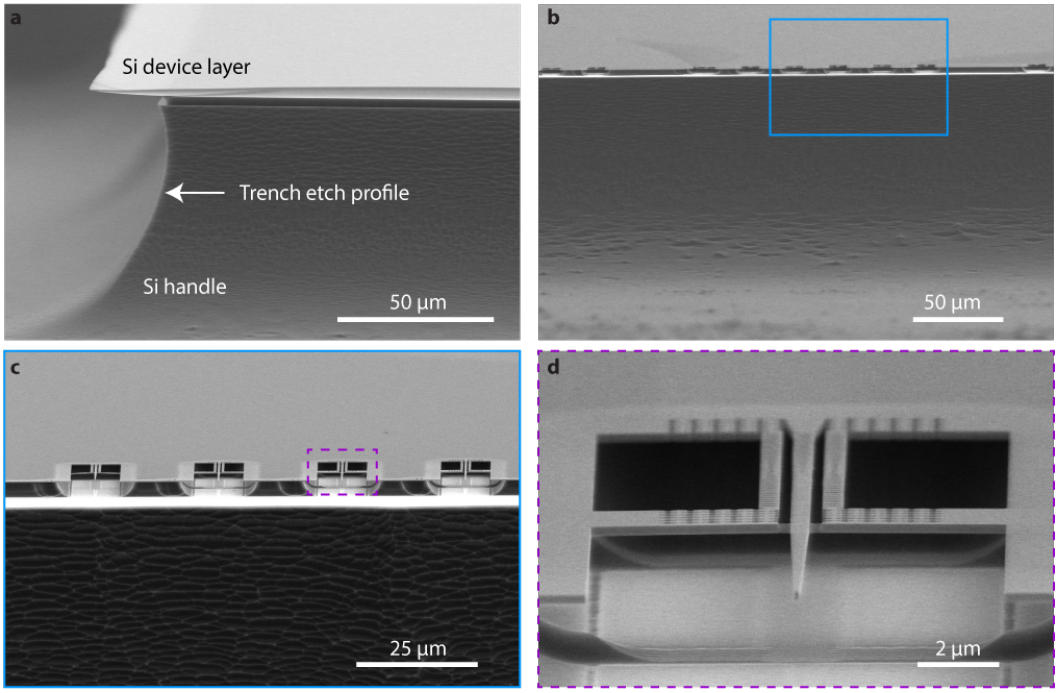

Figure 3.3: **End-fire device illustration.** Scanning electron microscope (SEM) image of an illustrative device sample fabricated using the end-fire process outlined in Table 3.1. (a) At the edge of the sample chip the SF_6 trench etch profile in the handle silicon is visible. The isotropic etch yields a "cresting wave" profile in the handle silicon. (b) Edge-on view of a device array patterned in the silicon device layer. The depth of the trench allows fiber access; the optical axis of the fiber will be approximately along the line-of-sight of this image. (c) Closer view of the device array. (d) An individual end-fire nanobeam device having a nanobeam OMC on either side of a central coupling waveguide.

cause it does not rely upon any wet etching steps which would more tightly restrict the number of material systems with which it is compatible, and is applicable to a broad range of nanofabrication applications in which in-plane optical access to device arrays is desirable without etching large fiber-alignment features into the substrate handle. The process has been applied to other research areas within the Painter Group, and in particular to the fabrication of integrated opto-electromechanical transducers for frequency conversion between the microwave and optical domains. The basic principle of such a device is to use a zipper optomechanical cavity (see, for example, Refs. [18, 53]) coupled to a superconducting Al lumped-element LC resonator, in which the mechanical motion couples to both the optical mode and the microwave LC-resonance. This is accomplished by forming a long ($\sim$ 60 μm) "double nanostring" silicon beam pinned at the center, in which one end of the

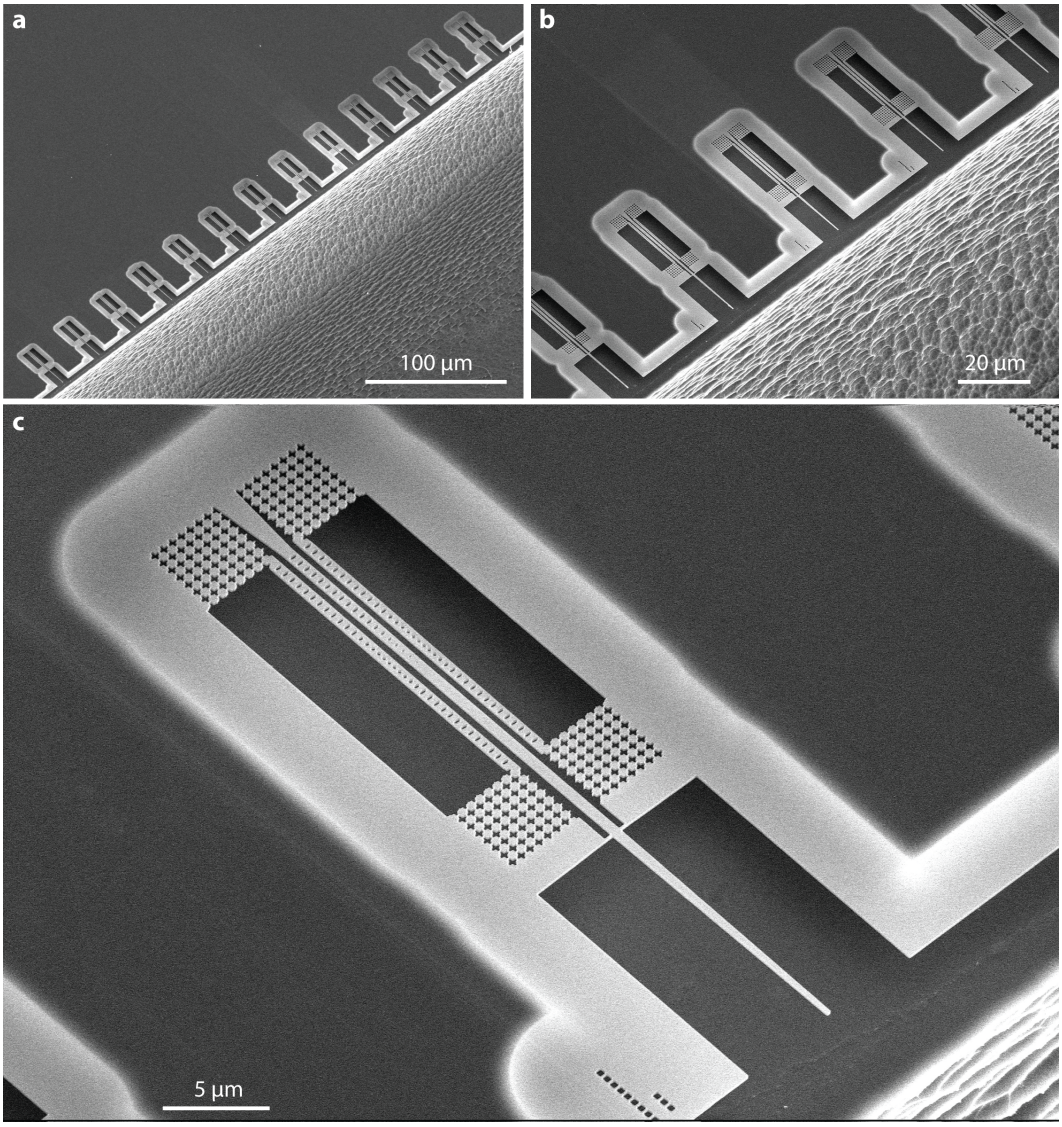

Figure 3.4: **Example of a fabricated nanobeam device array. a,** SEM of an individual device array with the cross shield period number scaled from $0-10$ from left to right. **b**, Closer view of the device array showing the deep handle Si etch aligned to the optical-coupling waveguides. **c**, Overall view of one end-fire coupled nanobeam device with seven periods of acoustic shielding.

double-beam forms the zipper optical cavity and the other forms a mechanically-compliant nano-gap capacitor with gaps on the order of 50 nm. The fundamental bowstring mode near 8 MHz then couples to both the optical and electrical resonances. The entire region of the device layer Si near the device is undercut with a vapor-HF release step, leaving the patterned device sitting upon a suspended Si membrane. Initial measurements on such a converter have been made at milliKelvin temperatures, but further studies are ongoing at the time of writing. A representative

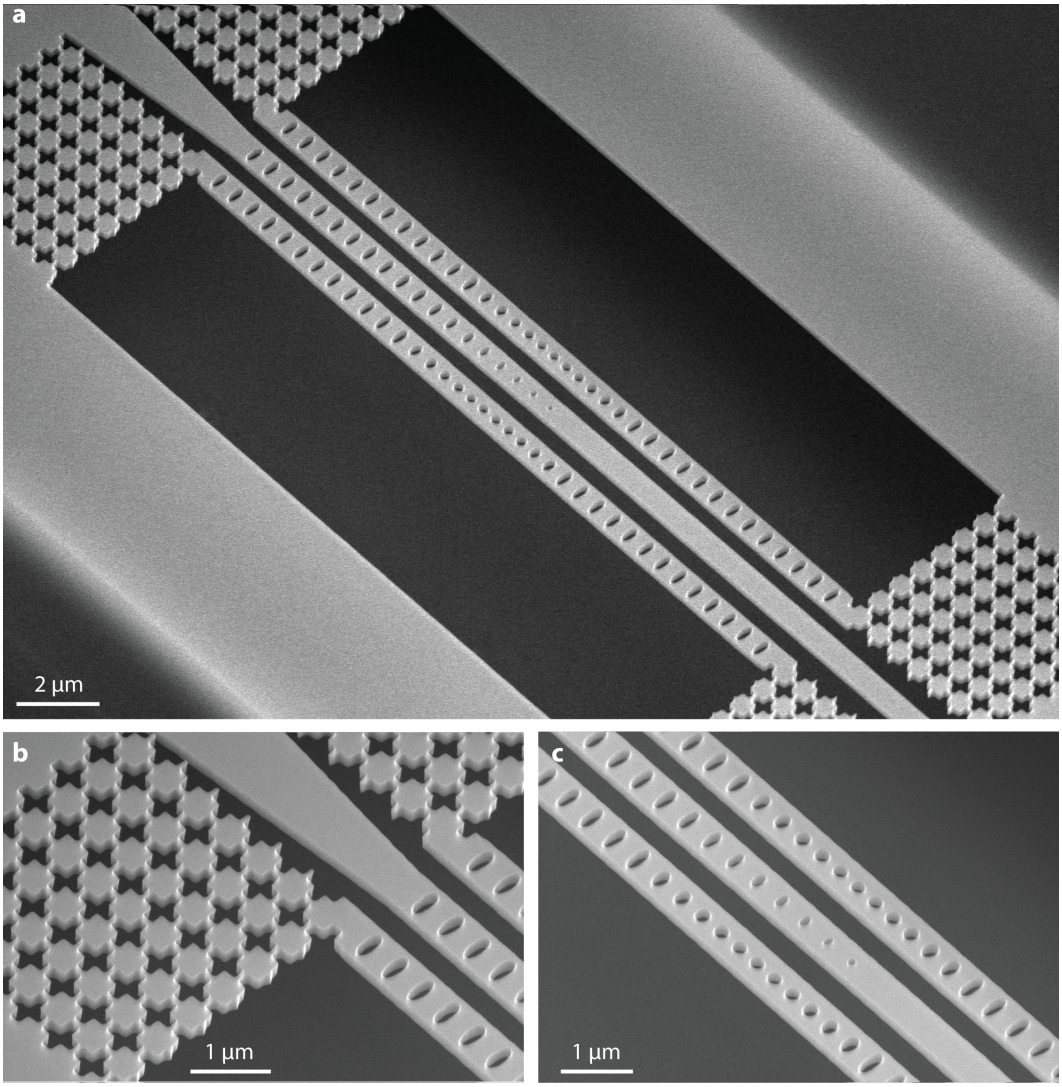

Figure 3.5: **The nanobeam OMC device cavity region. a,** Overall view of two nanobeam OMCs coupled to a central waveguide beam. **b**, Close view of the clamping region featuring the acoustic bandgap shielding cross pattern. **e**, Close view of the OMC cavity defect regions.

device fabricated using the end-fire process is shown in Figure 3.6. Of particular concern in the fabrication of such a device, in which a metallization layer is integrated with the silicon photonic device, is the ability to protect the superconducting coil and its delicate crossover bridges within resist during the trench-etching steps. We find that the Megaposit SPR resist encapsulates the coil resonator to protect it effectively during trench etching, and resist removal in a solvent such as NMP leaves the coils intact with high yield (Figure 3.6c). Under such a constraint, alternative fabrication methods such as cleaving the chip at a plane near the waveguide facet

would be impossible without flipping the chip and destroying the coil resonators, so a deterministic and reproducible fabrication technique is valuable.

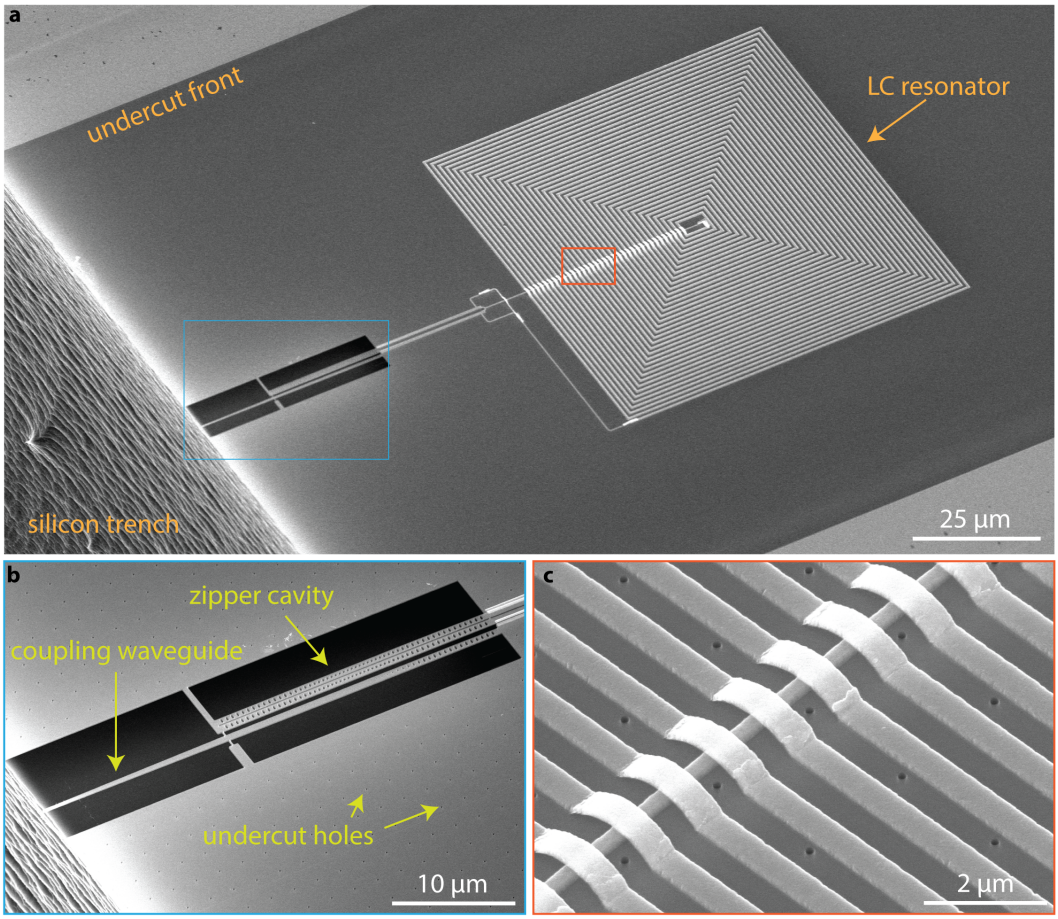

Figure 3.6: **Application of the end-fire fabrication process to integrated opto-electromechanical transducers.** **a**, SEM of an experimental on-chip integrated opto-electromechanical transducer for optical-microwave frequency conversion using an optical "zipper" cavity [53] coupled to a superconducting Al LC-resonator via a shared mechanical resonance. The end-fire fabrication process is compatible with integrated metallized device architectures. Optical access is made by alignment to a waveguide at the lower-left of the image. The LC coil features cross-overs which must not be destroyed during the end-fire process and etching steps. The thick photoresist used for trench etching is readily removed from the coils with high fabrication yield. **b**, Close view of the optomechanical component of the device. The zipper cavity and nano-gap capacitor are suspended by a release step in which pinholes etched in the silicon device layer allow vapor-HF access for undercutting. **c**, Aluminum cross-over bridges after photoresist removal.

Electron-Beam Lithography Considerations

The minimum critical features sizes in the nanobeam device are about 50 nm, at the smaller end of the state-of-the art e-beam and ICP-RIE lithography patterning capability for device layer thicknesses of order 200 nm. However, most of the feature sizes, including elliptical holes and straight-edge gaps between the neanobeams, and the height h_c of the acoustic shield cross pattern, are somewhat larger, typically 200-400 nm. In this size range, most of the fabrication disorder is due to randomness in the realized position and edges of etched holes due to run-to-run variability in the lithography step. A major source of variability is the so-called feature *blow-out*, causing enlargement of realized negative features (holes, where Si will be removed) relative to the sizes requested of the e-beam pattern generator (EBPG) [54]. Feature blow-out arises in two main ways. First, the finite size of the electron writing beam, as well as the back-scattering of electrons which have already passed through the resist once, result in developed features which are larger than the requested sizes. These effects are summarized as *proximity* effects and can be mitigated to some extent using standard algorithms for modulating the local distribution of e-beam dosage admitted to the resist. Second, an etching blow-out arises from anisotropicity in the plasma etching step. The degree of anisotropicity for a given etch can be minimized to a great extent by adjusting the DC bias voltage and gas chemistry. These blow-out effects can have varied impact on the realized device dimensions from one region of a device to another, and are particularly sensitive to the local exposed feature sizes through e-beam proximity and mass-loading during plasma etching. Additionally, transfer of the e-beam pattern to the resist during development invariably involves local fluctuations in temperature and flow of the developer over the resist. Figure 3.7 shows a representative result of image analysis for an individual end-fire coupled device consisting of two nanobeam OMCs. The hole edges are identified using a simple contrast edge-detection algorithm, and the measured hole sizes are compared to designed target values to generate feedback for the following fabrication iteration. The overall feature-size-dependent blow-out is also characterized in this way, and for typical nanobeam feature sizes is ≈ 40 nm for the optimized ICP-RIE etch recipe summarized in Table 3.3.

The devices studied here were fabricated using the Raith EBPG5200+ electron-beam lithography system in the Kavli Nanoscience Institute at Caltech. The tool uses a peak accelerating voltage of 100 kV to write features with a minimum writing resolution of 1 nm over a 1060×1060 μm^2 main-field, with the minimum writing resolution achieved for beam currents of 100 – 200 pA (beam spot size 10 –

15 nm). The cleanroom environment is held stable at a temperature of 21 °C, relative humidity ~ 40%, and with an ETS-Lindgren active magnetic field-cancellation system.

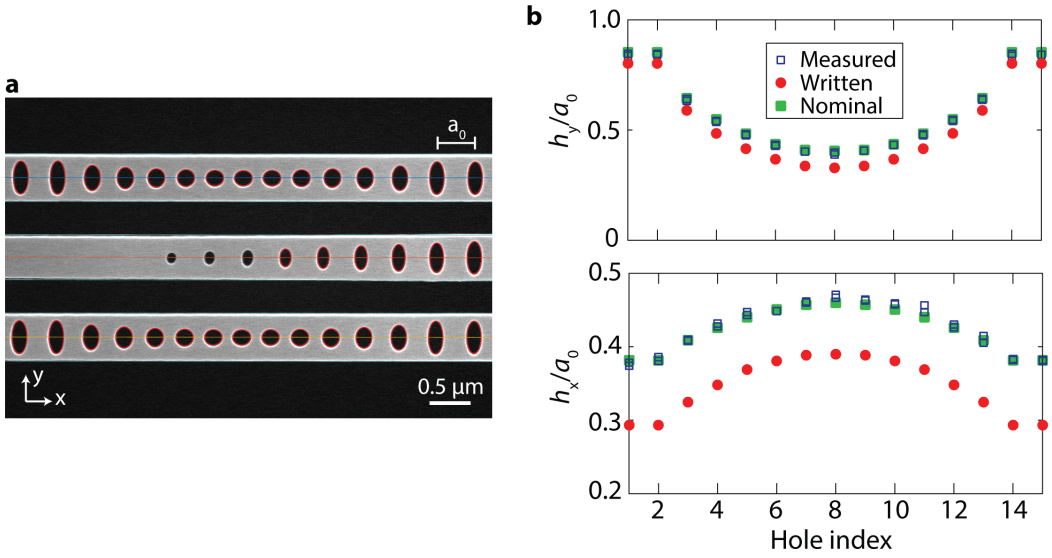

Figure 3.7: **Lithography corrections and SEM image fitting for nanobeam devices. a**, SEM image of an end-fire nanobeam OMC device showing the central waveguide beam for optical coupling to a nanobeam OMC on each side. The nanobeam defect region is shown. Hole edges and beam edges are detected in image processing. Large arrays of devices are studied in this way to generate fabrication disorder statistics. Typical randomness in hole size and hole positions is 3 – 4 nm. **b**, Lateral and longitudinal hole sizes of the nanobeam defect region normalized to the nominal lattice constant a_0 = 534 nm. These measurements are iteratively used to generate the lithography patterns in fabrication until the realized dimensions converge to the design values.

For typical feature sizes of the nanobeam OMC, randomness in hole size and beam width on the order of 0.25% corresponds to a displacement of the optical resonance by of order (0.0025) × 1550 nm = 4 nm. Imaging of large collections of realized structures indicates typical variability in hole sizes is approximately 4 nm for device arrays in which the greatest degree of care is taken to account for blow-out and process variability. An important strategy in realizing the best individual OMC devices by reducing fabrication-induced randomness is to embed the target devices within a large array of dummy or "barrier" devices. This ensures that long-range e-beam proximity effects across the extent of any one individual device are minimal; in other words, that the local on-chip environment of the target device is as uniform as is practical in all directions. Uniformity of the device array pattern not only

impacts the long-range e-beam proximity effect, but also ensures a homogeneous mass-load during ICP-RIE etching in the vicinity of the target device.

3.2 Dilution Refrigerator Optical Techniques

In order to perform measurements in a low-temperature environment in which the thermal bath occupancy of the mechanics is frozen out ($T \ll \hbar\omega_m/k_\mathrm{B} \approx 240$ mK), we use a ^{3}He/^{4}He dilution refrigerator from BlueFors cryogenics in Helsinki, Finland. We feed single-mode optical fiber (Corning SMF28e) through teflon vacuum fiber-feed-throughs at the top plate of the fridge and couple to OMC device chips mounted on the mixing chamber plate.

Optically coupling to the device inside the fridge requires a robust and easily-aligned fiber coupling scheme, ideally with large single-pass coupling efficiency $\gtrsim 50\%$, which will allow coupling to a large number of individual devices on-chip during a single cooldown. This precludes coupling methods which involve affixing a fiber to the chip prior to cooldown, for example by epoxy or a mechanical alignment ferrule. One technique that meets these criteria is to use a dimpled optical fiber-taper, in which a single-mode optical fiber is thinned and dimpled such that the guided mode is largely evanescent. This technique was developed by and has been used extensively within the Painter Group [55]. In this technique, coupling to on-chip devices can be achieved by positioning the fiber-taper a few tens or hundreds of nm from an optical cavity. This coupling technique is used routinely in the Group for device characterization at room temperature, and has been used at low-temperature in helium cryostats on various early nanobeam OMC experiments as well as zipper optical cavity experiments [18, 19, 20, 56]. The Davis Research Group at the University of Alberta has made impressive demonstrations of fiber-taper coupling to optomechanical bottle resonators inside a dilution fridge [57, 58], achieving overall transmission efficiencies over 70%. This setup requires *in-situ* imaging for alignment of the taper to devices, which the Davis Group achieves with a cryogenic bundle of $\sim 37,000$ imaging fibers. They demonstrate that the challenges associated with porting this technology into a dilution refrigerator are daunting but manageable. Additionally, fiber tapers are relatively floppy and support many vibrational modes ranging from sub-kHz to several tens of kHz [59]. Such vibrations modulate coupling to the cavity and must be deconvolved from measurement dynamics of interest. We note that recent work from the Lukin Group at Harvard [60] demonstrates highly efficient (transmission $> 97\%$) coupling to an on-chip waveguide using a single-sided conical optical fiber taper. In this scheme, adiabatic coupling between the taper and chip

waveguide is achieved by contacting the two waveguides over a transition region extending about 10 μm. This allows for robust alignment with high efficiency. To meet the various challenges outlined above for robust low-temperature optical coupling, we employ a lensed optical fiber in an *end-fire* configuration which requires no low-temperature imaging in order to achieve alignment. The lensed-fiber tip focuses the ~ 8 μm diameter Gaussian mode of a single-mode fiber to a beam waist of 2.5 μm at a working distance of approximately 14 μm from an on-chip waveguide facet, and single-pass coupling efficiencies as high as 72% are realizable [30].

Adiabatic Waveguide Coupling

In our devices silicon is used as a material for its large optomechanical coupling, but it has the drawback of being quite floppy (in particular relative to silicon nitride structures, in which the material tensile stress can exceed 1 GPa). This floppiness limits the length of a released optical waveguide on chip to about 16 μm, effectively limiting our ability to satisfy the adiabaticity criteria. Still, using a waveguide taper of this length the theoretical taper efficiency is $\eta_{\text{taper}} > 90\%$, and in experiments we achieve typical overall single-pass coupling efficiencies of $\eta_{\text{cpl}} = 62\%$.

Optical Alignment at Low Temperature

We employ standard cryogenic mounting techniques to ensure that the microchip device sample and its sub-mount are thermalized to the cold mixing chamber plate as well as possible. Indium foil is placed at all metal interfaces in the mount and between the mount and cold plate of the fridge. Additionally gold braiding is used to thermally link the cold plate with the sample mount. The sample itself is thermalized to the sub-mount using high-thermal-conductivity cryogenic vacuum grease (Apiezon N Grease) and mechanical contact with a copper clamp and bulk copper on all three edges of the chip which are not needed for fiber access.

The lensed fiber is mounted in a groove on a plate fixed atop a 3-axis nanopositioning piezo motor stack (Attocube ANPx101, ANPz101 stepper positioner series, controller Attocube ANC350). The Attocube stack and sample sub-mount are fixed on a custom copper mounting plate. During preparation for cooling a sample, the entire mount is detached from the mixing chamber plate of the fridge and moved to an adjacent imaging setup where the lensed-fiber can be easily brought into alignment with any individual on-chip device. After this pre-alignment is performed, ideally the mount would simply be reattached to the mixing chamber and the cooldown commenced. However, cooling any complex mechanical mount consisting of mul-

tiple materials and parts from 300 K to 0.01 K will introduce a significant amount of thermal expansions and contractions, resulting in misalignment of the fiber from the device. For this reason, the fiber is typically retracted by about 200 μm in the longitudinal and vertical directions from the position of optimal coupling when the cooldown is begun. After the fridge reaches base temperature, the fiber is re-aligned by shining laser light into the fridge and searching for a reflection signal as the positioner stages are stepped toward the expected optimal-coupling position. When a reflection signal is found, the position of the fiber is optimized to increase the signal. Still, once the fiber is aligned to a device at low-temperature, one needs a method for identifying which particular on-chip device is being probed (again, this is done without any cryogenic imaging). The thermorefractive effect in silicon results in an approximately 15 nm shift of the device optical modes to shorter wavelength during cooldown, while the variations in wavelength between adjacent devices are typically of order 1 nm due to fabrication disorder; hence it is generally difficult to identify a specific device simply by knowing its mode wavelength at room temperature. Instead we must measure the optical mode wavelengths of many devices in a given device array at room temperature prior to cooling down, then again at low temperature, and correlate our two optical mode maps to pinpoint the fiber position within a device array as shown in Figure 3.8b. Typical samples may contain 5 – 10 such device arrays with varied parameters of interest for testing, such as designed optical wavelength, optical loading parameter η_κ, cross shield period number, or blow-out correction.

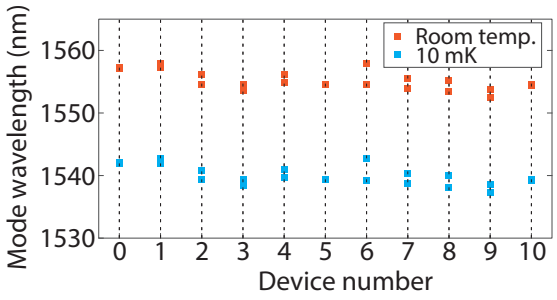

Figure 3.8: **Map of optical mode wavelengths in an array of devices at room temperature and T_f = 10 mK. a** Measured mode wavelengths for a typical device array at room temperature (orange) and T_f = 10 mK (blue). The optical wavelength map is used to identify coupled devices without real-time imaging inside the fridge.

Side-Coupling

In the end-fire coupling scheme outlined above, we have so far neglected the question of routing light from the on-chip waveguide to the optical cavity itself. There are two evident methods to achieve this: end-coupling and side-coupling. In end-coupling, the on-chip waveguide is connected end-on with the nanobeam optical cavity. Coupling is controlled using a variable number of mirror cells between the waveguide and the cavity, effectively controlling the reflectivity of one cavity end-mirror in discrete steps set by the number of mirror holes. This has the drawback that fine-tuning of the loading parameter $\eta_\kappa = \kappa_e/\kappa$ is not available without modifying the local geometry of the holes, and furthermore that one end of the nanobeam cavity is effectively anchored to the bulk by the waveguide. This becomes problematic when we aim to clamp our nanobeam with a full bandgap acoustic shield pattern. To circumvent the limitations of end-coupling, we employ a side-coupling method in which the waveguide mode is evanescently coupled to a nanobeam optical cavity located adjacent to the waveguide but is not co-linear in the propagation direction. In this scheme, the cavity loading parameter η_κ is tunable through the continuous variable g_{cpl}, the gap size between the nanobeam and waveguide beam, as shown in Figure 3.9. The coupling or "extrinsic" optical quality factor $Q_e \equiv \omega_c/\kappa_e$ theoretically increases exponentially with g_{cpl}. This configuration also allows placement of a nanobeam cavity on either side of the waveguide, doubling the number of devices which may be probed by alignment to a single waveguide. Perhaps most importantly for this work, however, is the fact that by side-coupling we are able to optically couple to the nanobeam without any mechanical contact to the routing waveguide. The nanobeam may therefore be clamped on both sides using an acoustic bandgap patterned material, and no asymmetries or mechanical defects are introduced through the method of optical coupling.

Single-photon detectors

The SPDs used in this work are amorphous WSi-based superconducting nanowire single-photon detectors developed in collaboration between the Jet Propulsion Laboratory and NIST [62]. The SPDs are mounted on the still stage of the dilution refrigerator at $\sim$ 700 mK. Single-mode optical fibers are passed into the refrigerator through vacuum feedthroughs and coupled to the SPDs via a fiber sleeve attached to each SPD mount. The radio-frequency output of each SPD is amplified by a cold-amplifier mounted on the 50 K stage of the refrigerator as well as a room-temperature amplifier, then read out by a triggered PicoQuant PicoHarp 300

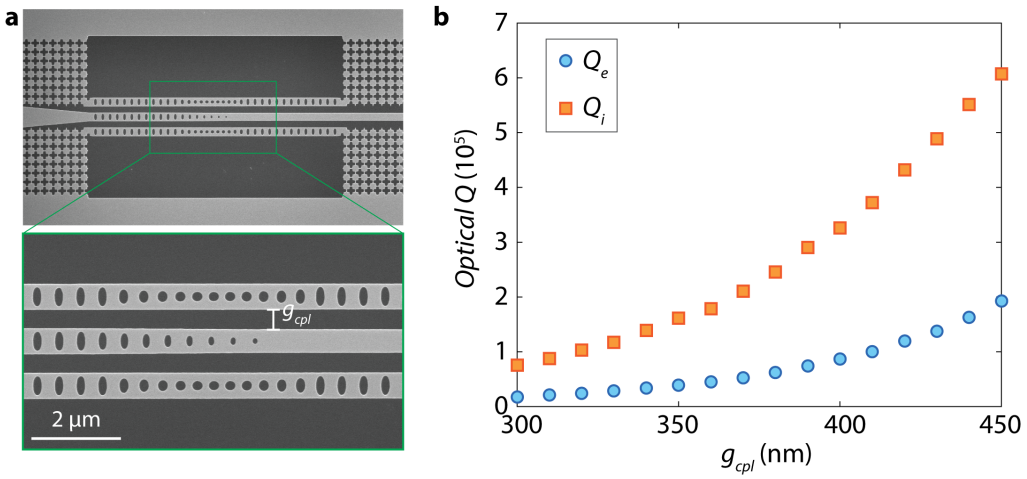

Figure 3.9: **Side-coupling and tuning of the extrinsic optical quality factor. a**, Two nanobeam devices are evanescently coupled to a guided mode of a central waveguide beam. Close view: the cavity loading parameter η_κ depends exponentially on the waveguide-nanobeam gap g_{cpl}. **b**, FDTD simulations using Lumerical [61] of the extrinsic and intrinsic quality factors of the optical cavity mode. An increase in Q_e with g_{cpl} reflects the exponentially decreasing overlap between the cavity mode and the waveguide mode as g_{cpl} increases, while an increase in the intrinsic quality factor Q_i is attributed to decreased scattering losses experienced by the cavity mode as a result of increased separation from the surfaces of the waveguide beam.

time-correlated single photon counting module. We have observed SPD dark count rates as low as ~ 0.6 c.p.s. and SPD quantum efficiency $\eta_{\mathrm{SPD}} \simeq 60\%$ as summarized in Figure. 3.10.

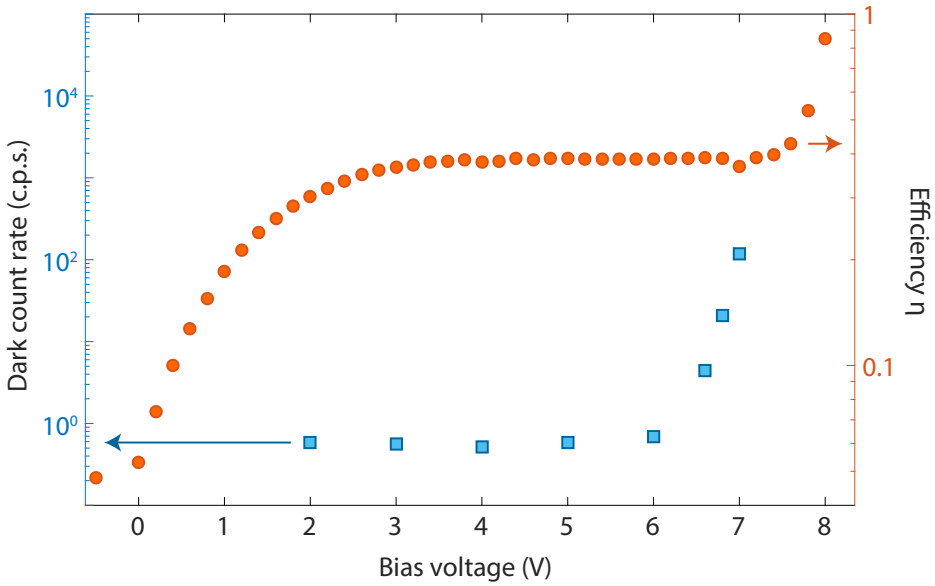

Figure 3.10: **SPD calibration curve.** Efficiency and dark-count rate calibrations for an SPD used in this work, plotted against the D.C. bias voltage applied through the nanowire (series resistance from bias voltage source was 5 MΩ, input count rate for calibration was $\Gamma_{\text{in}} = 10^5$ c.p.s.). At high bias current ($I_{\text{bias}} \gtrsim 1.5\ \mu$A), the SPD switches into a normal state and its response is no longer linear. We operate in the saturated region of the curve, where the linear efficiency $\eta = \Gamma/\Gamma_{\text{in}}$ of the SPD is not sensitive to small fluctuations in bias current. Here η includes all losses from the input to the dilution fridge port to the SPD itself. Note that through fiber-coiling techniques, black-body radiation isolation, and minimization of stray light entering the optical path, we are able to operate the SPDs with ultra-low intrinsic dark-count rates below 1 c.p.s.

3.3 Optical Characterization and Calibration at MilliKelvin Temperatures

Each device we have measured in this work was characterized optically in order to determine its optical resonance frequency ω_{c}, total optical linewidth κ, waveguide-cavity coupling efficiency $\eta_\kappa = \kappa_{\text{e}}/\kappa$, and fiber-to waveguide coupling efficiency η_{cpl}. In particular, the waveguide-cavity coupling efficiency η_κ is measured by placing the laser far off-resonance and using the VNA to drive an intensity modulator to sweep an optical sideband through the cavity frequency. The cavity response is measured on a high-speed PD (after amplification by the EDFA) connected to the VNA signal port, as shown in Figure 3.11. From this we obtain the amplitude and phase response of the cavity, which are fitted to determined η_κ.

The theoretical amplitude and phase responses of the optical cavity can be derived in a simple classical analysis, neglecting small effects due to optomechanical coupling.

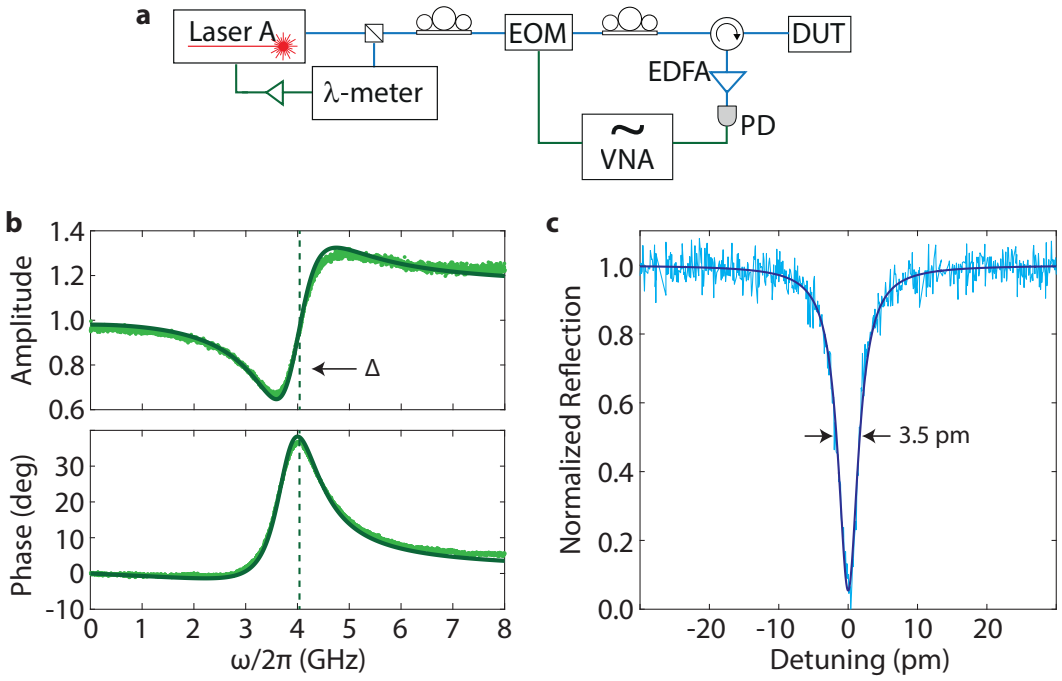

Figure 3.11: **Characterization of the optical cavity. a**, Simplified schematic of the measurement setup used for characterization of the optical cavity. EOM: electro-optic modulator, λ-mater: wavemeter, VNA: vector network analyzer, EDFA: erbium-doped fiber amplifier, PD: photodetector, DUT: device under test. **b**, Amplitude and phase responses of a typical nanobeam optical cavity obtained by parking the laser at a detuning $\Delta > \kappa$ from resonance. An EOM is driven using a VNA to sweep a probe sideband through the cavity frequency. Solid lines are fits to the data. Expression 3.7 is used to fit the response as obtained by the VNA. Here, we extract a waveguide-cavity coupling efficiency $\eta_\kappa = \kappa_e/\kappa = 0.301$ using $\Delta/2\pi = -4.039$ GHz. **c**, Normalized reflection as a function of wavelength for a typical optical cavity mode. A tunable laser is swept through the cavity resonance and the reflection spectrum is fitted to the Lorentzian response function $R(\omega) = 1 - \kappa_e\kappa_i/((\Delta - \omega)^2 + (\kappa/2)^2)$. Here we extract the mode wavelength $\lambda = 1540.3$ nm ($\omega_c/2\pi = 194.63$ THz), total linewidth $\kappa/2\pi = 446.4$ MHz ($Q_t = 4.36 \times 10^5$), and $\kappa_i/2\pi = 274.9$ MHz ($Q_i = 7.08 \times 10^5$). From the reflection spectrum only, we can also estimate $\eta_\kappa = (1 - \sqrt{R_{\min}})/2 = 0.384$.

Starting with the input-output boundary condition 2.33:

$$\hat{a}_{\text{out}} = \hat{a}_{\text{in}} - \sqrt{\kappa_{\text{e}}}\hat{a}, \tag{3.1}$$

we can directly write the optical reflection coefficient $r(\omega) \equiv \hat{a}_{\text{out}}/\hat{a}_{\text{in}}$ as

$$r(\omega) = 1 - \sqrt{\kappa_{\text{e}}}\frac{\hat{a}}{\hat{a}_{\text{in}}} \tag{3.2}$$

$$= 1 - \frac{\kappa_{\text{e}}}{i(\Delta - \omega) + \kappa/2}, \tag{3.3}$$

where we have used the optical susceptibility $\chi_a(\omega)$ as in Equation 2.44. Here we are neglecting quantum noise operators and considering only the large coherent field amplitudes; to make this explicit we will write $\hat{a} \longrightarrow \alpha$ in the following steps. The VNA will weakly modulate a carrier tone of amplitude α_0 to generate a sideband at frequency ω and amplitude α_1. Upon reflection from the cavity, the total field will be the sum

$$\alpha_{\text{out}}(\omega) = r(0)\alpha_0 + r(\omega)\alpha_1, \tag{3.4}$$

whereupon detection the photocurrent will be proportional to the squared amplitude

$$|\alpha_{\text{out}}(\omega)|^2 = |r(0)\alpha_0|^2 + |r(\omega)\alpha_1|^2 + (r(0)\alpha_0)^* r(\omega)\alpha_1 + r(0)\alpha_0(r(\omega)\alpha_1)^*. \tag{3.5}$$

The first two terms are DC offsets that do not contribute to the frequency response. In general we may consider the two input sideband amplitudes to be in phase with each other at phase angle θ relative to the intracavity field, allowing us to factor out real a real number $\bar{\alpha} = \alpha_0\alpha_1$ from the frequency response signal. Thus the explicit amplitude and phase response expressions for fitting are respectively $|S|$ and $\text{Arg}\{S\}$, having forms shown in Figure 3.11, where

$$S(\omega, \Delta, \kappa, \kappa_{\text{e}}) = \bar{\alpha}e^{i\theta}\left[\left(1 - \frac{\kappa_{\text{e}}}{-i\Delta + \kappa/2}\right)\left(1 - \frac{\kappa_{\text{e}}}{i(\Delta - \omega) + \kappa/2}\right)\right. \tag{3.6}$$

$$\left. + \left(1 - \frac{\kappa_{\text{e}}}{i\Delta + \kappa/2}\right)\left(1 - \frac{\kappa_{\text{e}}}{-i(\Delta - \omega) + \kappa/2}\right)\right]. \tag{3.7}$$

Similarly, the bare optical cavity reflection is measured using a single laser tone scanned through the cavity resonance, yielding a characteristic Lorentzian normalized reflection signal

$$R(\omega) = |r(\omega)|^2 = \left|1 - \frac{\kappa_e}{i(\Delta - \omega) + \kappa/2}\right|^2 \tag{3.8}$$

$$= 1 + \frac{\kappa_e^2}{(\Delta - \omega)^2 + (\kappa/2)^2} - 2\mathrm{Re}\left\{\frac{\kappa_e}{i(\Delta - \omega) + \kappa/2}\right\} \tag{3.9}$$

$$= 1 - \frac{\kappa_e \kappa_i}{(\Delta - \omega)^2 + (\kappa/2)^2}. \tag{3.10}$$

We can see that the resonant coupling depth, defined as

$$R_{\mathrm{min}} \equiv R(\omega = \Delta) = 1 - \frac{\kappa_e \kappa_i}{(\kappa/2)^2}, \tag{3.11}$$

vanishes under the critical-coupling condition $\kappa_e = \kappa_i = \kappa/2$. For non-vanishing resonant coupling depth, one can calculate the deviation from critical coupling $|\kappa_e/\kappa - 0.5| = \sqrt{(1 - R_{\mathrm{min}})/2}$, but cannot determine unambiguously whether the cavity is over- or under-coupled without performing the phase-sensitive measurement described above.

Calibration of the Vacuum Optomechanical Coupling Rate

The measurements presented in this work rely on accurate calibration of the vacuum optomechanical coupling rate g_0, which physically represents the optical frequency shift due to the zero-point motion of the mechanical resonator. We employ various techniques for calibrating g_0 both at room temperature and at mK temperatures. From Eqn. 2.54 we see that the optically-induced damping rate broadens the mechanical linewidth by γ_{OM} for red-detuned driving. A measurement of the linear dependence of the total mechanical linewidth γ as a function of pump photon number n_c then allows us to extract the coefficient $4g_0^2/\kappa$, and with κ known from a reflection scan as shown in Figure 3.11, we obtain g_0.

At room temperature, the mechanical mode occupancy of our 5 GHz nanobeam OMC breathing mode is thermally occupied with about $\bar{n} = 1,200$ phonons. Under mechanically-detuned optical driving, then, the mechanical motion imparts a phase modulation of the carrier tone with an effective modulation index of $\beta = g_0\sqrt{\langle n \rangle}/\omega_m \sim 5 \times 10^{-3}$ at room temperature, which is easily observed using a

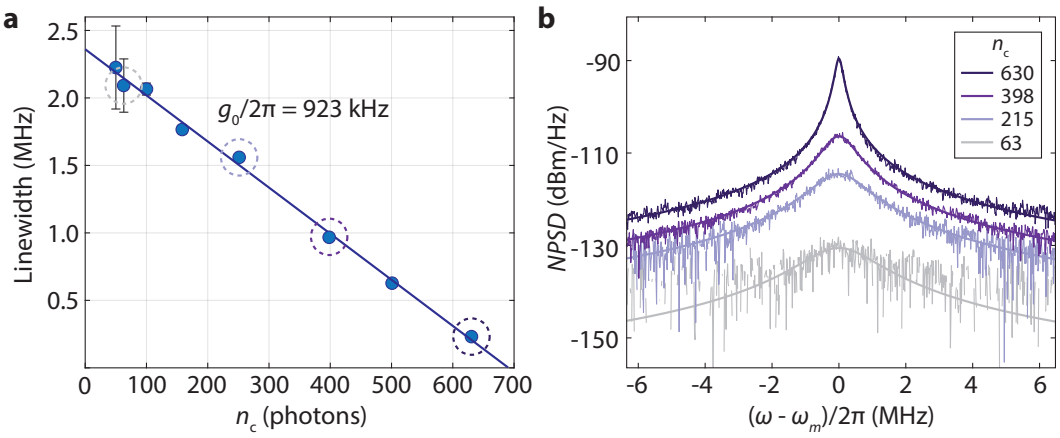

Figure 3.12: **Room-temperature calibration of the vacuum optomechanical coupling rate in a nanobeam OMC. a**, Direct detection (single-port heterodyne) is used to observe the mechanical NPSD using a blue-detuned probe laser ($\Delta = -\omega_m$). The total linewidth is measured as a function of intracavity photon number n_c, given by Equation 3.12, which is proportional to the pump laser power P_{in}. The total mechanical mode linewidth is given by $\gamma = \gamma_i - \gamma_{OM}$, which is fitted to the data to extract a vacuum optomechanical coupling of $g_0/2\pi = 923$ kHz for this representative device. Device parameters are: (κ, κ_e, g_0, ω_m) = 2π(997 MHz, 324 MHz, 923 kHz, 5.39 GHz). We also extract the intrinsic linewidth $\gamma_i/2\pi = 2.3$ MHz. Note that at higher intracavity photon number, the condition $\gamma_{OM} > \gamma_i$ corresponds to a regime of self-sustained oscillations. **b**, Several representative mechanical NPSD curves measured as a function of n_c.

simple single-port heterodyne detection (sometimes referred to as *direct detection*) as described in Section 2.4. The intracavity photon number is related to the input pump power P_{in} by

$$n_c = \langle \hat{a}^\dagger \hat{a} \rangle = \frac{P_{in}}{\hbar \omega_L} \frac{\kappa_e}{\Delta^2 + (\kappa/2)^2}. \tag{3.12}$$

For typical device parameters $\kappa/2\pi \sim 800$ MHz, $\kappa_e/\kappa \sim 0.5$, for red- or blue-detuned driving ($\Delta = \pm\omega_m$), we have $n_c \approx 7$ photons per μW input power (on resonance, $\Delta = 0$, $n_c \approx 5,000$ photons per μW). The results of an illustrative power sweep are shown in Figure 3.12, in which the mechanical lineshape is measured at driving powers ranging over an order of magnitude from $n_c = 50 \longrightarrow 630$. The total mechanical linewidth is

$$\gamma = \gamma_i - \gamma_{OM} = \gamma_i - \frac{4g_0^2 n_c}{\kappa}, \tag{3.13}$$

from which we extract in this case $g_0/2\pi = 923$ kHz. The zero-power intercept of the curve in Figure 3.12 represents the intrinsic mechanical damping rate $\gamma_i/2\pi = 2.3$ MHz at room temperature and pressure, corresponding to a mechanical Q-factor of $\approx 2,200$. In these conditions the room-temperature mechanical-Q is limited primarily by thermoelastic damping and clamping losses, as detailed in Chapter 7.

Chapter 4

PHONON COUNTING AND PHONON INTENSITY INTERFEROMETRY

Measurement of the properties of mechanical systems in the quantum regime typically involves heterodyne detection of a coupled optical or electrical field, yielding a continuous signal proportional to the displacement amplitude [63]. An alternative method, particularly suited to optical read-out, is to utilize photon counting as a means to probe the quantum dynamics of the coupled optomechanical system [64, 65]. Photon counting can be readily adapted to study intensity correlations in an optical field, and has been used not only in the astronomical HBT studies of thermal light, but also in early studies of the photon statistics of laser light and single-atom fluorescence [66, 67]. In the field of photon-correlation spectroscopy, such intensity interferometry techniques have found widespread application in the measurement of particle and molecular motion in materials [68]. More recently, photon counting of Raman scattering events in diamond has heralded and verified the quantum entanglement of a THz phonon shared between two separate bulk diamond crystals [69]. In the case of engineered cavity optomechanical systems, much longer phonon coherence times are attainable, albeit at lower mechanical frequencies (MHz-GHz) which limit the temperature of operation and the optical power handling capability of such structures. Quantum optical schemes for manipulation of the quantum state of motion in cavity optomechanical systems thus rely on a large per-phonon scattering rate and efficient detection of scattering events. Here we embed a high-Q, GHz-frequency mechanical resonator inside an optical nanocavity, greatly enhancing the phonon-photon coupling rate and channeling optical scattering into a preferred optical mode for collection. Single photon detection of this scattered light then allows for a precise counting of single-phonon emission or absorption events, effectively phonon counting (although this terminology should not be confused with Fock state detection or quantum non-demolition measurement of phonon number). The highly engineered and optimized nature of this optomechanical resonator furthermore yields a sub-phonon-level counting sensitivity of the intracavity mechanical resonator occupancy.

4.1 Phonon Counting Theory

We consider the explicitly case of a sideband-resolved system under red-detuned ($\Delta = +\omega_m$) driving, and calculate the detected photon count rate for sideband-scattered photons at the cavity frequency. In the presence of a large coherent driving tone, the total output from the cavity will be the sum of the coherent reflected tone and the fluctuation term given by Equation 2.44:

$$\hat{a}_{\text{out}}(\omega)\Big|_{\Delta=+\omega_m} = \alpha_{\text{out}}\delta(\omega) + r(\omega;+)\hat{a}_{\text{in}}(\omega) + n(\omega;+)\hat{a}_i(\omega) + s(\omega;+)\hat{b}_{\text{in}}(\omega). \quad (4.1)$$

The output field coming from interaction with the mechanics will occur where the scattering coefficient $s(\omega;+)$ is peaked at $\omega \approx +\omega_m$ (specifically, $|\omega - \omega_m| \lesssim \kappa$, due to the optical cavity susceptibility). We are thus motivated to filter out the strong optical pump around $\omega \approx 0$ and keep only signal within a narrow bandwidth ($\ll \kappa$) of the cavity frequency. We can model this post-filtering of the optical output by a complex filter transmission function

$$\mathrm{F_f}(\omega;\omega_{\text{f}}) = \frac{\kappa_{\text{f}}/2}{i(\omega-\omega_{\text{f}}) + \kappa_{\text{f}}/2}, \quad (4.2)$$

with filtering bandwidth κ_{f}, and as we are usually interested in filtering at the cavity frequency as mentioned above we will set $\omega_{\text{f}} = \omega_m$. The filtered output from the cavity takes the form

$$\hat{a}_{\text{filt}}(\omega)\Big|_{\Delta=+\omega_m} = \mathrm{F_f}(\omega;\omega_m)\Big(\alpha_{\text{out}}\delta(\omega)+r(\omega;+)\hat{a}_{\text{in}}(\omega)+n(\omega;+)\hat{a}_i(\omega)+s(\omega;+)\hat{b}_{\text{in}}(\omega)\Big). \quad (4.3)$$

The time-dependent photon count rate detected at the filtered optical output is

$$\begin{aligned}\Gamma(t) &= \langle \hat{a}^\dagger_{\text{filt}}(t)\hat{a}_{\text{filt}}(t)\rangle \\ &= \frac{1}{2\pi}\int_{-\infty}^{\infty} d\omega \int_{-\infty}^{\infty} d\omega' e^{i(\omega+\omega')t}\langle \hat{a}^\dagger_{\text{filt}}(\omega)\hat{a}_{\text{filt}}(\omega')\rangle \\ &= \frac{1}{2\pi}\Big(|\mathrm{F_f}(0;\omega_m)|^2|\alpha_{\text{out}}|^2 + \\ &\int_{-\infty}^{\infty} d\omega \int_{-\infty}^{\infty} d\omega' e^{i(\omega+\omega')t}\mathrm{F_f^*}(\omega;\omega_m)\mathrm{F_f}(\omega';\omega_m)s^*(\omega;+)s(\omega';+)e^{i(\omega+\omega')t}\langle \hat{b}^\dagger_{\text{in}}(\omega)\hat{b}_{\text{in}}(\omega')\rangle\Big),\end{aligned} \quad (4.4)$$

where we have used the fact that the vacuum noise terms $\hat{a}_{\mathrm{in}}$ and $\hat{a}_i$ do not contribute to real photon counts and therefore neglected terms arising from these optical noise operators. Using the scattering matrix expression in Appendix A.4 we identify this expression as

$$\Gamma(t) = \frac{1}{2\pi}\left(|\mathrm{F_f}(0;\omega_m)|^2|\alpha_{\mathrm{out}}|^2 + \frac{\kappa_{\mathrm{e}}}{\kappa}\gamma_{\mathrm{OM}}\int_{-\infty}^{\infty} d\omega\ |\mathrm{F_f}(\omega;\omega_m)|^2 S_{\hat{b}\hat{b}}[\omega;\langle n\rangle]\right) \tag{4.5}$$

$$= \frac{1}{2\pi}\left(|\mathrm{F_f}(0;\omega_m)|^2|\alpha_{\mathrm{out}}|^2 + \frac{\kappa_{\mathrm{e}}}{\kappa}\gamma_{\mathrm{OM}}\langle n\rangle\right) \tag{4.6}$$

$$\approx A|\alpha_{\mathrm{out}}|^2 + \frac{\kappa_{\mathrm{e}}}{\kappa}\gamma_{\mathrm{OM}}\langle n\rangle, \tag{4.7}$$

where we have assumed that the filter bandwidth is large compared to γ (satisfying $\gamma \ll \kappa_{\mathrm{f}} \ll \kappa$) allowing us to set $\mathrm{F_f}(\omega_m;\omega_m) = 1$ in Equation 4.7, and also defined a pump attenuation factor $A \equiv |\mathrm{F_f}(0;\omega_m)|^2/(2\pi)$. Further we have used Equation A.22 evaluating the integral of the phonon spectral density. A completely analogous expression obtains in the case of blue detuning, where the integral is instead performed over $S_{\hat{b}^\dagger\hat{b}^\dagger}[\omega;\langle n\rangle]$, resulting in the substitution $\langle n\rangle \longrightarrow \langle n\rangle + 1$.

Here we can directly see that in the idealized case in which the filter has completely rejected the coherent pump tone with flux $|\alpha_{\mathrm{out}}|^2$, the *signal* photon count rate is proportional to $\langle n\rangle$, illustrating the formal equivalence of photon counting with phonon counting. Hereafter we will use the term *phonon counting* to describe the detection method outlined above. In practice, inefficiencies in the optical path lead to photon loss which we model with an overall detection efficiency η. Let us define a *pump noise* photon count rate $\Gamma_{\mathrm{pump}} = \eta A|\alpha_{\mathrm{out}}|^2 + \Gamma_{\mathrm{noise}}$ consisting of the coherent pump tone which leaks through the sideband filtering as well as any additional noise counts arising from technical laser noise, including laser phase noise. The total measured count rate will also include a dark-count rate Γ_{dark}, which will be used to describe both *intrinsic* dark counts of the SPD as well as counts arising from stray radiation (e.g., due to thermal blackbody radiation inside the fridge, or environmental light sources coupling into the optical fiber path). To summarize, we find that for red- and blue-detuning the total measured output photon count rate is

$$\Gamma(t) = \begin{cases} \Gamma_{\mathrm{pump}} + \Gamma_{\mathrm{dark}} + \Gamma_{\mathrm{SB},0}\langle n\rangle & \text{if } \Delta = +\omega_m \\ \Gamma_{\mathrm{pump}} + \Gamma_{\mathrm{dark}} + \Gamma_{\mathrm{SB},0}(\langle n\rangle + 1) & \text{if } \Delta = -\omega_m \end{cases},$$

where we have defined the *per-phonon* count rate as $\Gamma_{\mathrm{SB},0} \equiv \eta \frac{\kappa_e}{\kappa} \gamma_{\mathrm{OM}}$.

In the case of resonant driving ($\Delta = 0$) again with filtering at $\omega_f = \pm\omega_m$, a similar expression is obtained after replacing $s(\omega; +)$ in Equation 4.4 with the corresponding effective scattering matrix element for $\Delta = 0$, which is simply suppressed by the sideband-resolution factor $\kappa/(2\omega_m)$. Explicitly, the substitution

$$s(\omega; +) \longrightarrow s_{\mathrm{eff}}(\omega; 0) = \frac{\kappa}{2\omega_m} s(\omega; +) \tag{4.8}$$

yields a modified per-phonon count rate of $\left(\frac{\kappa}{2\omega_m}\right)^2 \Gamma_{\mathrm{SB},0}$ at both the upper- and lower-frequency mechanical sidebands of the cavity. This will be useful in situations where it is desirable to perform thermometry at large intracavity photon number but with negligible back-action damping of the mechanics (see Section 6.3).

4.2 Phonon Counting Sensitivity

A useful parameterization of these quantities is the amount of noise (in units of mechanical occupation quanta) as a proportion of the signal generated by a single phonon in the OMC. Alternatively, this noise-equivalent phonon number n_{NEP} can be interpreted as the mechanical occupation which would produce a phonon-counting SNR of 1. We obtain n_{NEP} then by dividing the noise count rates by the per-phonon sideband photon count rate $\Gamma_{\mathrm{SB},0} = \eta|\gamma_{\mathrm{OM}}|$, where η is the total efficiency of the setup, including the system efficiency of the SPDs as well as optical insertion loss along the path from cavity to detector. For a coherent pump, this yields

$$n_{\mathrm{NEP}} = \frac{\kappa^2 \Gamma_{\mathrm{dark}}}{4\eta\kappa_e g_0^2 n_c} + A\left(\frac{\kappa\omega_m}{2\kappa_e g_0}\right)^2. \tag{4.9}$$

The above equation makes clear the benefits of large cavity-enhanced optomechanical coupling g_0, both in terms of the low power sensitivity limited by detector dark counts and the high power sensitivity limited by pump bleed-through.

The measured sensitivity follows the expected curve at low power due to detector dark counts (solid red curve), but at high n_c saturates to a value several times larger than expected for the filter suppression of the pump (solid blue curve). In order to better understand this excess noise, Fig. 4.1b shows measurements of the n_{NEP} as a function of filter-pump detuning, Δ_{filter}, at a high power where the pump transmission dominates the noise ($n_c \approx 65$). A strong dependence on Δ_{filter} is observed, with a

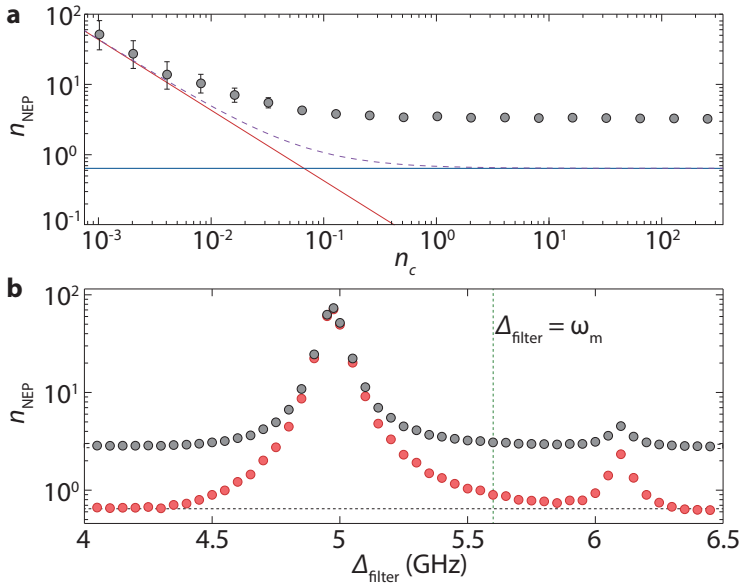

Figure 4.1: **Phonon counting sensitivity.** **a**, Noise equivalent phonon number n_{NEP} versus intracavity photon number n_{c} calculated using the measured signal and noise count rates for the detection setup in 2015 (grey circles). Solid lines indicate the theoretically expected contributions due to dark counts (red) and pump bleed-through (blue), based on the measured system efficiency and pump suppression, with the sum of the two contributions displayed as a purple dashed line. Error bars show one standard deviation determined from the measured count rates, assuming Poissonian counting statistics. **b**, n_{NEP} versus filter-pump detuning Δ_{filter} for $n_{\mathrm{c}} \approx 65$, with (red) and without (grey) an additional C-band band-pass filter inserted. The vertical green line indicates the detuning corresponding to the data from **a**, and the horizontal black line indicates the expected limiting sensitivity.

peak in the noise at 5 GHz and a secondary peak at 6.1 GHz, consistent with phase-noise of our pump laser [70]. With the addition of a C-band bandpass filter prior to the SPD to remove broadband spontaneous emission from the pump laser, and at frequencies far from the laser phase-noise peaks, the measured n_{NEP} agrees well with the theoretical predictions based on the filter pump suppression (horizontal dashed curve). At the relevant detuning of $\Delta_{\mathrm{filter}} = \omega_{\mathrm{m}}$ (vertical dashed curve), we measure a limiting sensitivity of $n_{\mathrm{NEP}} = 0.89 \pm 0.05$. While this sensitivity is directly measured at $n_{\mathrm{c}} \approx 65$, n_{NEP} is observed in Fig. 4.1a to be pump-limited for $n_{\mathrm{c}} \gtrsim 1$, implying that this setup setup (ca. 2015) achieves $n_{\mathrm{NEP}} < 1$ for n_{c} of order unity.

4.3 Phonon Intensity Interferometry

In this section, we focus on measurements made with a blue-detuned pump ($\Delta = -\omega_m$), in which the optomechanical back-action results in instability and self-oscillation of the acoustic resonator [70, 71]. The Stokes sideband count rate detected on a single SPD, shown versus n_c in Figure 4.2a, displays a pronounced threshold, with an exponential increase in output power beginning at $n_c \approx 1200$, where $C \equiv |\gamma_{OM}|/\gamma_i \approx 0.8$, in agreement with the expected onset of instability around $C = 1$ ($\gamma = 0$). This sharp oscillation threshold can also be observed from the measured NPSD (Fig. 4.2b), in which the amplitude of the mechanical spectrum is seen to rapidly increase with a simultaneous reduction in linewidth, and in plots of the in-phase and in-quadrature components of the photocurrent fluctuations, which show a transition from thermal noise to a large amplitude sinusoidal oscillation. Also shown in Figure 4.2a is the inferred phonon occupancy $\langle n \rangle$. Below threshold, the photon count rate is simply related to $\langle n \rangle$ via the simple linear relation $\Gamma_{tot} = \eta|\gamma_{OM}|\,(\langle n \rangle + 1)$. At and above threshold, self-consistent determination of the oscillation amplitude indicates that even at our highest pump power the mechanical amplitude remains small enough that this linear approximation remains valid.

The statistical properties of the resonator near the self-oscillation threshold can also be characterized by measuring photon correlations using a Hanbury Brown and Twiss (HBT) setup. Blue-detuned pumping produces anti-normally ordered phonon correlations. In this case $g^{(2)}(\tau)$ refers to the anti-normally ordered second-order phonon correlation function, defined by

$$g^{(2)}(\tau) = \frac{\langle \hat{b}(0)\hat{b}(\tau)\hat{b}^\dagger(\tau)\hat{b}^\dagger(0)\rangle}{\langle \hat{b}(0)\hat{b}^\dagger(0)\rangle^2}. \tag{4.10}$$

For measurements made with a red-detuned pump, as shown in Fig. 4.3b, $g^{(2)}(\tau)$ refers to the normally ordered phonon correlation function,

$$g^{(2)}(\tau) = \frac{\langle \hat{b}^\dagger(0)\hat{b}^\dagger(\tau)\hat{b}(\tau)\hat{b}(0)\rangle}{\langle \hat{b}^\dagger(0)\hat{b}(0)\rangle^2}. \tag{4.11}$$

In the case of the classical states measured here, there is no observable difference between the normally and anti-normally ordered correlation functions. As the oscillation threshold is crossed, the state of the acoustic resonator will transition from a thermal state into a displaced thermal state (DTS), and the normalized phonon intensity correlation function near $\tau = 0$ should show a transition from

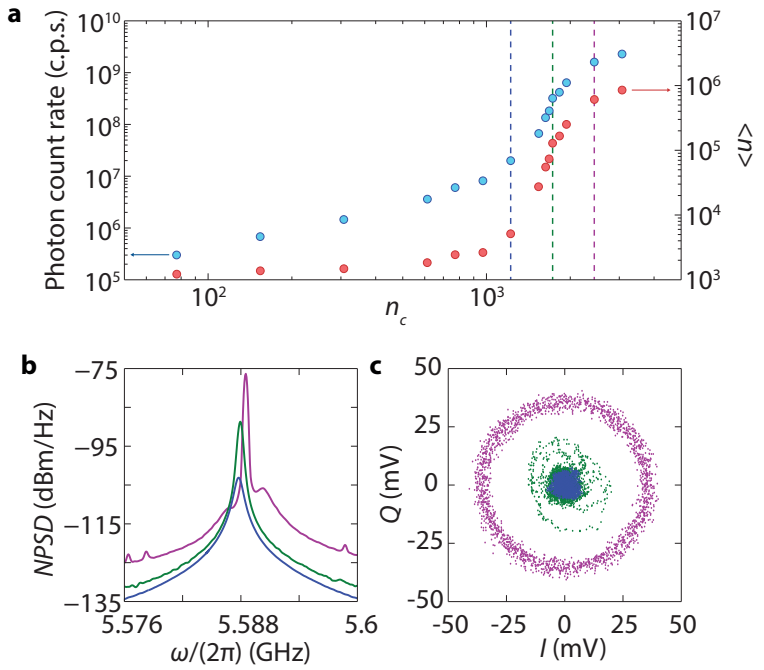

Figure 4.2: **Phonon lasing.** **a**, Phonon count rate (blue) and inferred phonon occupancy $\langle n \rangle$ (red) as a function of intracavity photon number for $\Delta = -\omega_{\mathrm{m}}$. Dashed lines indicate points below (blue), at (green), and above (magenta) threshold. **b**, Noise power spectral densities (NPSD) corresponding to the dashed lines in **a**.The small satellite peaks in the thermal emission background of the above threshold spectrum correspond to beating of the phonon laser line with low frequency modes of the nanobeam structure. **c**, Phase plots of the in-phase (I) and in-quadrature (Q) amplitudes of the optical heterodyne signal for each of the dashed lines in **a**, acquired in a 36 MHz span around 5.588 GHz over a 60 second time interval.

bunching ($g^{(2)}(0) > 1$) to Poissonian statistics ($g^{(2)}(\tau) = 1$ for all τ). Plots of $g^{(2)}(\tau)$ below, at, and above threshold are shown in Figure 4.3. Below threshold bunching is clearly visible, with $g^{(2)}(0) = 2$ as expected for a purely thermal state. In Figure 4.3b $g^{(2)}(0)$ is plotted versus n_{c} for both blue- and red-detuned pump light. For a blue-detuned pump a smooth decrease from $g^{(2)}(0) = 2$ to $g^{(2)}(0) = 1$ is observed in the threshold region, while for a red-detuned pump the oscillator is observed to remain in a thermal state through threshold and beyond. The decay rate of the acoustic resonator, measured from both the linewidth of the NPSD and from an exponential fit to $g^{(2)}(\tau)$ below threshold, is plotted in Figure 4.3. The decay rate as measured from the NPSD, which includes both phase and amplitude fluctuations, is seen to increase around threshold before continuing to decrease. This behavior is commonly observed in semiconductor lasers where a coupling exists between the

gain and the cavity refractive index, and a similar effect arises in optomechanical oscillators due to the optical spring effect [72]. The decay rate measured from $g^{(2)}(\tau)$, on the other hand, which measures intensity fluctuations, begins to deviate from the measured linewidth in the vicinity of threshold. Thermal phonon emission dictates a strict correspondence between the second-order and first-order coherence functions [66]; however, above threshold where the phonon statistics are no longer purely thermal, such a deviation is possible, and in fact predicted for self-sustaining oscillators [73]. The Fano factor, defined as

$$F = \frac{(\Delta n)^2}{\langle n \rangle} = 1 + \langle n \rangle (g^{(2)}(0) - 1), \tag{4.12}$$

provides additional statistical information about the fluctuations of the oscillator, and is useful for defining a precise oscillator threshold [74] as well as distinguishing between states that may have similar or identical values of $g^{(2)}(0)$ (e.g., a coherent state versus a DTS) [72]. The Fano factor of our mechanical oscillator, computed from the measured $g^{(2)}(0)$ and the inferred values of $\langle n \rangle$, is displayed in Figure 4.3d and shows the expected increase and peak in fluctuations at threshold. Above threshold, the Fano factor drops again due to saturation in the optomechanical gain, approaching a measured value consistent with that expected for a DTS ($F \sim 2n_\mathrm{b}+1$).

Although we have emphasized the analogy between the optomechanical oscillator studied here and a laser, there are unique differences which arise due to the intrinsically nonlinear nature of the radiation pressure interaction in an optomechanical cavity. Recent theoretical studies [64, 72, 75] indicate that a laser-driven optomechanical oscillator will enter a nonclassical mechanical state with anti-bunched phonon statistics ($F < 1$), and under slightly more restrictive conditions, strongly negative Wigner density. Surprisingly, this is predicted to be observable even for classical parameters, i.e., outside the single-photon strong-coupling regime ($g_0/\kappa < 1$), and in the presence of thermal noise. Beyond phonon correlation spectroscopy of optomechanical oscillators, it is envisioned that sensitive photon counting of the filtered motional sidebands may be utilized in the preparation and heralding of non-Gaussian quantum states of a mechanical resonator [76]. For the OMC cavities of this work, with their large optomechanical coupling rate and near millisecond-long thermal decoherence time at sub-Kelvin temperatures [30], the phonon addition and subtraction processes of Ref. [76] should be realizable with high fidelity and at rates approaching a megahertz. Whether for studies of the quantum behavior of mesoscopic mechanical objects or in the context of proposed quantum information

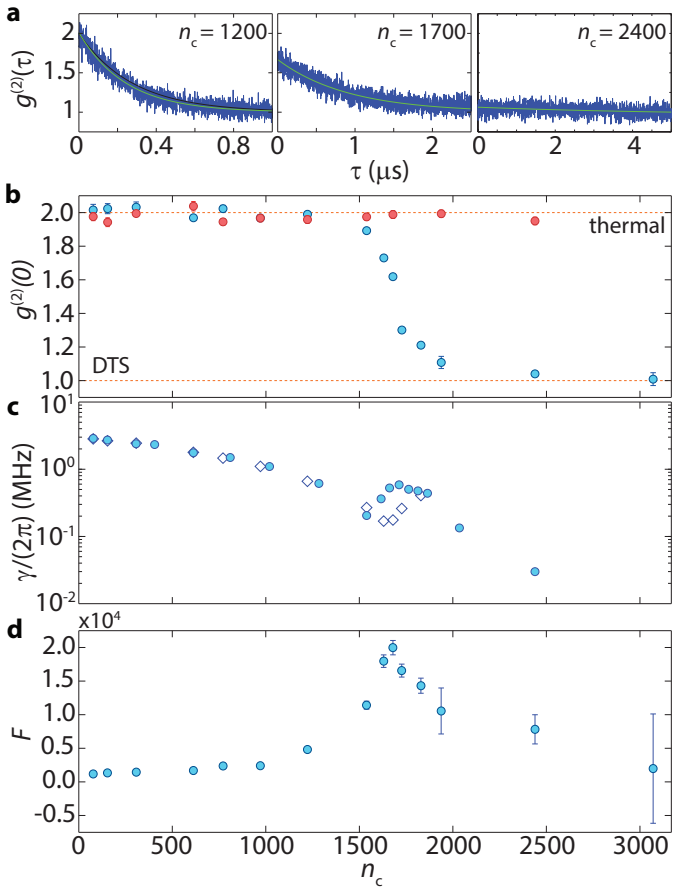

Figure 4.3: **Phonon intensity correlations.** **a**, Normalized anti-normally ordered second-order intensity correlation function $g^{(2)}(\tau)$ for $\Delta = -\omega_m$, shown below, at and above threshold (left to right, respectively). Green lines show a simple exponential fit, while black lines indicate the expected theoretical curve using decay rates measured from fitting the NPSD linewidth. **b**, Phonon correlation at zero time delay versus n_c for $\Delta = -\omega_m$ (blue) and $\Delta = \omega_m$ (red). The top and bottom dashed lines indicate the expected values for purely thermal or displaced thermal states (DTS), respectively. Error bars show one s.d. determined from the fit value of $g^{(2)}(0)$. **c**, Mechanical decay rate versus n_c for $\Delta = -\omega_m$, determined from the measured linewidth of the NPSD (circles) and from the exponential fit to $g^{(2)}(\tau)$ (diamonds). **d**, Fano factor versus n_c. Error bars show one s.d. determined from the measured count rates, assuming Poissonian counting statistics, and the fit value of $g^{(2)}(0)$.

processing architectures utilizing phonons and photons [77], such photon counting methods are an attractive way of introducing a quantum nonlinearity into the cavity optomechanical system.

Chapter 5

PULSED EXCITATION DYNAMICS OF OPTOMECHANICAL CRYSTALS AT LOW TEMPERATURES

The recent cooling of nanomechanical resonators to their motional quantum ground state [20, 78, 79] opens the possibility of utilizing engineered mechanical systems strongly coupled to optical or microwave fields for a variety of quantum metrology and information processing applications [80], amongst them the preparation and optomechanical conversion of highly non-classical mechanical states [76, 81, 82, 83] and coherent frequency conversion between microwave and optical signals [19, 84, 85, 86, 87]. A particularly interesting device architecture for realizing large radiation pressure coupling between light and mechanics is the thin-film optomechanical crystal (OMC) [88, 89], in which optical and acoustic waves can be guided and co-localized via patterning of the surface layer of a microchip. Based largely upon the OMC concept, new ideas for phononic quantum networks [83, 90] and optomechanical metamaterials [91] have been proposed, in which arrays of cavity-optomechanical resonators are coupled together via optical or acoustic degrees of freedom, and in which laser light is used to parametrically control the emergent network or material properties. Similar nanobeam OMC device architectures have been used to demonstrate optical readout of nonclassical states of GHz acoustic modes [92], including intensity interferometry of nonclassical states generated at the single-phonon level [93], as well as remote quantum entanglement between two such nanomechanical oscillators [94]. These initial measurements demonstrate the potential of this device platform as a key state-transduction component in future hybrid quantum networks based on optomechanical device arrays, although as we will detail below, substantial technical challenges remain in order to achieve more complete quantum coherent control over the mechanical state in these OMC devices in the presence of steady-state optical-absorption heating. Moreover, demonstrations of such non-classical state preparation and manipulation in devices having long-lived ($\sim$ 1 second) acoustic modes is an outstanding challenge, as the acoustic lifetime effectively limits the repetition rate which can be used in probabilistic state-preparation protocols based on state-heralding or entanglement post-selection [82,

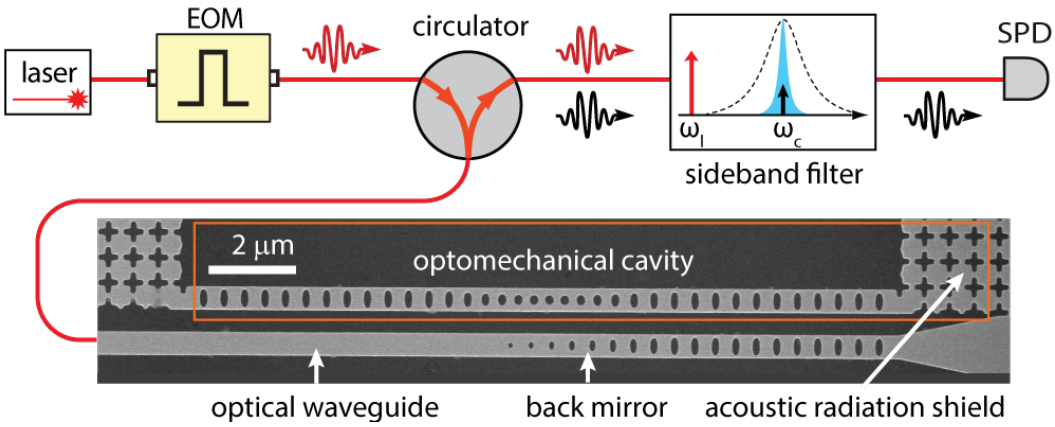

Figure 5.1: **Schematic of the pulsed-excitation phonon counting technique.** Laser pump light at frequency ω_L (red arrows) is passed through an EOM to generate pulsed light. The optical pulses are directed to a nanobeam OMC cavity inside a dilution fridge via an optical circulator. The cavity reflection is then filtered at the cavity frequency ω_c (black arrows) and directed to a SPD.

92, 93].

Recent measurements at millikelvin (mK) bath temperatures of an OMC resonator formed from single crystal silicon [21, 88] have shown substantial mechanical mode heating and mechanical damping due to weak sub-bandgap optical absorption [30]. Although optical Q-factors in excess of 10^6 are realized in these highly optimized structures [21], the large impact of even very weak optical absorption can be attributed to a combination of the relatively large energy per photon, and the sharp drop in thermal conductance with temperature in the low temperature limit [95]. Further complications arise from the seemingly contradictory requirements of isolating the mechanical resonator from its environment to obtain high mechanical Q-factor, and that of providing large thermal anchoring to a low temperature bath for cooling of the mechanical resonator.

In this work we utilize pulsed optical excitation and single phonon counting [96] as outlined in Chapter 4 to study the transient dynamics of optical back-action, heating, and damping of the 5 GHz mechanical mode of a silicon optomechanical crystal resonator at mK bath temperatures. Phonon counting yields simultaneously a high time resolution ($\sim$ 10 ns) and mechanical mode occupancy sensitivity ($< 10^{-2}$). Measurement of both Stokes and anti-Stokes sidebands also yields an absolute calibration of the occupancy of the resonator mode in terms of mechanical vacuum noise [39, 56, 97]. In addition to measuring initial phonon mode occupancies as

low as $\langle n \rangle = 0.017 \pm 0.007$ and mechanical decay times as long as $\tau = 1.21$ s, we observe a slow ($\sim$ 740 ns) turn-on time for the optical-absorption-induced phonon bath that both heats and damps the mechanical resonator mode. Taken together, these measurements demonstrate the feasibility of using short pulsed measurements for quantum optical state engineering of the mechanics in silicon optomechanical crystals, despite the presence of large steady-state optical heating.

5.1 Pulsed Excitation Phonon-Counting Measurement Methods

The full measurement setup used for device characterization is shown in Figure 5.2. The light source is a *C*-band fiber-coupled tunable external-cavity diode laser (ECDL), of which a small portion is sent to a wavemeter (λ-meter) for frequency stabilization. The light is then sent to high-finesse tunable fiber Fabry-Perot filter (Micron Optics FFP-TF2, bandwidth 50 MHz, FSR 20 GHz) to reject laser phase noise at the mechanical frequency, which can contribute to noise-photon counts on the SPDs [26]. After this prefiltering, the light is routed to an electro-optic phase modulator (ϕ-mod) which is driven by an RF signal generator at the mechanical frequency to generate optical sidebands used for locking the detection-path filters. The light is then directed via 2×2 mechanical optical switches into a "high-extinction" path consisting of a series of modulator components which are driven by a digital pulse generator to generate high-extinction-ratio optical pulses. The digital pulse generator is used to synchronize the switching of the modulation components as well as to trigger the time-correlated single-photon-counting (TCSPC) module. Of these modulation components, one is a 200 MHz acousto-optic modulator (AOM, Gooch & Housego) which provides ~57 dB of fast extinction (~20 ns rise and fall times), and two are Agiltron NS 1×1 switches (rise time 100 ns, fall time ~30 μs) which provide a total of 36 dB of additional extinction. The AOM and its driver are shown in Figure 5.3.

The total optical extinction achieved in generating these optical pulses is approximately 93 dB, which is greater than the cross-talk specification (60 dB) of our mechanical optical switches. For this reason we use two 2×2 switches in parallel (SW2 in Figure 5.2) to isolate the high-extinction path to ensure that our off-state optical power is limited by our high-extinction modulation components rather than by cross-talk through the mechanical switches. The light is then passed through a variable optical attenuator (VOA) to control the input pulse on-state power level to the cavity, and sent to a circulator which directs the light to a lensed-fiber tip for end-fire coupling to devices inside the dilution refrigerator. The reflected signal is

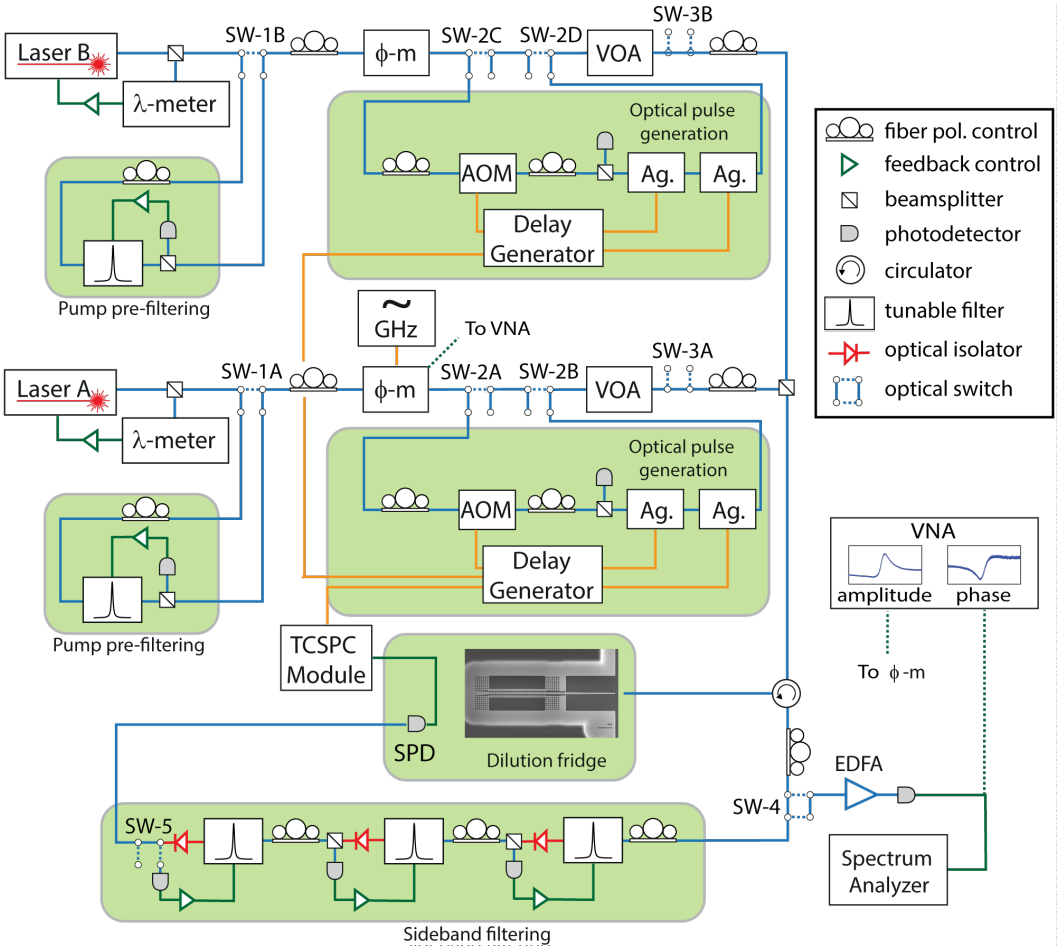

Figure 5.2: **Pulsed-excitation phonon counting measurement setup.** Simplified diagram of the experimental setup used for low-temperature optomechanical device characterization and phonon-counting measurements. Lasers A and B are passed through 50 MHz-bandwidth filters to suppress broadband spontaneous emission noise. Both lasers are equipped with modulation components (AOM, Ag.) for generating high-exctinction optical pulses. The modulation components are triggered by a digital delay generator (Laser B components are triggered by the "master" Laser A generator). Upon reflection from the device under test, a circulator routes the outgoing light to either (1) an EDFA and spectrum analyzer, or (2) a sideband-filtering bank consisting of three cascaded fiber Fabry-Perot filters (Micron Optics FFP-TF2) and the SPD operated at $\sim$ 760 mK. λ-meter: wavemeter, ϕ-m: electro-optic phase modulator, EOM: electro-optic intensity modulator, AOM: acousto-optic modulator, Ag.: Agiltron 1x1 MEMS switch, SW: optical 2×2 switch, VOA: variable optical attenuator, EDFA: erbium-doped fiber amplifier, VNA: vector network analyzer, SPD: single photon detector, TCSPC: time-correlated single photon counting module (PicoQuant PicoHarp 300).

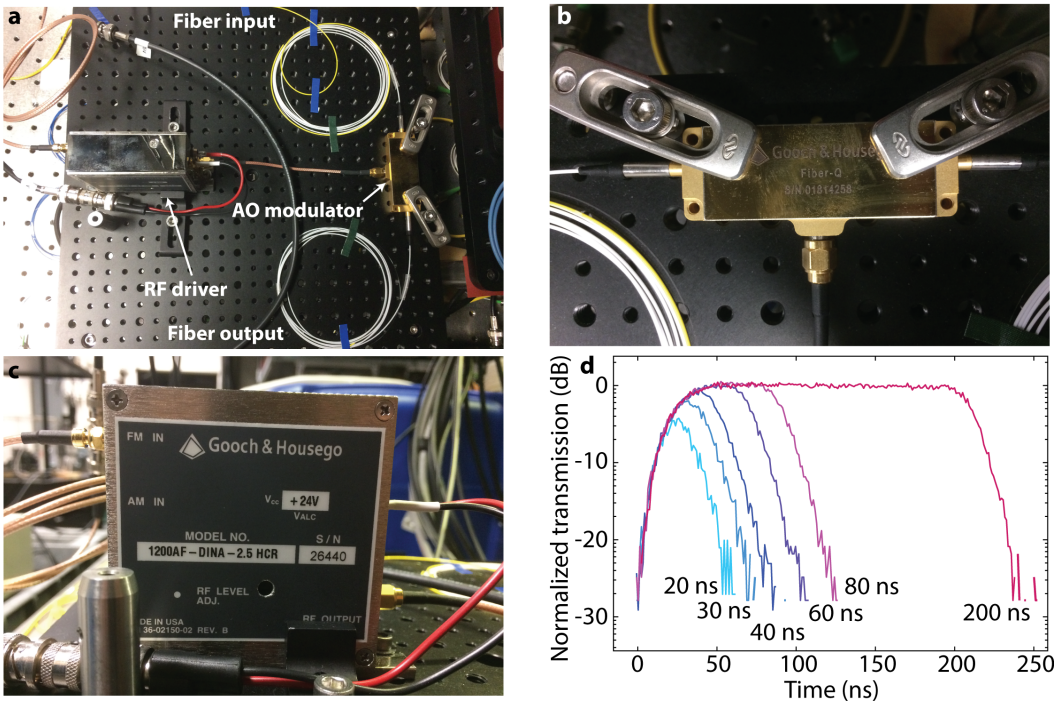

Figure 5.3: **Acousto-optic modulator fiber-Q switch for optical pulse generation.** **a**, View of the fiber-coupled AOM components for generation of high-extinction optical pulses. The RF driver is triggered using a digital delay generator and drives a fiber-Q switch using a 200 MHz AOM. The RF driver is heat-sinked to the optical breadboard. Optical fiber inputs are spliced to the rest of the optical measurement train, and the total insertion loss of of the AOM is $\sim$ 3.5 dB. **b**, Close view of the Gooch & Housego AOM fiber-Q switch clamped to its optical breadboard mount. **c**, The AOM RF driver. Fine tuning of the D.C. level is necessary to ensure maximum pulse extinction ratio over a wide range of duty cycles from $< 10^{-4}\%$ to $> 50\%$. **d**, Output optical pulse from the AOM component at several short pulse widths (time binning is 1 ns). We measure a 90% rise-time of $\tau_{\text{rise}} = 41$ ns. At pulse trigger lengths shorter than $\sim$ 80 ns, diminished peak output power will be delivered through the AOM due to partial turn-on of the switch. Maximum on-off extinction ratio is approximately 57 dB.

then routed back to either one of two detection setups. The first includes an erbium-doped fiber amplifier (EDFA) and a high-speed photodetector (PD) connected to a spectrum analyzer (SA) and a vector network analyzer (VNA). The second detection path is used for the phonon counting measurements. Here the light passes through three cascaded high-finesse (bandwidth 50 MHz, FSR 20 GHz) tunable fiber Fabry-Perot filters (Micron Optics FFP-TF2) inside an insulating housing and then to the SPD inside the dilution refrigerator.

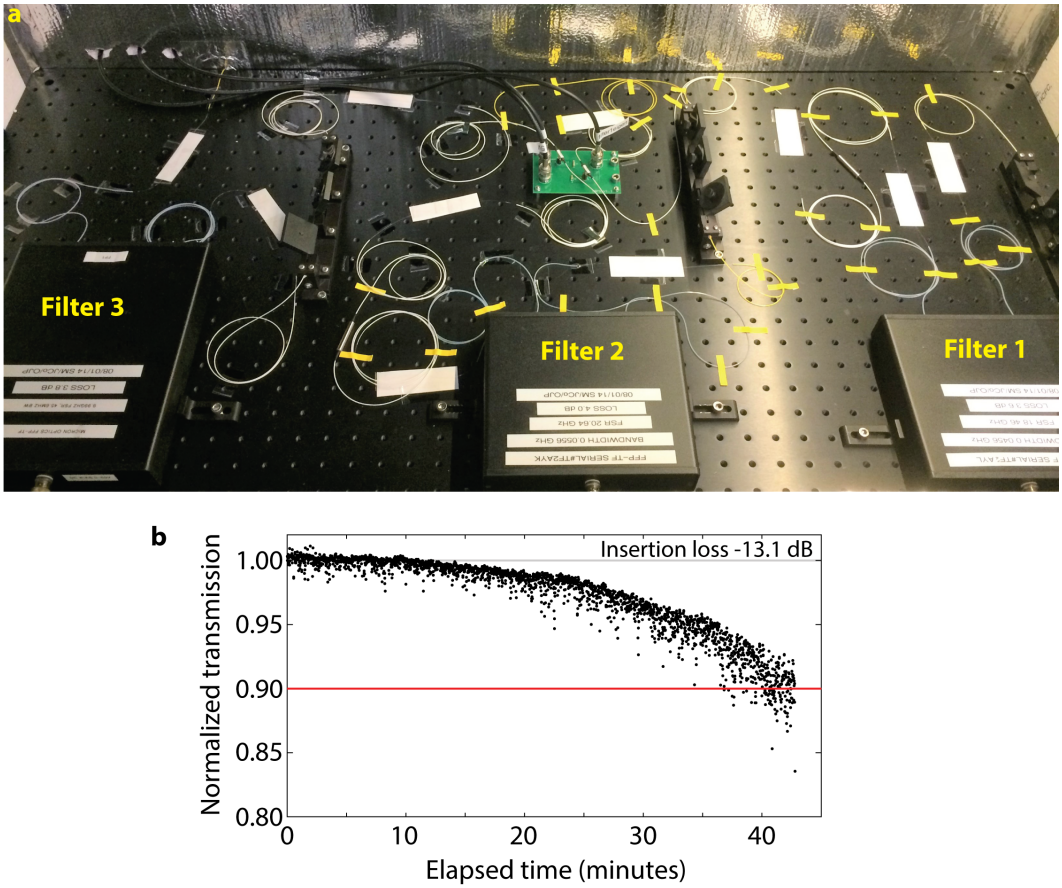

Figure 5.4: **Transmission stability of the FFP filter stack used in phonon-counting experiments. a**, Optical breadboard assembly of the cascaded FFP filter stack. **b**, Normalized transmission plotted versus measurement duration. Drift of the filters due to thermal and acoustic fluctuations in the laboratory causes a 10% decline in transmission typically in a period of $\sim$ 40 minutes. Measurements are stopped at regular intervals to allow re-locking and stabilization of the filters, and the transmission through the filter stack is recorded periodically during measurements. The insertion loss of the cascaded filter bank is $\eta_{\mathrm{Filt}} = -13.1$ dB.

The cascaded fiber Fabry-Perot (FP) filters are aligned to the optical cavity resonance frequency ω_{c} during measurement such that the signal reaching the SPDs consists of sideband-scattered photons and a small contribution of laser-frequency pump-bleed-through. In total the filters suppress the pump by >100 dB. This bleed-through is calibrated by positioning the laser far off-resonance of the optical cavity, such that the device acts simply as a mirror, while fixing the relative detuning of the filters and the pump laser at the mechanical frequency $\omega_{\mathrm{m}}/2\pi$ and measuring the photon count rate on the SPDs as a function of laser power.

Additionally, both the FP-filters and the EOMs will drift during measurement and must be periodically re-locked. Figure 5.4b plots the normalized transmission through the FP filter stack following stabilization of the filters to illustrate the time period over which the FP filter stack is stable during measurement when no active stabilization can be performed. The average transmission drops by 10% over a period of about 40 minutes. We therefore regularly stop the measurement every $2-6$ minutes to check the filter stack transmission (discarding data sets during which the transmission has dropped by $\geq 10\%$) and perform a re-locking routine. First, we re-lock the EOMs by applying a sinusoidal dithering signal of $\sim$1 V to them while monitoring the optical transmission, then decrease the dithering amplitude gradually to lock to the minimum of transmission. Next we switch out of the high-extinction pulse path (SW-2A,2B) and out of the SPD path (SW-5) to prevent blinding of the detectors, drive the phase modulator with a large RF power at frequency $\omega_{\mathrm{m}}/2\pi$ to generate large optical sidebands at the cavity resonance frequency, and send this light into the FP-filter stack. The transmission through each filter is monitored while a dithering sinusoidal voltage is applied to each filter successively, and the amplitude and DC offset of the dithering signal are adjusted until the optical transmission signal at the desired sideband is maximized. The offset voltage is then held fixed during the subsequent measurement run. The filters will drift due to both thermal fluctuations and acoustic disturbances in their environment, so in order to further improve the filters' stability we have placed them inside a custom-built insulated housing as shown in Figure 5.4a.

5.2 Calibration of the mechanical vacuum noise

In phonon-counting measurements the mechanical mode vacuum noise enters the detection signal via the mechanical noise-power spectral density of Equation A.20, giving for a blue-detuned pump a detected count rate which includes a vacuum noise term:

$$\Gamma(\Delta = -\omega_{\mathrm{m}}) = \Gamma_{\mathrm{SB},0}(\langle n \rangle + 1), \tag{5.1}$$

where here $\Gamma_{\mathrm{SB},0} = \eta_{\mathrm{det}}\eta_{\mathrm{cpl}}\eta_{\kappa}\gamma_{\mathrm{OM}}$ is the *detected* photon scattering rate per phonon (including experimental set-up efficiencies) and $\gamma_{\mathrm{OM}} = 4g_0^2 n_{\mathrm{c}}/\kappa$ is the optomechanical damping rate. In the absence of mechanical occupancy, pump photons may be spontaneously scattered by the mechanics owing to the nonzero mechanical susceptibility at the pump frequency. These real photons scattered by the mechanical

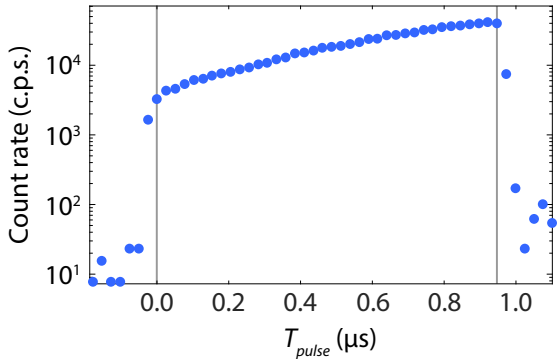

Figure 5.5: **Calibration of the mechanical vacuum noise for thermometry.** Pulsed measurements of the sideband count rate $\Gamma_{SB,0}$ for a blue-detuned probe laser (n_c = 101 photons during the pulse-on state) with $1/T_{per}$ = 4 kHz, measured on a zero-shield nanobeam device with $\gamma_0/2\pi$ = 14.1 kHz. The count rate during the initial measurement bin during the pulse, marked with a gray vertical line, corresponds to a per-phonon scattered photon count rate of $\Gamma_{SB,0} = 3.263 \times 10^3$ c.p.s. During the pulse, optomechanical back-action amplifies the mechanical occupancy at a rate $\gamma_{OM} - \gamma_i$, while in the pulse-off state the mechanics undergoes free decay to a local fridge bath temperature with effective bath occupancy $n_0 \sim 10^{-3}$.

vacuum noise in the presence of a pump laser are detected at a rate $\Gamma_{SB,0}$ according to Equation 5.1, providing a calibration of the per-phonon count rate directly to the vacuum noise. Here η_{det} is the measured overall detection efficiency of the setup, including losses in the fiber runs and circulator, insertion losses in the filters, the fiber run inside the dilution refrigerator, and the detection efficiency of the SPD. To calibrate $\Gamma_{SB,0}$ (for a fixed intracavity photon number n_c), a blue-detuned pump ($\Delta = -\omega_m$) pulsed with a repetition time of T_{per} drives the mechanics. In the initial time bin during the pulse, $\langle n \rangle \ll 1$ (if $1/T_{per} \ll \gamma_0$) and we can approximate the sideband photon count rate $\Gamma \approx \Gamma_{SB,0}$. Including detection non-idealities such as bleed-through of the pump laser to the SPD and dark counts on the SPD, the detected count rate is $\Gamma(T_{pulse} = 0) = \Gamma_{DCR} + \Gamma_{pump} + \Gamma_{SB,0}$. This measurement provides an absolute calibration of the detection photon count rate to the mechanical vacuum noise, where the count rate is proportional to intracavity photon number, allowing calibrated thermometry with a precision that is independent of knowledge of the losses in the optical path. Additional knowledge of the optical path losses enables the inference of γ_{OM} from a measurement of $\Gamma_{SB,0}$, which can be used to calibrate the vacuum optomechanical coupling rate. For one representative device, as shown in Figure 5.5, we measure $\Gamma_{SB,0} = 3.263 \times 10^3$ c.p.s. using a measurement photon

number of $n_c = 101$, and with κ known from independent measurements we extract $g_0/2\pi = 713$ kHz, consistent with previous measurements on similar devices.

5.3 Thermal Ringdown and Bath Turn-On Dynamics

We perform thermally-excited ringdown measurements of the mechanical breathing mode by impinging a series of red-detuned ($\Delta = \omega_m$) optical excitation pulses on the device at a series of different repetition rates f_{pulse}. For each f_{pulse}, the photon count rate during the pulse is averaged over many measurement cycles to generate a histogram of the mode occupancy $\langle n \rangle$ as a function of time T_{pulse} in the pulse-on state. The ratio n_i/n_f of the initial to final mode occupancy during the pulse is the effective decay ratio of the mechanical mode and is fitted to obtain an intrinsic decay rate γ_0. At milliKelvin temperatures, the dynamics of $\langle n \rangle$ during the pulse is dominated by two processes: back-action cooling via the red-detuned pump, and optical-absorption heating which has previously been characterized in similar devices at milliKelvin temperatures [30, 98]. The optical absorption and subsequent phonon-assisted relaxation processes can be modeled phenomenologically by introducing an effective local phonon bath of occupancy n_p which couples to the mode of interest at a rate γ_p (see Section 6.3). Thus, during the pulse-on state the total mechanical damping rate is $\gamma = \gamma_0 + \gamma_p + \gamma_{OM}$, where γ_0 is the intrinsic damping rate to the local milliKelvin fridge-temperature bath of occupancy n_0. As detailed in Ref. [98], the effective rate equation for the mode occupancy during the pulse can be modeled as $\dot{\langle n \rangle} = -\gamma \langle n \rangle + \gamma_p n_p (1 - \delta_b e^{-\gamma_S t}) + \gamma_0 n_0$, where δ_b is a fraction of the hot phonon bath which turns on slowly at a rate γ_S and $(1 - \delta_b)$ is the fraction which turns on effectively instantaneously. This rate equation has the solution

$$\langle n \rangle(t) = \langle n \rangle(0) e^{-\gamma t} + n_f (1 - e^{-\gamma t}) + n_\delta (e^{-\gamma_S t} - e^{-\gamma t}) \tag{5.2}$$

in terms of the steady-state occupancy $n_f = (\gamma_p n_p + \gamma_0 n_0)/\gamma$, where $n_\delta \equiv \gamma_p n_p \delta_b / (\gamma_S - \gamma)$. Here the variable t labels the elapsed time since the pulse turn-on.

The hot phonon bath does not leave the nanobeam structure instantaneously after the pulse is turned off, but rather introduces a transient heating lasting from several μs to several ms, depending on the details of the device geometry and surface preparation. This residual bath results in heating of the cavity mode to a peak occupancy n_{peak} after the end of the optical pulse. At longer times T_{off} in the pulse-off state, the mechanics ultimately undergoes free exponential decay such that

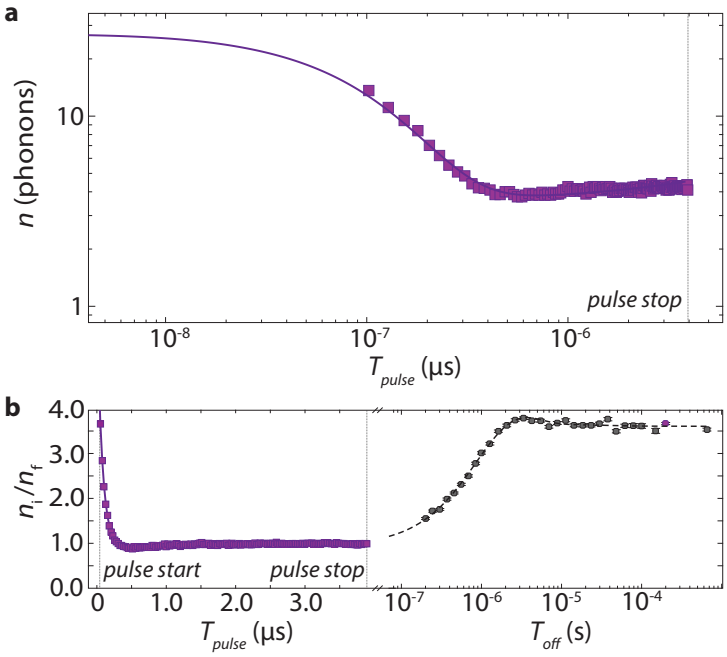

Figure 5.6: **Phonon dynamics during the red-detuned excitation pulse.** **a**, Phonon number as a function of time T_{pulse} during the red-detuned ($\Delta = +\omega_m$) optical excitation pulse, measured with T_{off} = 654 μs and on-state photon number n_c = 569. Squares are data points and the solid line is a best fit to the dynamical model. The nanobeam device has six periods of acoustic shielding, and device parameters are (κ, κ_e, g_0, ω_m, γ_0) = 2π (1.13 GHz, 605 MHz, 713 kHz, 5.013 GHz, 0.21 Hz). During the pulse, back-action cooling occurs at a timescale $\gamma_{OM}^{-1} \approx 100$ ns. Note that the initial mode occupancy n_i = 27 phonons is determined by extrapolating the model fit back to T_{pulse} = 0, while the earliest measurement bin has an occupancy of 13.6 phonons. The optical-absorption-induced bath heats the mode at a rate $\gamma_p n_p$ according to Equation 5.2, such that at long T_{pulse} a steady-state mode occupancy n_f is reached. Here n_f = 4.2 phonons. The bin size is 10.24 ns. **b**, Normalized phonon occupancy during and after the optical pulse. In the pulse-off state (gray squares), the residual phonon bath heats the mode at a rate $\gamma_p(t)n_p(t)$, where the bath damping and effective occupancy are explicitly time-dependent. A full dynamical model of the bath heating is used to generate the fit (dotted line). The purple data point in the off-state plot indicates the pulse shown in the on-state plot (T_{off} = 200 μs).

$$n_{\mathrm{i},k+1} = n_{\mathrm{peak},k} e^{-\gamma_0 \mathrm{T_{off}}}, \tag{5.3}$$

where the subscript k labels the k^{th} pulse. In steady-state, all pulses are identical, and the decay ratio becomes simply $n_{\mathrm{i}}/n_{\mathrm{f}} = Ae^{-\gamma_0 \mathrm{T_{off}}}$, where we have defined the normalization constant $A \equiv n_{\mathrm{peak}}/n_{\mathrm{f}}$. Figure 5.6a shows a representative measurement of the pulse occupancy with high time-resolution (10.24 ns) for a high-Q device having six periods of acoustic shielding, obtained using a pulse delay time of $\mathrm{T_{off}} = 654$ μs and a large readout photon number of $n_{\mathrm{c}} = 569$ in the pulse-on state.

A series of measurements of the pulse occupancy at various $\mathrm{T_{off}}$ values allows fitting of the decay of the initial occupancy $n_{\mathrm{i}} = An_{\mathrm{f}}e^{-\gamma_0 \mathrm{T_{off}}}$, as shown in Figure 5.7. The final pulse occupancy n_{f} is approximately constant for each measurement, so plotting the initial occupancy is approximately equivalent to plotting the normalized decay ratio $n_{\mathrm{i}}/n_{\mathrm{f}}$. For sufficiently long $\mathrm{T_{off}}$, the initial peak in the pulse occupancy decays to below the steady state occupancy n_{f}. From this decay curve we extract a decay constant of $\gamma_0/2\pi = 0.24$ Hz, corresponding to a mechanical Q-factor of 2.09×10^{10}. We choose the pulse duration (here 10 μs) such that the effects of back-action cooling and bath-induced heating reach a steady-state during the pulse, ensuring that the normalized decay ratio is referenced to a constant n_{f} for different $\mathrm{T_{off}}$. The measured decay rate for this high-Q mode corresponds to an inferred thermal decoherence time given by $\tau_{\mathrm{th}} = (\gamma_0(n_0 + 1/2))^{-1} = 662$ ms, which is representative of measurements made on a large number of similar devices summarized later in Figure 6.3. This result represents a promising improvement of more than two orders of magnitude in measured fQ-products for OMC devices.

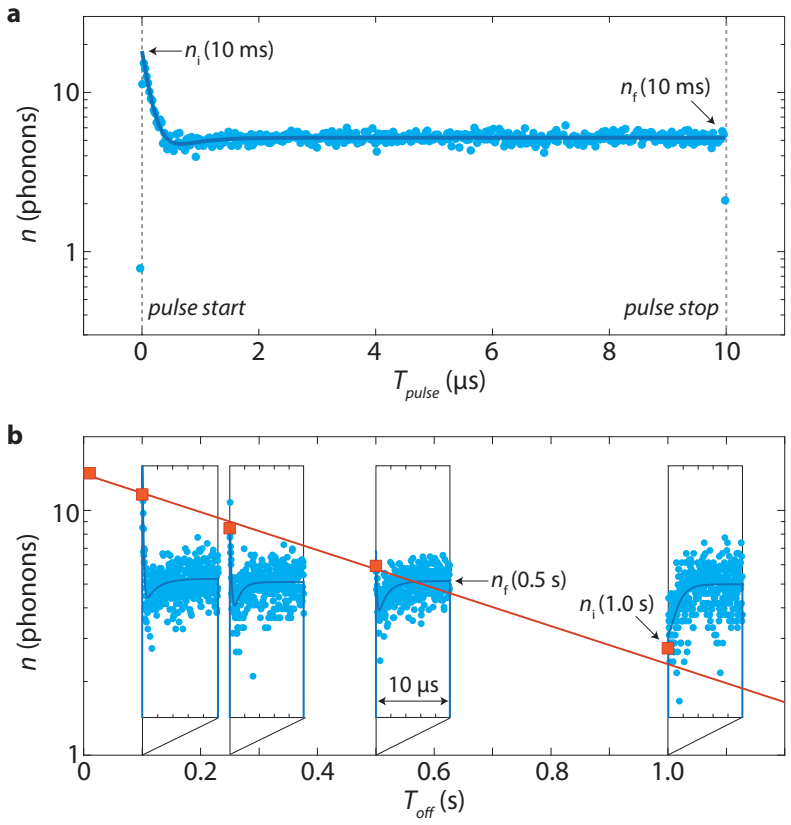

Figure 5.7: **Thermal ringdown measurement of an ultra-high-Q acoustic mode.** **a**, Measured phonon occupancy during a red-detuned pulse with T_{off} = 10 ms for a device having seven acoustic shield periods. Solid line is a fit to the dynamical model Equation 5.2. **b**, Diagram of a ringdown measurement performed by varying the delay T_{off} between subsequent pulses. The initial phonon occupancy n_i (orange squares) is measured for T_{off} = (10, 100, 250, 500, 1000) ms using a readout photon number n_c = 320. The phonon amplitude decay is fitted to extract an intrinsic mechanical damping rate $\gamma_0/2\pi$ = 0.24 Hz, corresponding to a mechanical Q-factor of 2.09×10^{10} (τ_{th} = 662 ms). Device parameters are (κ, κ_e, ω_m) = 2π (1.21 GHz, 362 MHz, 5.014 GHz). Insets show the measured occupancy during the pulse at each T_{off} value; blue circles are data and solid lines are fits.

5.4 Electromagnetically Induced Transparency at MilliKelvin Temperatures Using Single-Photon Detectors

Electromagnetically induced transparency (EIT), or its cavity-optomechanical analogue optomechanically-induced transparency (OMIT) allows for a spectral measurement of the mechanical mode response function via observation of a transparency window in the optical cavity reflection spectrum [16, 99, 100]. A pump laser tone at ω_c is amplitude modulated to generate a weak probe tone at $\omega_{s,\pm} = \omega_c \pm \Delta_p$. If the pump-cavity detuning is fixed on either the red- or blue-side of the optical cavity ($\Delta = \pm\omega_m$), the optical susceptibility of the cavity strongly suppresses one of the probe sidebands (at $\omega_{s,\mp}$) and only the other probe sideband will have an appreciable intracavity population. For a red-detuned pump, the interaction of the pump tone and mechanics with the probe sideband yields a reflection coefficienct $r(\Delta, \delta)$ for the probe which contains a transparency window having a bandwidth equal to the mechanical mode linewidth.

Derivation of Reflection Coefficient

To see the form of the reflection coefficient, we begin with the usual optomechanical Heisenberg-Langevin equations of motion for the optical and mechanical fields. In this semiclassical treatment we will ignore vacuum noise and be concerned only with large coherent field amplitudes, making the replacement $(\hat{a}, \hat{b}) \longrightarrow (\alpha, \beta)$ and similarly for the noise input operators $(\hat{a}_{in}, \hat{b}_{in}) \longrightarrow (\alpha_{in}, \beta_{in})$. The equations of motion are then

$$\dot{\alpha} = -\left(i\Delta + \frac{\kappa}{2}\right)\alpha - ig_0\alpha(\beta^* + \beta) + \sqrt{\kappa_e}\alpha_{in}, \tag{5.4}$$

$$\dot{\beta} = -\left(i\omega_m + \frac{\gamma_i}{2}\right)\beta - ig_0|\alpha|^2 + \sqrt{\gamma_i}\beta_{in}, \tag{5.5}$$

We can explicitly separate the input field and intracavity field amplitudes at the carrier and modulated-sideband tone frequencies,

$$\alpha \approx \alpha_0 + \alpha_- e^{-i\Delta_p t} + \alpha_+ e^{i\Delta_p t}, \tag{5.6}$$

$$\beta \approx \beta_0 + \beta_- e^{-i\Delta_p t} + \beta_+ e^{i\Delta_p t}. \tag{5.7}$$

Assuming that the sideband amplitudes are much weaker than the carrier, $|\alpha_\pm| \ll |\alpha_0|$, we can assume the carrier amplitude is unaffected and solve for the sideband

amplitudes in the frequency domain by grouping terms oscillating at the same frequencies:

$$-i\Delta_{\mathrm{p}}\alpha_{\pm} = -\left(i\Delta + \frac{\kappa}{2}\right)\alpha_{\pm} - ig_0\alpha_0\beta_{\pm} + \sqrt{\kappa_{\mathrm{e}}}\alpha_{\mathrm{in},\pm}, \tag{5.8}$$

$$-i\Delta_{\mathrm{p}}\beta_{-} = -\left(i\omega_m + \frac{\gamma_i}{2}\right)\beta_{-} - ig_0(\alpha_0^*\alpha_{-} + \alpha_0\alpha_{+}^*) + \sqrt{\gamma_i}\beta_{\mathrm{in,\text{-}}}. \tag{5.9}$$

Consider the case of a red-detuned pump for which $\Delta = +\omega_m > 0$. Then in the rotating wave approximation we may ignore terms like α_+ which are far detuned from the cavity, and the mechanical amplitude can then be written

$$\beta_{-} = \frac{-ig_0(\alpha_0^*\alpha_{-}) + \sqrt{\gamma_i}\beta_{\mathrm{in,\text{-}}}}{-i(\Delta_{\mathrm{p}} - \omega_m) + \frac{\gamma_i}{2}}, \tag{5.10}$$

and insert this into our equation of motion for α_-. The result is

$$\alpha_{-} = \left(i(\Delta - \Delta_{\mathrm{p}}) + \frac{\kappa}{2} + \frac{|G|^2}{-i(\Delta_{\mathrm{p}} - \omega_m) + \gamma_i/2}\right)^{-1}\left(\frac{iG\sqrt{\gamma_i}\beta_{\mathrm{in,\text{-}}}}{-i(\Delta_{\mathrm{p}} - \omega_m) + \gamma_i/2} - \sqrt{\kappa_{\mathrm{e}}}\alpha_{\mathrm{in,\text{-}}}\right), \tag{5.11}$$

where as usual we have defined the enhanced optomechanical coupling rate $G = g_0\alpha_0$. Using Equation 5.11 together with the usual input-output formalism boundary condition

$$\alpha_{\mathrm{out,\text{-}}} = \alpha_{\mathrm{in,\,\text{-}}} - \sqrt{\kappa_{\mathrm{e}}}\alpha_{-}, \tag{5.12}$$

the reflection coefficient is found to be

$$r(\delta) = \frac{\alpha_{\mathrm{out,\text{-}}}}{\alpha_{\mathrm{in,\text{-}}}} = 1 - \frac{\kappa_{\mathrm{e}}}{i(\Delta - (\delta + \omega_{\mathrm{m}})) + \frac{\kappa}{2} + \frac{|G|^2}{-i\delta + \gamma_{\mathrm{i}}/2}}, \tag{5.13}$$

where we have defined an effective mechanical detuning $\delta \equiv \Delta_{\mathrm{p}} - \omega_{\mathrm{m}}$.

EIT Using SPDs: Measurement Data

We measure the reflection amplitude $R = |r|^2$ given in Equation 5.13 by driving an EOM weakly to generate a probe tone and observing the count rates of sideband-scattered probe photons. The pump is locked at $\Delta = +\omega_{\mathrm{m}}$ and the cascaded filter stack is locked to the cavity frequency. The RF modulation power is chosen to generate a sideband intracavity photon number much smaller than the carrier photon number ($n_{\mathrm{c},+} \ll n_{\mathrm{c}}$) while maintaining a large count rate $\sim 10^5$ c.p.s. at the SPDs to minimize data integration times. This corresponds to modulation indices in the range of $\xi \sim 5 \times 10^{-4} - 3 \times 10^{-3}$ for our system parameters. The modulation frequency Δ_{p} is swept over a range of about 1 MHz, with the reflected count rate measured at each step, to map out the transparency window. This range is large enough to include the optomechanically-broadened mechanical linewidth which sets the bandwidth of the transparency window, but much narrower than the bandwidth of the FFP filters (≈ 50 MHz), allowing for the filters to be stably locked at a single position in the center of the optical cavity line throughout the measurement. Figure 5.8 shows the normalized reflection level detected for various optical probe power levels n_{c}, as well as fits to the data using the model Equation 5.13. The extracted total mechanical linewidth $\gamma = \gamma_{\mathrm{i}} + \gamma_{\mathrm{p}} + \gamma_{\mathrm{OM}}$ is plotted in Figure 5.8. At low probe-power, $\gamma/2\pi$ saturates to a value ≈ 50 kHz, which represents time-averaged broadening of the intrinsic mechanical linewidth due to jitter of the mechanical frequency. With κ and n_{c} known, the linear portion of the curve is fitted to extract $g_0/2\pi = 833$ kHz.

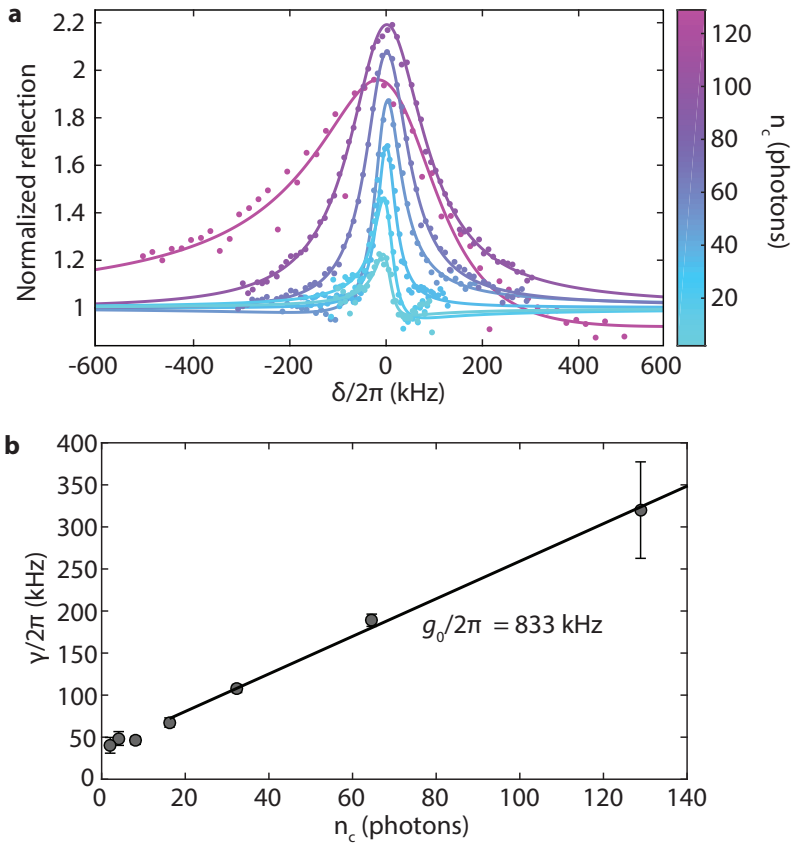

Figure 5.8: **EIT mechanical spectroscopy performed at $T_f = 10$ mK using single-photon detectors.** **a**, Normalized reflection amplitude for probe photons as a function of pump photon number. The reflection peak represents an EIT-like transparency window approximately centered within the bare optical cavity line (a Lorentzian with width $\kappa/2\pi \sim 1$ GHz). Asymmetry in the trace at $n_c = 129$ can be attributed to an effective detuning shift, likely caused by thermal shifting of the cavity at high input power. These EIT measurements were performed on a device having seven acoustic shield periods and mechanical $Q = 1.5 \times 10^{10}$ measured via ringdown. **b**, Plot of the fitted total mechanical linewidth γ versus pump photon number. At low n_c, $\gamma/2\pi$ saturates to ≈ 50 kHz due to mechanical frequency jitter. At higher n_c, the mechanical mode is broadened by γ_{OM} and we extract $g_0/2\pi = 833$ kHz. Device parameters are $(\kappa, \kappa_e, \omega_m, \gamma_0) = 2\pi$ (1.244 GHz, 261 MHz, 4.98 GHz, 0.33 Hz).

5.5 Mode Thermalization Measurements

At the lowest milliKelvin temperatures, the mechanical mode thermalizes to a bath temperature T_b which is related to the applied fridge temperature T_f through the thermal conductance G_th of the structure (see Figure 7.1, inset) which is dependent upon the details of the local device geometry and material. As detailed in Section 6.3, the finite dimensions of the thin-film nanobeam OMC modify the phonon density of states of the phonon bath at low temperature, giving rise to a quasi-discrete spectrum of bath modes well-approximated by a 2D density of states. A simple model for the thermal conductance valid for a 2D density of states of bath modes, $G_\mathrm{th} \propto T_\mathrm{b}^2$, yields an effective temperature offset between the fridge temperature and the bath thermalization temperature:

$$T_\mathrm{b} = T_\mathrm{f} + \frac{\mathrm{P_{th}}}{G_\mathrm{th}} = T_\mathrm{f} + \frac{\mathrm{P_{th}}}{AT_\mathrm{b}^2}, \tag{5.14}$$

where $\mathrm{P_{th}}$ is an effective heating power of the bath upon the mode of interest. We aim to measure the minimum temperature T_b to which the mode thermalizes at the lowest fridge temperature $T_\mathrm{f} = 10$ mK, and the corresponding true low-temperature fridge bath occupancy n_0. We perform this measurement using a low-power ($n_\mathrm{c} = 10$) red-detuned pulsed probe and a device having relatively low mechanical $Q = 3.57 \times 10^5$, such that for a rapid measurement repetition rate $1/\mathrm{T_{per}}$ the mode is well thermalized to its base temperature between subsequent incident optical pulses. The initial mode occupancy during the pulse then approximately corresponds to the "off-state" occupancy n_0. However, as the optical probe turns on during the first several time bins of the pulse, the mode is heated such that the initial observed occupancy exceeds n_0. We therefore extract n_0 by fitting the pulse on-state occupancy data to the full dynamical heating and damping model, and extrapolate the fit back to $T_\mathrm{pulse} = 0$ to measure the true bath occupancy n_0.

Figure 5.9 shows the fit to the pulse occupancy in the on-state, which yields a best fit value $T_\mathrm{b} = 35.6$ mK, corresponding to an initial fridge bath occupancy of $n_0 = 1.1 \times 10^{-3}$. While the fit is not tightly constrained by the bath temperature, the best fit corresponds well to previously estimated values [26] and is a small modification to the temperature of the *measured* initial occupancy, which yields 60 mK. From these points we can set reasonable bounds on the bath temperature, as shown in Figure 5.9a, where the lower bound of 10 mK is set by the minimum applied fridge temperature, and the upper bound 60 mK corresponds to the directly

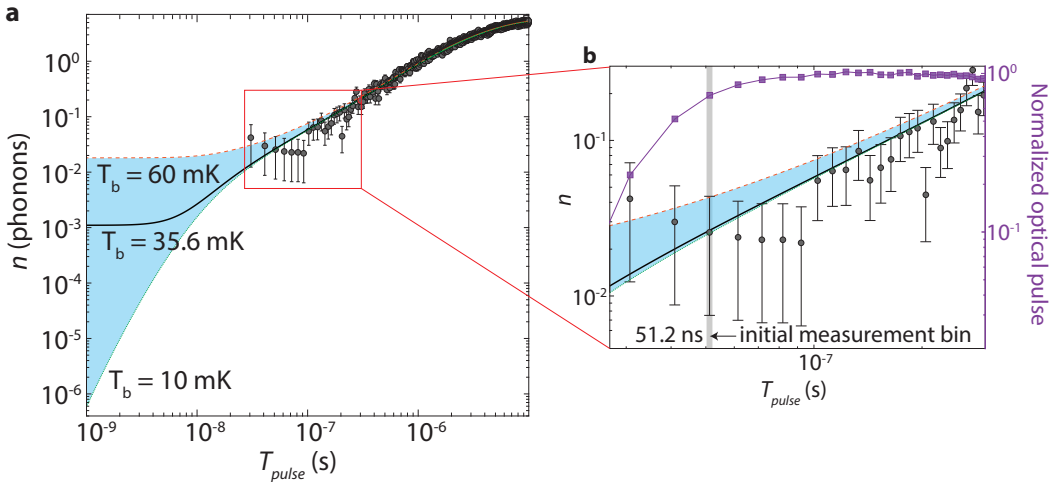

Figure 5.9: **Base temperature phonon occupancy measurement and pulse turn-on dynamics due to heating.** **a**, Mode occupancy during the pulse on-state of a zero-shield device. The photon number $n_c = 10$ is chosen to be small to minimize parasitic heating during the initial time bins of the pulse (bin size is 10.24 ns.). The model best-fit corresponds to $T_b = 35.6$ mK ($n_0 = 1.1 \times 10^{-3}$). Bounding curves to the fit are shown for $T_b = 60$ mK (orange dashed line) and $T_b = 10$ mK (green dotted line). **b**, Overlay plot of the initial time bins of the mode occupancy curve and the input optical pulse (purple squares). Time bins earlier than 51.2 ns occur during the fast rise of the pulse, which occurs at a timescale set by the rise of the EOMs and optical switches. The first measurement bin is chosen at $T_{\text{pulse}} = 51.2$ ns, where the input optical pulse has reached $> 70\%$ of its nominal on-state value (here $n_c = 10$). For 10.24 ns binning as shown here, the initial measurement bin is bin number 5. Device parameters are $(\kappa, \kappa_e, \omega_m, \gamma_0) = 2\pi$ (1.507 GHz, 778 MHz, 5.050 GHz, 14.1 kHz).

observed occupancy value in the initial measurement bin.

Measurement Sensitivity

The sensitivity of the mode thermalization measurement can be estimated using the expression

$$n_{\text{NEP}} = \frac{\kappa^2 \Gamma_{\text{dark}}}{4\eta\kappa_e g_0^2 n_c} + A\left(\frac{\kappa\omega_m}{2\kappa_e g_0}\right)^2. \tag{5.15}$$

and the known setup efficiencies and device parameters for the zero-shield device on which the thermalization measurement was made. Compared to the sensitivity measurement in Figure 4.1, the setup has undergone various improvements. First, the detector dark count rate was decreased to ~ 0.8 c.p.s. by additional coiling of the optical fiber inside the fridge and isolation of the fiber paths outside the fridge

from environmental lighting. Additionally, the overall detection path efficiency was improved by $\sim$ 5 dB by replacing various fiber-unions in the detection path with fiber-splices. In particular, the insertion loss of the cascaded filter bank was improved by 4.5 dB between experimental runs performed in 2015 and 2017. The resulting measured sensitivity plot is shown below (Figure 5.10), obtained in 2017. The minimum effective sensitivity $n_{\mathrm{NEP}} = 0.010$ is achieved for photon number $n_{\mathrm{c}} \gtrsim 100$. Note that this effective sensitivity depends upon the filter bleed-through through the parameter A in Equation 4.9, which is frequency-dependent as illustrated in Figure 4.1 due to the laser phase noise characteristic and the filter response functions. The sensitivity of $n_{\mathrm{NEP}} = 0.010$ obtained for a device having mechanical frequency 5.05 GHz, whereas the ultimate maximum sensitivity ever measured using this setup is $n_{\mathrm{NEP}} = 0.007$ for a device having mechanical frequency 5.6 GHz in Ref. [26]. Future improvements to the phonon counting sensitivity will be achievable in a number of ways via reduction of the pump bleed-through count rate. Notably, improvements in the cavity Q-factor are not immediately useful in reducing the technical phonon counting sensitivity, as the first term in Equation 4.9 is an order of magnitude smaller than the second term in the range of measurement photon numbers around $n_{\mathrm{c}} \sim 10 - 100$. The greatest improvements will come from technical improvements in the ability to filter the pump laser in the sideband filtering bank, either through alternative filter architectures or improved setup efficiency. Additionally, over-coupling of the optical cavity serves to reduce effective sensitivity, as does any substantial improvement to the optomechanical coupling rate which may be realized in next-generation (quasi-2D or other) OMC devices.

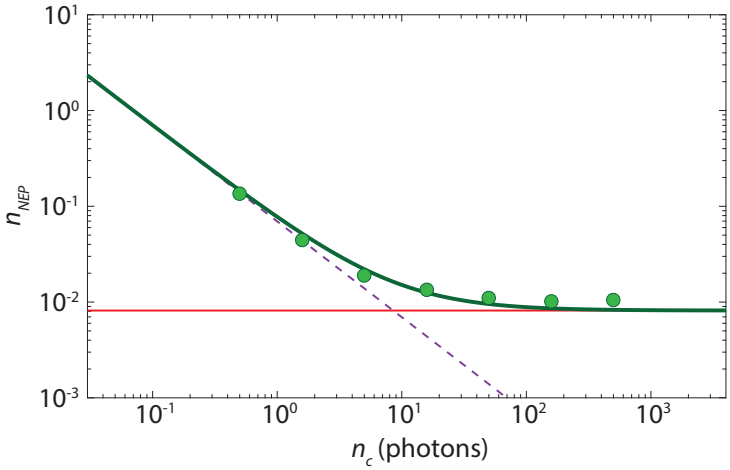

Figure 5.10: **Phonon counting sensitivity improvements.** Plot of the phonon counting sensitivity of the measurement setup as of 2017. Data were taken on the zero-shield device presented in Figure 6.7. Compared to Figure 4.1, a reduction in SPD dark counts to 0.8 c.p.s. has been made, as well as an increase in the overall optical path detection efficiency. The solid red line corresponds to the noise contribution from pump bleed-through counts, and the dashed purple line corresponds to the contribution from SPD dark counts. The thick green line is the total n_{NEP} as a function of n_{c} predicted by the model. We achieve maximum a maximum sensitivity of $n_{\mathrm{NEP}} = 0.010$ with these device parameters, (κ, κ_{e}, ω_{m}, γ_0) = 2π (1.507 GHz, 778 MHz, 5.050 GHz, 14.1 kHz).

Chapter 6

ULTRA-HIGH-QUALITY PHONON MODES IN NANOMECHANICAL RESONATORS

Mechanical resonators are used in a wide variety of technical applications, from precision time keeping and sensing, to the delay and filtering of microwave signals in mobile communication systems. Critical to many of these applications is the ability of a mechanical object to store vibrational energy at a well defined frequency of oscillation and with minimal damping. Energy damping can occur through acoustic radiation into the resonator support structure, or through impurities and defects in the resonator material, and is highly dependent on the temperature of operation due to the inherent anharmonic motion of atoms within solid-state materials. Here we present optical measurements down to milliKelvin temperatures of the acoustic mode properties of a crystalline silicon nanobeam cavity incorporating a three-dimensional phononic bandgap support structure for acoustic confinement. Utilizing pulsed laser light to excite a co-localized optical mode of the structure we are able to measure the dynamics of the internal cavity acoustic modes which are coupled to the light field via radiation pressure. These measurements represent an almost ideal scenario in which the ringdown occurs free of any additional mechanical or probe field contact, and where elastic scattering or radiation of the acoustic field does not lead to energy damping due to the full bandgap shield. The resulting ringdown measurements for the fundamental 5 GHz acoustic mode of the cavity show an exponential increase in phonon lifetime with phononic shield period number, which at a bath temperature of 35 mK saturates above six periods to a value as long as 1.5 s. This ultra-long lifetime, corresponding to an effective phonon propagation length of several kilometers, is found at the lowest temperatures to be consistent with damping from non-resonant tunneling states whose energy lies below the acoustic shield phononic bandgap, and which are most likely present in the amorphous etch-damaged region of the silicon surface. Other, more rapid forms of damping such as resonant tunneling state damping or three-phonon scattering are suppressed due to the phononic bandgap shield and the reduced density of phonon states in the effectively one-dimensional nanobeam geometry. Prospects for new applications of ultra-coherent nanoscale

mechanical resonators include tests various collapse models of quantum mechanics, or if appropriately integrated with microwave superconducting quantum circuits, as miniature quantum memory or processing units with potentially many-orders of magnitude longer coherence time than their electromagnetic counterparts.

In this chapter we present a summary of various measurement techniques used to study these ultra-high-Q confined acoustic modes, especially under coherent excitation to large phonon amplitude and in the presence of optical-absorption heating, as well as under the influence of back-action amplification to the regime of mechanical self-oscillation at extremely low threshold powers. The theoretical model of the optical-absorption heating phonon bath is developed in detail, and is compared with measurements of the bath properties as a function of laser power to constrain the effective dimensionality of the reduced bath phonon density of states proposed in the model. We exclude the possibility that the measured mechanical Q-factor is a residual effect of technical noise or unaccounted global lattice heating by obtaining consistent ringdown curves through three independent measurement techniques, in which the range of average optical power used to excite and probe the mechanical decay varies over more than three orders of magnitude. Furthermore, we observe an exponential relationship between the number of acoustic shielding periods and the mechanical Q-factor in agreement with numerical modeling results at low period number, as well as a saturation of the Q-factor at large period number which is quantitatively consistent with theoretical analyses of the intrinsic damping rate attributable to material defects and anharmonicity of the Si lattice (see Chapter 7). We conclude with a discussion of the relevance of these high-Q nanobeam OMCs to quantum coherent optomechanics featuring an analysis of the achievable quantum optomechanical cooperativity C_{eff} in the presence of large optical-absorption heating, and the technical limits thereof, proposing routes to further improvement of C_{eff} foreshadowing a discussion of quasi-2D planar OMCs in Chapter 8.

6.1 Impact of Fabrication Imperfections on Mechanical Q-Factor

Imperfections in the realized device structure due to randomness and disorder in the fabrication process will impact the energy loss rate of the mechanics, primarily by breaking symmetries of the structure and introducing coupling between the mode of interest and other mechanical modes below the acoustic shield bandgap which radiate acoustic energy into the bulk. We study the impact of fabrication imperfections numerically using FEM modeling of the full device geometry [42], as shown in Figure 6.1, by introducing randomness to the geometric parameters of the

simulated structure. The unit cells of the acoustic radiation shield are parameterized by nominal parameters $h_c = 503$ nm and $w_c = 169$ nm as introduced above, as well as a nominal center coordinate $\hat{c}_c$. Similarly, the unit cells of the nanobeam OMC are parameterized by the elliptical hole height h_h, width w_h, and center coordinate $\hat{c}_h$.

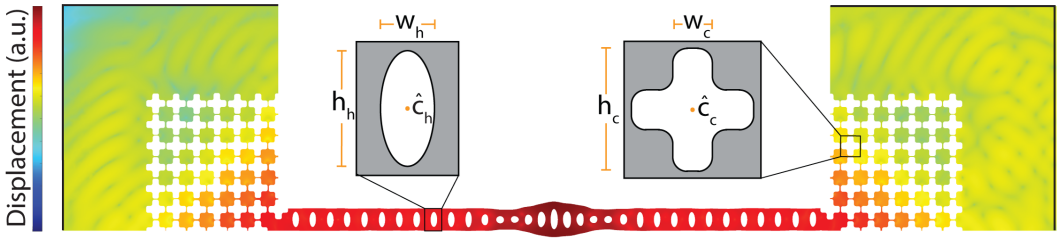

Figure 6.1: **Modeling of the breathing mode in the presence of fabrication disorder.** Finite-element method (FEM) simulation of the breathing-mode mechanical displacement field for a nanobeam OMC with $N_C = 6$ periods of acoustic shielding, illustrating localization of the vibrational energy. The geometry in the simulation consists of the nanobeam OMC, acoustic shielding, and the surrounding silicon substrate. The borders of the simulation geometry are modeled as an absorbing perfectly-matched layer (PML, outlined with solid black lines). The insets show critical parameters of the device geometry. To introduce disorder into the simulations, each of these geometric parameters is drawn from independent Gaussian distributions centered on the nominal design parameter value and having a standard deviation σ in units of nm.

The simulated structures are then generated by drawing each geometric parameter from an independent Gaussian random distribution centered on the nominal design value and having standard deviation σ in units of nm, analogous to the impact of random fabrication disorder upon realized structures. We separately consider randomness in the center coordinates $\hat{c}_c$ and $\hat{c}_h$ with a standard deviation σ_{posn} and in the hole-size parameters with σ_{size}. For the results plotted in Figure 6.2, we choose realistic randomness parameters, with $\sigma_{\text{size}} = 4$ nm fixed and varying $\sigma_{\text{posn}} = 2$, 4, and 8 nm. Absorbing perfectly-matched layer (PML) boundary conditions are used in all of our modeling. In Figure 6.2b we plot a line cut of the integrated acoustic energy density W along the longitudinal ($\hat{x}$) direction of the nanobeam. The partial bandgap of the mirror unit cells of the nanobeam provides some localization of the acoustic energy density, with a simulated cavity-mode mechanical Q-factor on the order of 10^5 for $\sigma_{\text{posn}} = 2$ nm, in reasonable agreement with measured values of $Q \approx 4 \times 10^5$. The acoustic energy density decays rapidly in the full-bandgap shield region. Here the modeling results yield a scaling $Q \propto e^{1.7 \times N_C}$, where N_C is the

number of cross shield periods. In simulation this trend of exponential increase of Q with shield period number continues to larger N_C, though as we detail below losses due to a combination of intrinsic material nonlinearity and strain-coupled defects are dominant for $N_C > 4$.

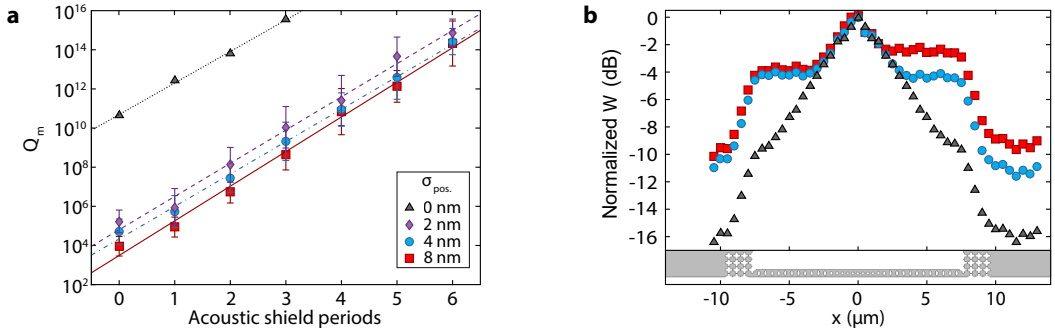

Figure 6.2: **Simulation of the impact of fabrication disorder on the mechanical Q-factor.** **a**, Plot of the simulated mechanical Q-factor due to acoustic radiation from the cavity through the acoustic shielding for randomness parameters σ_{posn} = 0, 2, 4, 8 nm. The straight lines are exponential fits. **b**, Plots of the normalized acoustic energy density W at various cut planes throughout the beam at longitudinal position x, for σ_{posn} = 2, 4, 8 nm.

6.2 Impact of Acoustic Bandgap Shielding on Mechanical Q-Factor

While the modeling results presented in Section 6.1 suggest an exponential increase in mechanical Q-factor with increasing period number of the acoustic bandgap shielding, one expects that effects not incorporated into the structural FEM modeling will ultimately cause deviations from this trend and a resulting saturation of the mechanical-Q to some maximum value. This saturation may be due to any of a variety of non-idealities not captured by the FEM modeling, including the intrinsic anharmonicity of the Si lattice, defects or impurities present in the crystal lattice, or coupling of the breathing mode to additional degrees of freedom in the amorphous material at the Si surface. Of particular interest is the amorphous surface material, which generally consists of a layer of etch-damaged Si as well as a thin native oxide growth which is well-known to contain two-level system (TLS) fluctuators and electronic defect states with large dipole coupling to strain and electromagnetic fields [101, 102]. The impact of these and other non-idealities to the lifetime and coherence of the mechanical mode will be addressed in detail in Chapter 7. Here we will only summarize the experimental indications that deviations from the radiative loss rate γ_0 through the acoustic shielding are observed.

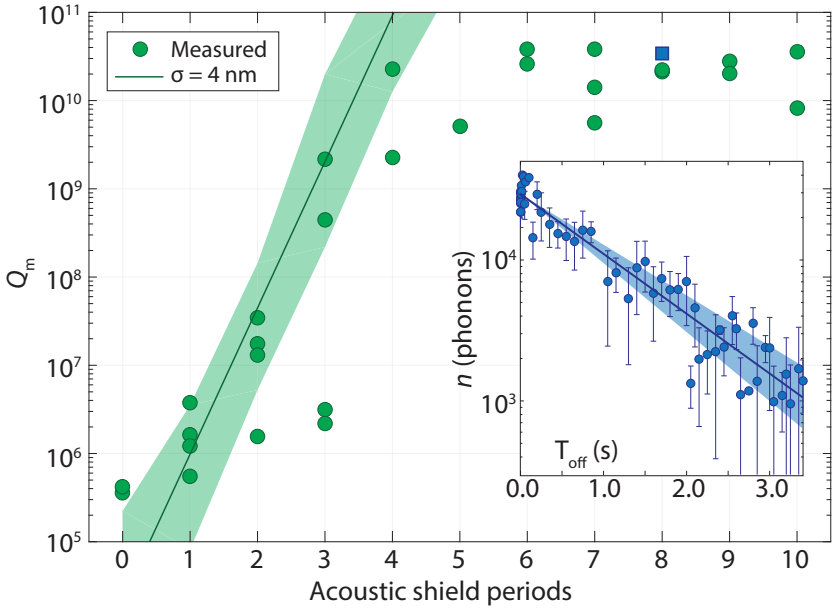

Figure 6.3: **Measured mechanical Q-factor at T_f = 10 mK versus number of acoustic shielding periods.** Arrays of otherwise identically-designed nanobeam OMC devices were fabricated with acoustic shield period number scaling from zero to ten. The green circles represent ringdown measurements performed using red-detuned excitation by optical-absorption heating to a thermal population of ~ 10 phonons. The blue square represents a ringdown measurement using coherent excitation of $\sim 3 \times 10^4$ phonons. The solid green line is a fit to the corresponding simulated Q-factor for device geometries having randomness parameter $\sigma = 4$ nm, with a shaded region corresponding to the standard deviation of the simulated Q-values. For devices with > 5 acoustic shield periods, the Q-factor is saturated to a few tens of billions, and is no longer limited by radiation through the acoustic shield. Inset: ringdown decay curve for the 8-shield device indicated by the blue square. The solid line is an exponential fit from which we extract $Q = 3.60^{+0.82}_{-0.56} \times 10^{10}$, and the shaded region represents a 90% confidence interval.

Figure 6.3 summarizes a series of ringdown measurements performed on nearly identical nanobeam devices at the base temperature T_f = 10 mK of a dilution refrigerator. Arrays of devices were fabricated as shown in Figure 3.3 wherein the optical and mechanical design parameters of the devices are held identical, and the number of acoustic shielding periods is varied from zero to ten. In this way, the only variations from one device to the next will be due to fabrication-induced randomness and the deliberate scaling of the acoustic shielding period number. Measurements of the mechanical-Q factor of each device were performed using the thermal excitation ringdown technique as illustrated in Figure 5.3, in which red-detuned pulses indirectly excite the mechanical mode to a thermal population of order

10 phonons through generation of a large optical-absorption phonon bath locally in the nanobeam. For devices having between zero and four acoustic shield periods, the Q-factor follows an approximately exponential trend with N_C, corresponding to the scaling predicted from modeling the full acoustic structure with a randomnes parameter of $\sigma_{\text{posn}} = 4$ nm. Note that there are large variations in Q-factor from one device to another of a fixed shield number, which is also consistent with the modeling results, and likely arises from variations in the realized geometry of the local optomechanical cavity defect. For $N_C > 5$, the Q-factor is observed to saturate to a value $\lesssim 5 \times 10^{10}$, representing a deviation from the ideal unbounded scaling predicted by FEM modeling. This saturation indicates that the dominant damping mechanism influencing the mechanics is not radiation through the acoustic shielding for sufficiently many periods of acoustic shielding, but rather that additional non-idealities are present as loss channels for the regime of $Q^{-1} \sim 10^{-10}$ (or at the frequency of interest, an energy damping rate of $\gamma/2\pi \sim 0.1$ Hz). In Chapter 7 we will explore the contributions of various material non-idealities and defects to the observed energy decay beyond the acoustic-shield radiation limit, relying primarily on temperature-dependent measurements of the total damping rate and theoretical models of the behavior of these various damping mechanisms as a function of temperature.

6.3 Properties of the Optical Heating Bath

Optical absorption induces additional heating and damping to the cavity mechanical mode in silicon OMC devices at milliKelvin temperatures, likely through excitation of sub-bandgap electronic defect states at the silicon surfaces which undergo phonon-assisted decay to generate a local bath of thermal phonons coupled to the cavity mode [30]. We may gain some understanding of the optically-induced bath which heats and damps the mode of interest by considering a simple model of the phonon-phonon interactions which couple the bath to our breathing mode. As we are concerned in this work with the phonon dynamics at low bath temperature ($T_b \lesssim 10$ K), the mean free path of the thermal phonons of the heating bath is large compared to the breathing mode wavelength. In this regime the phonon-phonon interactions leading to heating and damping of the breathing mode can be understood in terms of a Landau-Rumer scattering processes [103, 104], in which the anharmonicity of the silicon lattice gives rise to nonlinear phonon mixing processes (see Chapter 7). In this context, we may consider a simple model in which our mode of interest at frequency ω_m is coupled to higher-frequency bath phonon modes at

frequencies ω_1 and ω_2, with $\omega_2 - \omega_1 = \omega_m$. Then we may write the scattering rates into and out of the mode of interest to first order in perturbation theory [30, 103] as $\Gamma_+ = A(n_m + 1)(n_2 + 1)n_1$ and $\Gamma_- = An_m n_2(n_1 + 1)$, respectively, where n_1, n_2, and n_m are the number of phonons in each mode involved in the scattering and A is a constant describing the Si lattice anharmonicity. Then the overall rate of change in the occupancy of the mode of interest is

$$\dot{n}_m = \Gamma_+ - \Gamma_- = -A(n_1 - n_2)n_m + An_1(n_2 + 1). \tag{6.1}$$

This expression has exactly the form of a harmonic oscillator coupled to a thermal bath with rate $\gamma_\mathrm{p} = A(n_1 - n_2)$ and effective occupancy $n_\mathrm{p} = An_2(n_1 + 1)/\gamma_\mathrm{p}$.

In the real material system of the nanobeam, the local hot phonon bath at elevated temperature T_b is expected to be generated as THz-frequency electronic states undergo phonon-assisted relaxation processes, emitting a shower of high-frequency phonons which subsequently decay by a cascade of nonlinear multi-phonon interactions into a bath of GHz phonons. Due to the relatively large geometric aspect ratios of the thin-film nanobeam, the local density of phonon states becomes restricted at lower frequency, decreasing the rates of phonon-phonon scattering at low frequency relative to those of a bulk crystal with a 3D Debye density of states. The beam thickness (t = 220 nm, width $w \approx$ 560 nm, length $l \approx 15$ μm) corresponds to a relatively high cutoff frequency in the vicinity of $\omega_\mathrm{C}/2\pi \approx v_l/(2t_b) \approx 20$ GHz, where v_l = 8.433 km/s is the longitudinal-phonon velocity in Si. This cutoff frequency imposes an effective phonon *bottleneck* preventing further rapid thermalization to lower-lying modes and a resulting buildup in the bath phonon population above the bottleneck. For phonon frequencies below the cutoff, where the wavelength is large enough to approach the lattice constant of the acoustic bandgap clamping region, the reflectivity of the clamping region increases as ballistic radiation out of the nanobeam is suppressed. The result is a reduced density of phonon states near and below the cutoff, where the nanobeam supports quasi-discrete (and long-lived, especially in the vicinity of the mirror bandgap and acoustic shield bandgap) phonon modes at lower frequency as outlined in Figure 6.4. The phenomenological coupling rate γ_p describes the rate at which the lower-lying modes—in particular the breathing mode at 5 GHz—are coupled to the elevated-temperature bath of higher-frequency phonons above the bottleneck.

In the context of this proposed phonon-bottleneck model, we now consider instead of

a discrete pair of modes n_1 and n_2 a quasi-continuum of high-frequency bath modes coupled to the mode of interest via an anharmonicity matrix element $A(\omega;\omega_m)$. We will assume that the thermal phonons populating the bath have sufficient time to thermalize among each other before decaying, or in other words, that they couple to each other at a mixing rate γ_{mix} much greater than their coupling rates to their external environment or to the lower-lying modes. Under this assumption, we may define an effective local temperature T_{b} such that the occupancy of a bath phonon at frequency ω is given by the Bose-Einstein occupation factor

$$n_{\mathrm{bath}}(\omega) = \frac{1}{e^{\hbar\omega/k_{\mathrm{B}}T_{\mathrm{b}}} - 1}. \tag{6.2}$$

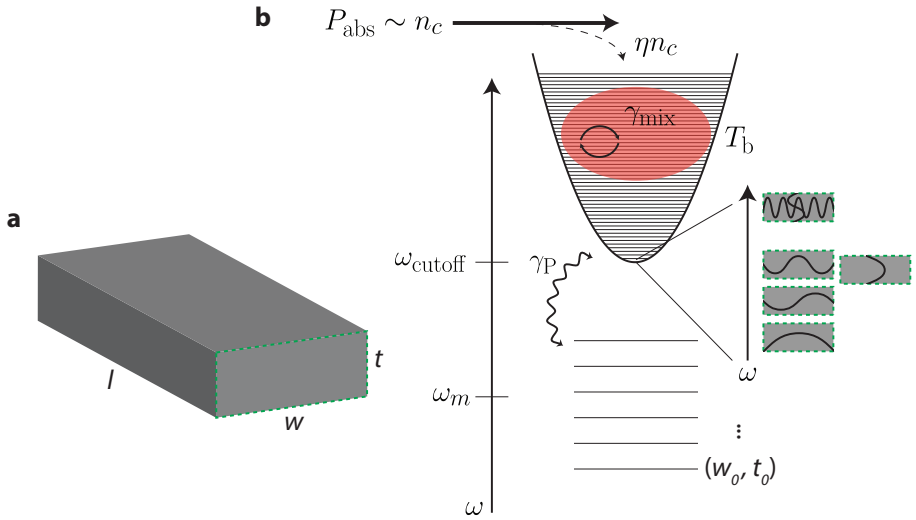

Figure 6.4: **Impact of the phonon-bottleneck on the optical-absorption bath. a**, Cross-sectional dimensions of the thin-film nanobeam. **b**, Absorption of sub-Si-bandgap photons gives rise to phonon-assisted decay of THz phonons into a local bath of GHz phonons in the nanobeam. This bath is expected to experience a bottleneck at a cutoff frequency corresponding to the cross-sectional dimensions of the nanobeam, such that a high-frequency phonon bath accumulates and thermalizes among itself to a local temperature T_{b} at rate γ_{mix}. In the vicinity of the bottleneck frequency the relevant normal modes of the beam are those shown in the inset (black lines are schematics of the local strain in the beam). The lowest-lying discrete mode (w_0, t_0) is a fundamental bowstring mode of the nanobeam at ~ 20 MHz.

The temperature T_{b} can then be simply related to the absorbed optical power P_{abs} using simple a simple model of the lattice thermal conductivity. Assuming the optical absorption process is linear, we can write the absorbed optical power as a fraction η of the optical pump power: $P_{\mathrm{abs}} = \eta P_{\mathrm{in}} = \eta' n_{\mathrm{c}}$. In steady state, the power

output into the phonon bath is equal to its input, $P_{\rm out} = P_{\rm abs} \sim n_{\rm c}$. Well-known models of the lattice thermal conductivity in silicon at low temperatures describe a thermal conductance scaling as the cube of temperature [105, 106], $G_{\rm th} \sim T_{\rm b}^3$, corresponding to a bath temperature scaling of $T_{\rm b} \sim G_{\rm th}^{1/3} \sim P_{\rm out}^{1/3} \sim n_{\rm c}^{1/3}$. This approximate scaling is expected to be valid for the high-frequency thermal photons with wavelength small compared to the dimensions of the beam [107] which are excited via decay of higher-lying electronic and acoustic states. Now, for a local phonon bath density of states $\rho(\omega)$, we can calculate the effective coupling rate $\gamma_{\rm p}$ between the local bath and the mode of interest in analogy with Equation 6.1:

$$\gamma_{\rm p} = \int_0^\infty d\omega\ A(\omega;\omega_m)\rho(\omega)\rho(\omega+\omega_m)[n_{\rm bath}(\omega) - n_{\rm bath}(\omega+\omega_m)], \tag{6.3}$$

In a simple continuum elastic model [30, 103], the product of the anharmonicity matrix element $A(\omega;\omega_m)$ and the density of states is taken to obey a polynomial scaling $A(\omega;\omega_m)\rho(\omega)\rho(\omega) = A'\omega^a$ for some constants A' and a, where we have introduced the cut-off frequency below which we assume the density of states is zero. With this assumption,

$$\gamma_{\rm p} \cong A' \int_{\omega_{\rm C}}^\infty {\rm d}\omega\ (\omega-\omega_{\rm C})^a\ (n_{\rm bath}[\omega] - n_{\rm bath}[\omega+\omega_{\rm m}]) \tag{6.4}$$

$$= A' \int_{\omega_{\rm C}}^\infty {\rm d}\omega\ (\omega-\omega_{\rm C})^a \left(\frac{n_{\rm bath}[\omega+\omega_{\rm m}](n_{\rm bath}[\omega]+1)}{n_{\rm B}[\hbar\omega_{\rm m}/k_{\rm B}T_{\rm p}]}\right) \tag{6.5}$$

$$= \frac{A'}{n_{\rm B}[\hbar\omega_{\rm m}/k_{\rm B}T_{\rm p}]+1} \int_{\omega_{\rm C}}^\infty {\rm d}\omega\ (\omega-\omega_{\rm C})^a\ (n_{\rm bath}[\omega](n_{\rm bath}[\omega+\omega_{\rm m}]+1)), \tag{6.6}$$

where in the last line we used the identity $n_{\rm B}[x+x'](n_{\rm B}[x]+1)/n_{\rm B}[x'] = (n_{\rm B}[x+x']+1)n_{\rm B}[x]/(n_{\rm B}[x']+1)$. Making a change of variables to $x \equiv \hbar(\omega-\omega_{\rm C})/k_{\rm B}T_{\rm p}$ in the integral in Eq. (6.6), we have

$$\gamma_{\rm p} \cong \left(\frac{A'}{n_{\rm B}[x_{\rm m}]+1}\right)\left(\frac{k_{\rm B}T_{\rm p}}{\hbar}\right)^{a+1} \int_0^\infty {\rm d}x\ x^a\ (n_{\rm B}[x](n_{\rm B}[x+x_{\rm m}]+1)) \tag{6.7}$$

where $x_{\rm m} = \hbar\omega_{\rm m}/k_{\rm B}T_{\rm p}$. The integral in Equation 6.7 depends on temperature only through $x_{\rm m}$, and in the small and large $x_{\rm m}$ limit (corresponding to low and high temperature), is relatively independent of $x_{\rm m}$. If we assume that the anharmonicity element $A[\omega;\omega_m]$ is approximately frequency independent, and the only frequency dependence in $A'(\omega-\omega_{\rm C})^a$ comes from the phonon density of states, then $a \approx 2(d-1)$

for a phonon bath of dimension d. We can thus make a general observation about the scaling of the bath-induced damping rate γ_p in the low ($x_\mathrm{m} \gg 1$) and high ($x_\mathrm{m} \ll 1$) temperature regimes:

$$\gamma_\mathrm{p} \propto \begin{cases} \left(\frac{k_\mathrm{B} T_\mathrm{p}}{\hbar}\right)^a \sim n_\mathrm{c}^{2(d-1)/(d+1)} & \text{for } T_\mathrm{p} \gg \frac{\hbar\omega_m}{k_\mathrm{B}}, \\ \left(\frac{k_\mathrm{B} T_\mathrm{p}}{\hbar}\right)^{a+1} \sim n_\mathrm{c}^{(2d-1)/(d+1)} & \text{for } T_\mathrm{p} \ll \frac{\hbar\omega_\mathrm{m}}{k_\mathrm{B}}, \end{cases} \tag{6.8}$$

for a generic hot phonon bath of dimension d. In a structure such as the OMC nanobeam cavity we expect the dimensionality of the effective bath density of states to be reduced relative to the Debye 3D density of states for a bulk crystal. Here we will assume that the phonon bath has a two-dimensional density of states corresponding to $a = 2$. In this case, we have the following scaling of the damping factor with intra-cavity photon number,

$$\gamma_\mathrm{p} \propto \begin{cases} \left(\frac{k_\mathrm{B} T_\mathrm{p}}{\hbar}\right)^2 \sim n_\mathrm{c}^{2/3} & \text{for } T_\mathrm{p} \gg \frac{\hbar\omega_\mathrm{m}}{k_\mathrm{B}}, \\ \left(\frac{k_\mathrm{B} T_\mathrm{p}}{\hbar}\right)^3 \sim n_\mathrm{c} & \text{for } T_\mathrm{p} \ll \frac{\hbar\omega_\mathrm{m}}{k_\mathrm{B}}. \end{cases} \tag{6.9}$$

Upon thermalizing with the hot phonon bath, the effective thermal occupancy n_p of the high-Q breathing mode of the acoustic cavity can be found from a similar rate equation analysis as considered for the 3-mode scattering in Eq. (6.1). Integrating over all the possible 3-phonon scattering events involving the mode of interest at frequency ω_m yields,

$$n_\mathrm{p} = \frac{1}{\gamma_\mathrm{p}} \int_{\omega_\mathrm{C}}^{\infty} \mathrm{d}\omega \; A[\omega;\omega_\mathrm{m}]\rho[\omega]\rho[\omega+\omega_\mathrm{m}] n_\mathrm{bath}[\omega+\omega_\mathrm{m}] \left(n_\mathrm{bath}[\omega]+1\right]) \tag{6.10}$$

$$\cong \frac{n_\mathrm{b}[\omega_\mathrm{C}+\omega_\mathrm{m}]A'}{\gamma_\mathrm{p}} \int_{\omega_\mathrm{C}}^{\infty} \mathrm{d}\omega \; \omega^a \left(n_\mathrm{bath}[\omega] - n_\mathrm{bath}[\omega+\omega_\mathrm{m}]\right) \tag{6.11}$$

$$= n_\mathrm{B}[\hbar\omega_\mathrm{m}/k_\mathrm{B}T_\mathrm{p}]. \tag{6.12}$$

We therefore have a characteristic scaling behavior for the effective phonon occupancy n_p coupled to the cavity mode of interest that is,

$$n_\mathrm{p} \propto \begin{cases} \left(\frac{k_\mathrm{B} T_\mathrm{p}}{\hbar\omega_\mathrm{m}}\right) \sim n_\mathrm{c}^{1/(d+1)} \overset{\mathrm{d=2}}{=} n_\mathrm{c}^{1/3} & \text{for } T_\mathrm{p} \gg \frac{\hbar\omega_\mathrm{m}}{k_\mathrm{B}}, \\ \exp\left\{[-\hbar\omega_\mathrm{m}/k_\mathrm{B}T_\mathrm{p}]\right\} & \text{for } T_\mathrm{p} \ll \frac{\hbar\omega_\mathrm{m}}{k_\mathrm{B}}. \end{cases} \tag{6.13}$$

Bath Measurements

In order to measure the additional bath-induced damping rate γ_p, we use a pump-probe technique employing two laser sources. The pump laser is tuned to optical resonance ($\Delta = 0$) to eliminate dynamical back-action effects ($\gamma_{OM} = 0$), and impinges upon the cavity in continuous-wave (CW) operation. The pump laser generates a steady-state intracavity photon population n_c and feeds an optical absorption phonon bath at elevated local temperature in the steady state. A second laser, the probe laser, is used to make pulsed measurements of the mode occupancy as described in Section 5.3. In the pulse-off state, but in the presence of the CW pump laser light, the mechanical mode occupancy relaxes to a steady-state occupancy of

$$\langle n \rangle = \frac{\gamma_p(n_c) n_p(n_c) + \gamma_0 n_0}{\gamma_p(n_c) + \gamma_0}, \tag{6.14}$$

at a modified total damping rate $\gamma_0 + \gamma_p(n_c)$, where γ_p and n_p are explicitly dependent upon the pump laser photon number. By observing this modified exponential decay rate we can directly extract γ_p, with γ_0 known from independent measurements. In Figure 6.5a, a ringdown measurement of the total damping rate in a high-Q nanobeam is shown for a pump laser photon number of $n_c = 10^{-2}$, from which we extract $\gamma_p/2\pi = 42.8$ Hz.

For larger power levels n_c, the steady-state occupancy $\langle n \rangle$ becomes comparable to the final occupancy n_f during the pulse due the additional heating term $\gamma_p n_p$ in Equation 6.14. In this range of optical power, which for the device presented here corresponds to n_c of order unity, no decay in the occupancy as a function of T_{off} will be observed via the thermally-excited ringdown technique. However, it is possible to probe the scaling behavior of γ_p at larger n_c by observing the relaxation of $\langle n \rangle$ to an *elevated* value greater than n_f in the pulse-off state, if the bath temperature is sufficiently high. In this case, we observe a ring-*up* in the pulse-off state from the final pulse occupancy n_f to the elevated $\langle n \rangle$, with an effective amplification rate given by the difference of the total heating rate and the total damping rate: $\gamma_p(n_c) - \gamma_0$. However, as we have previously discussed, the probe laser itself introduces a short-lived optical heating bath which results in net heating of the mechanics in the pulse-off state, and this probe heating must be distinguished from the heating caused by the pump laser in order to accurately extract the pump-induced damping $\gamma_p(n_c)$. Figure 6.5b shows a representative data set for extracting γ_p for power levels $n_c > 1$, where an initial rise is observed in the mode occupancy in the pulse-off state. The data are fitted to a full heating model in which the decay of the bath induced by the

readout laser at a total rate γ_S is modeled by an effective decay of γ_p at rate γ_R and of n_p at rate γ_T. The readout-induced bath parameters, with a subscript 1, satisfy in the model $\gamma_{p,1}(T_{off}) = \gamma_{p,1}(0)e^{-\gamma_R T_{off}}$ and $n_{p,1}(T_{off}) = n_{p,1}(0)e^{-\gamma_T T_{off}}$, where T_{off} is the time after the end of the pulse. The bath generated by the pump laser, with subscript 2, is maintained in steady-state. The resulting rate equation for the mode occupancy is

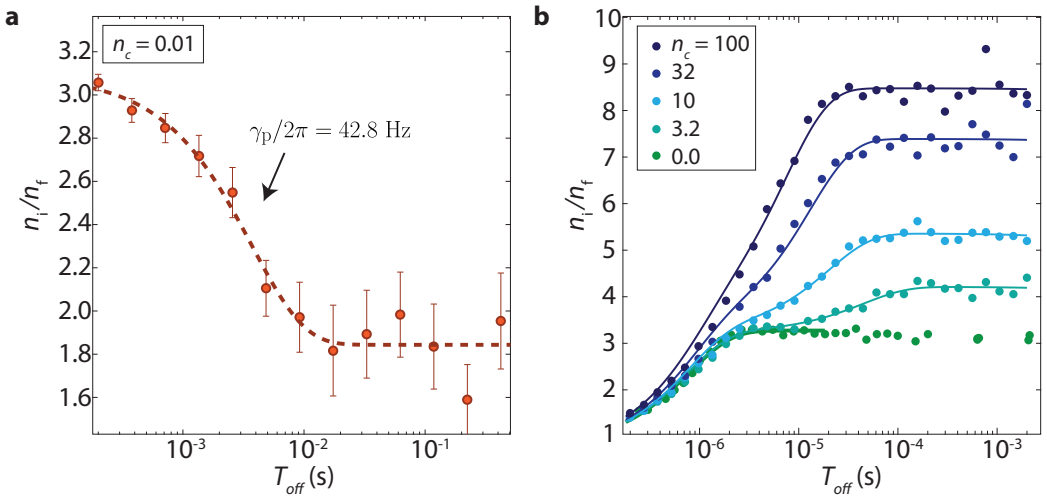

Figure 6.5: **Measurement techniques for extracting the optical-bath-induced damping rate γ_p at low ($n_c < 1$) and high ($n_c > 1$) power levels. a**, Ringdown measurement in the presence of a continuous-wave pump laser with an average intracavity photon number of $n_c = 10^{-2}$. The total mechanical energy decay rate is $\gamma = \gamma_p + \gamma_0$, and with γ_0 known from independent measurements, γ_p is extracted directly from the fitted decay rate. **b**, At larger n_c, the bath heating induced by the pump laser causes net heating in the pulse-off state. Here, the heating is fitted to a simple model Equation 6.16 to extract the effective heating rate γ_p. Measurements were performed on a six-acoustic-shield device with parameters (κ, κ_e, g_0, ω_m, γ_0) = 2π(1.13 GHz, 605 MHz, 713 kHz, 5.013 GHz, 0.21 Hz) and a readout photon number $n_c = 569$.

$$\langle \dot{n} \rangle = -\gamma(t)\langle n \rangle + (\gamma_{p,1}(t) + \gamma_{p,2})(n_{p,1}(t) + n_{p,2}) \tag{6.15}$$

$$= -(\gamma_0 + \gamma_{p,1}(0)e^{-\gamma_R t} + \gamma_{p,2})\langle n \rangle + (\gamma_{p,1}(0)e^{-\gamma_R t} + \gamma_{p,2})(n_{p,1}(0)e^{-\gamma_T t} + n_{p,2}), \tag{6.16}$$

where we have denoted T_{off} by t for convenience. We measure the decay of the readout-induced bath in the absence of the pump laser, as shown in the dark green curve in Figure 6.5b, and self-consistent fitting of Equation 6.16 yields $n_{p,1}(0) = 40$

(consistent with independent measurements of n_p at the appropriate readout power $n_\mathrm{c} = 569$, see Figure 6.7), $\gamma_{p,1}(0)/2\pi = 9.55$ kHz, $\gamma_\mathrm{R}/2\pi = 143$ kHz, $\gamma_\mathrm{T}/2\pi = 15.9$ kHz. With these values known, Equation 6.16 is numerically integrated for fitting to the heating curves in the pulse-off state to extract the additional pump-induced damping $\gamma_{p,2}$ as a function of n_c. The results are summarized in Figure 6.7, with measurements from a six-shield and a zero-shield nanobeam device. The observed power law scaling fits well to a power-law of $\gamma_\mathrm{p}/2\pi = (1.07\ \mathrm{kHz}) \times n_\mathrm{c}^{2/3}$, in agreement with the scaling predicted in Equation 6.9 for a model in which the bath phonon population is described by a 2D density of states.

In order to measure the bath occupancy n_p, again two different methods are used to probe the high- and low-photon-number dependencies of the bath. To measure the bath occupancy at photon numbers $n_\mathrm{c} \gtrsim 1$, a simple readout technique may be used in which a single readout laser is sent to the cavity in continuous-wave operation. The laser is tuned to cavity resonance ($\Delta = 0$), and as we derived in Section 4.1, the resulting sideband scattered photon count rate appearing at either the lower or upper frequency mechanical sideband ($\Delta = \pm\omega_m$) will be

$$\Gamma = \Gamma_\mathrm{noise} + \left(\frac{\kappa}{2\omega_m}\right)^2 \Gamma_{\mathrm{SB},0}\langle n\rangle. \tag{6.17}$$

With the sideband filters aligned to either of the mechanical sidebands of the cavity, the observed count rate is used to extract an equivalent occupancy $\langle n\rangle = n_\mathrm{p}$ at various pump powers n_c. The results are shown in Figure 6.7b (orange circles), exhibiting a power-law scaling of $n_\mathrm{p} = (7.94) \times n_\mathrm{c}^{1/3}$, in agreement with the model result in Equation 6.13 for a scaling of the bath occupancy with $n_\mathrm{c}^{1/3}$ in the limit of high bath temperature $T_\mathrm{p} \gg \hbar\omega_m/k_\mathrm{B}$. The right-hand axis of Figure 6.7 gives the effective bath temperature T_p corresponding to the measured occupancy.

At lower photon numbers $n_\mathrm{c} \lesssim 1$, the SNR of the counting of photons scattered from cavity resonance into either mechanical sideband begins to drop below 1, as for low bath occupancy we have $\Gamma_\mathrm{noise} = \Gamma_\mathrm{pump} + \Gamma_\mathrm{DCR} \sim \left(\frac{\kappa}{2\omega_m}\right)^2 \Gamma_{\mathrm{SB},0}\langle n\rangle$. In this regime, an alternative measurement method must be used in which the CW pump laser generates a steady-state optical-absorption bath while a second pulsed readout laser is used to probe the bath occupancy, as illustrated in Figure 6.6. The background pump laser is detuned to $\Delta/2\pi = 1$ GHz from the cavity resonance to minimize back-action as well as bleed-through counts through the sideband filters, which are aligned to $\Delta = 0$. The initial measured occupancy n_m^0 during the pulse is a measure

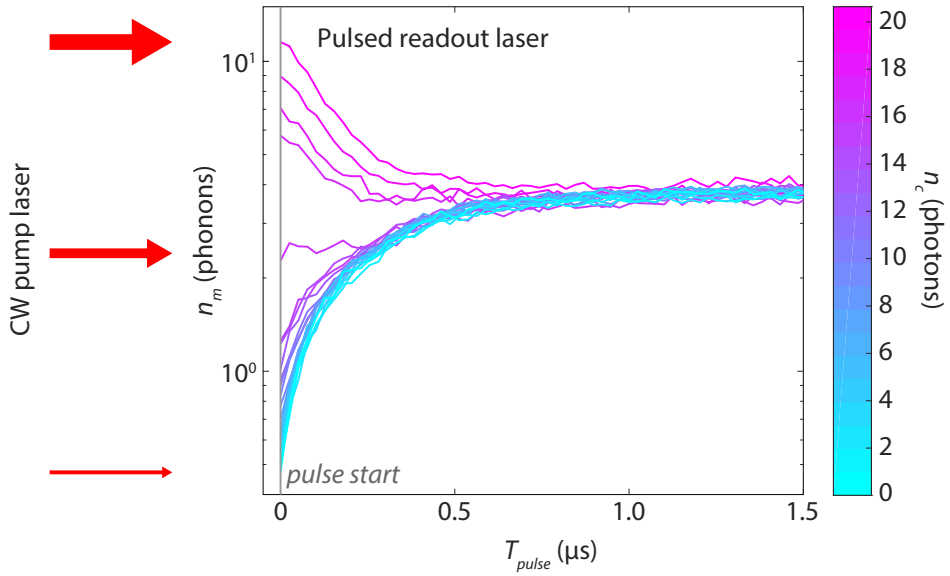

Figure 6.6: **Pulsed measurements of the bath occupancy in a low-Q nanobeam.** A continuous-wave background laser (red arrows, detuning $\Delta/2\pi \approx 1$ GHz) is used to generate a constant stead-state absorption bath, while a pulsed readout laser (readout $n_{\mathrm{c,readout}} = 50.6$) is used to probe the resulting bath occupancy for various background laser powers n_{c}. The initial measured occupancy during the pulse is given by $n_{\mathrm{m}}^0 \approx (n_{\mathrm{p}}\gamma_{\mathrm{p}} + n_0\gamma_0)/(\gamma_{\mathrm{p}} + \gamma_0)$ as described in the text. Measurements were performed on the zero-shield device detailed in Figure 6.7.

of the pump-induced bath occupancy, but it will include a small residual occupancy $\tilde{n}_0 \approx 0.04$ due to heating caused by the readout laser prior to the first measurement time bin of the pulse-on state. We define a corrected occupancy $n_{\mathrm{m}}^* \equiv n_{\mathrm{m}}^0 - \tilde{n}_0$ which denotes the measured mode occupancy which is coupled to the fridge bath as well as the absorption-bath induced by the pump laser:

$$n_{\mathrm{m}}^* = \frac{n_{\mathrm{p}}\gamma_{\mathrm{p}} + n_0\gamma_0}{\gamma_{\mathrm{p}} + \gamma_0}. \tag{6.18}$$

With n_0, γ_0, and the power-dependence of γ_{p} known from independent measurements, we can estimate the equivalent bath occupancy

$$n_{\mathrm{p}}(n_{\mathrm{c}}) = \frac{n_{\mathrm{m}}^*\gamma_{\mathrm{p}}(n_{\mathrm{c}}) + (n_{\mathrm{m}}^* - n_0)\gamma_0}{\gamma_{\mathrm{p}}(n_{\mathrm{c}})}. \tag{6.19}$$

The behavior of the effective bath occupancy n_{p} as a function of pump laser power n_{c} is shown in Figure 6.7b (purple squares), measured for a zero-shield device with

intrinsic damping rate $\gamma_0/2\pi = 14.1$ kHz. Again we find good agreement with a power-law scaling $n_\mathrm{p} \propto n_\mathrm{c}^{1/3}$ for $T_\mathrm{b} \gg \hbar\omega_m/k_\mathrm{B}$, consistent with the expectation that the phonon bath has a quasi-2D density of states. For $n_\mathrm{c} \lesssim 1$, $\gamma_\mathrm{p}(n_\mathrm{c}) \approx \gamma_0$ and the measured occupancy n_m^* will deviate substantially from n_p. In this range we have plotted n_m^* in translucent purple squares for clarity.

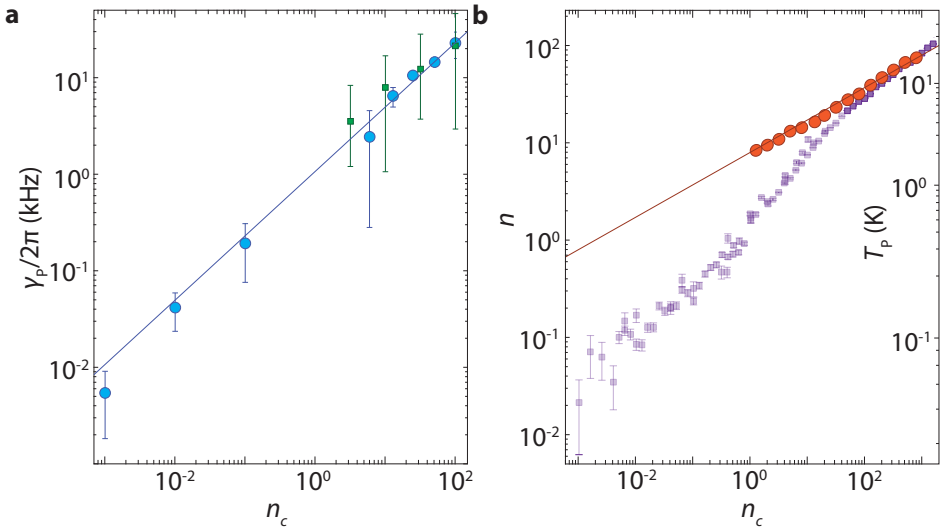

Figure 6.7: **Properties of the optical-absorption heating bath in the nanobeam OMC at low temperature.** **a**, Plot of γ_p versus n_c for six-shield (blue circles) and zero-shield (green squares) devices. The solid line is a power-law fit to the six-shield device data: $\gamma_\mathrm{p}/2\pi = (1.07\ \mathrm{kHz}) \times n_\mathrm{c}^{2/3}$. The zero-shield device has parameters $(\kappa, \kappa_\mathrm{e}, g_0, \omega_\mathrm{m}, \gamma_0) = 2\pi(1.507\ \mathrm{GHz}, 778\ \mathrm{MHz}, 713\ \mathrm{kHz}, 5.053\ \mathrm{GHz}, 14.1\ \mathrm{kHz})$. The six shield device has parameters $(\kappa, \kappa_\mathrm{e}, g_0, \omega_\mathrm{m}, \gamma_0) = 2\pi(1.13\ \mathrm{GHz}, 605\ \mathrm{MHz}, 713\ \mathrm{kHz}, 5.013\ \mathrm{GHz}, 0.21\ \mathrm{Hz})$. **b**, Plot of n_p versus n_c for zero-shield (purple symbols) and six-shield (orange circles) devices. Purple squares represent the measured mode occupancy corrected for heating induced by the readout laser tone. The right-hand axis gives the effective bath temperature T_p which corresponds to the measured bath occupancy. Translucent squares show data taken in the regime where the intrinsic decay rate γ_0 is comparable to the bath-induced damping γ_p, indicating that the raw measured occupancy begins to deviate substantially from the inferred occupancy given in the plot. The solid line is a fit to the six-shield data, giving $n_\mathrm{p} = (7.94) \times n_\mathrm{c}^{1/3}$.

A useful quantity when considering the magnitude of the heating and damping of the absorption-induced phonon bath may be defined as the effective heating rate per intracavity photon,

$$\beta_{\mathrm{p}} \equiv \frac{\gamma_{\mathrm{p}}(n_{\mathrm{p}}+1)}{n_{\mathrm{c}}} \sim \mathrm{cnst.}, \tag{6.20}$$

under the general assumption that the heating rate $\gamma_{\mathrm{p}}(n_{\mathrm{p}}+1)$ will be a linear function of the power input to the cavity. We will see in Section 6.5 that achieving large effective cooperativity in OMCs such as the nanobeam in the presence of power-dependent baths will be equivalent to achieving the condition

$$\beta_{\mathrm{p}} < \frac{4g_0^2}{\kappa} \tag{6.21}$$

while the bare cooperativity $C = \gamma_{\mathrm{OM}}/\gamma_0 > 1$. For the sake of comparison with further measurements presented in later chapters, we quote that the measured bath damping rates γ_{p} and occupancy n_{p} here correspond to $\beta_{\mathrm{p}} = 9.57$ kHz per photon. The best loaded optical Q-factors measured in nanobeam OMCs are about 7×10^5, with $g_0/2\pi \sim 1$ MHz, giving a per-photon back-action damping rate (for $\Delta = \pm\omega_m$) of $4g_0^2/\kappa \approx 14\,\mathrm{kHz} > \beta_{\mathrm{p}}$, however, for more typical device parameters with optical Q-factors of 3×10^5 and $g_0/2\pi = 800$ kHz, we have $4g_0^2/\kappa \approx 4$ kHz $< \beta_{\mathrm{p}}$. The optical-absorption heating bath continues to limit the utility of OMCs at low temperature for optical control of the acoustic mode at the level of single-phonons (although the optical thermometry sensitivity far exceeds the single-phonon limit). In Section 6.5 we discuss in greater detail the outlook for improving device performance in the presence of optical absorption, and in Chapter 8 we outline a path toward high cooperativity in steady-state using planar OMC designs based on quasi-2D photonic crystals, which have greatly enhanced thermal conductance to the silicon substrate compared to that of the nanobeam.

6.4 Coherent Excitation and Spectral Response of the Mechanical Mode

While the ringdown measurements presented in Figure 5.7 demonstrate a promising measurement of an extremely long microwave-frequency acoustic lifetime, they are limited to the regime of mechanical excitation on the level of individual phonons. Moreover, the mechanical element is excited via incoherent heating by the optical-absorption-induced local phonon bath, resulting in a population of thermal phonons with no phase coherence. Much can be learned from making analogous measurements of the mechanical lifetime for a coherently-excited population of phonons at large mechanical amplitude. First, it is well known that resonant TLS defects coupled to confined modes can become saturated at sufficiently high field amplitude,

and in scenarios in which resonant TLS limit the intrinsic damping rate, this can in principle lead to an enhanced mode lifetime. Second, observation of a consistent mode lifetime under multiple regimes of mechanical excitation can eliminate the possibility that the observed long-lived mechanical excitations are an indirect result of unwanted technical effects or global lattice heating, as substantially lower laser powers can be used to coherently excite the mechanics than are necessary to thermally excite the mode.

Additionally, the ultimate utility of a long-lived microwave acoustic mode such as those in these thin-film silicon OMCs for applications in storage of quantum information will depend upon achieving both a large thermal decoherence time τ_{th} (equivalently, a large energy decay time T_1) as well as a large dephasing time T_2^*. Previous measurements on nanobeam OMCs at milliKelvin temperatures have observed evidence of spectral diffusion of the mechanical mode at the level of 10 kHz [30]. Such measurements have typically been limited by the technical ability to probe the mechanical lineshape at sufficiently low optical pump powers, well below an intracavity photon number of order unity, where the mechanical frequency jitter rather than optical back-action damping is expected to dominate the time-averaged mechanical mode linewidth. Here we present measurements of the mechanical mode lineshape at sub-photon power levels and on rapid timescales (resolution bandwidths ~ 100 Hz), clearly indicating that the time-averaged mechanical mode spectral width of several kHz arises due to spectral diffusion of a narrow (300 – 500 Hz) instantaneous mechanical mode lineshape. The narrow intrinsic linewidth corresponds to a large intrinsic acoustic mode dephasing time $T_2 \sim 500$ μs. While it is difficult to directly measure this dephasing time using a Ramsey Echo or similar coherent detection scheme due to the presence of optical heating during excitation and read-out, and while we are limited to measurement power levels of order several 10^{-2} intracavity photons, these measurements represent a new ability to probe the mechanical decoherence time effectively "in the dark."

Blue-Detuned Pumping

In the limit of high phonon amplitude, we perform ringdown using a pulse sequence consisting of a blue-detuned excitation pulse followed by a red-detuned readout (or *probe*) pulse. Two separate laser sources are used, as shown in Figure 5.2, for generating the excitation and readout pulses in order to allow a fixed detuning of each laser to avoid instabilities associated with rapid stabilization of the laser frequency on the timescale of the pulse sequencing (tens of μs). Owing to the

extremely narrow instantaneous mechanical mode linewidth, a very small back-action amplification rate $\gamma_{\rm OM}/2\pi \lesssim 8$ Hz is required to drive the mechanics into the self-oscillation regime (see Section 6.6). This enables operation at low driving pulse photon number $n_{\rm c,blue} = 0.15 \gg n_{\rm c,thresh} = 2\times10^{-3}$, in order to minimize the effective temperature and coupling rate of the absorption-induced phonon bath. The steady-state phonon amplitude in the presence of the driving pulse is saturated to $\langle n\rangle \approx 5\times10^4$. The driving pulse is turned off and after a variable delay time $T_{\rm off}$ a red-detuned pulse from the readout laser is used to probe the mode occupancy.

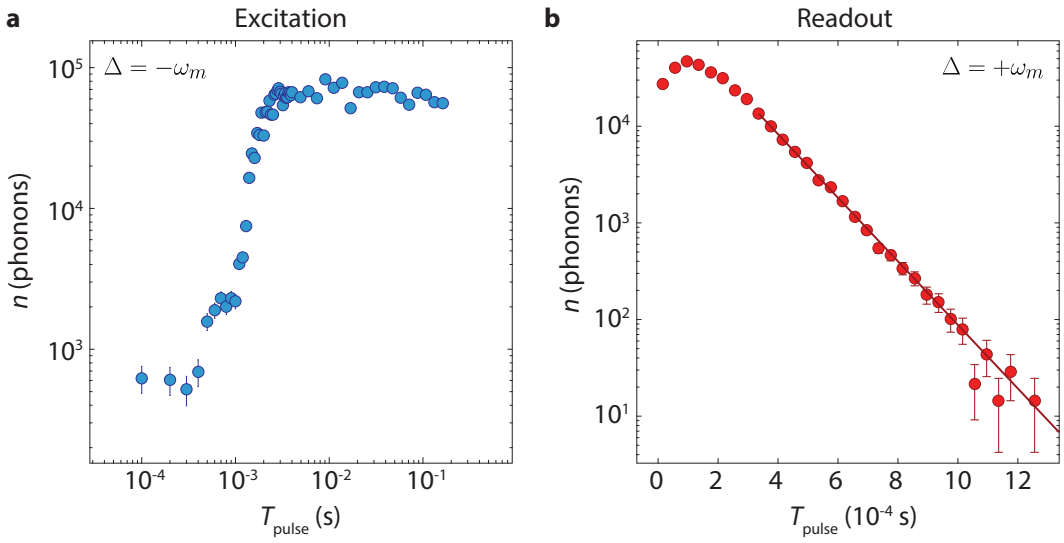

Figure 6.8: **Measurement of the mode occupancy during excitation and readout pulses for high-amplitude ringdown.** **a**, A blue-detuned ($\Delta = -\omega_m$) laser with pulse-on photon number $n_{\rm c,blue} = 0.15$ drives the mechanics into self-oscillation in a timescale of 2 ms, with a saturated phonon occupancy $\langle n\rangle \approx 5\times10^4$. **b**, a red-detuned ($\Delta = +\omega_m$) probe laser with pulse-on photon number $n_{\rm c,red} = 0.30$ serves to reads out the mode occupancy after a variable delay time $T_{\rm off}$. The probe laser cools and damps the mode at a measured rate $\gamma = \gamma_{\rm OM} + \gamma_{\rm p} = 2\pi(1.206)$ kHz (neglecting the small intrinsic decay rate γ_0), from which we extract a back-action damping rate of $\gamma_{\rm OM}/2\pi = 722$ Hz.

The readout photon number $n_{\rm c,red} = 0.30$ is again chosen small to minimize absorption bath effects, as well as to give a total count rate $\Gamma \propto \Gamma_{\rm SB,0}\langle n\rangle \propto n_{\rm c}\langle n\rangle$ within the dynamic range of the single-photon detector, which in our amplifier setup has sensitivity to a maximum count rate of $\sim 2\times10^6$ c.p.s. With the present setup efficiencies and device parameters (see caption of Figure 6.9), the detected count rate is approximately $\Gamma = 31$ c.p.s. per phonon per photon at $\Delta = \pm\omega_m$, and the resulting effective upper bound on $n_{\rm c,red}$ at which the SPD can efficiently detect is 2.2 photons. Now,

after the readout pulse is used to probe the mode occupancy, the mode occupancy is cooled via dynamical back-action to near its local bath temperature in preparation for the subsequent series of driving and readout pulses (effectively "re-setting" the measurement). In practice, a single red-detuned pulse is used for both readout and cooling (re-setting). The readout pulse-on photon number $n_{\mathrm{c,red}} = 0.30$ results in a back-action damping rate of $\gamma_{\mathrm{OM}}/2\pi \sim 1$ kHz, such that during a single pulse of duration $T_{\mathrm{red}} = 180$ μs an effective cooling factor of $e^{-T_{\mathrm{red}}\gamma_{\mathrm{OM}}} \approx 0.25$ is experienced by the mechanics. Combined with the free exponential decay occurring at a rate $\gamma_0/2\pi \approx 0.15$ Hz during the pulse period $\mathrm{T_{per}} = 4$ s, ($e^{-\gamma_0 \mathrm{T_{per}}} = 0.08$) we have an effective decay ratio of 50 between one readout pulse and the subsequent excitation pulse. In Figure 6.8 we show the phonon occupancy during both the driving pulse and the readout pulse. Note that the excited occupancy saturates to $\langle n \rangle \approx 5 \times 10^4$ from an initial occupancy $\langle n \rangle \lesssim 1 \times 10^3$, corresponding to our estimated decay ratio of 50 from one pulse period to the next. We also extract the true cooling rate $\gamma/2\pi = 1.206$ kHz during the readout pulse, where the overall cooling rate approximately obeys $\langle \dot{n} \rangle = -\gamma \langle n \rangle + \gamma_{\mathrm{p}} n_{\mathrm{p}}$, where $\gamma = \gamma_{\mathrm{OM}} + \gamma_{\mathrm{p}} + \gamma_0$. We estimate $\gamma_{\mathrm{p}}(n_{\mathrm{c,red}} = 0.30)/2\pi = 484$ Hz and $n_{\mathrm{p}}(0.30) = 5.3$ from Figure 6.7b, such that $\gamma_{\mathrm{p}} n_{\mathrm{p}} \ll \gamma \langle n \rangle$ and we may approximate the decay as an exponential, from which we extract the optomechanical cooling rate $\gamma_{\mathrm{OM}}/2\pi \approx 722$ Hz.

Using this method we find for a device having seven periods of acoustic shielding a decay rate $\gamma_0/2\pi = 0.146 \pm 0.027$ Hz, corresponding to a measured mechanical Q-factor of $Q = 3.60^{+0.82}_{-0.56} \times 10^{10}$, as shown in Figure 6.9 (error is given to a 90% confidence interval). Moreover, the decay is seen to be exponential over at least 1.5 orders of magnitude, indicating the absence of additional dynamical effects in that range, and consistent with the measured decay constant in similar seven-shield devices in the regime of thermal ringdown from a population of ~ 10 thermal phonons. The absence of a thermal lifetime enhancement relative to the mechanical decay at low phonon amplitude, as well as the exponential nature of the decay, suggests that the mechanical ringdown at low phonon amplitude is not limited by resonant TLS defects which may be saturated at large amplitude.

Modulated Pump-Probe Excitation and Ringdown

For finer control of the mechanical mode amplitude during excitation, microwave-frequency modulation of the excitation pulse was used to amplify the mechanics to a fixed phonon amplitude which is tunable by the depth of optical modulation placed on the pump laser tone. This technique allows us to probe the intrinsic

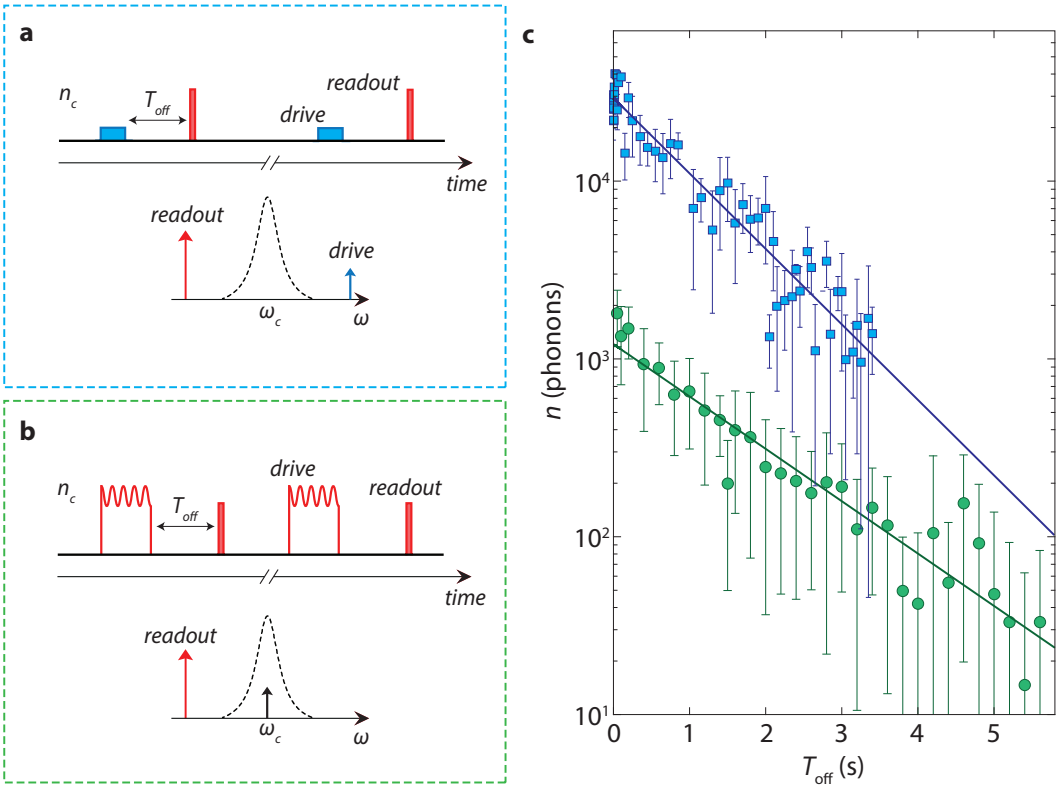

Figure 6.9: **Coherently-excited high-phonon-number ringdown.** **a**, A blue-detuned ($\Delta = -\omega_m$) driving pulse with pulse-on photon number $n_c = 0.15$ and duration $T_{blue} = 400$ ms excites the mechanics into self-oscillation to an initial phonon population of $\langle n \rangle = 2.93 \times 10^4$. The phonon population is probed after a variable delay time T_{off} using a red-detuned ($\Delta = +\omega_m$) readout pulse with pulse-on photon number $n_c = 0.30$ and duration $T_{red} = 180$ μs. **b**, A red-detuned pump laser is intensity-modulated with a modulation index of $\beta \sim 0.11$ to generate an intracavity photon number at the cavity frequency (the first-order modulated sideband) roughly equal to that at the pump frequency, $n_c = 1.3 \times 10^{-2}$. The driving pulse duration is fixed at 200 ms. A variable delay T_{off} sets the decay time before a 180 μs-long red-detuned probe laser is used to read out the phonon amplitude. In both the methods illustrated in **a** and **b**, the overall repetition rate $1/T_{per}$ is kept fixed as the delay T_{off} is varied, to eliminate the possibility of heating effects which are sensitive to the average power input to the cavity. **c**, Ringdown measurements performed by coherent excitation of the mechanics using blue-detuned pump (blue squares) and a modulated red-detuned pump (green circles). For blue-detuned driving, an initial phonon population of $\langle n \rangle = 2.93 \times 10^4$ is measured to decay with a rate $\gamma_0/2\pi = 0.146$ Hz. For modulated-pump driving, an initial occupation of $\langle n \rangle = 1.2 \times 10^3$ decays with a rate $\gamma_0/2\pi = 0.108$ Hz, corresponding to a mechanical Q-factor of 4.92×10^{10} ($\tau_{th} = 1.47$ s). Device parameters are: (κ, κ_e, ω_m) = 2π (575 MHz, 131 MHz, 5.31 GHz).

energy decay constant γ_0 in the regime lying intermediate between the level of single-phonons and the saturated high-phonon-amplitude limit of self-oscillation. In this measurement scheme, a radio-frequency (RF) signal generator is used to drive an electro-optic intensity modulator (EOM) at the mechanical resonance frequency $\omega_m/2\pi$ to generate the probe sideband. The excitation pulse consists of a red-detuned pump carrier tone which is weakly modulated (RF driving power -4 dBm applied to an EOM with $V_\pi = 4.1$ V, giving a modulation index $\beta = 0.11$) to generate a probe sideband at the cavity resonance frequency. Interference between the pump carrier and probe sideband generates a time-dependent radiation pressure force at the difference frequency $\omega_m/2\pi$, which resonantly excites the acoustic mode. A second pulsed laser source is then used to generate the readout optical pulse, which is a red-detuned pulse of fixed frequency and power. Using this method as shown in Figure 6.9, we measure an initial excited mechanical occupation of $\langle n \rangle = 1.2 \times 10^3$ having a decay rate $\gamma_0/2\pi = 0.108$ Hz at the lowest temperatures $T_\mathrm{f} = 10$ mK, corresponding to a mechanical Q-factor of 4.92×10^{10} ($\tau_\mathrm{th} = 1.47$ s). The decay is observed to be exponential over at least 1.5 orders of magnitude, consistent with measurements in both the high- and low-phonon number limit.

In both the case of blue-detuned driving and RF-modulated driving ring-up techniques, the total repetition rate of the pulse sequence $1/\mathrm{T_{per}}$ is fixed while only the variable delay $\mathrm{T_{off}}$ between the driving pulse and readout pulse is varied. This fixing of the overall duty-cycle of the pulse sequence is performed to eliminate systematic variations in the local absorption-induced bath temperature T_b which, in steady-state, is expected to depend on the average power circulating in the cavity (see Section 6.3). We find that the measured ringdown time constant is approximately consistent over more than three orders of magnitude in starting phonon population, from $\langle n \rangle \lesssim 10$ in the case of thermally-excited ringdown measurements to $\langle n \rangle > 2 \times 10^4$ in the case of coherently-excited phonon populations.

Spectral Mechanical Response and Mechanical Frequency Jitter

In Section 5.4 we presented spectral measurements of the acoustic mode at $T_\mathrm{f} = 10$ mK using a measurement of the electromagnetically-induced transparency performed using SPDs. Such a spectral measurement is one avenue for probing the dephasing coherence time T_2 of the mechanical mode at low pump powers. At the lowest temperatures, T_2 is likely limited by spectral diffusion (frequency jitter) of the mechanical mode arising from coupling of the breathing mode to the local hot-phonon bath at elevated temperature T_b. The measurement technique presented

below allows for rapid probing of the mechanical response function, limited to resolution bandwidths of order 100 Hz. A series of rapid measurements of the mechanical spectrum shows an instantaneous mechanical linewidth narrower than 300 Hz which is likely limited by measurement back-action rather than intrinsic spectral diffusion. Jitter of this spectrally narrow mechanical response over a range of several kHz results in a broadened time-averaged mechanical response with a characteristic Voigt lineshape, modeling Gaussian spectral diffusion.

A closer look at the ringing-up technique presented in the previous section is warranted, in which we aim to compute the phonon amplitude and count rates resulting from weak modulated input tones to the cavity. Consider the mechanical amplitude in the presence of an optical input tone modulated at frequency ω, given by Equation 5.10:

$$\beta = \frac{-ig_0(\alpha_0^*\alpha_-) + \sqrt{\gamma_i}\beta_{\rm in}}{-i(\omega - \omega_m) + \frac{\gamma_i}{2}}, \tag{6.22}$$

where as before we have assumed that the optical pump α_0 is not depleted by interactions with the mechanics, that is, that $|\alpha_0| \gg |\alpha_-|$, where α_- is the optical modulated sideband amplitude. Then the phonon occupancy is given by

$$\langle n \rangle = |\beta|^2 = \frac{g_0^2|\alpha_0^*\alpha_-|^2 + \gamma_{\rm i}|\beta_{\rm in}|^2}{(\omega - \omega_m)^2 + (\frac{\gamma_{\rm i}}{2})^2}, \tag{6.23}$$

where the frequency-dependence of the mechanical response is given by the mechanical susceptibility $|\chi_b(\omega)|^2 = ((\omega - \omega_m)^2 + (\gamma_{\rm i}/2)^2)^{-1}$ and the magnitude has contributions both from the beating of the optical input tones and from thermal noise. At greater modulation depths of the input tone where the intracavity fields satisfy $\alpha_- \sim \alpha_0$, the above result is no longer valid. Here the fully nonlinear equations of motion must be solved exactly to estimate the steady-state phonon occupancy. Consider the Heisenberg-Langevin equations of motion for classical field amplitudes:

$$\dot{\alpha} = -\left(i\Delta + \frac{\kappa}{2}\right)\alpha - ig_0\alpha(\beta^* + \beta) + \sqrt{\kappa_{\rm e}}\alpha_{\rm in}, \tag{6.24}$$

$$\dot{\beta} = -\left(i\omega_m + \frac{\gamma_i}{2}\right)\beta - ig_0|\alpha|^2 + \sqrt{\gamma_i}\beta_{in}. \tag{6.25}$$

We numerically integrate Equations 6.25 for the case of a modulated input drive to obtain the theoretical curve shown in Figure 6.10, showing good quantitative agreement with the measured phonon occupancy dynamics during the ringing-up pulse. For the experimental system parameters used in the measurements, a steady-state phonon occupancy of $\langle n \rangle \approx 350$ is reached for driving pulse durations $> 160\ \mu$s.

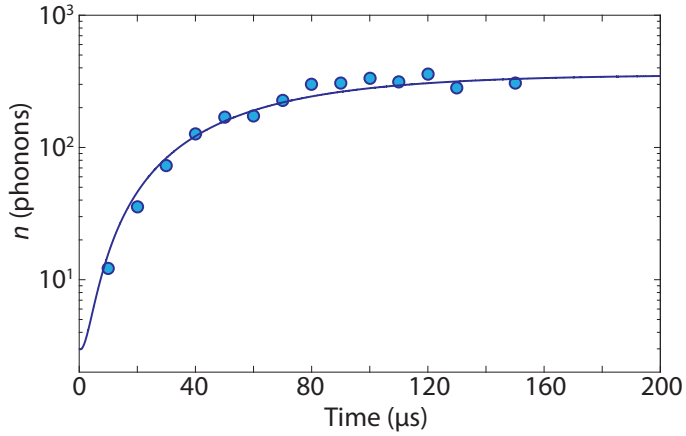

Figure 6.10: **Dynamics of the phonon occupancy under modulated driving ring-up.** Measurement of the phonon occupancy as a function of time during a modulated probe ringing-up pulse. The carrier tone at $\Delta = +\omega_m$ and the modulated sideband tone at $\Delta = 0$ populate equal intracavity photon numbers $n_{cav,0} = n_{cav,1} = 0.11$. The solid line is a numerical result obtained by integrating the Heisenberg-Langevin equations of motion with no free fitting parameters, using known setup efficiencies and EOM $V_\pi = 4.1$ V. Device parameters are: $(\kappa, \kappa_e, \omega_m, g_0, \gamma_0) = 2\pi(575$ MHz, 131 MHz, 5.31 GHz, 980 kHz, 0.11 Hz).

Measurements of the spectral response of the mechanical mode can be made by sweeping the modulation frequency ω through mechanical resonance while observing the reflected photon count rate at cavity resonance. The EIT transparency response generated by the mechanical motion is observed as a peak in the reflected count rate under modulation near the mechanical resonance, as described in Chapter 5.4. The instantaneous resonant response of the mechanics has a Lorentzian lineshape given by the mechanical susceptibility $\chi_b(\omega)$, including broadening due to intrinsic spectral diffusion. Figure 6.11 shows several individual rapid frequency scans in which the mechanical response is observed as a modification to the optical reflection from the cavity. The vertical axis in these scans is the normalized reflection contrast of the mechanical response peak. Jitter of the mechanical frequency occurs on timescales faster than the measurement time required to record an individual frequency scan (here 8 s), but sufficiently slowly that quasi-instantaneous

narrow mechanical peaks of bandwidth $\lesssim$ 300 Hz are observable, consistent with the expected magnitude of back-action induced broadening due to the pump tone (pump power level $n_{\mathrm{c,pump}} = 0.1$ photons). The corresponding lower bound to the intrinsic acoustic mode dephasing time is $T_2 \gtrsim 500$ μs. Technical improvements to the detection setup will be necessary to resolve the mechanical lineshape to resolution finer than about 100 Hz. The time-averaged mechanical response is shown in Figure 6.12. The time-averaged spectral response of the mechanics fits well to a Voigt lineshape, described by Gaussian spectral diffusion of a Lorentzian intrinsic response, where the total mechanical bandwidth is $\gamma/2\pi = 5.41$ kHz ($T_2^* = 29$ μs).

The likely source of the residual mechanical frequency jitter is coupling to the optically-induced phonon bath at elevated local temperature. We confirm that measurements of the time-averaged mechanical response linewidth and center frequency are largely insensitive to the environmental fridge temperature in the range from < 10 mK to ~ 1 K, as shown in Figure 6.13, consistent with a model in which the local temperature fluctuations driving mechanical frequency jitter are dominated by the local phonon bath induced by optical absorption. Another proposed mechanical of spectral diffusion is coupling to TLS defects. However, well-known models of contributions to spectral diffusion of non-resonant TLS predict shifts much smaller than the observed linewidths [108]. Resonant TLS may also introduce spectral diffusion, but such an effect is expected to be strongly temperature-dependent, and is inconsistent with the small changes of order $\sim$ kHz in the center frequency and linewidth we observe for temperatures below 1 K.

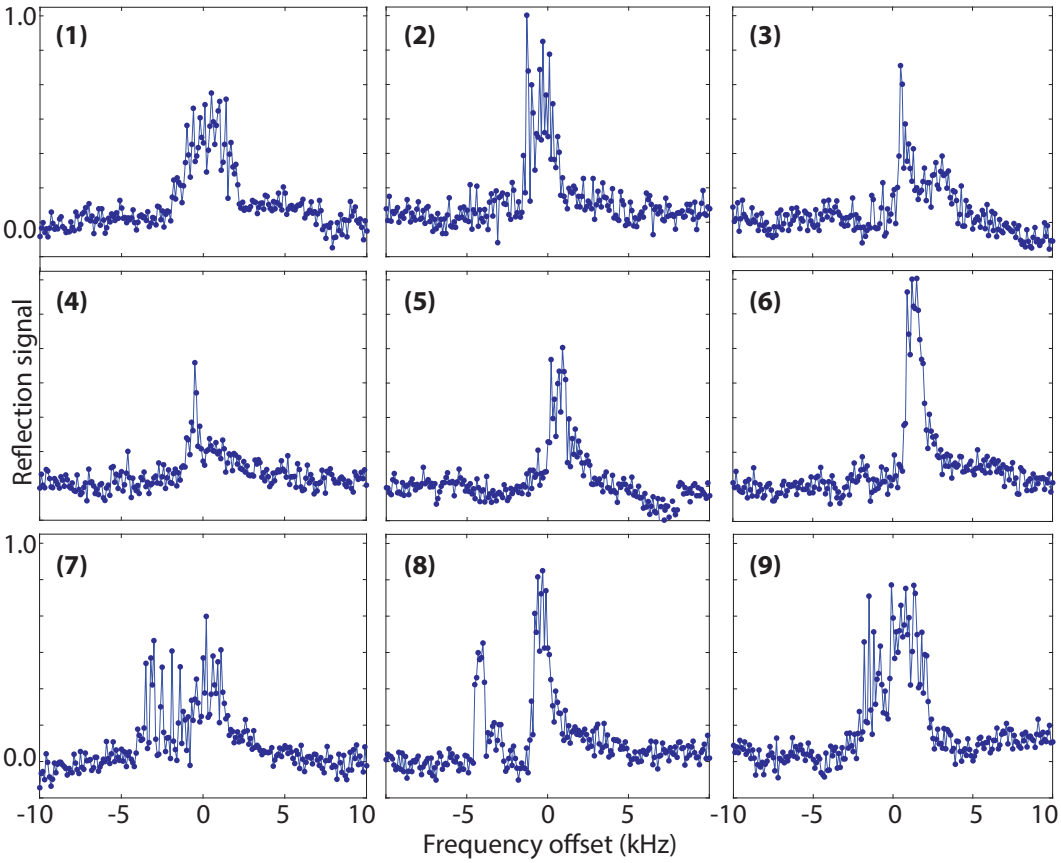

Figure 6.11: **Rapid measurements of the mechanical response spectral diffusion at T_f = 10 mK using pump-probe excitation.** Plots (1) through (9) are representative individual frequency scans in which the reflection contrast above the bare optical cavity background is plotted versus probe modulation frequency (offset to the nominal mechanical resonance frequency $\omega_\mathrm{m}/2\pi$ = 5.31 GHz). Jitter of the instantaneous mechanical frequency during the 8 s measurement time for each scan appears as a distribution of one or many individual narrow mechanical response peaks (bandwidth $\lesssim$ 300 Hz) over a full range of about 5 kHz. The narrow quasi-instantaneous mechanical linewidth of bandwidth $\lesssim$ 300 Hz (see scans (3), (4)) is consistent with estimates of the pump-induced optomechanical back-action at this power level. Frequency scans were taken with pump power $n_\mathrm{c,pump}$ = 0.1, probe power $n_\mathrm{c,probe} = 10^{-2}$, frequency resolution 100 Hz, and frequency step dwell time 10 ms. All plots have identical horizontal and vertical scales. The long-time average of many individual frequency sweeps is shown below in Fig. 6.12. Device parameters are the same as those in Fig. 6.10.

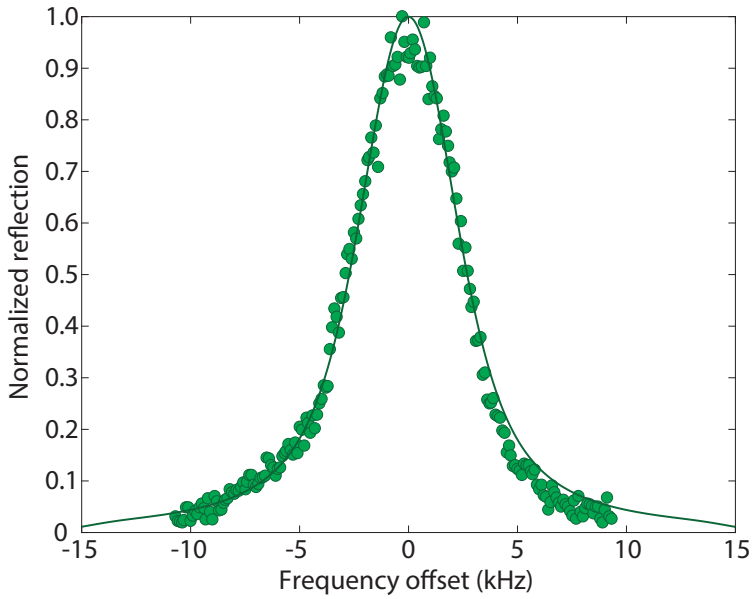

Figure 6.12: **Time-averaged mechanical spectral response at $T_\mathbf{f}$ = 10 mK.** A coherently-modulated excitation tone of pump power $n_{\mathrm{c,pump}} = 0.1$ and probe power $n_{\mathrm{c,probe}} = 10^{-2}$ resonantly excites the mechanical response. Spectral diffusion of the narrow mechanical response as illustrated in Fig. 6.11 fits well to a Voigt lineshape (solid green line), arising due to Gaussian spectral diffusion of a Lorentzian response function. The extracted full-width at half-max is $\gamma/2\pi = 5.41$ kHz. Device parameters are the same as those in Fig. 6.10.

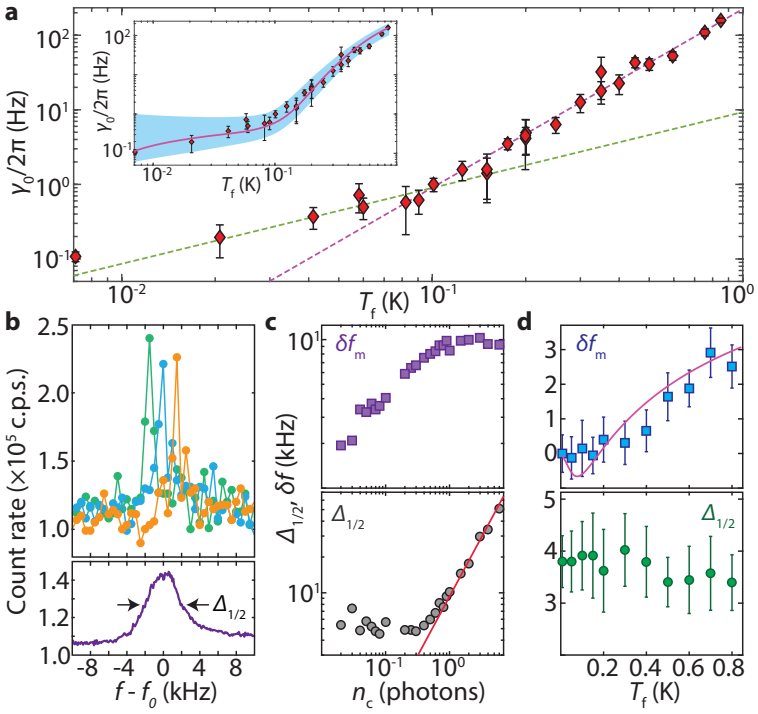

Figure 6.13: **Temperature dependence of acoustic damping, frequency, and frequency jitter.** a, Plot of the measured breathing mode energy damping rate, $\gamma_0/2\pi$, as a function of fridge temperature (T_f). Dashed green (magenta) curve is a fit with temperature dependence $\gamma_0 \sim T_\mathrm{f}^{1.01}$ ($\gamma_0 \sim T_\mathrm{f}^{2.39}$). Error bars are 90% confidence intervals of the exponential fit to measured ring down curves. Inset: Plot of measured damping data with estimated energy damping from a TLS model. The shaded blue region corresponds to the standard deviation of $\log(\gamma_0/2\pi)$ for 100 different random TLS distributions. **b**, Two-tone coherent spectroscopy signal. Upper plot: three individual spectrum of rapid frequency sweeps with a frequency step size of 500 Hz and dwell time of 1 ms (RBW $\approx$ 0.5 kHz). Lower plot: average spectrum of rapid scan spectra taken over minutes, showing broadened acoustic response with FWHM linewidth of $/2\pi$ = 4.05 kHz. The large on-resonance response corresponds to an estimated optomechanical cooperativity of $C \equiv \gamma_\mathrm{OM}/(\gamma_0 + \gamma_\mathrm{p}) \gtrsim 1.1$, consistent with the predicted magnitude of back-action damping $\gamma_\mathrm{OM}/2\pi \approx 817$ Hz and bath-induced damping $\gamma_\mathrm{p}/2\pi \approx 120$ Hz at the measurement pump power level $n_\mathrm{c} = 0.1$. **c**, Breathing mode resonance frequency shift and ensemble average FWHM-linewidth as a function of pump photon number n_c. Solid red curve is fit to back-action limited linewidth, yielding $g_0/2\pi$ = 1.15 MHz. **d**, Measured δf (upper plot) and (lower plot) versus T_f. Error bars are 90% confidence intervals from Voigt fit to measured spectra. The solid magenta curves in the inset of (**a**) and top panel of (**d**) corresponds to simulations of a single random TLS distribution.

6.5 Optomechanical Cooperativity

The utility of cavity optomechanical systems for performing coherent quantum operations between the optical and mechanical degrees of freedom is ultimately predicated upon the ability to simultaneously achieve $\langle n \rangle \ll 1$ and large cooperativity $C \equiv \gamma_{\mathrm{OM}}/\gamma_{\mathrm{b}}$, where $\gamma_{\mathrm{b}} = \gamma_0 + \gamma_{\mathrm{p}}$ is the total coupling rate between the mechanical resonator and its thermal baths. In the specific example of optomechanically mediated coherent transfer of photons between optical and superconducting microwave resonators [84, 85], the relevant figure of merit is the effective cooperativity $C_{\mathrm{eff}} \equiv C/n_{\mathrm{b}}$, where n_{b} is the effective bath occupancy defined such that $\gamma_{\mathrm{b}} n_{\mathrm{b}} = \gamma_0 n_0 + \gamma_{\mathrm{p}} n_{\mathrm{p}}$ [23]. The effective cooperativity must be much larger than unity in order to achieve low-noise photon conversion at the single quantum level [19, 87]. Explicitly, the effective cooperativity is

$$C_{\mathrm{eff}} = \frac{\gamma_{\mathrm{OM}}}{\gamma_0(n_0 + 1) + \gamma_{\mathrm{p}}(n_{\mathrm{p}} + 1)}, \tag{6.26}$$

with the +1 terms in the denominator arising from spontaneous decay. Using the measured absorption-heating bath occupancy and damping rates, we calculate an inferred effective cooperativity for the zero-shield and six-shield nanobeam devices summarized in Figure 6.7. The cooperativities calculated for these devices are shown in Figure 6.14. The relationship between C and C_{eff} is clarified by considering three regimes of driving power (equivalently, of n_{c}), and the ratio C_{eff}/C. As C_{eff} is necessarily less than C, we define an error term $0 < \epsilon < 1$ by $C_{\mathrm{eff}} = C(1 - \epsilon)$. It is straightforward to show that

$$\epsilon = 1 - \frac{C_{\mathrm{eff}}}{C} = \frac{1}{1 + \frac{\gamma_0 + \gamma_{\mathrm{p}}}{\gamma_0 n_0 + \gamma_{\mathrm{p}} n_{\mathrm{p}}}}. \tag{6.27}$$

From inspection of the form of ϵ, we can identify a regime of low n_{c} when $\gamma_{\mathrm{p}} n_{\mathrm{p}} \ll \gamma_0 n_0$, or approximately $\beta_{\mathrm{p}} n_{\mathrm{c}} \ll \gamma_0 n_0$, valid for $n_{\mathrm{c}} \ll \gamma_0 n_0/\beta_{\mathrm{p}}$. In this regime, ϵ simplifies to $\epsilon \approx n_0$, and we have $C_{\mathrm{eff}}/C \approx 1 - n_0$, where the small fridge bath occupancy is measured to be $n_0 = 1.1 \times 10^{-3}$. For intermediate $n_{\mathrm{c}} \sim n_0 \gamma_0/\beta_{\mathrm{p}}$, we can write the effective cooperativity as

$$C_{\mathrm{eff}} = \frac{C_0}{n_0 + 1 + \frac{\beta_{\mathrm{p}}}{\gamma_0} n_{\mathrm{c}}} \approx \frac{C_0}{1 + \frac{\beta_{\mathrm{p}}}{\gamma_0} n_{\mathrm{c}}}, \tag{6.28}$$

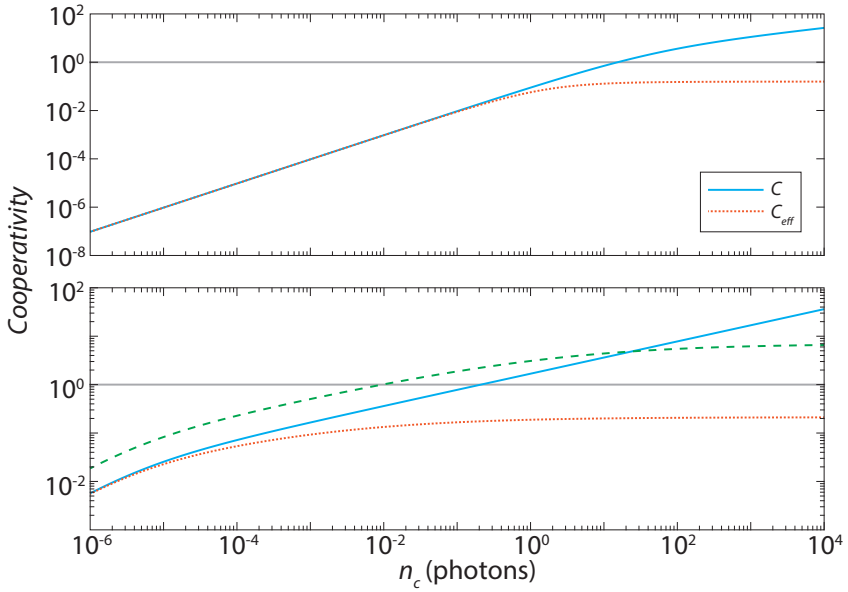

Figure 6.14: **Cooperativity in quasi-1D OMCs at low temperature.** Plots of the calculated bare optomechanical cooperativity C (solid blue lines) and effective cooperativity $C_{\rm eff}$ (dotted orange lines) for a zero-shield (upper plot, $\gamma_0/2\pi$ = 14.1 kHz) and a six-shield (lower plot, $\gamma_0/2\pi$ = 0.21 Hz) device, inferred using the bath scaling parameters presented in Figure 6.7. Device parameters are the same as those in Figure 6.7. The dashed green line shows an optimistic theoretical projection of $C_{\rm eff}$ for a device similar to the six-shield nanobeam but with the bath scaling $\beta_{\rm p}$ reduced by a factor of 10. Horizontal gray lines represent $C, C_{\rm eff} = 1$. In the high-$n_{\rm c}$ limit, due to the linear scaling of the bath heating rate $\gamma_{\rm p} n_{\rm p}$ with $n_{\rm c}$ in the linear-optical absorption model, $C_{\rm eff}$ saturates to an approximately constant $\langle n \rangle^{-1} \approx 4g_0^2/(\kappa\beta_{\rm p})$ while C scales like $\gamma_{\rm OM}/\gamma_{\rm p} \sim n_{\rm c}^{1/3}$.

where $C_0 \equiv \gamma_{\rm OM}/\gamma_0$ is the cooperativity in the absence of the optical-absorption bath and we have neglected the small term n_0. This intermediate-$n_{\rm c}$ regime is the regime in which the (fractional) difference ϵ between $C_{\rm eff}$ and C becomes appreciable, or in other words, in which the heating-induced bath damping becomes commensurate with the damping due to the fridge-temperature bath. The location of this crossover regime as a function of $n_{\rm c}$ scales linearly with γ_0, as illustrated in Figure 6.14, making explicit the fact that for ultra-high-Q modes the quantity of interest in the context of performing quantum coherent operations is $C_{\rm eff}$ for pump photon numbers down to $n_{\rm c} \lesssim 10^{-4}$. In the limit of high $n_{\rm c} \gg \gamma_0/\beta_{\rm p}$, we have a simple expression

$$C_{\rm eff} \approx \frac{C_0}{1 + \frac{\beta_{\rm p}}{\gamma_0} n_{\rm c}} \approx \frac{C_0}{\frac{\beta_{\rm p}}{\gamma_0} n_{\rm c}} = \frac{\gamma_{\rm OM}}{\beta_{\rm p} n_{\rm c}} = \frac{4g_0^2}{\kappa\beta_{\rm p}}. \tag{6.29}$$

Comparing this to the expression for the steady-state mode occupancy in the presence of back-action cooling [109]:

$$\langle n \rangle = \frac{\gamma_\mathrm{p} n_\mathrm{p} + \gamma_0 n_0}{\gamma_\mathrm{OM} + \gamma_\mathrm{p} + \gamma_0} \underset{C \gg 1}{\approx} \frac{\beta_\mathrm{p} n_\mathrm{c}}{\gamma_\mathrm{OM}}, \tag{6.30}$$

we have the approximate relation $C_\mathrm{eff} = 1/\langle n \rangle$ in the high-n_c limit [19]. In order to achieve coherent quantum operations in the $C_\mathrm{eff} > 1$ regime, we require $\beta_\mathrm{p} n_\mathrm{c} < \gamma_\mathrm{OM}$, or equivalently,

$$\beta_\mathrm{p} < \frac{4 g_0^2}{\kappa}, \tag{6.31}$$

where we recognize the quantity $4g_0^2/\kappa$ as the per-photon rate of dynamical back-action damping in the case of detuning to either mechanical sideband of the cavity ($\Delta = \pm\omega_m$). Typical nanobeam devices achieve $4g_0^2/\kappa \sim 4$ kHz per photon, while the best individual devices may exceed $4g_0^2/\kappa \sim 15$ kHz per photon, and for the devices measured in this work the bath heating parameter $\beta_\mathrm{p} = 9.57$ kHz per photon and our maximum effective cooperativity in steady-state driving is estimated to be $C_\mathrm{eff} = 0.21$. In order for future devices to achieve $C_\mathrm{eff} > 1$ in the presence of continuous-wave pumping, then, one or more routes must be pursued to increase the ratio of $\gamma_\mathrm{OM}/n_\mathrm{c}$ to β_p. Directly improving the optical quality factor and optomechanical coupling rate are viable routes to increasing the rate of back-action per photon (or, per unit input power to the cavity). Quasi-2D planar photonic crystal devices have been shown to exhibit optical Q-factors exceeding 9×10^6 [110]. Co-integrating a GHz-frequency mechanical resonance with large optomechanical coupling with the photonic crystal defect restrains the optical cavity design, preventing a direct adaptation of the optical design from Ref. [110]; however, preliminary measurements within the Painter Group of planar quasi-2D OMC cavity defects have shown optical Q-factors exceeding 5×10^5 while maintaining an optomechanical coupling rate as large as $g_0/2\pi \approx 1.1$ MHz to a 10 GHz acoustic cavity mode. Further improvements to the nanofabrication processes of such devices may enable yet higher optical Q-factors; more detail will be given in Chapter 8. A major additional benefit of moving to quasi-2D OMC designs is the corresponding increase in thermal conductance between the localized cavity volume and the bulk silicon through a factor of ~ 30 increase in contact area to the bulk, allowing better thermalization of the high-frequency bath at elevated temperature T_b to the surrounding fridge-temperature bath at $T_\mathrm{f} \approx 7$ mK. It should also be possible to directly reduce the linear

absorption coefficient η ($= P_{\mathrm{abs}}/P_{\mathrm{in}}$) through further improvements to the silicon surface passivation and cleaning. In particular, minimizing the duration of native oxide growth on the sample surface between the final fabrication undercutting step and mounting into the dilution fridge vacuum chamber should reduce the presence of electronic defect states at the material surface which serve as sub-bandgap absorption centers for the pump light [111, 112]. Additionally, we note that the Landau-Rumer scattering processes by which the phonon bath modes are populated via phonon-assisted relaxation of the surface electronic states yield a scaling of the effective bath temperature with the material anharmonicity $A(\omega;\omega_m)$ (see Equation 6.10). It is therefore possible in principle to directly reduce the bath temperature by choosing a less anharmonic substrate material.

6.6 Ultra-Low-Threshold Self-Oscillation

Owing to the extremely slow intrinsic damping rate γ_0 observed in the ultra-high-Q nanobeam devices at low temperature, it is possible to drive the mechanics into the regime of self-sustained oscillations with a blue-detuned pumping laser at very low input optical powers, or equivalently, a very low rate of measurement back-action. The total effective damping rate experienced by the mechanics in the presence of a blue-detuned drive laser is $\gamma = \gamma_{\mathrm{i}} - \gamma_{\mathrm{OM}}$, where the intrinsic damping rate $\gamma_{\mathrm{i}} = \gamma_0 + \gamma_{\mathrm{p}}$ includes damping γ_0 from both the cold fridge bath (with occupancy $n_0 \approx 10^{-3}$) and from the optical absorption-induced phonon bath at rate γ_{p}. The usual condition for self-oscillation is that the damping rate is matched by the back-action amplification rate γ_{OM}:

$$\gamma_{\mathrm{OM}} = \gamma_0 + \gamma_{\mathrm{p}}. \tag{6.32}$$

We observe the onset of mechanical self-oscillation at $T_{\mathrm{f}} = 10$ mK similar to the results presented in Figure 4.2 at room temperature, in which a CW blue-detuned pump laser ($\Delta = -\omega_m$) drives the cavity and the sideband filters are aligned to the cavity resonance ($\Delta = 0$). The scattered photon count rate $\Gamma_{\mathrm{SB},0}$ is measured in steady-state. In the setup configuration used for these measurements, an additional VOA is placed in the optical path, elevating the measured SPD dark count rate to 10.8 c.p.s. Sweeping the input power (photon number) n_{c} results in a sharp increase in detected count rate at the self-oscillation threshold $n_{\mathrm{c,thresh}} = 2 \times 10^{-3}$ as shown in Figure 6.15, where we estimate the resulting steady-state phonon occupancy to be of order $\langle n \rangle \sim 5 \times 10^4$. At the threshold $n_{\mathrm{c,thresh}}$ we can estimate the back-action

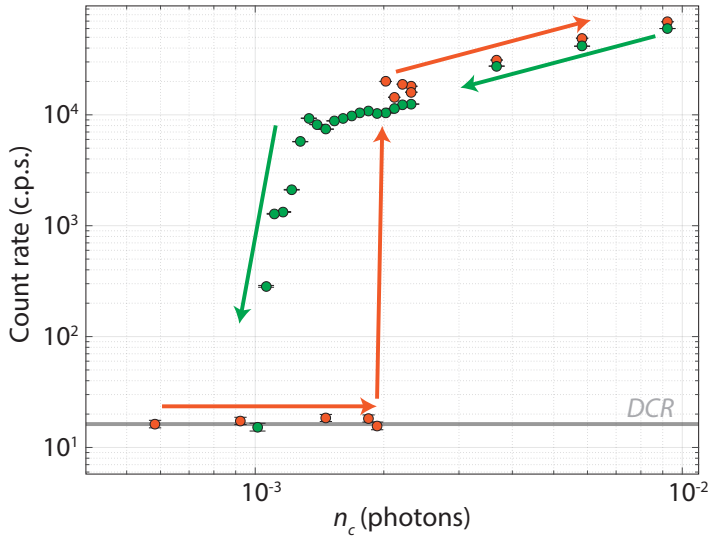

Figure 6.15: **Low-temperature measurement of the self-oscillation threshold in a high-Q nanobeam at $T_\mathrm{f} = 10$ mK.** Under blue-detuned ($\Delta = -\omega_m$) driving the self-oscillation threshold is reached when $\gamma_\mathrm{OM} = \gamma_\mathrm{i}$, here for $n_\mathrm{c,thresh} = 2 \times 10^{-3}$, or $\gamma_\mathrm{OM}/2\pi = 8$ Hz, for increasing optical power (orange points). Device parameters are: $(\kappa, \kappa_\mathrm{e}, \omega_\mathrm{m}, \gamma_0) = 2\pi$ (575 MHz, 131 MHz, 5.31 GHz, 0.108 Hz).

amplification rate $\gamma_\mathrm{OM}/2\pi = 4g_0^2 n_\mathrm{c,thresh}/\kappa \approx 8$ Hz from the known optical device parameters, indicating that the intrinsic damping γ_i is dominated by the bath damping rate: $\gamma_\mathrm{p}(n_\mathrm{c,thresh}) = \gamma_\mathrm{OM}(n_\mathrm{c,thresh}) - \gamma_0 \approx 2\pi(7.9)$ Hz, in good quantitative agreement with the trend measured on a similar device in Figure 6.7a. Upon decreasing the driving power (purple data in Figure 6.15), self-oscillation appears to relax at a decreased threshold of $n_\mathrm{c} = 1.4 \times 10^{-3}$, indicating a hysteresis in the measured count rates as a function of input power. This apparent hysteresis likely arises from a change in the *true* intracavity photon number as a function of driving power P_in. We have so far adhered to Equation 3.12 in determining the n_c as a function of P_in; this expression is used to generate the horizontal axis of Figure 6.15, and so does not represent the true intracavity photon number. However, in order to unambiguously calculate n_c in the presence of large phonon amplitude $\langle n \rangle$, a more thorough calculation is needed which accounts for the effective optical reflection profile in the presence of strong modulation by the mechanical motion.

Chapter 7

PHONON DECAY AND DECOHERENCE AT LOW TEMPERATURE

Implicit in the foregoing discussion has been the understanding that constructing a perfect mechanical oscillator in the laboratory is not attainable, but that it would be technologically and scientifically useful to make a best approximation of such an oscillator. In the context of nanoscale optomechanical devices, we are motivated to construct mechanical oscillators with the longest possible timescales for energy decay and decoherence. There are two main reasons for this. First, as an element for quantum state storage in future hybrid device architectures, the mechanical degree of freedom must retain excitations for timescales much longer than the time required for state preparation and manipulation tasks. The storage lifetime $\tau_{\rm th}$ sets an effective length scale $c\tau_{\rm th}$ over which entangling operations may be performed, so the mechanical lifetime directly constrains the distribution of entanglement in quantum networks using mechanical elements at its nodes. Second, minimization of incoherent loss channels for the mechanics directly corresponds to increased control of the mechanics by externally applied (e.g., optical or microwave) fields. Specifically, the optomechanical cooperativity per photon increases linearly with the mechanical lifetime.

It is generally understood that any realistic device as measured in a laboratory setting will suffer from some source of energy damping, decoherence, noise, disorder, or environmental factors which will cause any physical oscillator to fall short of the ideal harmonic oscillator. If we wish to construct an oscillator having properties as close to ideal as possible, it will be helpful to first consider the fundamental reasons why such a truly ideal oscillator is non-physical. In this context, an ideal oscillator is one having a perfectly well-defined periodic resonant frequency and an infinite response to resonant driving. First and foremost, we realize that an idealized linear harmonic oscillator exists in a perfectly harmonic potential, whereas a physical mechanical oscillator invariably exists within a nonlinear potential. At some finite amplitude of oscillation, the inter-atomic or inter-molecular restoring forces will reveal their nonlinearities, or else the finite material boundaries will modify the local potential.

Thus material nonlinearity is deeply related to fundamental performance limits of mechanical oscillators. In the measurements presented in this thesis, we have studied nanomechanical resonators in a setting which attempts to minimize the presence of unwanted channels of loss and decoherence. The key elements of this setting are: (1) The choice of material. Single-crystal silicon has minimal impurities, dopants, crystal defects, and material boundaries introducing disorder. (2) Low-temperature operation. Thermal noise is reduced. (3) Vacuum. Scattering of gas molecules from the resonator surface is minimized. (4) Acoustic bandgap clamping. Radiation loss to the sample bulk is eliminated. (5) Optical probing. No electrodes are present nor mechanical contact made to the oscillator under study. Optical measurements are designed to be as minimally invasive as possible with respect to the mechanical oscillator.

In this chapter we will explore the regimes of acoustic energy damping and phonon decoherence which are present in OMC devices at low temperature, under which conditions the phonon energy damping is not limited by radiation of ballistic phonons into the substrate bulk through the acoustic bandgap shield. We demonstrate that these devices allow us to probe interactions between the strain field in silicon and two-level system (TLS) tunneling state defects at GHz frequencies, as well as to observe additional regimes of damping characterized by multi-phonon scattering events and thermoelastic damping. Quantitative comparisons will be made between the measured damping rate in a high-Q nanobeam breathing mode at low temperatures and the predicted damping rates due to theoretical models of the listed damping mechanisms. The results of these analyses are summarized in Figure 7.1. At temperatures below 300 mK, a linear scaling of Q^{-1} with temperature is consistent with a proposed model of strain coupling to an ensemble of TLS defects themselves coupled to a phonon bath of one-dimensional density of states. Above 300 mK, three-phonon scattering processes involving phonons above the nanobeam cutoff frequency can contribute significantly to the damping.

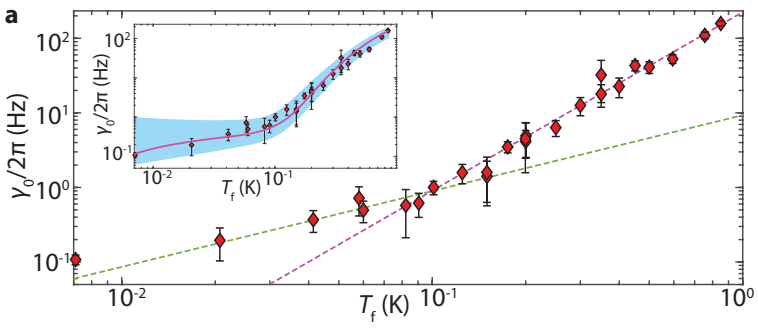

Figure 7.1: **a**, Plot of the measured breathing mode energy damping rate, $\gamma_0/2\pi$, as a function of fridge temperature (T_f). Dashed green (magenta) curve is a fit with temperature dependence $\gamma_0 \sim T_\mathrm{f}^{1.01}$ ($\gamma_0 \sim T_\mathrm{f}^{2.39}$). Error bars are 90% confidence intervals of the exponential fit to measured ring down curves. Inset: Plot of measured damping data with estimated energy damping from a TLS model. The shaded blue region corresponds to the standard deviation of $\log(\gamma_0/2\pi)$ for 100 different random TLS distributions.

7.1 Mechanical Quality Factor: A Closer Look

Consider an ideal mechanical oscillator with position $x(t)$, damping rate γ, and resonance frequency ω_0. Its equation of motion is simply

$$\ddot{x}(t) + \gamma\dot{x}(t) + \omega_0^2 x(t) = 0. \tag{7.1}$$

If we search for periodic solutions of the form $x(t) = x_0 e^{-i\omega t+\phi}$ given some initial amplitude x_0 and phase ϕ, we obtain a quadratic equation for the oscillation frequency:

$$\omega^2 + i\gamma\omega - \omega_0^2 = 0, \tag{7.2}$$

which has a physical solution $\omega = (\omega_0^2 - \gamma^2/4)^{1/2} - i\gamma/2$ (the non-physical solution corresponds to anti-damping). Using this expression for ω, we see that the solution for the oscillator position is $x(t) = x_0 exp[-it\sqrt{\omega_0^2 - \gamma^2/4} - (\gamma/2)t + \phi]$, which evidently decays at a rate $\gamma/2$. To quantify the damping of energy, the mechanical *quality factor* Q is defined by [113]

$$Q \equiv 2\left|\frac{\mathrm{Re}\{\omega\}}{\mathrm{Im}\{\omega\}}\right| = \frac{\sqrt{\omega_0^2 - \gamma^2/4}}{\gamma} \approx \frac{\omega_0}{\gamma}. \tag{7.3}$$

The factor of 2 comes from the fact that the oscillator energy scales like the average of x^2, and the approximation is valid when $Q \gg 1$. Conceptually, the Q-factor is equal to the fraction of energy lost per radian of vibration. In the context of traveling elastic waves in a solid, it is also convenient to define a corresponding attenuation length l_e, the propagation distance which corresponds to an energy decay to $1/e$ its initial value: $l_e = 2v/\gamma$, where v is the phase velocity of the traveling wave or acoustic mode.

Generally, a large number of independent damping channels interact with the oscillator. If the various damping mechanisms are well approximated as being independent, then their effects add incoherently and result in a single overall damping parameter $\gamma \sim Q^{-1}$. The overall quality factor can then be deconstructed into various contributions:

$$Q^{-1} = Q_A^{-1} + Q_B^{-1} + Q_C^{-1} + \dots. \tag{7.4}$$

In this chapter we will examine various such damping mechanisms and discuss how these damping mechanisms contribute to the overall mechanical losses in our devices in different temperature regimes.

7.2 Thermoelastic Damping

Thermoelastic damping is a fundamental source of energy damping in mechanical resonators over many orders of magnitude in size scale [114]. First theoretically studied in detail by Zener in the 1930s [115, 116], thermoelastic damping (TED) arises from local fluctuations in temperature generated by strain fields in solids. Strain fields generated by either traveling waves in a solid or by normal modes result in regions of compression and rarefaction in the solid. If the timescale of the strain field is sufficiently slow, these strain gradients yield local variations in temperature which tend to thermalize among themselves via nonlinear phonon interactions, resulting in entropic dissipation of energy from the mode of interest. Experimental evidence for TED begain in 1990 with measurements by Roszhart [117].

The coupling between strain and temperature fields necessarily occurs in materials with a nonzero linear coefficient of thermal expansion:

$$\alpha = \frac{1}{L}\frac{\partial L}{\partial T} \neq 0, \tag{7.5}$$

but in order for TED to become appreciable in its damping of a mechanical mode, it is necessary that the frequency of the strain field variations be slow compared to that of the thermal phonons generated by local temperature fluctuations. In other words, the mean free path of the thermal phonons must be much smaller than the wavelength of the mode of interest,

$$l_{\text{th}} \ll \lambda_m, \tag{7.6}$$

allowing one to define a local temperature field $\theta(\mathbf{r}, t)$ in the material. This is referred to as the *diffusive thermal phonon regime*. Even in this regime and in the presence of nonzero α, not all elastic waves experience TED. In particular, early studies aimed at finding analytical expressions for the attenuation and dispersion of elastic waves [118, 119, 120] showed that transverse elastic waves (which do not generate local density changes) do not experience TED, while longitudinal waves do. Zener developed a general theory of the anelastic solid [121], in which the Young's modulus is taken to have an equilibrium value E and an *adiabatic* or *unrelaxed* value E_{ad}. In this model, Hooke's law relating the stress τ and strain ϵ is generalized to [113, 121]

$$\tau + \tau_\epsilon \frac{d\tau}{dt} = E\left(\epsilon + \tau_\tau \frac{d\epsilon}{dt}\right), \tag{7.7}$$

where τ_ϵ and τ_τ are characteristic time constants related to the unrelaxed and relaxed Young's modulus by $E_{\text{ad}} = (\tau_\tau/\tau_\epsilon)E$. Normal mode solutions to Zener's Equation 7.7 give rise to approximate expressions for the damping Q^{-1} due to thermoelastic relaxation. In the particular case of rectangular beam under flexure, Zener arrived at $Q^{-1} \approx \omega\bar{\tau}\Delta/(1 + \omega^2\bar{\tau}^2)$, where $\Delta = (E_{\text{ad}} - E)/E$. Later work by Lifshitz and Roukes [114] generalized Zener's early results and concluded with an exact analytical expression for the damping Q^{-1} of a flexural beam mode:

$$Q^{-1} = \frac{E\alpha^2 T_0}{C}\left(\frac{6}{\xi^2} - \frac{6}{\xi^2}\frac{\sinh\xi + \sin\xi}{\cosh\xi + \cos\xi}\right), \tag{7.8}$$

where $\xi = b\sqrt{\omega_{\text{m}}/(2\chi)}$, b is the beam width, χ is the material thermal diffusivity, and C is the heat capacity. An analysis of the maximum Q^{-1} due to TED is Si flexural beams of various aspect ratios is given in Ref. [114], where the authors find that at temperatures below 10 K, typically $Q^{-1} \ll 10^{-10}$. TED is ruled out

as a limiting factor in the low-temperature acoustic damping rate of the nanobeam, although at room temperature TED is expected to limit the damping rate [32].

7.3 Phonon-Phonon Scattering Processes

Anharmonicity in the atomic potential in crystalline solids is responsible for a number of material phenomena which would otherwise not be present in a linear system governed by a perfectly harmonic potential. These effects include thermal expansion and — arising from phonon-phonon scattering events — modified phonon relaxation rates [122] and reductions in lattice thermal conductivity at low temperature [105, 123]. Early theoretical work studying the impact of phonon-phonon scattering events due to material anharmonicity was typically aimed at identifying scaling laws as a function of temperature and frequency for phonon relaxation times [106, 124, 125] or to reconcile experimental observations of decreased thermal conductivity in crystalline semiconductors at low temperature with the fact that a simple harmonic potential calculation of the lattice thermal condutivity diverges [123, 125]. Herring in 1954 [125] obtained a fairly comprehensive catalogue of approximate scalings for the single-phonon relaxation time τ at low temperature due to cubic anharmonicity in a variety of crystal lattice configurations, in which $\tau \sim \omega^a T^{5-a}$ for some constant a. In a cubic lattice such as silicon, $a = 2$ and one obtains the scaling $\tau \sim T^3$ commonly referenced as a signature of phonon-phonon scattering in the low-temperature limit. In the silicon nanobeam, the modified local density of phonon states is expected to substantially modify the temperature scaling behavior of the phonon relaxation time τ at low temperature. We have performed theoretical modeling as outlined below to calculate the impact of phonon-phonon scattering processes on decay of the acoustic breathing mode, and compare the results to measured decay times at various temperatures from $0.010 - 4$ K.

The precise relative importance of different proposed mechanisms of nonlinear phonon energy damping at GHz-THz frequencies have never been fully understood, even in ubiquitous material systems such as Si or AlN, due to the presence of extrinsic effects such as surface scattering or clamping losses and the difficulty of obtaining quantitative theoretical predictions in specific device geometries. In view of the expanding role of nano- and micro-mechanical oscillators in sensing applications ranging from detection of charge and spin to ever-weaker forces and smaller masses [126, 127], increased theoretical attention [114, 128, 129] has lately been directed toward *ab initio* calculations of the energy damping rates and dephasing experienced by confined and surface phonon modes in the presence of anharmonic

phonon-phonon interactions. Of particular importance is the phonon decay regime first identified by L. D. Landau and G. Rumer in 1937 [130], in which anharmonicity in the atomic potential gives rise to three-phonon scattering processes. In this *Landau-Rumer* regime, the frequency ω of the mode of interest is large compared to the thermalization rate $1/\tau_{\text{th}}$ of local thermally excited phonons, $\omega\tau_{\text{th}} \gg 1$. This constraint allows the assumption that during the decay of a single phonon in the mode of interest, the surrounding thermal phonons approximately remain in thermal equilibrium–otherwise known as the single-mode relaxation regime. In the alternative *Akhiezer* regime, in which the thermal phonon relaxation time is short compared to the mode frequency $\omega\tau_{\text{th}} \ll 1$, the mode of interest perturbs the local thermal phonon populations giving rise to entropy-driven relaxation as the thermal phonons return to equilibrium [131]. At GHz frequencies in Si, Akhiezer damping is expected to be the dominant nonlinear phonon scattering process at room temperature [132] while at cryogenic temperatures relevant to the measurements presented here, Landau-Rumer scattering becomes the dominant anharmonic damping mechanism as a result of decreased thermal excitation of high-frequency phonons satisfying $\omega\tau_{\text{th}} \gg 1$.

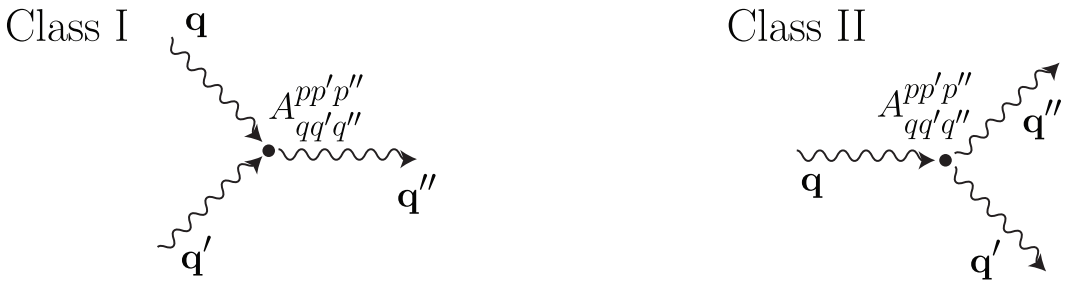

Figure 7.2: **Landau-Rumer decay processes.** Three-phonon-mixing decay processes may be either Class I or Class II. The scattering matrix element A is dependent upon the scattering phonon wave-vectors and polarizations. Due to the reduced density of states at low frequency in the quasi-1D nanobeam structure, Class I processes are expected to dominate over Class II.

Recent experimental studies of phonon lifetimes in Si have provided some quantitative validation of the Landau-Rumer theory for three-phonon scattering processes and Akhiezer damping for modes in the GHz-THz range, both for confined phonon modes [122, 132, 133] and for surface acoustic/Rayleigh waves [134], and have suggested that confined cavity-acoustic modes may have longer lifetimes than bulk modes of similar frequencies [133]. In the nanobeam OMC, the thin-film Si imposes a bottle-neck cutoff frequency in the vicinity of $\omega_{\text{C}}/2\pi \gtrsim v_l/(2t_b) \approx 20$ GHz,

where $v_l = 8.433$ km/s is the longitudinal-phonon velocity in Si and $t_b = 220$ nm is the membrane thickness. For temperatures well below the corresponding cutoff temperature $T_C = \hbar\omega_C/(\ln(2)k_B) = 1.3$ K, the thermal phonon density of states is reduced below the 3D Debye density of states (Sections [ref earlier bottleneck and bath damping sections]). Consequently the effective temperature of the breathing mode, $\hbar\omega_m/(\ln(2)k_B) = 346$ mK, does not necessarily demarcate a transition between the Landau-Rumer and Akhiezer regimes, but rather at temperatures well below T_C we expect $\omega\tau_{th} \gg 1$ while at temperatures well above T_C we expect a transition to the Akhiezer regime with $\omega\tau_{th} \ll 1$. In the low-temperature limit it is possible to calculate the energy relaxation time τ_{LR}^{-1} due to three-phonon scattering processes for comparison with the measured temperature-dependent damping rate γ_0 for the acoustic breathing mode of a nanobeam with acoustic bandgap shielding. To first order in perturbation theory, where the lowest-order anharmonic term in the Hamiltonian is given by $\hat{H}_3$, the scattering rate is given by Fermi's Golden Rule:

$$W_{qq'q'} = \frac{2\pi}{\hbar}|\langle f|\,\hat{H}_3\,|i\rangle|^2\delta(E_f - E_i), \tag{7.9}$$

where the delta function imposes energy conservation for each scattering event and the notation $\hat{H}_3$ indicates that the perturbing Hamiltonian is the lowest-order term of cubic order in the atomic coordinates. At temperatures well below the Debye temperature it is safe to neglect terms of higher perturbative order which correspond to four-phonon scattering events [135]. The resulting phonon relaxation rate can be written within the single-mode relaxation approximation, assuming a linear Boltzmann transport equation, as a sum of transition rates of the form in Equation 7.9. Specifically, Ref. [123] conceptually identifies the inverse relaxation time τ_{LR}^{-1} as

$$\tau_{LR}^{-1} = -\lim_{N_0 \to N_0^0} \frac{(dN_0/dt)_c}{N_0 - N_0^0}, \tag{7.10}$$

where N_0 is the occupancy of the relaxation mode, $(dN_0/dt)_c$ is the total rate of change of N_0 due to scattering, and N_0^0 is the thermal equilibrium value of N_0. Given expressions for the anharmonic scattering matrix elements of $\hat{H}_3$ (some such are given in Ref. [136]), one may use Equation 7.9 to calculate τ_{LR}^{-1} directly. In practice, the scattering rates will be expanded using approximate expressions for the matrix elements, $A_{qq'q''}^{pp'p''}$, where $\mathbf{q}$ is the wave-vector of the mode of interest (mode 0), $\mathbf{q}'$ and $\mathbf{q}''$ for the thermal scattering phonons, and p, p', p'' represent the phonon

mode polarizations (either longitudinal or transverse). The resulting phonon decay rate is calculated in Ref. [122], and can be expressed as

$$\tau_{\mathrm{LR}}^{-1} = \frac{\pi\hbar}{4\rho_{\mathrm{Si}}^3 N_0 \omega_{qp}} \sum_{q'p',q''p''} \Bigg[|A_{qq'q''}^{pp'p''}|^2 \frac{qq'q''}{v_p v_{p'} v_{p''}} \tag{7.11}$$

$$\times \left\{ \frac{n_{q'p'}(n_{q''p''}+1)}{n_{qp}+1} \delta(\omega_{qp} + \omega_{q'p'} - \omega_{q''p''}) \delta_{q+q',q''+G} \right. \tag{7.12}$$

$$\left. + \frac{1}{2} \frac{n_{q'p'} n_{q''p''}}{n_{qp}} \delta(\omega_{qp} - \omega_{q'p'} - \omega_{q''p''}) \delta_{q+G,q'+q''} \right\} \Bigg]. \tag{7.13}$$

Here $\mathbf{G}$ is the total change in crystal momentum during a scattering event, n are the equilibrium mode occupancies, and v are the corresponding mode group velocities. The first term curly brackets represents mixing of mode 0 with another phonon to produce a higher-frequency phonon, satisfying energy conservation with $\hbar(\omega_{qp} + \omega_{q'p'}) = \hbar\omega_{q''p''}$ (a Class I event in the language of Ref. [103]). The corresponding momentum-change condition is $\mathbf{q} + \mathbf{q}' = \mathbf{q}'' + \mathbf{G}$. The second term in brackets represents the decay of mode 0 into two lower-lying modes, with energy conserved according to $\hbar\omega_{qp} = \hbar(\omega_{q'p'} + \omega_{q''p''})$ and momentum change condition $\mathbf{q} + \mathbf{G} = \mathbf{q}' + \mathbf{q}''$ (Class II event). At low temperatures is it generally assumed that elastic scattering processes for which $\mathbf{G} = 0$, called Normal (N-type), are dominant over inelastic ($\mathbf{G} \neq 0$, Umklapp, U-type) scattering processes due to the low energy of the thermal phonons involved in scattering [132]. Additionally, in considering phonon relaxation in the nanobeam, we restrict our attention to Class I scattering events due to the diminished density of phonon states at low frequency. Confinement of the modes at frequencies below the acoustic radiation shield bandgap results in a quasi-discrete band-structure, greatly suppressing the scattering rates of phonons into these modes relative to the modes at elevated frequency with wavelengths small compared to the characteristic dimensions of the nanobeam.

Expressions for the anharmonic interaction matrix elements $A_{qq'q''}^{pp'p''}$ are derived by Refs. [103, 128] in terms of material parameters, and can be expressed as

$$|A_{qq'q''}^{pp'p''}|^2 = \frac{4\rho_{\mathrm{Si}}^2}{\bar{v}^2} \gamma^2 v_p^2 v_{p'}^2 v_{p''}^2, \tag{7.14}$$

where γ is the mode-averaged Grüneisen parameter [137] and $\bar{v}^2 = (2v_t^2 + v_l^2)/3$ is the squared sound velocity averaged over mode polarizations. Simplifying the expression Equation 7.13 is in general extremely difficult due to the nontrivial dispersion relations for the thermal phonon modes [128]. To obtain analytical results for the phonon lifetime, a simplified Debye model is typically used in which the scattering phonons are assumed to follow a linear dispersion. In this case, a simplified expression for the three-phonon scattering damping rate is given by [122]:

$$\gamma_{3\text{-ph}} = \frac{\hbar\omega_\mathrm{m}}{4\pi\rho_\mathrm{Si}\bar{v}^2}\gamma^2 \sum_{p',p''} \frac{1}{v_{p'}^2 v_{p''}^2} \int_{s',s''} \omega'_{s'}\, \omega'^2_{s'}(\omega_\mathrm{m}+\omega'_{s'})^2 \frac{n(\omega'_{s'})[n(\omega''_{s''})+1]}{n(\omega_\mathrm{m})+1}. \quad (7.15)$$

Equation 7.15 can be numerically integrated making a simple change of variables, $x \equiv \hbar\omega/(k_\mathrm{B}T)$. Figure 7.3 shows the calculated damping rate $\gamma_{3\text{-ph}}$ due to three-phonon scattering in the nanobeam, where we have assumed like Ref. [122] that scattering involving only longitudinal modes dominates the damping rate. The numerical prefactor in Equation 7.15 is modified by a correction factor $\eta = 0.52$ to obtain a best fit to the measured damping, but agreement within a factor of 2 indicates strong quantitative agreement between the physical model and measurement data.

In the Akhiezer regime ($\omega\tau_\mathrm{th} \ll 1$), an analogous calculation can be made for the relaxation time τ_Akh^{-1} due to Akhiezer processes. Ref. [132] gives a simplified expression,

$$\tau_\mathrm{Akh}^{-1} = \frac{CT}{\rho_\mathrm{Si} v_l^2} \frac{\omega^2\tau_\mathrm{th}}{\omega^2\tau_\mathrm{th}^2+1}(\langle\gamma^2\rangle - \langle\gamma\rangle^2), \quad (7.16)$$

where C is the volumetric heat capacity, γ is the Grüneisen parameter, and $\langle\cdot\rangle$ represents an average over modes.

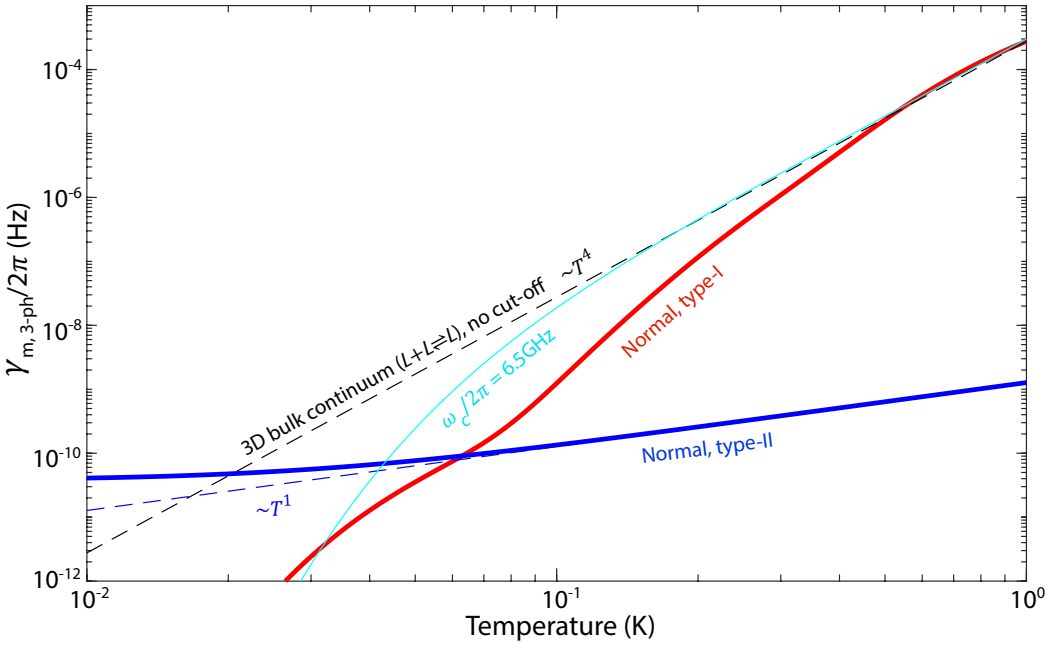

Figure 7.3: **3-phonon scattering model.** Simulation of the acoustic damping due to 3-phonon scattering of the localized breathing mechanical mode with other quasi-modes of the OMC cavity structure. Both type I (solid red curve) and type II (solid blue curve) scattering processes involving the breathing mode are modeled. For comparison, we also plot the estimated 3-phonon-scattering damping rate due to type-I processes for longitudinally polarized phonons ($L + L \rightleftharpoons L$) in bulk Si. For the bulk simulation we plot the estimated damping rate without a low-frequency cut-off (dashed black curve), and with a low-frequency cut-off (solid cyan curve) corresponding to the top of the first phononic bandgap ($\omega_c/2\pi = 6.5$ GHz). In all cases we only include Normal scattering processes, and neglect Umklapp scattering, due to the low temperature range considered ($T \lesssim 1$ K).

7.4 Strain Coupling to Two-Level Systems

At the lowest temperatures studied in this work, the phonon damping is likely dominated by strain coupling to non-resonant tunneling states (TS) with energies lying below the bandgap of the acoustic shielding. The presence of these TS in both amorphous and crystalline materials has been shown to account for universal temperature-scaling laws of thermal conductance at low temperature, as well as modifications to the energy damping rate and speed of sound in these materials [138, 139, 140, 141], and arises from local microscopic variations in the material properties in the form of atomic and molecular displacements or impurities. When modeled as two-level system (TLS) tunneling states, or fluctuators, these defects are generally described by a double-well potential experienced by some local degree of

freedom present in the material, for which the energy splitting of the double well is labeled by an asymmetry energy Δ and the effective tunneling barrier between the wells is given by Δ_0. In general, such TLS tunneling states result in local variations in the dissipative environment of a confined electromagnetic or acoustic mode, and can be modeled to produce an effective dipole moment (or as the case may be, an effective strain dipole moment) which couples to the field of a mode of interest to introduce energy damping and phase/frequency noise. Substantial theoretical work has been devoted to predicting the impact of TLS defects on confined modes [142], both electromagnetic and acoustic, as they often limit the performance of MEMS and NEMS devices in systems which rely on quantum coherent interactions ranging from superconducting quantum circuits to electro- and opto-mechanical metrology applications.

The microscopic defects which are likely origins of TLS are typically of a size scale much smaller than either an acoustic or electromagnetic mode wavelength in experiment, so a simple dipole approximation is typically used to describe coupling between the TLS and the mode of interest. Dissipation from the mode of interest then arises through a number of possible channels. A distribution of TLS may couple either resonantly or non-resonantly to a local bath of additional modes in its environment, serving as a leaky channel for energy decay between the mode of interest and the environment. In our nanobeam device, it is expected that amorphous glassy material at the surface of the nanobeam houses a distribution of TLS with a large number of defects having energy below the bandgap of the acoustic shield. The amorphous material is likely due to etch-damage in the outermost $10 - 20$ nm of silicon caused during device fabrication [50, 143], as well as a thin (~ 200 pm) native silicon oxide grown at the silicon surface. In this energy regime below the acoustic bandgap, as discussed in Section 6.3, the local density of states of phonon modes transitions to an effectively one-dimensional density of states, and we will therefore constrain the physical model of TLS-induced damping of the breathing mode to modeling the TLS as coupled to a 1D density of phonon states at the lowest temperatures. Previous experimental studies [102] have found evidence of a linear scaling between the energy damping rate and temperature for low-temperature nanomechanical resonators in which the dominant phonon bath exhibits a 1D density of states, and we observe a similar scaling in measurements of the nanobeam OMC. At elevated temperatures $T > \hbar\omega_C/k_B$ above the phonon bottleneck cutoff frequency of $\omega_C/2\pi \sim 20$ GHz, thermally populated phonon states occupying a 3D Debye density of states are coupled to the TLS, and the scaling of the TLS-induced

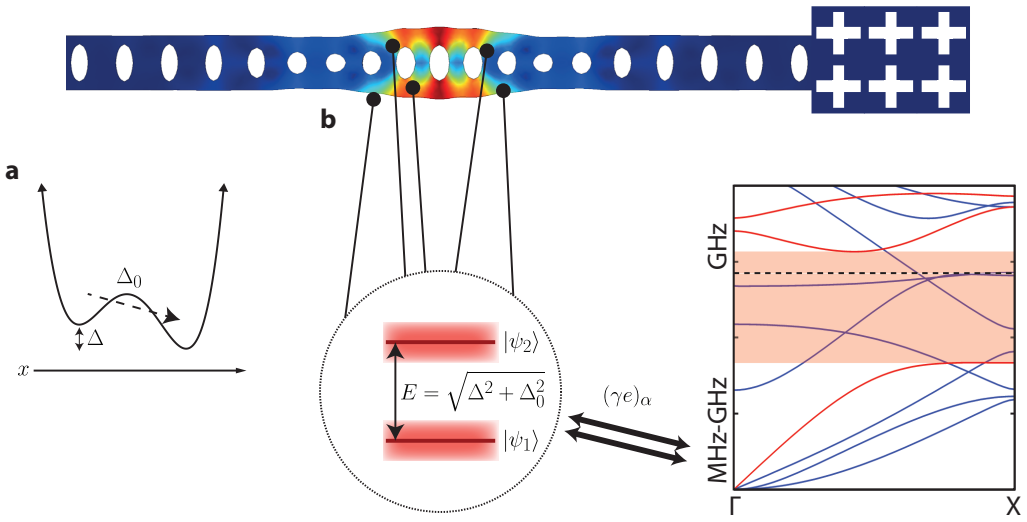

Figure 7.4: **Illustration of the two-level system (TLS) tunneling state material defects present in the nanobeam OMC. a**, TLS modeled as a double-well potential with respect to a microscopic configuration coordinate x. The defect is described by an asymmetry energy Δ and effective tunneling energy Δ_0. **b**, In the nanobeam OMC, TLS are present in the amorphous surface layer material. In the energy representation the two lowest-lying states of the defect, $|\psi_1\rangle$ and $|\psi_2\rangle$, are separated in energy by $E = \sqrt{\Delta^2 + \Delta_0^2}$. A distribution of low-lying defects with energy below the acoustic shield bandgap is coupled with an effective strain-coupling constant γe (dependent on the acoustic mode polarization α) to a local quasi-1D bath of phonon modes as well as to the breathing mode, acting as a leaky channel for energy relaxation and dephasing of the breathing mode. Band structure adapted from Ref. [20].

damping is modified relative to the case of a quasi-1D density of states.

These TLS fluctuators are typically present in some distribution in energy scales (Δ, Δ_0), and therefore a key ingredient in effectively modeling the energy damping induced by the presence of TLS will be to make an estimate of the density and distribution of TLS as a function of (Δ, Δ_0). The distribution function $f = f(\Delta, \Delta_0)$ is usually taken to be broad and symmetric in Δ as a result of the intrinsic symmetry of the potential well modeling the TLS. In amorphous materials, the scale of energies Δ is also estimated from the scale of energy available at the glass transition temperature of the material, typically 100 – 1000 K [139]. These energy scales are much larger than the energy scales of the experiment at milliKelvin temperatures, and hence it is usually assumed that f is effectively independent of Δ for cryogenic studies. The dependence of f on the tunneling energy parameter Δ_0 will be specific to the material and the local material environment in question, but a usual choice is

$f(\Delta, \Delta_0) = P/\Delta_0$ for a constant defect density P. This choice of distribution function is justified on the grounds that the tunneling energy will depend exponentially on an effective tunneling length λ, and that even small variations in λ arising from the microscopic forms of the defects will give rise to a broad range of Δ_0. We will assume this form for the distribution function f.

The impact of TLS defects on the energy decay of the acoustic cavity mode of our nanobeam OMC at low temperature may be elucidated by considering a simple time-dependent analysis of the populations of the eigenstates of each potential well. Following closely with Ref. [101], we write the ground states of the individual potential wells as $|\phi_1\rangle$ and $|\phi_2\rangle$, having energies E_1 and E_2 respectively. If we choose the energy to be referenced to the average $(E_1 + E_2)/2$, it is straightforward to show that the energy eigenstates of the double-well have energies $\pm E/2$, where $E = (\Delta^2 + \Delta_0^2)^{1/2}$ and can be written $|\psi_1\rangle = \cos\theta\,|\phi_1\rangle + \sin\theta\,|\phi_2\rangle$, $|\psi_2\rangle = \sin\theta\,|\phi_1\rangle - \cos\theta\,|\phi_2\rangle$, where $\tan 2\theta = \Delta_0/\Delta$. Now, using the time-dependent Schrödinger equation we write the TLS state as

$$|\Psi(x,t)\rangle = a_1(t)\,|\psi_1(x)\rangle\, e^{-iE_1 t/\hbar} + a_2(t)\,|\psi_2(x)\rangle\, e^{-iE_2 t/\hbar}, \tag{7.17}$$

where the complex amplitudes a_1 and a_2 are explicitly time-dependent, and the corresponding occupation probabilities of the two energy eigenstates are $p_1 = |a_1|^2$ and $p_2 = |a_2|^2$, satisfying the normalization condition $p_1 + p_2 = 1$. We can find an expression for the transition rates [144] using a standard detailed-balance approach in thermal equilibrium:

$$\dot{p}_1(t) = -p_1(t)\omega_{12} + p_2\omega_{21}, \tag{7.18}$$

$$\dot{p}_2(t) = -p_2(t)\omega_{21} + p_1\omega_{12}, \tag{7.19}$$

with ω_{12} being the transition rate from $|\psi_1\rangle$ to $|\psi_2\rangle$. Enforcing thermal equilibrium at temperature T such that the steady-state occupation of the two states satisfy

$$\frac{p_2}{p_1} = e^{-E/k_B T} = \frac{\omega_{12}}{\omega_{21}}, \tag{7.20}$$

we arrive at the rate equation

$$\dot{p_1}(t) = -(\omega_{12} + \omega_{21})p_1(t) + \omega_{21}. \tag{7.21}$$

We identify an effective decay rate for the TLS, $\gamma_{\mathrm{TLS}} \equiv (\omega_{12} + \omega_{21}) = \omega_{12}(1 + exp[E/k_{\mathrm{B}}T])$. Using first-order perturbation theory the transition rate ω_{12} can be evaluated according to Fermi's Golden Rule as

$$\omega_{12} = \sum_{\alpha} \frac{2\pi}{\hbar} |\langle \psi_1 | \hat{H}_{\mathrm{int}} | \psi_2 \rangle|^2 g(E) n(E), \tag{7.22}$$

where α indexes strain field polarizations (longitudinal l, transverse t, flexural f) and $n(E) = (exp[E/k_{\mathrm{B}}T] - 1)^{-1}$ is the Bose-Einstein occupancy factor. The interaction Hamiltonian has taken the form in the energy representation

$$\hat{H}_{\mathrm{int}} = \frac{\Delta}{E}\sigma_z + \frac{\Delta_0}{E}\sigma_x \gamma e. \tag{7.23}$$

The per-phonon strain amplitude per unit volume is given by $e = (\frac{\hbar}{2\rho\omega})^{1/2} q_\alpha$, where ρ is the material mass density ($\rho_{\mathrm{Si}} = 2.33 \times 10^3$ kg/m^3) and $q_\alpha = \omega / v_\alpha$ is the phonon wave-vector for a specific polarization α. The coupling constant γ is defined in direct analogy to the electric dipole moment, where the product γe of the coupling constant and the (strain) field amplitude replaces the usual electromagnetic product term $p_0 \cdot \mathcal{E}$ of a dipole p_0 in an electric field $\mathcal{E}$. The coupling constant will in general depend on the polarization of the strain field. Evaluating the $\hat{H}_{\mathrm{int}}$ matrix element gives

$$|\langle \psi_1 | \hat{H}_{\mathrm{int}} | \psi_2 \rangle|^2 = \left(\frac{\Delta_0}{E} e \gamma_\alpha \right)^2, \tag{7.24}$$

and we make note of the simple product

$$n(E)\left(1 + e^{E/k_{\mathrm{B}}T}\right) = \coth\left[\frac{E}{2k_{\mathrm{B}}T}\right]. \tag{7.25}$$

Finally, we can write the TLS relaxation rate as a sum over phonon polarizations and a function of E in the form [145]

$$\gamma_{\mathrm{TLS}}(E) = \sum_{\alpha} \frac{2\pi}{\hbar} \left(\frac{\Delta_0}{E} \right)^2 e^2 \gamma_\alpha^2 g(E) \coth\left[\frac{E}{2k_{\mathrm{B}}T}\right]. \tag{7.26}$$

The above expression is general and is expected to be valid for an arbitrary local acoustic mode density of states $g(E)$ coupled to the TLS, assuming the first-order

perturbation theory is still valid for the corresponding strain field profiles of the modes. Now, if we consider the response of such a thermal distribution of TLS with energy E and asymmetry Δ to an impinging acoustic field, it is possible to write an expression for the overall energy relaxation of the acoustic field in the presence of the TLS in terms of the TLS relaxation rate γ_{TLS}. The analysis is given explicitly in Ref. [101]. In the low-energy limit in which the TLS energy E is less than the energy of thermal phonons to which the TLS are coupled, the phonons can be expected to be distributed according to a 3D Debye density of states, $g(E) = E^2/(2\pi^2\hbar^3 v_\alpha^3)$. This scenario is relevant to an array of prior experimental works in crystalline and amorphous resonators at low temperature [139, 146]. The resulting effective damping rate $\gamma_{\mathrm{ph,TLS}} \propto Q^{-1}$ for the cavity mode is expressed in Ref. [101] as an integral over the distribution function $f(\Delta, \Delta_0)$:

$$\gamma_{\mathrm{TLS,ph}} = \sum_\alpha \frac{\gamma_\alpha^2}{4\rho_{\mathrm{Si}} v_\alpha^2 k_{\mathrm{B}} T} \iint d\Delta\, d\Delta_0 \left(\frac{\Delta}{E}\right)^2 f(\Delta, \Delta_0)\gamma_{\mathrm{TLS}}(E)\,\mathrm{sech}^2\left[\frac{E}{2k_{\mathrm{B}}T}\right] \quad (7.27)$$

$$= \frac{\pi^3}{24}\frac{\gamma^2 P}{\rho^2 v^2 \hbar^4}\left(\sum_\alpha \frac{\gamma_\alpha^2}{v_\alpha^5}\right) k_{\mathrm{B}}^3 T^3, \quad (7.28)$$

giving a characteristic scaling of $Q^{-1} \sim T^3$ for non-resonant TLS coupled to a 3D density of phonon states. In the case of the nanobeam OMC, this situation is expected to be most relevant for temperatures $\gtrsim 1-2$ K, above the bottleneck cutoff frequency, where the phonon density of states in the nanobeam can be approximated as three-dimensional. In the low-temperature limit in the milliKelvine regime, however, the phonon density of states is strongly modified by the quasi-1D geometry of the nanobeam, effectively giving a discrete spectrum of modes according to a 1D density of states distribution. In this limit, we can write expressions for the quasi-1D phonon density of states in the structure explicitly to evaluate the effective TLS-induced damping $\gamma_{\mathrm{ph,TLS}}$. Let t_b and w_b be the nanobeam thickness and width, respectively, and v_α be the speed of sound for acoustic modes of polarization α. Table 7.1 summarizes the density of states, effective coupling constants γ_α, and sound velocities assumed in the physical model. The resulting damping rate, in analogy to Equation 7.28, is given by,

$$\gamma_{\mathrm{TLS,ph}} = \frac{\pi}{2\hbar}\frac{1}{k_{\mathrm{B}}T}\sum_\alpha \frac{e^2}{\rho}\frac{\gamma_\alpha^2}{v_\alpha^2}\iint d\Delta\, d\Delta_0 P \frac{\Delta^2\Delta_0}{E^4}\,\mathrm{sech}^2\left[\frac{E}{2k_{\mathrm{B}}T}\right]\coth\left[\frac{E}{2k_{\mathrm{B}}T}\right]. \quad (7.29)$$

Table 7.1: Acoustic mode properties in the TLS damping model.

Property	$\alpha = l$	$\alpha = t$	$\alpha = f$	Notes
v_α	8.4 km/s	5.8 km/s	5.8 km/s	From Ref. [101]
γ_α/q_e	1.6	1.0	1.0	q_e : electron charge
$g_{1\mathrm{D},\alpha}^{-1}$	$\pi\hbar(t_b w_b)v_l$	$\pi\hbar(t_b w_b)v_t$	$\pi\hbar(t_b w_b)v_t\sqrt{\frac{E^2}{\hbar\omega_{\mathrm{cut}}}}$	ω_{cut} : cutoff frequency

We are poised to extract a theoretical temperature scaling of the damping rate for our nanobeam breathing mode from Equation 7.29 which may be readily compared to the experimentally observed temperature scaling law, analogous to the $Q^{-1} \sim T^3$ scaling law predicted for phonon bath with a 3D Debye density of states in Ref. [101]. The integrals over Δ and Δ_0 are not generally amenable to analytical solutions, but numerical calculations yield an overall scaling of $\gamma_{\mathrm{TLS,ph}} \sim T$ for temperatures below the maximum tunneling asymmetry energy, $T < \Delta_{0,\mathrm{max}}/k_{\mathrm{B}}$, in agreement with the scaling $Q^{-1} \sim T$ predicted by Ref. [145]. Figure 7.1 shows the measured mechanical damping rate $\gamma_0/2\pi$ for a high-Q device measured as a function of temperature. At the lowest temperatures $T_{\mathrm{b}} < 300$ mK, the damping due to three-phonon scattering processes is negligible as the energy scale is well below that required for thermal excitation of a phonon bath above the acoustic shield bandgap. The dominant damping rate in this temperature range, then, is likely caused by coupling to TLS defects as suggested above. The low-temperature scaling of the observed mechanical damping rate follows $\gamma_0 \sim T$, with the simple power-law scaling predicted by the model of coupled non-resonant TLS in Equation 7.29.

For more quantitative comparison of Equation 7.29 to experiment, we compare the measured damping rate as a function of temperature to the numerical results obtained from Equation 7.29. Early estimates of the TLS density in silicon oxides were inferred from phonon echo experiments [147, 148] from which a defect density of $P = 5.45\times10^{44}$ states J^{-1} m^{-3} was extracted. A decade later, Ref. [101] suggested a TLS density $P = 3\times10^{44}$ states J^{-1} m^{-3} in dehydrated vitreous silica (Suprasil W), which we take as a benchmark estimate. The effective volume of amorphous material is in actuality only a fraction of the total volume of Si from which the resonator is constructed, as the bulk resonator material is single-crystal Si; assuming a typical native surface oxide thickness $t_{\mathrm{ox}} = 250$ pm and an effectively amorphous etch-damaged surface layer of thickness $t_{\mathrm{et}} = 15$ nm [50], the effective defect density per unit energy is

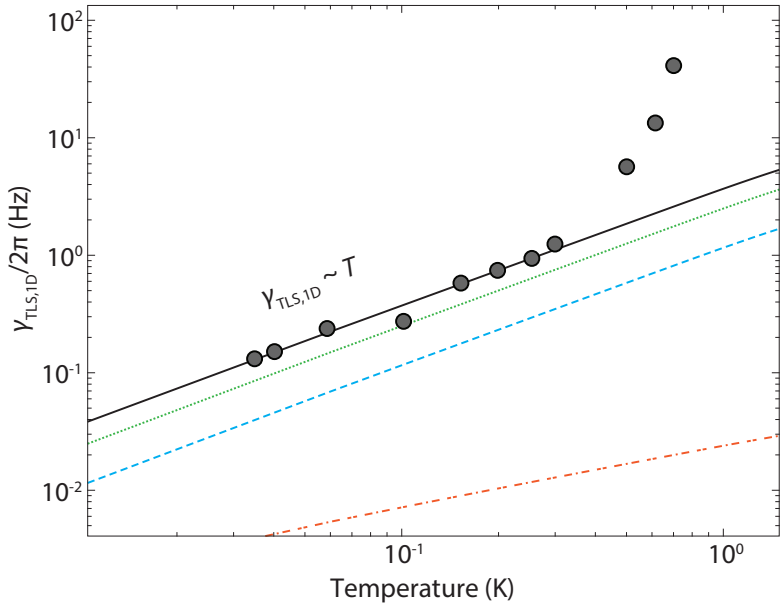

Figure 7.5: **Temperature scaling of acoustic damping for TLS coupled to a 1D phonon bath.** Plot of numerical calculation of the predicted contribution to the mechanical damping rate for a mode coupled to a distribution of non-resonant TLS in a bath of phonons with a quasi-1D density of states. Measurement data for the device presented in Figure 2.3 are included, showing quantitative agreement with the model. The low-temperature scaling power law $\gamma_{\mathrm{TLS,ph}} \sim T$ arises for temperatures below an upper asymmetry cutoff energy, given by $\Delta_{0,\mathrm{max}}/k_{\mathrm{B}}$. Contributions to the total damping rate from different phonon mode polarizations are represented by: longitudinal (green dotted line), torsional (blue dashed line), flexural (orange dot-dashed line), and the sum $\gamma_{\mathrm{TLS,ph}}$ is the solid black line. Material parameters used in the calculation are summarized in Table 7.1. A best fit to the data gives an effective TLS defect density of $P_{\mathrm{eff}} = 8.66 \times 10^{43}$ states J^{-1} m^{-3}, where $P_{\mathrm{eff}} = \eta_P P$ accounts for a fractional volume of amorphous material in the resonator structure.

$$P_{\mathrm{eff}} = \left[\left(\frac{2t_{\mathrm{ox}}}{t_b}\right) + \left(\frac{4t_{\mathrm{et}}}{w_b}\right)\right] P \equiv \eta_P P. \tag{7.30}$$

Substituting this effective defect density $P \longrightarrow P_{\mathrm{eff}}$ in Equation 7.29, we can find strong quantitative agreement between the measurement data of the low-temperature damping rate and the damping rate predicted by the physical model, to within a factor of about 2, where the material properties summarized in Table 7.1 have been used in the calculation. The calculation results are presented along with the measurement data in Figure 7.5. We estimate a surface-volume fraction of $\eta_P \approx 0.12$ for our structure, and a best-fit to the measurement data gives a defect density of $P_{\mathrm{eff}} = 8.66 \times 10^{43}$ states J^{-1} m^{-3}. This result corresponds to an overall scaling factor

of $\beta = 2.36$ relative to the defect density esimated in Ref. [101]. This overall scaling represents an effective uncertainty in the true number or density of TLS defects in the material, as well as reflecting the fact that we have used a simplified model for the distribution function $f(\Delta, \Delta_0)$ to obtain numerical results. The scaling factor may be considered a multiplier of the effective fractional volume of amorphous material η_P, of the density of defect states in that material, of the deformation potential which sets the coupling between phonons and TLS, or of deviations of the true TLS distribution to the function f used in the model. Using these fitting results we can obtain a simple order-of-magnitude estimate of the total number of TLS defects constituting the ensemble coupled to the cavity mode. The number of defects within a given mechanical bandwidth δ is,

$$N(\delta) = \int dV \int d\Delta_0 \; f(\Delta_0), \tag{7.31}$$

where the first integral is taken over the mode volume of the cavity mode, approximately equal to $V = m_{\text{eff}}/\rho_{\text{Si}}$. With $m_{\text{eff}} = 136$ fg [20] and $\rho_{\text{Si}} = 2.328 \times 10^3$ kg m^{-3}, we have an effective mode volume of $V = 5.84 \times 10^{-20}$ m^3. Then

$$N(\delta) = V P_{\text{eff}} \int_{\Delta_{0,\text{min}}}^{\Delta_{0,\text{max}}} \frac{d\Delta_0}{\Delta_0} = V P_{\text{eff}} \log\left[\frac{\Delta_{0,\text{max}}}{\Delta_{0,\text{min}}}\right]. \tag{7.32}$$

The integral over Δ_0 is performed over a range of tunneling energies from $\Delta_{0,\text{min}}$ to $\Delta_{0,\text{max}}$, which are taken to correspond to the range of energies or temperatures relevant to the experiment. Here we nominally take $\Delta_{0,\text{min}} = 1$ mK and $\Delta_{0,\text{max}} = 5$ K, although the result is sensitive to only the logarithm of the ratio of these tunneling energies, which for the temperature ranges concerned here will generally give a pure numerical factor of order 10. Recasting the energy density of $N(\delta)$ as a spectral density ($J^{-1} \longrightarrow 2\pi\hbar J^{-1} = 6.626 \times 10^{-34}$ Hz^{-1}), we have $N(\delta) \approx 3.3 \times 10^{-8}$ states Hz^{-1}. A crude estimate of the number of states lying below the cutoff frequency at about 20 GHz then gives $N \sim 660$ states ($\sim 10^4$ states per μm^3). Further knowledge of the nature of the amorphous surface material will be required for more accurate modeling results and no *a posteriori* modifications to the overall magnitude of the damping predicted by the model.

Chapter 8

EPILOGUE: FUTURE DIRECTIONS FOR OPTOMECHANICAL CRYSTALS AND ULTRA-HIGH-QUALITY PHONON MODES

The results presented in the previous chapters represent a promising improvement to the state-of-the-art in optically-coupled high-frequency mechanical resonators in thin-film semiconductor devices. While the long thermal decoherence lifetimes, low thermal noise, and deep quantum ground state mechanical thermometry have increased our understanding of the limits to mechanical dissipation in optomechanical systems at cryogenic temperatures, significant technical limitations remain to the utility of thin-film OMC devices in quantum coherent control of mechanical and optical degrees of freedom at the single-quantum level. Frequency-conversion of individual photons, efficient generation of nonclassical vibrational states and entanglement between distant resonators, and other quantum-coherent applications of OMCs rely upon the ability to reach large cooperativity, or equivalently, to engineer the mechanical baths to be dominated by coherent interactions with the optical field. Achieving $C_{\mathrm{eff}} > 1$ in the nanobeam OMC requires the best individual devices. An alternative is to engineer device architectures in which the locally-generated phonon bath can rapidly thermalize with the surrounding milliKelvin environment. This requires increasing the thermal contact area between the cavity defect and the Si bulk without sacrificing the isolation of the cavity mode and a large mechanical-Q.

In the presence of large steady-state absorption heating, pulsed laser protocols may be used in which short pulses are used to probabilistically generate nonclassical mechanical states. As detailed in Refs. [26, 94], a pulsed source detuned to the Stokes sideband of the cavity can generate correlated photon-phonon pairs through a scattering event in which a cavity-frequency photon is emitted alongside a correlated phonon. If the product of the pulse duration $\mathrm{T}_{\mathrm{pulse}}$ and back-action damping rate γ_{OM} is sufficiently small, the scattering probability is approximately $p = \gamma_{\mathrm{OM}}\mathrm{T}_{\mathrm{pulse}}$, and subsequent detection of a photon at the cavity frequency heralds the mechanics into a single-photon Fock state with high fidelity [26, 82]. Moreover, for pulses of sufficiently short duration ($\mathrm{T}_{\mathrm{pulse}} \lesssim 300\,\mathrm{ns}$), it is possible to maintain $C_{\mathrm{eff}} > 1$ throughout the pulse and realize quantum coherent operations due to the relatively slow turn-on

of the optical heating bath. Protocols such as these for probabilistically exciting an optomechanical system into a single-phonon state may be used in entanglement distribution applications [149, 150], in which a quantum network consisting of optomechanical device nodes is used to distribute entanglement first between spatially proximate primitive links (i.e., two adjacent nodes) and subsequently among distant links via entanglement swapping [151, 152, 153]. As outlined in Figure 8.1, the distance over which entanglement may be distributed in primitive links is limited by the lifetime of the excitation at the node (here the phonon lifetime $\tau_0 \lesssim 1.5$ seconds) to $c\tau_0/n_{\mathrm{Si}} \sim 10^8$ m, although in practice erasure of the which-path information at recombination of the cavity outputs by fluctuations in the optical path lengths is a severe limitation [154, 155].

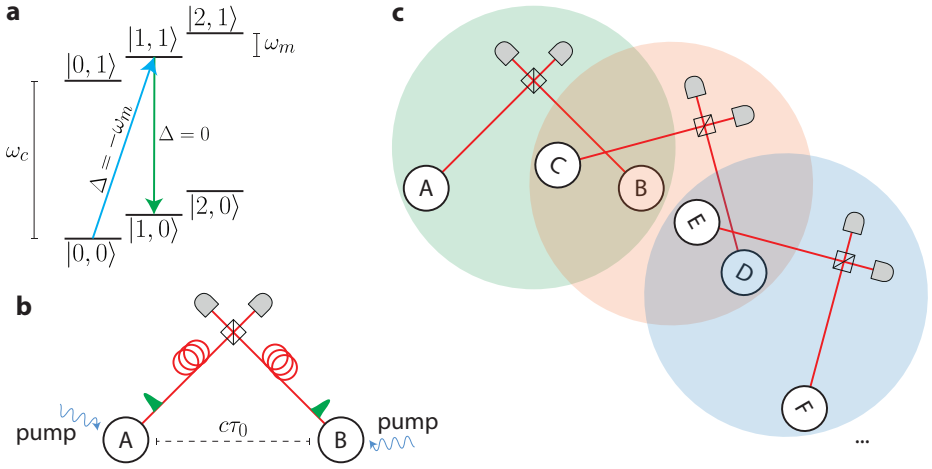

Figure 8.1: **Entanglement distribution using optomechanical devices.** **a**, Level diagram for a single optomechanical device, with $|n, m\rangle$ indicating a state of n phonons and m cavity-frequency photons. Driving a cavity with a blue-detuned laser pulse of duration $\mathrm{T}_{\mathrm{pulse}}$ can generate a correlated photon-phonon pair with small probability $p \approx \gamma_{\mathrm{OM}}\mathrm{T}_{\mathrm{pulse}}$. **b**, Simultaneous driving of two optomechanical devices (nodes A and B), followed by combination of the output cavity photons on a beam-splitter and detection on photon-counting detectors, prepares an entangled state over the link (A,B) given by $|\psi\rangle = (|1,1\rangle_A |0,0\rangle_B + |0,0\rangle_A |1,1\rangle_B e^{i\phi})/\sqrt{2}$ where ϕ is a relative phase. The phonon lifetime τ_0 limits the distance between the nodes to $\sim c\tau_0$, effectively limiting the spatial extent of a single entangling operation. **c**, Entanglement may be distributed over greater distances using DLCZ or another entanglement-swapping protocol, in which primitive links (A,B), (C,D), (E,F), etc. initially share entaglement.

Further applications for exploiting the long mechanical lifetimes of GHz phonon modes for applications to quantum information processing forego optical coupling altogether, and instead rely on an engineered piezoelectrically-mediatiated coupling

between a cavity acoustic mode and a superconducting resonator or qubit. In such a hybrid device, a superconducting microwave-frequency qubit with typical energy decay and dephasing times of order $T_1 \sim T_2 \sim 50$ μs (for example, a transmon/X-mon [156]) can serve as a platform for performing gate operations on a stored state for quantum information processing tasks, while a coupled acoustic cavity mode with $> 10,000$ times longer lifetime may serve as a storage element for the state of the qubit. To accomplish this, one must couple the qubit to the acoustic mode. A promising approach for achieving this coupling relies on an a multi-cavity approach, wherein a qubit is inductively coupled to a "mediating" resonator consisting of a superconducting LC resonator and piezoelectrically coupled to a mechanical resonance in a piezoelectric material such as polycrystalline AlN. The piezo-material acoustic resonance is then coupled mechanically to a high-Q acoustic cavity mode via an on-chip phonon waveguide. This approach is designed to retain the material purity of the Si acoustic mode in order to preserve high mechanical-Q factors, but suffers from the complexity of integrating multiple material systems (superconducting resonators, piezoelectric material, and single-crystal cavity mode material) without sacrificing mechanical or microwave quality factors or introducing excessive qubit decoherence.

8.1 Quasi-2D Snowflake Optomechanical Crystals

A highly desirable route toward minimizing the deleterious effects of optical-absorption heating in thin-film semiconductor OMCs is the transition to studying planar quasi-2D OMCs, as opposed to quasi-1D OMCs such as the nanobeam, to enhance thermal conductance between the cavity and the surrounding cold fridge-temperature bath. In such a device, the thermal contact area between the cavity and the surrounding bulk Si is increased by a factor of ~ 30 relative to the nanobeam, allowing the optically-excited bath of hot phonons to dissipate at an increased rate and lessen the effective bath temperature experienced by the cavity mode. Substantial work has been done toward the design and fabrication of quasi-2D OMCs within the Painter Group [17, 157], but achieving large optomechanical coupling ($g_0 \sim$ MHz) to a well-defined cavity mode in the absence of spurious mechanical membrane modes has proved difficult. Early designs were based on the quasi-2D "snowflake" OMC, consisting of a hexagonal lattice of etched features and a central defect region.

Recent design work based on the snowflake geometry, to be presented in more detail in the forthcoming Ph.D. thesis by Hengjiang Ren, has extended the concepts 2D

OMCs to a new cavity defect design in which the optical mode has large overlap with the strain field of the cavity acoustic mode.

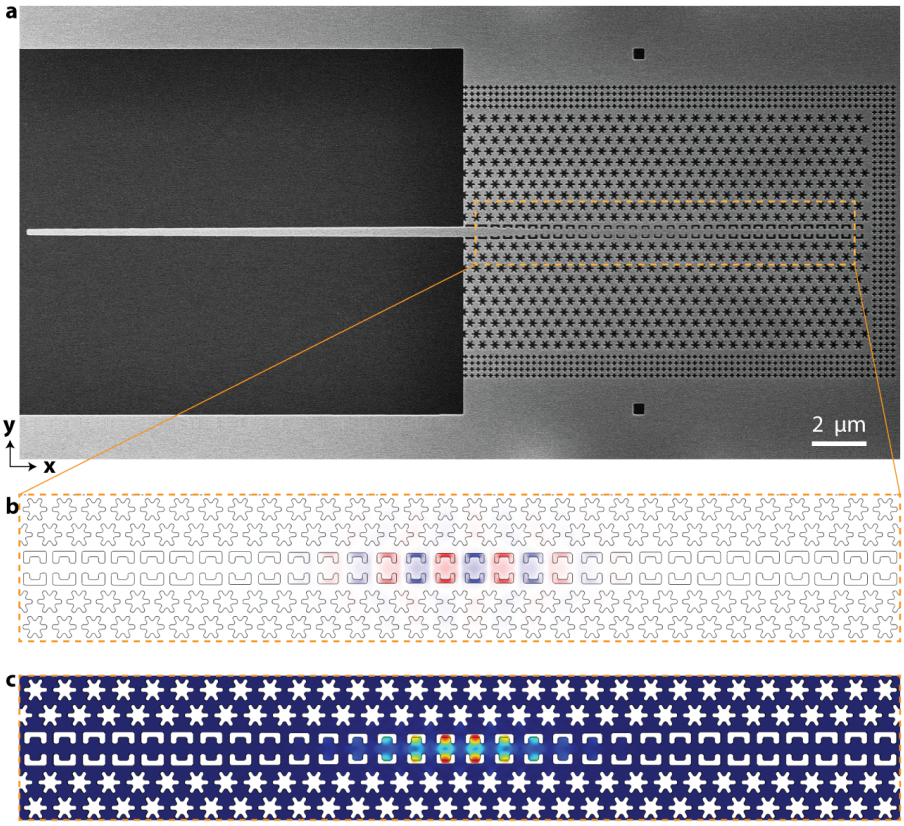

Figure 8.2: **2D OMC device optical and mechanical cavity modes.** **a**, SEM image of a quasi-2D OMC device fabricated with an on-chip waveguide suitable for end-fire coupling with a lensed optical fiber. The planar "snowflake" pattern supports an optical pseudo-bandgap in the vicinity of the cavity mode at 194 THz and a two-dimensional mechanical bandgap from approximately $9-11$ GHz. **b**, The in-plane electric field magnitude $|E_y|$ for the cavity defect mode at wavelength 1550 nm. The simulated scattering-limited optical Q-factor of the mode is of order 10^7, about an order of magnitude larger than for the optical cavity mode of the nanobeam. **c**, In-plane ($\hat{y}$) displacement amplitude for the 10.3 GHz mechanical "breathing" mode of the defect cavity. Simulated and measured optomechanical coupling rates between the modes in **a** and **b** are $g_0/2\pi \sim 1.4$ MHz and 1.1 MHz, respectively.

Initial measurements of fabricated 2D OMC devices at low temperature have yielded promising device parameters. Measured optical Q-factors above 5×10^5 are achievable, as well as mechanical frequencies of 10.0 GHz with mechanical $Q > 10^9$, and optomechanical coupling rates $g_0/2\pi > 1$ MHz; see Figure 8.3 for representative device measurements. We have demonstrated sideband cooling of a 2D OMC device

to a steady-state phonon occupancy $\langle n \rangle < 1$, consistent with an effective quantum cooperativity $C_{\text{eff}} > 1$. These initial measurements hold promise for planar thin-film OMCs as a platform for quantum coherent cavity optomechanics.

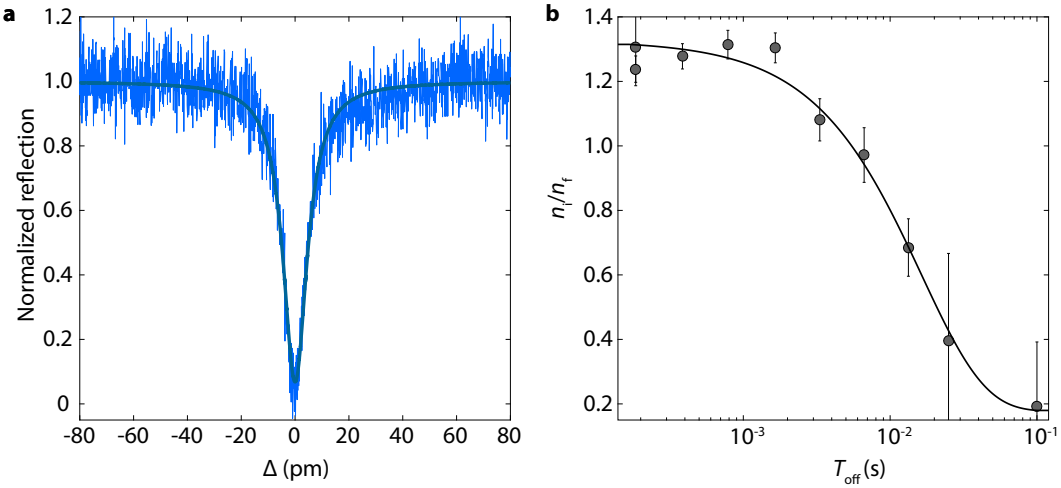

Figure 8.3: **Characterization of a quasi-2D OMC device at $T_f = 10$ mK. a**, Wavelength scan of the optical mode of a quasi-2D OMC device. We extract a resonance wavelength $\lambda_0 = 1548.0$ nm, loaded optical $Q = 2.26 \times 10^5$ ($\kappa/2\pi = 1.19$ GHz), and waveguide-cavity coupling efficiency $\eta_\kappa = 0.367$. **b**, Ringdown measurement performed at $T_f = 10$ mK using $n_c = 60$ at the red-detuned sideband. We extract a decay constant of $\gamma_0/2\pi = 9.72$ Hz for the 10.02 GHz mode, corresponding to a mechanical Q-factor of 1.03×10^9.

Thermalization and Bath Occupancy of 2D OMCs

The low-temperature thermalization of the 2D OMC is measured as described in Section 5.5. A readout laser at low power (corresponding to $n_c = 9.9$ photons) is pulsed with a period much greater than the mechanical lifetime, $T_{per} \gg \gamma_0^{-1}$, such that between each subsequent pulse the acoustic mode thermalizes to a milliKelvin bath temperature T_b with effective occupancy n_0. The measured mode occupancy in the initial portion of the pulse (the first measurement bin) will be $n_0 + \tilde{n}_0$, and from fitting to the heating model we extract the pulse-off-state base occupancy n_0. In order to minimize data integration times, a mode having large γ_0 is chosen for the measurements; in particular, we choose a device having no additional cross shield periods, with a mechanical $Q = 4.69 \times 10^5$. Figure 8.5 summarizes the results of the mode thermalization measurements. First, A ringdown measurement is performed (Figure 8.4) to determine the intrinsic energy decay rate $\gamma_0/2\pi = 21.83$ kHz, verifying that a pulsing period $T_{per} = 250$ μs satisfies $T_{per} \gg \gamma_0^{-1}$. From fitting the pulse-on data, the base mode temperature can only be restricted to a range of

approximately 10 mK $< T_\mathrm{b} <$ 130 mK, the upper range of which corresponds to an occupancy of $n_0 \lesssim 10^{-2}$. Recall that the nanobeam base mode temperature was estimated to be $T_\mathrm{b} = 35$ mK (Section 5.5).

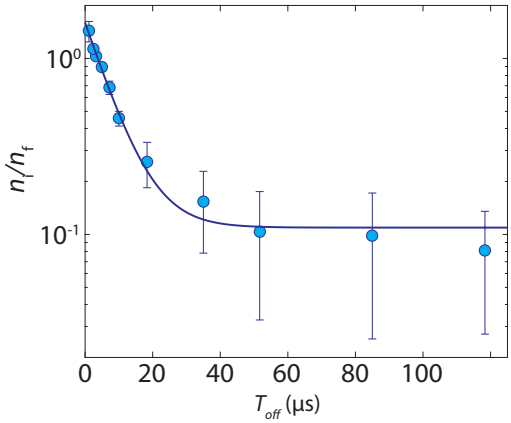

Figure 8.4: **Ringdown measurement of a 2D OMC at $T_\mathrm{f} = 10$ mK.** Ringdown measurement of 2D OMC acoustic mode performed on a device having no cross bandgap shielding, yielding an intrinsic decay rate $\gamma_0/2\pi = 21.83$ kHz (mechanical $Q = 4.69 \times 10^5$, plotted as a decay ratio $n_\mathrm{i}/n_\mathrm{f}$. Readout photon number is $n_\mathrm{c} = 60.5$ and pulse length $\mathrm{T_{pulse}} = 15$ μs. The plateau in $n_\mathrm{i}/n_\mathrm{f}$ for $\mathrm{T_{off}} > 50$ μs is due to the presence of a residual phonon bath maintained by high-duty-cyle ($> 10\%$) pulsing. Device parameters are $(\kappa, \kappa_\mathrm{e}, \omega_\mathrm{m}) = 2\pi(1.23$ GHz, 502 MHz, 10.24 GHz)

With the thermalization behavior of the 2D OMC acoustic mode known, the temperature and scaling behavior of the optical-absorption bath in the 2D OMC was measured using the method described in Section 6.3. A continuous-wave laser pump was detuned to cavity resonance ($\Delta = 0$), and the sideband-scattered photons at the upper-frequency mechanical sideband were detected at a rate $\Gamma = (\frac{\kappa}{2\omega_\mathrm{m}})^2 \Gamma_{\mathrm{SB},0}$. The resulting bath occupancy values are shown in Figure 8.6, where we have plotted the measured occupancy n_m^*. This measured occupancy is a close approximation of the bath occupancy n_p at power levels n_c where the equivalent bath temperature T_p is much greater than the fridge temperature to which the mode thermalizes, T_b. Here for a CW pump power level of $n_\mathrm{c} = 1$ we measure $n_\mathrm{m}^* = 0.94$, corresponding to a mode temperature of 665 mK, far exceeding the fridge bath temperature $T_\mathrm{p} \gg T_\mathrm{b} \lesssim 130$ mK. Thus we may make the approximation

$$n_\mathrm{m}^* = \frac{n_\mathrm{p}\gamma_\mathrm{p} + n_0\gamma_0}{\gamma_\mathrm{p} + \gamma_0} \underset{\gamma_0 n_0 \ll 1}{\approx} n_\mathrm{p}. \tag{8.1}$$

As in the case of the nanobeam, we observe good agreement with the characteristic

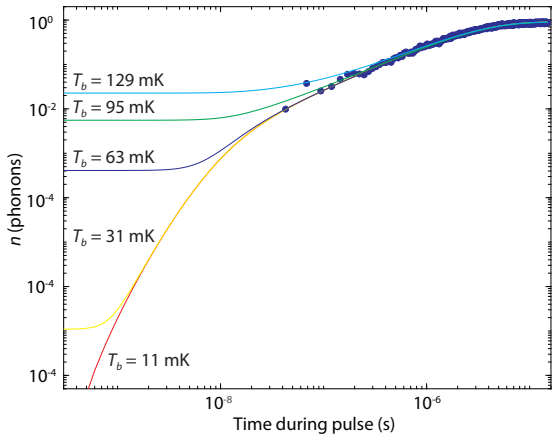

Figure 8.5: **Measurement of the theramlization bath temperature T_b in a 2D OMC at T_f = 10 mK.** Measurement of the base temperature thermalized occupancy of the 2D OMC phonon mode at an applied fridge temperature of T_f = 10 mK. Measurement parameters are: readout n_c = 9.9, $\mathrm{T_{pulse}}$ = 15 μs, $\mathrm{T_{per}}$ = 250 μs, bin size 25.6 ns. Fitting to the heating model yields a base mode temperature T_b between a 10 mK and about 130 mK ($n_0 \sim 10^{-2}$). The initial measurement bin during the pulse is indicated with a vertical gray line at $\mathrm{T_{pulse}}$ = 51.2 ns and corresponds to a measured occupancy of $n_0 = 1.8 \times 10^{-2}$ ($\tilde{n}_0 = 1.0 \times 10^{-2}$). Device parameters are (κ, κ_e, ω_m) = 2π(1.23 GHz, 502 MHz, 10.24 GHz)

scaling of the bath occupancy versus power of $n_\mathrm{p} \propto n_\mathrm{c}^{1/3}$, consistent with model predictions in the case that the dominant phonon bath coupled to the cavity mode is has a quasi-2D density of states. The overall absorption-bath temperature measured in the 2D OMC is significantly reduced relative to the bath of the nanobeam. For a single intracavity photon in steady-state, n_c = 1, the measured local bath temperature T_b = 665 mK and corresponding bath occupancy n_p = 0.94 phonons represents a > 9 dB reduction in the absorption-bath compared to the nanobeam, where a single intracavity photon produced a steady-state bath occupancy of n_p = 7.94 corresponding to a bath temperature of T_b = 2 K (Section 6.3). Considering the optical-absorption bath temperature as a function of input laser power, the reduction in bath temperature is even more apparent. As discussed previously, for a fixed detuning we typically approximate $n_\mathrm{c} = \frac{P_\mathrm{in}}{\hbar\omega_\mathrm{L}} \frac{\kappa_\mathrm{e}}{\Delta^2+(\kappa/2)^2}$, that is the intracavity photon number is proportional to the laser power incident on the cavity at fixed detuning. Here we have a detuning (at a mechanical frequency cavity sideband) of $\Delta/2\pi$ = 10 GHz, compared to the case of the nanobeam where $\Delta/2\pi$ = 5 GHz. Hence to achieve the same intracavity photon number, approximately a factor of 4 greater incident laser power is needed for the 10 GHz OMC compared to the nanobeam OMC. In this sense, we have a > 15 dB reduction in the magnitude of the

bath occupancy per unit laser power, commensurate with the factor of ∼ 30 increase in thermal contact area.

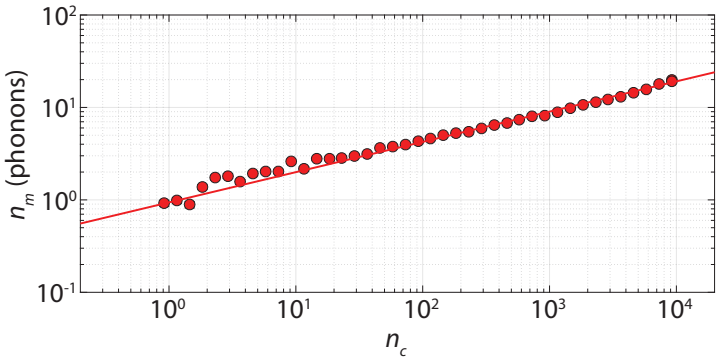

Figure 8.6: **Properties of the optical heating bath in 2D OMCs at low temperature.** Measured mode occupancy as a function of pump power n_c in the absence of back-action damping ($\Delta = 0$) for an 8-shield 2D OMC device. The solid line is a fit curve $n_p = 0.94 \times n_c^{1/3}$. Device parameters are (κ, κ_e, ω_m, γ_0) = 2π(1.19 GHz, 336 MHz, 10.02 GHz, 9.72 kHz).

Mechanical Linewidth and Cooperativity Measurements

More complete characterization of the optical heating bath in the 2D OMC device requires a measurement of the bath-induced damping rate γ_p, analogous to the results presented for the nanobeam device in Section 6.3. However, unlike the bath damping measurements of the nanobeam, here the lowered bath occupancy imposes a difficulty on measuring a ringdown or ring-up decay rate using a pulsed thermal ringdown technique similar to that of Figure 6.7. The dynamic range over which such a phonon decay may be observed is limited by the final heated occupancy in the pulse-off state, n_{peak}. An alternative approach is to make a spectral measurement of the mechanical response at sufficiently large power levels n_c that the total mechanical linewidth γ is dominated by hot bath-induced damping γ_p rather than by intrinsic jitter or damping due to the fridge-temperature bath. To perform these measurements we use a balanced heterodyne technique as outlined in Section 2.4 and shown in Figure 8.7. A 90/10 beam-splitter divides the filtered laser source into local oscillator (LO, 90%) and signal (10%) beams. The LO is modulated to generate a sideband at $\delta/2\pi = 50$ MHz from the mechanical frequency. The signal beam carrying mechanical noise sidebands at $\omega_L \pm \omega_m$ is recombined with the LO on a tunable variable optical coupler (VC), the outputs of which are sent to a balanced photodetector (BPD). The detected difference photocurrent will contain a beat note with an approximate bandwidth γ near the LO detuning δ, chosen

to lie within the detection bandwidth of the BPD.

We minimize optical back-action damping γ_{OM} by choosing a resonant probe ($\Delta = 0$) such that the total mechanical linewidth is equal to the sum of the intrinsic damping rate γ_{i} and the optical absorption bath-induced damping γ_{p}. In this case, we may generalize the expressions 2.81 and 2.83 for the case of resonant detuning to model the observed difference photocurrent NPSD. The scattering coefficient $s(\omega; \Delta = 0)$ is given by $s(\omega; \pm)$ suppressed by a factor of the sideband resolution parameter, namely:

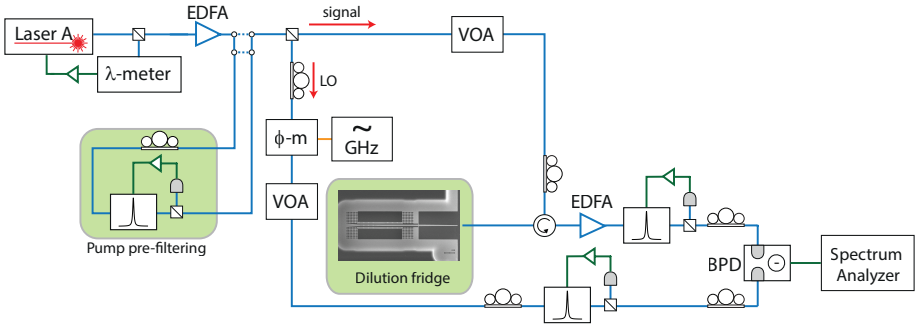

Figure 8.7: **Optical measurement setup for balanced heterodyne detection.** A 90/10 beam-splitter separates the light source into a high-power ($\sim 0.5 - 1$ mW) local oscillator (L.O.) and a signal beam. An RF signal generator drives an EOM to generate a sideband at $\omega = \omega_{\mathrm{m}} - \delta$ which is selected with a fiber-Fabry-Perot filter, such that upon recombining with the reflected signal tone a beat-note is produced at $\delta/2\pi \approx 50$ MHz, within the bandwidth of a balanced photodetector (BPD). The signal beam reflects from the device and is combined with the LO on a variable coupler (VC, not shown) before being sent to a BPD. The difference photocurrent output of the BPD is observed on a real-time spectrum analyzer (RSA).

$$s(\omega; 0) \approx \left(\frac{\kappa}{2\omega_{\mathrm{m}}}\right) s(\omega; +) = \left(\frac{\kappa}{2\omega_{\mathrm{m}}}\right) \frac{\sqrt{\kappa_{\mathrm{e}}}}{\kappa} \frac{iG\sqrt{\gamma}}{i(\omega_{\mathrm{m}} - \omega) + \gamma/2}. \tag{8.2}$$

The difference photocurrent power spectral density is then

$$S_{\hat{I}_-\hat{I}_-}[\omega]\Big|_{\Delta=0} = 2\pi|\beta|^2 \left(1 + n_{\mathrm{b}}(|s(\omega; 0)|^2 + |s(-\omega; 0)|^2)\right) \tag{8.3}$$

$$= 2\pi|\beta|^2 \left(1 + n_{\mathrm{b}} \frac{\kappa_{\mathrm{e}}}{2\omega_{\mathrm{m}}^2} \frac{\gamma G^2}{(\omega_{\mathrm{m}} - \omega)^2 + (\gamma/2)^2}\right). \tag{8.4}$$

Here the intrinsic linewidth $\gamma = \gamma_{\mathrm{i}} + \gamma_{\mathrm{p}}$ is the total time-averaged mechanical mode linewidth. The intrinsic damping term γ_{i} includes spectral diffusion of the mechanical mode, and is distinct from the intrinsic energy decay rate γ_0. Figure 8.8 shows

the measured mechanical NPSD using a balanced heterodyne detection technique. Resonant detuning not only eliminates back-action damping of the mechanics, but also allows for efficient loading of the optical cavity; for the device parameters here, an input power of 100 μW generates an average intracavity photon population of about $n_c \sim 3.2 \times 10^4$. The measured total linewidth approximately follows a power-law scaling of $\gamma \propto n_c^{0.4}$, and at lower powers $n_c \sim 10$ we expect the linewidth to be dominated by intrinsic damping γ_i rather than bath-induced damping. However, as we cannot strictly separate γ and γ_p from a single measurement of linewidth versus pump power, we plot the total linewidth and an estimated inferred γ_p by assuming γ saturates to $\approx \gamma_i$ at the lowest n_c (that is, $\gamma(n_c = 26)/2\pi = 11.8$ kHz $\approx \gamma_i/2\pi$).

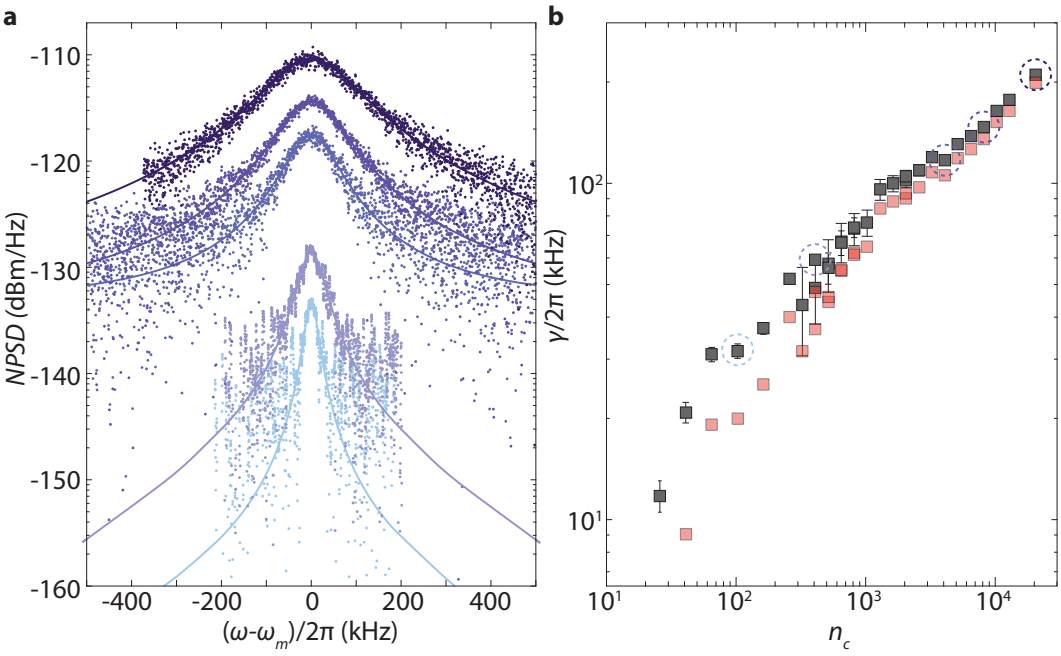

Figure 8.8: **Measurement of the total mechanical linewidth γ versus power using heterodyne detection.** **a,** The mechanical noise power spectral density (NPSD) observed on a balanced photodetector with a resonantly-detuned ($\Delta = 0$) optical probe. In the absence of back-action damping, the total linewidth is $\gamma = \gamma_i + \gamma_p$. **b**, Plot of the total mechanical linewidth extracted from the Lorentzian NPSD as a function of n_c (gray squares). Translucent squares represent an inference of γ_p calculated by subtracting the low-power linewidth from the data set: $\gamma_p(n_c > 26) \approx \gamma - \gamma(n_c = 26)$. Device parameters are the same as those in Fig. 8.6. Dashed circles indicate data extracted from the correspondingly-colored curves in **a**.

A more direct measurement of the cooperativity can be made by observing the cooled mechanical occupancy $\langle n \rangle = (\gamma_p n_p + \gamma_0 n_0)/(\gamma_0 + \gamma_{OM} + \gamma_p)$ in the presence of a continuous wave pump detuned to the red sideband ($\Delta = \omega_m$). Figure 8.9 shows

the results of steady-state mechanical occupancy measurements in the presence of red-detuned driving, as a function of the drive laser power n_c. For large $n_c > 600$, the mechanical occupancy drops below unity, indicating we are near the quantum cooperativity $C_{\text{eff}} > 1$ regime. The corresponding estimated $C_{\text{eff}} \approx 1/\langle n \rangle$ is shown in Figure 8.9b. As outlined previously in Section 6.5, a naïve model of the optical absoprtion indicates that due to the approximate scaling $\gamma_p(n_p + 1) \propto n_c$, at high power we should observe a saturation of $C_{\text{eff}} = 4g_0^2/(\kappa\beta_p)$. Here we observe that at sufficiently high powers, C_{eff} appears not to saturate to a constant value, and moreover, that our estimate of the bath-induced damping scales as $\sim n_c^{1/2}$ ($\gamma_p n_p \sim n_c^{5/6}$) indicating the breakdown of the simple linear absorption model. This is consistent with the expectation that at high intracavity photon number nonlinear absorption processes may be activated, as well as more complex bath dynamics which break the simplifying assumption that the high-frequency phonon bath will be populated according to a simple power-law model of the low-temperature thermal conductance.

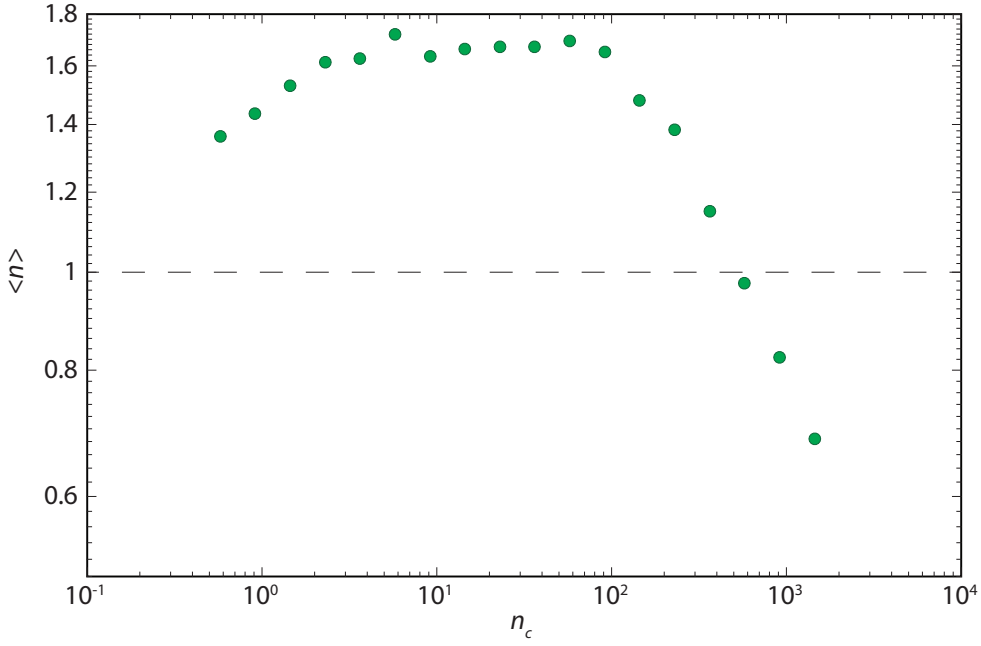

Figure 8.9: **Measurement of the steady-state phonon occupancy $\langle n \rangle$ at T_f = 10 mK as a function of drive laser power. a**, A red-detuned pump ($\Delta = +\omega_m$) drives the device in CW operation. At high power levels corresponding to cavity photon numbers $n_c \gtrsim 600$, the phonon occupancy $\langle n \rangle$ drops below unity and $C_{\text{eff}} \approx 1/\langle n \rangle$ exceeds unity (gray dashed line). Device parameters are the same as those in Fig. 8.6.

Nevertheless, these initial measurements demonstrate the promise of quasi-2D OMC

devices for steady-state operation in the quantum high-cooperativity regime. While we still observe C_{eff} of order unity, the observed steady-state cooperativity represents a great improvement over the nanobeam OMC due to a reduced phonon bath occupancy. Straightforward improvements to the device cleaning and surface preparation–in order to minimize the thickness of the native silicon oxide layer, thereby lowering the density of optical absorption centers feeding the high-temperature phonon bath–should allow for even greater improvements to the achievable cooperativity in thin-film OMCs.

BIBLIOGRAPHY

[1] Johannes Kepler. *De Cometis Libelli Tres*. Augsburg, 1619 (cit. on p. 3).

[2] W. Crookes. "On attraction and repulsion resulting from radiation". In: *Philosophical Transactions Royal Society of London* 164 (1874), pp. 501–527 (cit. on p. 3).

[3] J. C. Maxwell. "On stresses in rarified gases arising from inequalities of temperature". In: *Philosophical Transactions Royal Society of London* 170 (1879), pp. 231–256 (cit. on p. 3).

[4] James Clerk Maxwell. *A treatise on electricity and magnetism*. Vol. 2. Clarendon Press, Oxford, 1873 (cit. on p. 3).

[5] E. F. Nichols and G. F. Hull. "A preliminary communication on the pressure of heat and light radiation". In: *Phys. Rev.* 13 (1901), pp. 307–320 (cit. on p. 3).

[6] A. Einstein. "On the present status of the radiation problem". In: *Phys. Z.* 10 (1909), pp. 185–193 (cit. on p. 3).

[7] A. L. Schawlow and C. H. Townes. "Infrared and Optical Masers". In: *Phys. Rev.* 112.6 (Dec. 1958), pp. 1940–1949 (cit. on p. 3).

[8] A. Ashkin. "Trapping of Atoms by Resonance Radiation Pressure". In: *Physical Review Letters* 40.729 (1978), pp. 729–732 (cit. on p. 4).

[9] Stig Stenholm. "The semiclassical theory of laser cooling". In: *Rev. Mod. Phys.* 58 (1986), pp. 699–739 (cit. on p. 4).

[10] I. Bloch, J. Dalibard, and W. Zwerger. "Many-body physics with ultracold gases". In: *Reviews of Modern Physics* 80.885 (2008), pp. 885–964 (cit. on p. 4).

[11] A. Dorsel et al. "Optical Bistability and Mirror Confinement Induced by Radiation Pressure". In: *Physical Review Letters* 51.17 (1983), pp. 1550–1553 (cit. on p. 4).

[12] C. M. Caves. "Quantum-Mechanical Radiation-Pressure Fluctuations in an Interferometer". In: *Physical Review Letters* 45.2 (1980), pp. 75–79 (cit. on p. 4).

[13] A.F. Pace, M.J. Collett, and D.F. Walls. "Quantum limits in interferometric detection of gravitational radiation". In: *Physical Review A* 47.4 (1993), pp. 3173–3189 (cit. on p. 5).

[14] M. T. Jaekel and S. Reynaud. "Quantum Limits in Interferometric Measurements." In: *Europhysics Letters* 13.4 (1990), pp. 301–306 (cit. on p. 5).

[15] P.-F. Cohadon, A. Heidmann, and M. Pinard. “Cooling of a Mirror by Radiation Pressure”. In: *Phys. Rev. Lett.* 83.16 (Oct. 1999), pp. 3174–3177 (cit. on p. 5).

[16] Amir H. Safavi-Naeini et al. “Electromagnetically induced transparency and slow light with optomechanics”. In: *Nature* 472 (2011), pp. 69–73 (cit. on pp. 6, 88).

[17] Amir H. Safavi-Naeini et al. “Optomechanics in an ultrahigh-Q slotted 2D photonic crystal cavity”. In: *Appl. Phys. Lett.* 97 (2010), p. 181106 (cit. on pp. 6, 149).

[18] Amir H. Safavi-Naeini et al. “Squeezed light from a silicon micromechanical resonator”. In: *Nature* 500 (2013), pp. 185–189 (cit. on pp. 6, 49, 55).

[19] Jeff T. Hill et al. “Coherent optical wavelength conversion via cavity optomechanics”. In: *Nature Commun.* 3 (June 2012), p. 1196 (cit. on pp. 6, 8, 55, 76, 123, 125).

[20] Jasper Chan et al. “Laser cooling of a nanomechanical oscillator into its quantum ground state”. In: *Nature* 478 (2011), pp. 89–92 (cit. on pp. 6, 7, 10, 16–18, 21, 55, 76, 140, 146).

[21] Jasper Chan et al. “Optimized optomechanical crystal cavity with acoustic radiation shield”. In: *Appl. Phys. Lett.* 101.8 (Aug. 2012), p. 081115 (cit. on pp. 6, 10, 77).

[22] W. P. Bowen and G. J. Milburn. *Quantum Optomechanics*. CRC Press, Taylor & Francis Group, LLC, 2016 (cit. on p. 6).

[23] M. Aspelmeyer, T.J. Kippenberg, and F. Marquardt. “Cavity optomechanics”. In: *Reviews of Modern Physics* 86.4 (2014), pp. 1391–1452 (cit. on pp. 7, 123).

[24] S. Galliou et al. “Extremely Low Loss Phonon-Trapping Cryogenic Acoustic Cavities for Future Physical Experiments”. In: *Scientific Reports* 3.2132 (2013), pp. 1–6 (cit. on p. 7).

[25] P. Kharel et al. “Ultra-high-Q phononic resonators on-chip at cryogenic temperatures”. In: *arXiv* 1 (2018) (cit. on pp. 7, 8).

[26] S. M. Meenehan, J.D. Cohen, G. S. MacCabe, F. Marsili, M. D. Shaw, and O. J. Painter. “Pulsed Excitation Dynamics of an Optomechanical Crystal Resonator near Its Quantum Ground State of Motion”. In: *Physical Review X* 5.041002 (2015). DOI: 10.1103/PhysRevX.5.041002. (Cit. on pp. 7, 10, 47, 78, 92, 94, 147).

[27] T. Aref et. al. *Quantum Acoustics with Surface Acoustic Waves. In: Hadfield R., Johansson G. (eds) Superconducting Devices in Quantum Optics. Quantum Science and Technology.* Springer, Cham, 2016 (cit. on p. 8).

[28] M. J. A. Schuetz et al. “Universal Quantum Transducers Based on Surface Acoustic Waves”. In: *Physical Review X* 5.031031 (2015), pp. 1–30 (cit. on p. 8).

[29] R. Maneti et al. “Circuit quantum acoustodynamics with surface acoustic waves”. In: *Nature Communications* 8.975 (2017), pp. 1–6 (cit. on p. 8).

[30] Seán M. Meenehan et al. “Silicon optomechanical crystal resonator at millikelvin temperatures”. In: *Phys. Rev. A* 90 (2014), p. 011803 (cit. on pp. 9, 10, 47, 56, 73, 77, 84, 101, 102, 104, 112).

[31] J.D. Cohen, S. M. Meenehan, G. S. MacCabe, S. Gröblacher, A. H. Safavi-Naeini, F. Marsili, M. D. Shaw, and O. J. Painter. “Phonon counting and intensity interferometry of a nanomechanical resonator”. In: *Nature* 520 (2015), pp. 522–525. DOI: 10.1038/nature14349. (Cit. on pp. 10, 27, 47).

[32] Jasper Chan. “Laser cooling of an optomechanical crystal resonator to its quantum ground state of motion”. PhD thesis. California Institute of Technology, 2012 (cit. on pp. 10, 133).

[33] I. Tittonen et al. “Interferometric measurements of the position of a macroscopic body: Towards observation of quantum limits”. In: *Phys. Rev. A* 59 (1999), pp. 1038–1044 (cit. on p. 13).

[34] C Doolin et al. “Multidimensional optomechanical cantilevers for high-frequency force sensing”. In: *New Journal of Physics* 16.3 (2014), p. 035001 (cit. on p. 13).

[35] Kartik Srinivasan et al. “Optomechanical Transduction of an Integrated Silicon Cantilever Probe Using a Microdisk Resonator”. In: *Nano Letters* 11.2 (2011), pp. 791–797 (cit. on p. 13).

[36] R. W. Peterson et al. “Laser Cooling of a Micromechanical Membrane to the Quantum Backaction Limit”. In: *Phys. Rev. Lett.* 116 (6 Feb. 2016), p. 063601 (cit. on p. 13).

[37] T. P. Purdy, R. W. Peterson, and C. A. Regal. “Observation of Radiation Pressure Shot Noise on a Macroscopic Object”. In: *Science* 339 (2013), pp. 801–804 (cit. on p. 13).

[38] T. P. Purdy et al. “Strong Optomechanical Squeezing of Light”. In: *Phys. Rev. X* 3 (2013), p. 031012 (cit. on p. 13).

[39] T. P. Purdy et al. “Optomechanical Raman-ratio thermometry”. In: *arXiv:1406.7247* (2014) (cit. on pp. 13, 77).

[40] N. S. Kampel et al. “Improving Broadband Displacement Detection with Quantum Correlations”. In: *Phys. Rev. X* 7 (2 Apr. 2017), p. 021008 (cit. on p. 13).

[41] A. Schliesser et al. “High-sensitivity monitoring of micromechanical vibration using optical whispering gallery mode resonators”. In: *New J. Phys.* 10.9 (2008), p. 095015 (cit. on p. 13).

[42] COMSOL Multiphysics 3.5, http://www.comsol.com/ (cit. on pp. 14, 97).

[43] J. D. Joannopoulos, R. D. Meade, and J. N. Winn. *Molding the Flow of Light*. Princeton University Press, 1995 (cit. on p. 15).

[44] John David Jackson. *Classical electrodynamics*. 3rd ed. Wiley, 1999. ISBN: 9780471309321 (cit. on p. 15).

[45] Thiago P. Mayer Alegre et al. “Quasi-two-dimensional optomechanical crystals with a complete phononic bandgap”. In: *Opt. Express* 19 (2011), pp. 5658–5669 (cit. on p. 18).

[46] C. Cohen-Tannoudji, B. Diu, and F. Laloe. *Quantum Mechanica, Volume I and II*. Wiley, 1991 (cit. on p. 21).

[47] Steven G. Johnson et al. “Perturbation theory for Maxwell’s equations with shifting material boundaries”. In: *Phys. Rev. E* 65 (6 June 2002), p. 066611 (cit. on p. 21).

[48] A. Yariv and P. Yeh. *Optical Waves in Crystals*. Wiley-Interscience, 1983 (cit. on p. 22).

[49] C. W. Gardiner and M. J. Collett. “Input and output in damped quantum systems: Quantum stochastic differential equations and the master equation”. In: *Phys. Rev. A* 31 (1985), pp. 3761–3774 (cit. on p. 28).

[50] G. S. Oehrlein and J. F. Rembetski. “Plasma-based Dry Etching Techniques in the Silicon Integrated Circuit Technology”. In: *IBM J. Res. Dev.* 36.2 (Mar. 1992), pp. 140–157. ISSN: 0018-8646 (cit. on pp. 42, 139, 144).

[51] Michael David Henry. “ICP Etching of Silicon”. PhD thesis. California Institute of Technology, 2010 (cit. on p. 42).

[52] F. Laermer and A. Schilp. “Method of anisotropically etching silicon”. 5501893. Mar. 1996. URL: `http://www.freepatentsonline.com/5501893.html` (cit. on p. 43).

[53] Matt Eichenfield et al. “A picogram- and nanometre-scale photonic-crystal optomechanical cavity”. In: *Nature* 459 (2009), pp. 550–555 (cit. on pp. 49, 52).

[54] Geraint Owen and Paul Rissman. “Proximity effect correction for electron beam lithography by equalization of background dose”. In: *Journal of Applied Physics* 54.6 (1983), pp. 3573–3581 (cit. on p. 53).

[55] C. P. Michael et al. “An optical fiber-taper probe for wafer-scale microphotonic device characterization”. In: *Opt. Express* 15 (2007), pp. 4745–4752 (cit. on p. 55).

[56] Amir H. Safavi-Naeini et al. “Observation of Quantum Motion of a Nanomechanical Resonator”. In: *Phys. Rev. Lett.* 108.3 (Jan. 2012), p. 033602 (cit. on pp. 55, 77).

[57] A. J. R. MacDonald et al. “Optical microscope and tapered fiber coupling apparatus for a dilution refrigerator”. In: *Review of Scientific Instruments* 86.013107 (2015), pp. 1–7 (cit. on p. 55).

[58] P. H. Kim et al. “Approaching the standard quantum limit of mechanical torque sensing”. In: *Nature Communications* 7.13165 (2016), pp. 1–6 (cit. on p. 55).

[59] Alexander G. Krause et al. “A high-resolution microchip optomechanical accelerometer”. In: *Nature Photonics* 6 (Oct. 2012), pp. 768–772 (cit. on p. 55).

[60] T. G. Tiecke et al. “Efficient fiber-optical interface for nanophotonic devices”. In: *Optica* 2.2 (2015), pp. 70–75 (cit. on p. 55).

[61] Lumerical Solutions Inc. http://www.lumerical.com/tcad-products/fdtd/ (cit. on p. 59).

[62] F. Marsili et al. “Detecting single infrared photons with 93% system efficiency”. In: *Nature Photon.* 7 (2013), pp. 210–214 (cit. on p. 58).

[63] A. A. Clerk et al. “Introduction to quantum noise, measurement, and amplification”. In: *Rev. Mod. Phys.* 82 (2010), pp. 1155–1208 (cit. on p. 66).

[64] Jiang Qian et al. “Quantum Signatures of the Optomechanical Instability”. In: *Phys. Rev. Lett.* 109.25 (Dec. 2012), p. 253601 (cit. on pp. 66, 73).

[65] Andreas Kronwald, Max Ludwig, and Florian Marquardt. “Full photon statistics of a light beam transmitted through an optomechanical system”. In: *Phys. Rev. A* 87.1 (Jan. 2013), p. 013847 (cit. on p. 66).

[66] Roy J. Glauber. “The Quantum Theory of Optical Coherence”. In: *Phys. Rev.* 130.6 (June 1963), pp. 2529–2539 (cit. on pp. 66, 73).

[67] H. J. Kimble, M. Dagenais, and L. Mandel. “Photon Antibunching in Resonance Fluorescence”. In: *Phys. Rev. Lett.* 39 (1977), p. 691 (cit. on p. 66).

[68] Roy Pike. “Lasers, photon statistics, photon-correlation spectroscopy and subsequent applications”. In: *J. Eur. Opt. Soc. - Rapid Publications* 5 (June 2010), 10047S (cit. on p. 66).

[69] K. C. Lee et al. “Entangling Macroscopic Diamonds at Room Temperature”. In: *Science* 334 (Dec. 2011), pp. 1253–1256 (cit. on p. 66).

[70] Amir H. Safavi-Naeini et al. “Laser noise in cavity-optomechanical cooling and thermometry”. In: *New J. Phys.* 15 (2013), p. 035007 (cit. on pp. 70, 71, 174).

[71] Ivan S. Grudinin et al. “Phonon Laser Action in a Tunable Two-Level System”. In: *Phys. Rev. Lett.* 104.8 (Feb. 2010), p. 083901 (cit. on p. 71).

[72] D. A. Rodrigues and A. D. Armour. “Amplitude noise suppression in cavity-driven oscillations of a mechanical resonator”. In: *Phys. Rev. Lett.* 104 (2010), p. 053601 (cit. on p. 73).

[73] M. Lax. “Classical noise V: Noise in self-sustained oscillators”. In: *Phys. Rev.* 160 (1967), p. 290 (cit. on p. 73).

[74] Perry R. Rice and H. J. Carmichael. “Photon statistics of a cavity-QED laser: A comment on the laser-phase-transition analogy”. In: *Phys. Rev. A* 50 (1994), p. 4318 (cit. on p. 73).

[75] Niels Lörch et al. “Laser Theory for Optomechanics: Limit Cycles in the Quantum Regime”. In: *Phys. Rev. X* 4.1 (Jan. 2014), p. 011015 (cit. on p. 73).

[76] M. R. Vanner, M. Aspelmeyer, and M. S. Kim. “Quantum State Orthogonalization and a Toolset for Quantum Optomechanical Phonon Control”. In: *Phys. Rev. Lett.* 110.1 (Jan. 2013), p. 010504 (cit. on pp. 73, 76).

[77] K. Stannigel et al. “Optomechanical Quantum Information Processing with Photons and Phonons”. In: *Phys. Rev. Lett.* 109 (July 2012), p. 013603 (cit. on p. 75).

[78] A. D. O’Connell et al. “Quantum ground state and single-phonon control of a mechanical resonator”. In: *Nature* 464 (2010), pp. 697–703 (cit. on p. 76).

[79] J. D. Teufel et al. “Sideband cooling of micromechanical motion to the quantum ground state”. In: *Nature* 475 (2011), pp. 359–363 (cit. on p. 76).

[80] Markus Aspelmeyer, Tobias J. Kippenberg, and Florian Marquardt. “Cavity optomechanics”. In: *Rev. Mod. Phys.* 86 (4 Dec. 2014), pp. 1391–1452 (cit. on p. 76).

[81] K. Børkje, A. Nunnenkamp, and S. M. Girvin. “Proposal for Entangling Remote Micromechanical Oscillators via Optical Measurements”. In: *Phys. Rev. Lett.* 107.12 (Sept. 2011), p. 123601 (cit. on p. 76).

[82] Christophe Galland et al. “Heralded single phonon preparation, storage and readout in cavity optomechanics”. In: *Phys. Rev. Lett.* 112 (Mar. 2014), p. 143602 (cit. on pp. 76, 147).

[83] Andrey A. Rakhubovsky and Radim Filip. “Photon-phonon-photon transfer in optomechanics”. In: *Scientific Reports* 7 (2017), pp. 1–7 (cit. on p. 76).

[84] K. Stannigel et al. “Optomechanical Transducers for Long-Distance Quantum Communication”. In: *Phys. Rev. Lett.* 105 (2010), p. 220501 (cit. on pp. 76, 123).

[85] Amir H. Safavi-Naeini and Oskar Painter. “Proposal for an optomechanical traveling wave phonon-photon translator”. In: *New J. Phys.* 13 (2011), p. 013017 (cit. on pp. 76, 123).

[86] Joerg Bochmann et al. “Nanomechanical coupling between microwave and optical photons”. In: *Nature Physics* 9 (Nov. 2013), pp. 712–716 (cit. on p. 76).

[87] R. W. Andrews et al. “Bidirectional and efficient conversion between microwave and optical light”. In: *Nature Physics* 10 (Mar. 2014), pp. 321–326 (cit. on pp. 76, 123).

[88] Matt Eichenfield et al. “Optomechanical crystals”. In: *Nature* 462 (2009), pp. 78–82 (cit. on pp. 76, 77).

[89] Amir H. Safavi-Naeini and Oskar Painter. “Design of optomechanical cavities and waveguides on a simultaneous bandgap phononic-photonic crystal slab”. In: *Opt. Express* 18.14 (July 2010), pp. 14926–14943 (cit. on p. 76).

[90] S. J. M. Habraken et al. “Continuous mode cooling and phonon routers for phononic quantum networks”. In: *New J. Phys.* 14 (Nov. 2012), p. 115004 (cit. on p. 76).

[91] Michael Schmidt, Vittorio Peano, and Florian Marquardt. “Optomechanical Metamaterials: Dirac polaritons, Gauge fields, and Instabilities”. In: *arXiv:1311.7095* (2013) (cit. on p. 76).

[92] Ralf Riedinger et al. “Non-classical correlations between single photons and phonons from a mechanical oscillator”. In: *Nature* 530 (2016), pp. 313–316 (cit. on pp. 76, 77).

[93] Sungkun Hong et al. “Hanbury Brown and Twiss interferometry of single phonons from an optomechanical resonator”. In: *Science* 358.6360 (2017), pp. 203–206 (cit. on pp. 76, 77).

[94] Ralf Riedinger et al. “Remote quantum entanglement between two micromechanical oscillators”. In: *Nature* 556 (2017), pp. 473–477 (cit. on pp. 76, 147).

[95] M.M. Asheghi et al. “Temperature-Dependent Thermal Conductivity of Single-Crystal Silicon Layers in SOI Substrates”. In: *ASME. J. Heat Transfer* 120.1 (1998), pp. 30–36 (cit. on p. 77).

[96] J. D. Cohen et al. “Phonon counting and intensity interferometry of a nanomechanical resonator”. In: *arXiv:1410.1047* (2014) (cit. on p. 77).

[97] A. J. Weinstein et al. “Observation and interpretation of motional sideband asymmetry in a quantum electromechanical device”. In: *Phys. Rev. X* 4 (2014), p. 041003 (cit. on p. 77).

[98] Seán M. Meenehan et al. “Pulsed Excitation Dynamics of an Optomechanical Crystal Resonator near Its Quantum Ground State of Motion”. In: *Phys. Rev. X* 5 (4 Oct. 2015), p. 041002 (cit. on p. 84).

[99] G. S. Agarwal and Sumei Huang. “Electromagnetically induced transparency in mechanical effects of light”. In: *Phys. Rev. A* 81.4 (Apr. 2010), pp. 041803– (cit. on p. 88).

[100] Stefan Weis et al. “Optomechanically Induced Transparency”. In: *Science* 330 (2010), pp. 1520–1523 (cit. on p. 88).

[101] W. A. Phillips. “Two-level states in glasses”. In: *Rep. Prog. Phys.* 50 (1987), pp. 1657–1708 (cit. on pp. 99, 141, 143, 144, 146).

[102] F. Hoehne et al. “Damping in high-frequency metallic nanomechanical resonators”. In: *Phys. Rev. B* 81 (18 May 2010), p. 184112 (cit. on pp. 99, 139).

[103] G. P. Srivastava. *The Physics of Phonons*. Taylor and Francis Group, 1990 (cit. on pp. 101, 102, 104, 136).

[104] P. S. Zyryanov and G. G. Taluts. “On the theory of sound absorption in solids”. In: *JETP* 22.6 (June 1966), pp. 1326–1330 (cit. on p. 101).

[105] M. G. Holland. “Analysis of Lattice Thermal Conductivity”. In: *Phys. Rev.* 132 (6 Dec. 1963), pp. 2461–2471 (cit. on pp. 104, 133).

[106] Joseph Callaway. “Model for Lattice Thermal Conductivity at Low Temperatures”. In: *Phys. Rev.* 113 (4 Feb. 1959), pp. 1046–1051 (cit. on pp. 104, 133).

[107] Renkun Chen et al. “Thermal Conductance of Thin Silicon Nanowires”. In: *Phys. Rev. Lett.* 101.10 (Sept. 2008), p. 105501 (cit. on p. 104).

[108] Jiansong Gao. “The Physics of Superconducting Microwave Resonators”. PhD thesis. California Institute of Technology, 2008 (cit. on p. 119).

[109] Florian Marquardt et al. “Quantum Theory of Cavity-Assisted Sideband Cooling of Mechanical Motion”. In: *Phys. Rev. Lett.* 99 (2007), p. 093902 (cit. on p. 125).

[110] Hiroshi Sekoguchi et al. “Photonic crystal nanocavity with a Q-factor of 9 million”. In: *Opt. Express* 22.1 (Jan. 2014), pp. 916–924 (cit. on p. 125).

[111] A. Stesmans. “Passivation of P_{bo} amd P_{b1} interface defects in thermal (100) Si/SiO_2 with molecular hydrogen”. In: *App. Phys. Lett.* 68 (1996) (cit. on p. 126).

[112] M. Borselli et al. “Surface encapsulation for low-loss silicon photonics”. In: *Appl. Phys. Lett.* 91.13 (Sept. 2007), p. 131117 (cit. on p. 126).

[113] Andrew Cleland. *Foundations of Nanomechanics*. Springer-Verlag, 2002 (cit. on pp. 130, 132).

[114] Ron Lifshitz and M. L. Roukes. “Thermoelastic damping in micro- and nanomechanical systems”. In: *Phys. Rev. B* 61.8 (Feb. 2000), pp. 5600–5609 (cit. on pp. 131–133).

[115] Clarence Zener. “Internal Friction in Solids II. General Theory of Thermoelastic Internal Friction”. In: *Phys. Rev.* 53.1 (Jan. 1938), pp. 90–99 (cit. on p. 131).

[116] C. Zener, W. Otis, and R. Nuckolls. “Internal Friction in Solids III. Experimental Demonstration of Thermoelastic Internal Friction”. In: *Phys. Rev.* 53.1 (Jan. 1938), pp. 100–101 (cit. on p. 131).

[117] T. V. Roszhart. “Proceedings of the Solid-State Sensor and Actuator Workshop, Hilton Head Island, SC 1990”. In: *IEEE, New York* (1990), p. 13 (cit. on p. 131).

[118] M. A. Biot. “Thermoelasticity and Irreversible Thermodynamics”. In: *Journal of Applied Physics* 27.3 (1956), pp. 240–253 (cit. on p. 132).

[119] H. Deresiewicz and R. D. Mindlin. “Waves on the Surface of a Crystal”. In: *Journal of Applied Physics* 28.6 (1957), pp. 669–671 (cit. on p. 132).

[120] F. J. Lockett. “Effect of thermal properties of a solid on the velocity of Rayleigh waves”. In: *Journal of the Mechanics and Physics of Solids* 7.1 (1958), pp. 71–75 (cit. on p. 132).

[121] Clarence M. Zener. *Elasticity and Anelasticity of Metals*. University of Chicago Press, 1948 (cit. on p. 132).

[122] J. Cuffe et al. “Lifetimes of Confined Acoustic Phonons in Ultrathin Silicon Membranes”. In: *Phys. Rev. Lett.* 110 (9 Feb. 2013), p. 095503 (cit. on pp. 133, 134, 136, 137).

[123] P. G. Klemens. “The thermal conductivity of dielectric solids at low temperatures (Theoretical)”. In: *Proceedings of the Royal Society of London A: Mathematical, Physical and Engineering Sciences* 208.1092 (1951), pp. 108–133. ISSN: 0080-4630. DOI: 10.1098/rspa.1951.0147 (cit. on pp. 133, 135).

[124] P.C. Sharma and M.Frank Rose. “Three-phonon scattering processes and their role in phonon thermal conductivity of silicon”. In: *Journal of Solid State Chemistry* 73.1 (1988), pp. 92–97. ISSN: 0022-4596 (cit. on p. 133).

[125] C. Herring. “Role of Low-Energy Phonons in Thermal Conduction”. In: *Phys. Rev.* 95 (4 Aug. 1954), pp. 954–965 (cit. on p. 133).

[126] G. A. Steele et al. “Strong Coupling Between Single-Electron Tunneling and Nanomechanical Motion”. In: *Science* 325.5944 (2009), pp. 1103–1107. ISSN: 0036-8075 (cit. on p. 133).

[127] Benjamin Lassagne et al. “Coupling Mechanics to Charge Transport in Carbon Nanotube Mechanical Resonators”. In: *Science* 325.5944 (2009), pp. 1107–1110. ISSN: 0036-8075 (cit. on p. 133).

[128] A. AlShaikhi and G. P. Srivastava. “Theoretical investigations of phonon intrinsic mean-free path in zinc-blende and wurtzite AlN”. In: *Phys. Rev. B* 76 (19 Nov. 2007), p. 195205 (cit. on pp. 133, 136, 137).

[129] Juan Atalaya et al. “Nonlinear damping and dephasing in nanomechanical systems”. In: *Phys. Rev. B* 94 (19 Nov. 2016), p. 195440 (cit. on p. 133).

[130] L. D. Landau and G. Rumer. “Absorption of sound in solids”. In: *Phys. Z. Sowjetunion* 11.18 (1937) (cit. on p. 134).

[131] A. Akhieser. In: *USSR J. Phys.* 1.277 (1939) (cit. on p. 134).

[132] B. C. Daly et al. “Picosecond ultrasonic measurements of attenuation of longitudinal acoustic phonons in silicon”. In: *Phys. Rev. B* 80 (17 Nov. 2009), p. 174112 (cit. on pp. 134, 136, 137).

[133] Florian Hudert et al. “Confined longitudinal acoustic phonon modes in free-standing Si membranes coherently excited by femtosecond laser pulses”. In: *Phys. Rev. B* 79 (20 May 2009), p. 201307 (cit. on p. 134).

[134] Dhruv Gelda et al. “Reducing extrinsic damping of surface acoustic waves at gigahertz frequencies”. In: *Journal of Applied Physics* 119.16 (2016), p. 164301 (cit. on p. 134).

[135] I. Pomeranchuk. “On the Thermal Conductivity of Dielectrics”. In: *Phys. Rev.* 60 (11 Dec. 1941), pp. 820–821 (cit. on p. 135).

[136] André Herpin. “Contribution à l´étude de la théorie cinétique des solides”. In: *Ann. Phys.* 12.7 (1952), pp. 91–139 (cit. on p. 135).

[137] W. B. Gauster. “Low-Temperature Grüneisen Parameters for Silicon and Aluminum”. In: *Phys. Rev. B* 4 (4 Aug. 1971), pp. 1288–1296 (cit. on p. 137).

[138] S. Hunklinger and A. K. Raychaudhuri. “Thermal and Elastic Anomalies in Glasses at Low Temperatures”. In: *Progress in Low Temperature Physics* 9 (1986), pp. 265–344 (cit. on p. 138).

[139] R. N. Kleiman, G. Agnolet, and D. J. Bishop. “Two-level systems observed in the mechanical properties of single-crystal silicon at low temperatures”. In: *Phys. Rev. Lett.* 59 (18 Nov. 1987), pp. 2079–2082 (cit. on pp. 138, 140, 143).

[140] Pablo Esquinazi, Miguel A. Ramos, and Reinhard König. “Acoustic Properties of Amorphous Solids at Very Low Temperatures: The Quest for Interacting Tunneling States”. In: *Journal of Low Temperature Physics* 135.1 (Apr. 2004), pp. 27–38 (cit. on p. 138).

[141] C. Seoanez, F. Guinea, and A. H. Castro Neto. “Dissipation due to two-level systems in nano-mechanical devices”. In: *EPL (Europhysics Letters)* 78.6 (2007), p. 60002 (cit. on p. 138).

[142] R. O. Behunin, F. Intravaia, and P. T. Rakich. “Dimensional transformation of defect-induced noise, dissipation, and nonlinearity”. In: *Phys. Rev. B* 93 (22 June 2016), p. 224110 (cit. on p. 139).

[143] Lingkuan Meng and Jiang Yan. “Mechanism study of sidewall damage in deep silicon etch”. In: *Applied Physics A* 117.4 (Dec. 2014), pp. 1771–1776 (cit. on p. 139).

[144] B. Golding and J. E. Graebner. *Amorphous Solids, Low-Temperature Properties*. Springer, New York, 1981 (cit. on p. 141).

[145] W. A. Phillips. “Comment on "Two-Level Systems Observed in the Mechanical Properties of Single-Crystal Silicon at Low Temperatures"”. In: *Phys. Rev. Lett.* 61 (22 Nov. 1988), pp. 2632–2632 (cit. on pp. 142, 144).

[146] P. Berberich, P. Leiderer, and S. Hunklinger. “Investigation of the Lifetime of Longitudinal Phonons at GHz Frequencies in Liquid and Solid 4He”. In: *Journal of Low Temperature Physics* 22 (1975), pp. 61–84 (cit. on p. 143).

[147] B. Golding et al. “Nonlinear Phonon Propagation in Fused Silica below 1 K”. In: *Phys. Rev. Lett.* 30 (6 Feb. 1973), pp. 223–226 (cit. on p. 144).

[148] B. Golding and J. E. Graebner. “Phonon Echoes in Glass”. In: *Phys. Rev. Lett.* 37 (13 Sept. 1976), pp. 852–855 (cit. on p. 144).

[149] J. I. Cirac et al. “Quantum State Transfer and Entanglement Distribution among Distant Nodes in a Quantum Network”. In: *Phys. Rev. Lett.* 78 (16 Apr. 1997), pp. 3221–3224 (cit. on p. 148).

[150] H. J. Kimble. “The quantum internet”. In: *Nature* 453 (2008), pp. 1023–1030 (cit. on p. 148).

[151] C. Cabrillo et al. “Creation of entangled states of distant atoms by interference”. In: *Phys. Rev. A* 59 (2 Feb. 1999), pp. 1025–1033 (cit. on p. 148).

[152] S. Bose et al. “Proposal for Teleportation of an Atomic State via Cavity Decay”. In: *Phys. Rev. Lett.* 83 (24 Dec. 1999), pp. 5158–5161 (cit. on p. 148).

[153] Nicolas Sangouard et al. “Quantum repeaters based on atomic ensembles and linear optics”. In: *Rev. Mod. Phys.* 83 (2011), p. 33 (cit. on p. 148).

[154] D. Bouwmeester et al. “Experimental quantum teleportation”. In: *Nature* 390 (1997), pp. 575–579 (cit. on p. 148).

[155] Q. C. Sun et al. “Quantum teleportation with independent sources and prior entanglement distribution over a network”. In: *Nature Photonics* 10 (2016), pp. 671–675 (cit. on p. 148).

[156] R. Barends et al. “Coherent Josephson Qubit Suitable for Scalable Quantum Integrated Circuits”. In: *Phys. Rev. Lett.* 111 (8 Aug. 2013), p. 080502 (cit. on p. 149).

[157] Amir H. Safavi-Naeini et al. “Two-dimensional phononic-photonic bandgap optomechanical crystal cavity”. In: *Phys. Rev. Lett.* 112 (Apr. 2014), p. 153603 (cit. on p. 149).

[158] Stephen M. Barnett and Paul M. Radmore. *Methods in Theoretical Quantum Optics*. Clarendon Press, 2003 (cit. on pp. 175, 176).

[159] Howard J. Carmichael. *Statistical Methods in Quantum Optics: Master Equations and Fokker-Planck Equations*. Springer, 1999 (cit. on pp. 175, 179).

Appendix A

NOTATION

A.1 Fourier Transforms and Power Spectral Densities of Classical and Quantum Variables

Throughout this thesis we make use of a convention regarding notation of operators, their Fourier transforms, and power spectral densities. In particular, for a classical time-dependent variable $f(t)$ we denote the Fourier transform $\mathcal{F}\{f(t)\}[\omega]$ by

$$f[\omega] = \int_{-\infty}^{\infty} \frac{dt}{\sqrt{2\pi}}\, f(t) e^{i\omega t}, \tag{A.1}$$

and inverse Fourier transform

$$f(t) = \int_{-\infty}^{\infty} \frac{d\omega}{\sqrt{2\pi}}\, f[\omega] e^{-i\omega t}. \tag{A.2}$$

The classical autocorrelation function of $f(t)$ is denoted

$$\mathcal{G}_{ff}(t,t') = \langle f(t) f(t') \rangle_{\text{ens}} \underset{\text{stat}}{=} \mathcal{G}_{ff}(\tau) = \langle f(\tau) f(0) \rangle_{\text{ens}}, \tag{A.3}$$

where $\langle \cdot \rangle_{\text{ens}}$ denotes the ensemble average of a classical variable and the central equality holds if $f(t)$ is a stationary variable. The simplified Wiener-Khinchin Theorem for classical noisy variables can then be expressed in terms of the classical noise power spectral density (NPSD) $\mathcal{S}_{ff}[\omega]$:

$$\mathcal{S}_{ff}[\omega] = \int_{-\infty}^{\infty} d\tau\; e^{i\omega\tau} \mathcal{G}_{ff}(\tau). \tag{A.4}$$

Similarly, for a time-dependent quantum operator $\hat{f}(t)$ in the Heisenberg picture, the Fourier transform $\mathcal{F}\{\hat{f}(t)\}[\omega]$ is

$$\hat{f}[\omega] = \int_{-\infty}^{\infty} \frac{dt}{\sqrt{2\pi}}\, \hat{f}(t) e^{i\omega t}, \tag{A.5}$$

with inverse Fourier Transform

$$\hat{f}(t) = \int_{-\infty}^{\infty} \frac{d\omega}{\sqrt{2\pi}}\, \hat{f}[\omega] e^{-i\omega t}. \tag{A.6}$$

In this convention we denote the Fourier transform of the Hermitian conjugate $\hat{f}^\dagger(t)$ by $\hat{f}^\dagger[\omega]$. Note that this implies the relation $\hat{f}^\dagger[\omega] = (\hat{f}[-\omega])^\dagger$. The two-sided quantum noise-power spectral density (NPSD) of the operator $\hat{f}(t)$ is given by

$$S_{\hat{f}\hat{f}}[\omega] = \int_{-\infty}^{\infty} d\tau\; e^{i\omega\tau} \langle \hat{f}^\dagger(\tau)\hat{f}(0)\rangle \tag{A.7}$$

$$= \int_{-\infty}^{\infty} \frac{d\omega'}{2\pi}\; \langle \hat{f}^\dagger(\omega)\hat{f}(\omega')\rangle, \tag{A.8}$$

where $\langle\cdot\rangle$ denotes the quantum expectation value, and $\hat{f}$ may be any (not necessarily Hermitian) Heisenberg operator. We also define the symmetrized PSD of operator $\hat{f}$ as

$$\bar{S}_{\hat{f}\hat{f}}[\omega] = \frac{S_{\hat{f}\hat{f}}[\omega] + S_{\hat{f}\hat{f}}[-\omega]}{2}. \tag{A.9}$$

A.2 Operator Constructions

Consider a bosonic mode annihilation operator $\hat{a}$ (creation operator $\hat{a}^\dagger$). For any $\alpha \in C$, we define the displacement operator

$$\hat{D}(\alpha) \equiv e^{\alpha\hat{a}^\dagger - \alpha^*\hat{a}}. \tag{A.10}$$

A coherent state is defined as an eigenstate of $\hat{a}$, satisfying $\hat{a}\,|\alpha\rangle = \alpha\,|\alpha\rangle$, and has the property that $\hat{D}(\beta)\,|\alpha\rangle = |\alpha + \beta\rangle$ for any $\beta \in C$.

Similarly, we define the Hermitian quadrature operators of $\hat{a}$ in terms of a real phase angle λ. The *position* or *in-phase* quadrature is given by

$$\hat{x}_\lambda \equiv \frac{1}{\sqrt{2}}\left(e^{-i\lambda}\hat{a} + e^{i\lambda}\hat{a}^\dagger\right), \tag{A.11}$$

and the *momentum* or *quadrature* quadrature is given by

$$\hat{x}_{\lambda+\frac{\pi}{2}} \equiv \frac{-i}{\sqrt{2}}\left(e^{-i\lambda}\hat{a} - e^{i\lambda}\hat{a}^\dagger\right). \tag{A.12}$$

A.3 Mechanical Power Spectral Density

Using the Heisenberg-Langevin equation of motion for the mechanical fluctuations in the absence of optomechanical coupling,

$$\dot{\hat{b}}(t) = -\left(i\omega_m + \frac{\gamma_i}{2}\right)\hat{b}(t) + \sqrt{\gamma_i}\hat{b}_{\rm in}(t), \tag{A.13}$$

we use Equation A.8 to evaluate the spectral density of the mechanical resonator annihilation operator:

$$S_{\hat{b}\hat{b}}[\omega] = \int_{-\infty}^{\infty} d\omega' \, \langle \hat{b}^\dagger(\omega)\hat{b}(\omega')\rangle \tag{A.14}$$

$$= \int_{-\infty}^{\infty} d\omega' \left(\frac{-\sqrt{\gamma_i}}{-i(\omega_m+\omega)+\gamma_i/2}\right)\left(\frac{-\sqrt{\gamma_i}}{i(\omega_m-\omega')+\gamma_i/2}\right)\langle \hat{b}^\dagger_{\rm in}(\omega)\hat{b}_{\rm in}(\omega')\rangle \tag{A.15}$$

$$= \gamma_i n_{\rm b} \int_{-\infty}^{\infty} d\omega' \left(\frac{1}{-i(\omega_m+\omega)+\gamma_i/2}\right)\left(\frac{1}{i(\omega_m-\omega')+\gamma_i/2}\right)\delta(\omega+\omega') \tag{A.16}$$

$$= \frac{\gamma_i n_{\rm b}}{(\omega_m+\omega)^2+\gamma_i/2}. \tag{A.17}$$

Similarly, for the creation operator we obtain

$$S_{\hat{b}^\dagger\hat{b}^\dagger}[\omega] = \frac{\gamma_i(n_{\rm b}+1)}{(\omega_m-\omega)^2+\gamma_i/2}. \tag{A.18}$$

In the presence of optomechanical coupling the mechanical susceptibility (c.f. Equations 2.52 and 2.54) will be modified, and we define analogous spectral density functions in terms of the shifted ω_m, total damping rate γ, and average phonon number $\langle n\rangle$ according to

$$S_{\hat{b}\hat{b}}[\omega;\langle n\rangle] = \frac{\gamma\langle n\rangle}{(\omega_m+\omega)^2+\gamma/2}, \tag{A.19}$$

$$S_{\hat{b}^\dagger\hat{b}^\dagger}[\omega;\langle n\rangle] = \frac{\gamma(\langle n\rangle+1)}{(\omega_m-\omega)^2+\gamma/2}. \tag{A.20}$$

Note that $S_{\hat{b}\hat{b}}[\omega;\langle n\rangle]$ is peaked at ω_m and should be understood to represent the ability of the mechanics to *emit* energy, while $S_{\hat{b}^\dagger\hat{b}^\dagger}[\omega;\langle n\rangle]$ is peaked at $+\omega_m$ and

represents the ability of the mechanics to *absorb* energy. We will also use the definite integrals of these spectral densities:

$$\int_{-\infty}^{\infty} \frac{d\omega}{2\pi} S_{\hat{b}\hat{b}}[\omega; \langle n \rangle] = \langle n \rangle, \tag{A.21}$$

$$\int_{-\infty}^{\infty} \frac{d\omega}{2\pi} S_{\hat{b}^\dagger\hat{b}^\dagger}[\omega; \langle n \rangle] = \langle n \rangle + 1. \tag{A.22}$$

A.4 Scattering Matrix Elements

In the context of sideband resolved ($\kappa \ll \omega_m$) cavity-optomechanics, we may refer to Equations 2.60 and 2.61 for the output field $\hat{a}_{\text{out}}$ in the case of red- or blue-detuning ($\Delta = \pm\omega_m$). These expressions give the output field in terms of optical and mechanical noise fluctuation operators as well as scattering matrix elements $r(\omega; \pm)$, $n(\omega; \pm)$, and $s(\omega; \pm)$, which are given by [70]:

$$r(\omega; \pm) = 1 - \frac{2\kappa_e}{\kappa} \pm \frac{\gamma_{\text{OM}}\kappa_e}{\kappa} \frac{1}{\pm i(\omega_m \mp \omega) + \gamma/2}, \tag{A.23}$$

$$n(\omega; \pm) = \pm \frac{\sqrt{\kappa_i \kappa_e}}{\kappa} \left(\frac{\gamma_{\text{OM}}}{\pm i(\omega_m \mp \omega) + \gamma/2} \mp 2 \right), \tag{A.24}$$

$$s(\omega; \pm) = \sqrt{\frac{\kappa_e}{\kappa}} \frac{i\sqrt{\gamma_i \gamma_{\text{OM}}}}{\pm i(\omega_m \mp \omega) + \gamma/2}. \tag{A.25}$$

The scattering matrix elements also satisfy $|r(\omega; \pm)|^2 + |n(\omega; \pm)|^2 \pm |s(\omega; \pm)|^2 = 1$.

Appendix B

OPTICAL CAVITY COUPLED TO A THERMAL BATH

In this section we derive the noise power spectral density of a quantum harmonic oscillator in thermal equilibrium with a bath consisting of a continuum of modes indexed by frequency ω. The physics of this system is generically useful when considering sub-systems of bosonic degrees of freedom, such as optical or microwave electromagnetic modes or acoustic modes considered in this thesis, and provides intuition for the spectral signatures of general bosonic modes coupled to thermal baths [158, 159]. We consider a single-mode optical cavity of frequency ω_c with bosonic annihilation operator $\hat{a}$ coupled to a thermal bath with average photon occupancy $\bar{n}$. Let the thermal bath also be single-mode and have continuum annihilation operator $\hat{r}_{\omega_r}$ at each frequency ω. The Hamiltonian of the system can be written

$$\hat{H} = \hbar\omega_c \hat{a}^\dagger \hat{a} + \int d\omega_r \, \hbar\omega_r \hat{r}^\dagger_{\omega_r} \hat{r}_{\omega_r} + \left(\int d\omega_r \, \hbar\kappa_r(\omega_r) \hat{r}^\dagger_{\omega_r} \hat{a}^\dagger + h.c. \right), \tag{B.1}$$

where the coupling coefficient $\kappa_r(\omega_r)$ is in general frequency-dependent but here assumed to be constant (i.e., we are making the Markov approximation) and small compared to ω_c (the Born approximation). Note the dimensions of these terms are $[\hat{r}_{\omega_r}] = \mathrm{s}^{1/2}$, $[\kappa_r] = \mathrm{s}^{-1/2}$, and $\hat{a}$ is dimensionless.

We first derive the Quantum Langevin Equation (QLE) for the cavity operator $\hat{a}$ using the Heisenberg equations of motion:

$$\dot{\hat{a}}(t) = \frac{i}{\hbar}[\hat{H}, \hat{a}] = -i\omega_c \hat{a} - i \int d\omega_r \, \kappa_r^* \hat{r}_{\omega_r}. \tag{B.2}$$

For the bath operator $\hat{r}_{\omega_r}$ we make use of the bosonic operator commutation relation $[\hat{r}_{\omega_1}, \hat{r}^\dagger_{\omega_2}] = \delta(\omega_1 - \omega_2)$ to obtain

$$\begin{aligned}\dot{\hat{r}}_{\omega_r}(t) &= \frac{i}{\hbar}[\hat{H}, \hat{r}_{\omega_r}] \\ &= \frac{i}{\hbar}\left(\int d\omega_r' \, \hbar\omega_r' [\hat{r}^\dagger_{\omega_r'} \hat{r}_{\omega_r'}, \hat{r}_{\omega_r}] + \int d\omega_r' \, \hbar\kappa_r [\hat{r}^\dagger_{\omega_r'}, \hat{r}_{\omega_r}]\hat{a} + \int d\omega_r' \, \hbar\kappa_r^* [\hat{r}_{\omega_r'}, \hat{r}_{\omega_r}]\hat{a}^\dagger \right) \\ &= -i\omega_r \hat{r}_{\omega_r} - i\kappa_r \hat{a}.\end{aligned} \tag{B.3}$$

Formally integrating (B.3) yields

$$\hat{r}_{\omega_r}(t) = \hat{r}_{\omega_r}(0)e^{-i\omega_r t} - i\int_0^t dt' \, \hat{a}(t')\kappa_r e^{-i\omega_r(t-t')}, \tag{B.4}$$

and inserting this into (B.2) we obtain

$$\dot{\hat{a}}(t) = -i\omega_c \hat{a}(t) - 2\pi \left|\kappa_r\right|^2 \int_0^t dt' \, \hat{a}(t')\delta(t-t') - i\kappa_r^* \int d\omega_r \, \hat{r}_{\omega_r}(0)e^{-i\omega_r t}. \tag{B.5}$$

Defining an input bath operator $\hat{a}_{\text{in}}(t) = \int (d\omega_r/2\pi) e^{-i\omega_r t}(-ie^{-i\phi_r}\sqrt{2\pi}\hat{r}_{\omega_r})$, where $\kappa_r \equiv |\kappa_r| \, e^{i\phi_r}$, $\kappa \equiv 2\pi \left|\kappa_r\right|^2$, and $\hat{r}_{\omega_r} \equiv \hat{r}_{\omega_r}(t=0)$, allows us finally to write

$$\dot{\hat{a}}(t) = (-i\omega_c - \kappa)\hat{a}(t) + \sqrt{\kappa}\hat{a}_{\text{in}}(t). \tag{B.6}$$

In the Fourier domain then we have

$$\begin{aligned}\hat{a}(\omega) &= \frac{\sqrt{\kappa}\hat{a}_{\text{in}}(\omega)}{-i(\omega-\omega_c)+\kappa}, \\ \hat{a}^\dagger(\omega) &= \frac{\sqrt{\kappa}\hat{a}^\dagger_{\text{in}}(\omega)}{-i(\omega+\omega_c)+\kappa}.\end{aligned} \tag{B.7}$$

We will evaluate the noise spectral density (NSD) of the operator $\hat{a}(t)$ using these Fourier-domain expressions in conjunction with correlation functions of the bath continuum operators and the cavity mode Heisenberg operators. The bath operator correlation functions can be shown to be [158]:

$$\begin{aligned}\langle \hat{r}^\dagger_\omega \hat{r}_{\omega'} \rangle &= \bar{n}\delta(\omega-\omega') \\ \langle \hat{r}_\omega \hat{r}^\dagger_{\omega'} \rangle &= (\bar{n}+1)\delta(\omega-\omega') \\ \langle \hat{r}_\omega \hat{r}_{\omega'} \rangle &= \langle \hat{r}^\dagger_\omega \hat{r}^\dagger_{\omega'} \rangle = 0.\end{aligned} \tag{B.8}$$

Then it is easy to show that $\hat{a}_{\rm in}(\omega) = -i\sqrt{2\pi}e^{-i\phi_r}\hat{r}_\omega$ and $\hat{a}^\dagger_{\rm in}(\omega) = i\sqrt{2\pi}e^{i\phi_r}\hat{r}^\dagger_{-\omega}$. From here we directly obtain the bath input mode correlation functions:

$$\begin{aligned}
\langle \hat{a}^\dagger_{\rm in}(\omega)\hat{a}_{\rm in}(\omega')\,\rangle &= 2\pi\bar{n}\delta(-\omega-\omega') \\
\langle \hat{a}_{\rm in}(\omega)\hat{a}^\dagger_{\rm in}(\omega')\rangle &= 2\pi(\bar{n}+1)\delta(\omega+\omega') \\
\langle \hat{a}_{\rm in}(\omega)\hat{a}_{\rm in}(\omega')\rangle &= \langle \hat{a}^\dagger_{\rm in}(\omega)\hat{a}^\dagger_{\rm in}(\omega')\rangle = 0.
\end{aligned} \tag{B.9}$$

By inverse-Fourier transform we then find that

$$\begin{aligned}
\langle \hat{a}^\dagger_{\rm in}(t)\hat{a}_{\rm in}(t')\rangle &= \bar{n}\delta(t-t') \\
\langle \hat{a}_{\rm in}(t)\hat{a}^\dagger_{\rm in}(t')\rangle &= (\bar{n}+1)\delta(t-t').
\end{aligned} \tag{B.10}$$

Now, using Eqn. B.7, we can write the correlation functions of the cavity mode operator in the frequency domain

$$\langle \hat{a}^\dagger(\omega)\hat{a}(\omega') = \frac{\kappa}{(-i(\omega+\omega_c)+\kappa)(-i(\omega'-\omega_c)+\kappa)}\langle \hat{a}^\dagger_{\rm in}(\omega)\hat{a}_{\rm in}(\omega')\rangle. \tag{B.11}$$

In the time domain we then have

$$\begin{aligned}
\langle \hat{a}^\dagger(t)\hat{a}(t')\rangle &= \kappa\int_{-\infty}^{\infty}\frac{d\omega}{2\pi}e^{-i\omega t}\int_{-\infty}^{\infty}\frac{d\omega'}{2\pi}e^{-i\omega' t'}\frac{2\pi\bar{n}\delta(\omega+\omega')}{(-i(\omega+\omega_c)+\kappa)(-i(\omega'-\omega_c)+\kappa)} \\
&= \bar{n}\kappa\int_{-\infty}^{\infty}\frac{d\omega}{2\pi}e^{-i\omega(t-t')}\frac{1}{(\omega+\omega_c)^2+\kappa^2}.
\end{aligned} \tag{B.12}$$

We define $\tau \equiv t - t'$ and re-write Eqn. B.12 as

$$\langle \hat{a}^\dagger(\tau)\hat{a}(0)\rangle = \bar{n}\kappa\int_{-\infty}^{\infty}\frac{d\omega}{2\pi}e^{-i\omega\tau}\frac{1}{(\omega+\omega_c)^2+\kappa^2}, \tag{B.13}$$

and recalling the Wiener-Khinchin Theorem we have

$$\langle \hat{a}^\dagger(\tau)\hat{a}(0)\rangle = \bar{n}\kappa\int_{-\infty}^{\infty}\frac{d\omega}{2\pi}e^{-i\omega\tau}\frac{1}{(\omega+\omega_c)^2+\kappa^2} = \int_{-\infty}^{\infty}\frac{d\omega}{2\pi}e^{-i\omega\tau}S_{\hat{a}\hat{a}}[\omega]. \tag{B.14}$$

Thus we identify the NSD of operator $\hat{a}$ as

$$S_{\hat{a}\hat{a}}[\omega] = \frac{\bar{n}\kappa}{(\omega + \omega_c)^2 + \kappa^2}, \tag{B.15}$$

which is peaked around the *negative* freqency $\omega = -\omega_c$ and can be understood to represent the ability of the cavity to emit energy. Similarly, one obtains for the creation operator $\hat{a}^\dagger$

$$S_{\hat{a}^\dagger\hat{a}^\dagger}[\omega] = \frac{(\bar{n} + 1)\kappa}{(\omega - \omega_c)^2 + \kappa^2}, \tag{B.16}$$

which is peaked around positive frequency ω_c and represents the ability of the cavity to absorb energy. Generally from these NSDs one can analogously evaluate the NSD $S_{\hat{x}_\lambda\hat{x}_\lambda}[\omega]$ of any quadrature $\hat{x}_\lambda = (\hat{a}e^{-i\lambda} + \hat{a}^\dagger e^{i\lambda})/\sqrt{2}$ of the cavity field to study the frequency spectrum of the noise-power emitted by the cavity in a quadrature (amplitude with $\lambda = 0$, phase with $\lambda = \pi/2$) of interest. A similar interpretation holds in the case of an acoustic cavity mode, in which one may be interested in the cavity mode noise power in the position ($\lambda = 0$) or momentum ($\lambda = \pi/2$) quadrature.

Appendix C

FIRST MARKOV APPROXIMATION IN A DISSIPATIVE OPEN SYSTEM

In the context of open quantum systems, the First Markov Approximation can be understood as the statement that the timescales over which correlations in the bath decay are fast compared to the dynamics of the system of interest. In other words, the bandwidth of the bath is considered to be large relative to the rates of the system, such that the bath thermalizes among itself faster than its interactions with the system. We illustrate the usual Markov Approximation using a simplified example system consisting of a discrete ground state $|g\rangle$ at frequency ω_g coupled to a continuum of "bath" excited states $|f_\omega\rangle$ having bandwidth $\Delta\omega$. Using the Markov Approximation, we show that the presence of the bath introduces a decay term to the ground state population as well as an effective Lamb shift of the ground state [159]. We assume the system is pumped coherently at frequency ω, and we can write the system Hamiltonian as

$$\hat{H} = \hbar\omega_g \left|g\right\rangle \left\langle g\right| + \hbar \int d\omega_f \, \omega_f \left|f_\omega\right\rangle \left\langle \omega_f\right| + \hbar \int d\omega_f \, W_f(\omega_f)(\left|g\right\rangle \left\langle f_\omega\right| e^{i(\omega t+\phi_f)} + \left|f_\omega\right\rangle \left\langle g\right| e^{-i\omega t+\phi_f}). \tag{C.1}$$

The terms $W_f(\omega_f)$ are generalized coupling terms representing the dipole interaction matrix element between the $|g\rangle$ and $|f\rangle$ states, and are in general frequency-dependent. Writing the Schrödinger-picture state as a linear combination of energy eigenstates of $\hat{H}$,

$$\left|\Psi(t)\right\rangle = b_g(t)e^{i\omega_g t}\left|g\right\rangle + \int d\omega_f \; b_f(t)e^{-i\omega_f t}\left|f\right\rangle, \tag{C.2}$$

where the time-dependent coefficients $b_g(t)$ and $b_f(t)$ respectively represent probability amplitudes for the ground and bath states. The Schrödinger equation then gives coupled differential equations for these coefficients:

$$\dot{b}_g(t) = -i \int d\Delta_f \; W_f e^{i\phi_f} b_f(t)e^{-i\Delta_f t} \tag{C.3}$$

$$\dot{b}_f(t) = -iW_f e^{-i\phi_f} b_g(t) e^{i\Delta_f t}, \tag{C.4}$$

where $\Delta_f \equiv (\omega_f - \omega_g) - \omega$ is the transition-pump detuning. Assuming the system is initialized in the state $|\Psi(0)\rangle = |g\rangle$ such that $b_f(0) = 0$, we may formally integrate (C.4) to obtain

$$b_f(t) = -iW_f e^{-i\phi_f} \int_0^t dt'\; b_g(t') e^{i\Delta_f t'}. \tag{C.5}$$

Inserting this into (C.3) gives

$$\begin{aligned} \dot{b}_g(t) &= -i \int d\Delta_f\; W_f e^{i\phi_f} \left(-iW_f e^{-i\phi_f} \int_0^t dt'\; b_g(t') e^{i\Delta_f t'} dt' \right) e^{-i\Delta_f t} \\ &= -\int_0^t dt' \underbrace{\left[\int d\Delta_f\; W_f^2 e^{-i\Delta_f (t-t')} \right]}_{\equiv K(t-t'),\ \text{Kernel}} b_g(t'). \end{aligned} \tag{C.6}$$

Now, in order to evaluate this we make the Markov Approximation by assuming that the coupling term W_f^2 is approximately constant over the bandwidth Δ_ω. This is equivalent to requiring that the kernel $K(t - t')$ is narrow compared to timescales $\tau = t - t' > 1/\Delta\omega$. Then the kernel is approximately a delta function, and we can write

$$\begin{aligned} \dot{b}_g(t) &= -\int_0^t dt'\; K(t - t') b_g(t') \simeq -b_g(t) \int_0^t d\tau\; K(\tau) \\ &\simeq -b_g(t) \lim_{\epsilon \to 0^+} \int_0^\infty d\tau\; K(\tau) e^{-\epsilon\tau}, \end{aligned} \tag{C.7}$$

where we have taken the limit to ensure convergence. This limit can be evaluated as

$$\begin{aligned} &\lim_{\epsilon \to 0^+} \int_0^\infty d\tau\; K(\tau) e^{-\epsilon\tau} = \lim_{\epsilon \to 0^+} \int_0^\infty d\tau \left(\int_0^\infty d\Delta_f\; W_f^2 e^{-i\Delta_f \tau - \epsilon\tau} \right) \\ &= \lim_{\epsilon \to 0^+} \int_{-\infty}^\infty d\Delta_f\; W_f^2 \left(\frac{e^{-i\Delta_f \tau - \epsilon\tau}}{-i\Delta_f - \epsilon} \Big|_{\tau=0}^\infty \right) = -i \lim_{\epsilon \to 0^+} \int d\Delta_f \frac{W_f^2}{\Delta_f - i\epsilon} \\ &= \pi W_f^2(\Delta_f = 0) - i \underbrace{\mathbb{P} \int d\Delta_f\; \frac{W_f^2}{\Delta_f}}_{-\delta\omega}, \end{aligned} \tag{C.8}$$

with $\mathbb{P}(\cdot)$ denoting the Cauchy principal value. Note that the term identified as $\delta\omega$ is divergent, and a full treatment in the formalism of QED is necessary to recover convergence in general. Then the time derivative of the ground state population is given within the Markov Approximation by

$$\dot{b}_g(t) \cong -(\pi W_f^2(0) + i\delta\omega) b_g(t), \tag{C.9}$$

and we have a decay term given by the square of the bath coupling matrix element, as well as an effective Lamb shift $\hbar\delta\omega$ to the ground state energy.

INDEX